Development of Methodology for treating Pressure Waves from Explosions accounting for Modeling and Data Uncertainties

Dissertation
for the award of the degree of

Doktoringenieur (Dr.-Ing.)

by **Arizal, M.Sc.**
born on September 22nd, 1980 in Batusangkar, Indonesia

accepted by the Faculty of Process and Systems Engineering
of the Otto-von-Guericke-University of Magdeburg

Reviewer: **Prof. Dr.-Ing. habil. Dr. h.c. Ulrich Hauptmanns**
Prof. Dr. rer. nat. habil. Axel Schönbucher
Dr.-Ing. Bernd Broeckmann

submitted on: July 1st, 2012

Graduation Colloqium on: August 23rd, 2012

Acknowledgments

The work for this thesis has been carried out at the Department of Process Design and Safety, the Institute of Process Equipment and Environmental Engineering, the Faculty of Process and Systems Engineering, the Otto-von-Guericke-University of Magdeburg, Germany.

First of all, let me express my sincere gratitude to my advisor, Professor Ulrich Hauptmanns, for his continuing support, advices, knowledges and insightful discussions as well as encouragement throughout my studies. I thank him for introducing me to this exciting field of study. His lively, enthusiastic and energetic has always inspired me in my career and life.

I would like to thank the other members of the promotion committee, in particular to Professor Axel Schönbucher, the University of Duisburg-Essen, and Dr. Bernd Broeckmann, the Managing Director of the Inburex Consulting GmbH, for being kindly refereeing my thesis. All important advices have certainly improved the quality of this report. I am thankful to Professor Eckehard Specht for being the chairman of the promotion committee.

To all my colleagues, both the present and former members of the Department: Dieter Gabel, Alex Bernhardt, Sebastian Jung, Sascha Grünbeck, Pascal Pöschko, Marcus Marx, Darek Jablonski and Jan Kleinert, thank you so much for the friendship and continuing support. I am particularly grateful for the discussions and suggestions. A special thank you goes to Professor Ulrich Krause for his support and motivation especially during the last few months of my stay at the Department. To Mrs. Fietz and Nancy, thank you very much for helping me with all organizational and administration problems that certainly make things much easier. To my colleagues at the INBUREX Consulting GmbH Hamm at which I spent several months before completing this thesis, I want to express my great appreciation to their supports and believe in me.

Many other friends have always inspired me and provided many helps during my stay in Magdeburg and Hamm. I greatly value and deeply appreciate this friendship. Thank you very much for such a nice time.

Last but not least, and perhaps the most important one in my life, I want to thank my family in Indonesia to whom I dedicate this thesis. I believe that none of this would have been possible without their endless moral support and patience. My parents have always been a constant source of motivation and strength for me all these years.

This thesis is dedicated to my parents and my brother
for their endless love and support throughout my life.
May God bless you all.

Declaration

I hereby declare that I prepared the work submitted without inadmissible assistance and without the use of any aids others than those indicated. Fact or ideas taken from other sources, either directly or indirectly have been marked as such.

In particular, I did not use the services of a commercial graduation consultation. Further I have not made payments to third parties either directly or indirectly for any work connected with the contents of the submitted dissertation.

The work has not so far submitted either in Germany or abroad in same or similar form as a dissertation and has also not yet been published as a whole.

Magdeburg, July 1st, 2012

Arizal

Abstract

This thesis analyses and presents the methodology for the treatment of blast waves from a vapor cloud explosion accounting for modeling and data uncertainties. In fact, there is no unified method for treating blast waves from a vapor cloud explosion. In this thesis, three empirical models, the TNT equivalent models, the TNO Multi-Energy model and the Baker-Strehlow-Tang model, have been reviewed and compared.

The blast propagation has been modeled by the Euler equations of gas dynamics which is solved numerically using by the Godunov scheme. A developed computer program incorporates the exact Riemann solver for evaluating the solution of the local Riemann problem at the cell interface boundary. It has been demonstrated that the solver can estimate the physical variables of the blast wave, including the pressure, density, velocity and temperature, at certain distances relative to the center of the blast source.

With respect to the implementation of the blast solver, the initial conditions of the blast source are required. The primitive variables such the density, velocity, pressure, temperature could have been obtained once the combustion process has been completed. However, the maximum overpressure inside the vapor cloud may also be estimated and assumed to be uniform inside the vapor cloud. Therefore, the blast wave modeling in this thesis is considered as an intermediate solution between the simple empirical models and the much more complex computational fluid dynamic models.

The determination of the maximum overpressure inside the vapor cloud as well as the prediction of the overpressure outside the vapor cloud reflects a large extent stochastically or judgment caused uncertainties. In this thesis, the integration of the uncertainty aspects into the prediction model of the blast overpressure has been proposed. In addition, the effect of uncertain parameters to the calculation of the vulnerable study for the risk assessment was also demonstrated. The implementation of the procedure in several case studies has indicated that an accurate quantification of uncertain parameters is also required for a better result.

Zusammenfassung

Die vorliegende Arbeit analysiert und stellt eine Methodik für ein Verfahren zur Modellierung der Druckwelle einer Dampfwolken-Explosion (VCE) vor. Dabei werden Modell- und Datenunsicherheiten bercksichtigt. Es gibt keine einheitliche Methode zur Berechnung von Druckwellen einer Dampfwolken-Explosion. In dieser Arbeit wurden drei empirische Modelle, das TNT-Äquivalent-Modell, das TNO Multi-Energy-Modell und die Baker-Strehlow-Tang Modell, geprüft und verglichen.

Die Druckwelle wurde durch die Euler-Gleichungen der Gasdynamik, numerisch mit Hilfe des Godunov Schema modelliert. Dabei wurde ein Computerprogramm zur exakten Lösung des Riemann-Problems an den Zellgrenzen entwickelt. Es wurde gezeigt, dass das Programm die physikalischen Größen Druck, Dichte, Geschwindigkeit und Temperatur der Druckwelle in definierten Abständen zur Quelle wiedergibt.

Im Hinblick auf die Umsetzung der Lösungsbeziehung für die Explosion sind die Anfangsbedingungen der Explosionsquelle erforderlich. Die grundlegenden Variablen wie Dichte, die Geschwindigkeit, der Druck und die Temperatur hätte berechnet werden können, wenn der Verbrennungsprozess abgeschlossen wäre. Jedoch kann der maximale Überdruck im Inneren der Dampfwolke auch abgeschätzt werden, wobei dieser als einheitlich in der Dampfwolke angenommen wird. Daher wird die Druckwellenmodellierung in dieser Arbeit als Zwischenlösung zwischen den einfachen empirischen Modellen und den sehr viel komplexeren CFD Modellen angesehen.

Die Bestimmung des maximalen Überdruck im Inneren der Dampfwolke sowie die Vorhersage des Überdruckes außerhalb der Dampfwolke spiegeln einen großen Teil der stochastisch oder auch ingenieurmäßige Abschätzung bedingten Unsicherheiten wider. In dieser Arbeit wurde die Integration der Unsicherheiten in das Prognosemodell des Explosionsüberdruckes vorgeschlagen. Darüber hinaus wurde auch die Wirkung von unsicheren Parameter für die Berechnung des betrachten Falles zur Bewertung des Risikos gezeigt. Die Anwendung des Verfahrens in mehreren Fallstudien hat gezeigt, dass eine genaue Quantifizierung von unsicheren Parametern für vertrauenswürdigere Ergebnisse erforderlich ist.

Table of Contents

Acknowledgments i

Declaration v

Abstract vii

Zusammenfassung viii

Table of Contents ix

List of Figures xiii

List of Tables xix

List of Symbols and Abbreviations xxi

1 Introduction 1

1.1 The background, motivation and scope 1

1.2 Thesis objectives 4

1.3 Thesis overview 4

2 Explosions in the Chemical Process Industries 6

2.1 The explosion phenomena 6

2.2 Explosions in the chemical process industries 7

2.2.1 Physical explosions 7

2.2.2 Chemical explosions 8

2.3 Mechanisms of deflagration and detonation 9

2.3.1 The premixed combustion 11

2.3.2 Deflagration phenomena 13

2.3.3 Detonation phenomena 18

2.3.4 Vapor cloud explosions in history 21

2.4 Explosion blast phenomena 25

3 Estimation of the Blast Wave Parameters by means of Empirical Techniques 31

3.1 The TNT equivalent model . . . 32
3.1.1 The TNT equivalent concept . . . 32
3.1.2 Important procedures . . . 34
3.1.2.1 Determination of the TNT equivalent mass . . . 34
3.1.2.2 TNT blast curves . . . 36
3.1.2.3 Important consideration for the application of the TNT equivalent model for the blast analysis of vapor cloud explosions . . . 41
3.2 The TNO Multi-Energy model . . . 43
3.2.1 Critical points with regard to the TNT equivalent model for the vapor cloud explosion analysis . . . 43
3.2.2 The Multi-Energy concept . . . 44
3.2.3 Important procedures . . . 45
3.2.3.1 Determination of the size of the blast source . . . 48
3.2.3.2 Determination of the initial strength of the blast source . . . 50
3.2.3.3 Fitted equations of the TNO Multi-Energy blast curve family . . . 55
3.3 The Baker-Strehlow-Tang model . . . 56
3.3.1 The basic concept of the Baker-Strehlow-Tang . . . 56
3.3.2 The important procedures . . . 58
3.3.2.1 Determination of the flame Mach number . . . 58
3.3.2.2 Fitted equations for the Baker-Strehlow-Tang blast curve family . 60

4 Modeling of the Propagation of the Blast Waves 62

4.1 Governing equations of the blast wave propagation . . . 62
4.1.1 The general expression of the Euler equations system . . . 63
4.1.2 The Euler equations system in the differential form . . . 65
4.1.3 Thermodynamic considerations . . . 67
4.1.3.1 Equation of state of ideal gases . . . 67
4.1.3.2 Thermodynamic considerations for a polytropic gas . . . 71
4.2 The Riemann Problem for the Euler equations . . . 72
4.2.1 Introduction to the Riemann problem and the exact Riemann solver . . . 72
4.2.2 Hyperbolic properties of the Euler equations of gas dynamics . . . 74
4.2.3 Basis structure of the Riemann waves . . . 75
4.2.4 Sampling procedure . . . 81
4.2.5 Important remarks to solve the multi-dimensional Riemann problem using the exact Riemann solver . . . 86
4.2.6 Testing the exact Riemann solver: The benchmark solution of Sod's shock tube problem . . . 87

4.3 Numerical solutions of the Euler equations using the finite volume method: The Godunov scheme . . . 89
4.3.1 The initial boundary value problem of the one-dimensional Euler equations 91
4.3.2 The discretization of the spatial and temporal domain . . . 91
4.3.3 The discretization of the Euler equations . . . 92
4.3.4 Determination of the numerical fluxes at the cell interface boundaries: the local Riemann problem . . . 95
4.3.5 Numerical solutions of the non-homogeneous equations: the integration of the source terms . . . 98
4.3.6 The procedure for solving the multi-dimensional time-dependent Euler equations of gas dynamics . . . 100
4.4 Implementation of the solver for simulating the blast wave propagation . . . 103
4.4.1 One-dimensional case in Cartesian coordinates system: The shock tube problem . . . 103
4.4.1.1 Sod's shock tube problem . . . 103
4.4.1.2 Testing some other recommended wave propagation problem in tube 103
4.4.2 One-dimensional case in spherical coordinates system: The spherically symmetric wave motion . . . 110
4.4.3 Two-dimensional cases in Cartesian coordinates system . . . 113
4.4.3.1 Test case I . . . 113
4.4.3.2 Test case II . . . 114

5 Uncertainties and the Calculation of the Blast Overpressure and Explosion Risk 123

5.1 Mathematical treatment of uncertainties . . . 123
5.1.1 Introduction . . . 123
5.1.2 Methods of representing and evaluating the uncertainty . . . 124
5.1.3 Techniques for the propagation and evaluation of uncertainty . . . 125
5.2 Relevant aspects for the risk assessment . . . 126
5.2.1 Event trees for representing typical events following the release incident . . 126
5.2.2 Vulnerability models for assessing the damage of the blast wave . . . 131
5.2.2.1 The probit function and damage probability . . . 131
5.2.2.2 Models for the probit function for the effect of the blast overpressure to the people . . . 133
5.3 Methodology for accounting uncertainties for the calculation of the explosion risk . 135
5.3.1 Important aspects to the determination of the blast overpressure . . . 135
5.3.2 Important aspects with regard to the probability distribution of the uncertain parameters . . . 136
5.4 Illustration example for the implementation of the procedure . . . 138
5.4.1 The vulnerability study for the risk assessment . . . 138

5.4.2 The determination of the maximum explosion and blast wave overpressure . 142

6 Conclusions and Outlook **149**

6.1 Conclusions 149

6.2 Outlook and recommendations 150

Bibliography **151**

Appendix A: Kingery-Bulmash Model **161**

Appendix B: Constants for the equations of the Blast curves **164**

B.1 Constants for the fitted equations for the TNO Multi-Energy blast curve family . . 164

B.2 Constants for the fitted equations for the Baker-Strehlow-Tang blast curve family . 165

Appendix C: Computational flow for solving the Euler equations of gas dynamics **167**

C.1 The Exact Riemann Solver Module 167

C.2 The Euler Equations Solver Module 168

List of Figures

Fig. 1.1 Typical important stages in performing the engineering risk analysis 2

Fig. 2.1 Explosion types with respect to the type of energy release 7

Fig. 2.2 Accidental sequences following the loss of process containment containing pressurized gases 9

Fig. 2.3 Accidental sequences following the loss of process containment containing pressurized liquefied gases/vaporizing liquids. If a proportion of the vapor cloud rains out, a pool of liquid is created. Therefore, in addition to the specified effects shown in this diagram, the possible of pool fire may also be added to the specified accidental outcomes. 10

Fig. 2.4 Composition of the fuel in the cloud must be within the boundaries of the explosion limits in order to get explosive. Otherwise, explosion would hardly to occur. 11

Fig. 2.5 Typical ranges of explosion limits for some hydrocarbon/hydrogen-air mixtures at 1 atm and 25^0C 11

Fig. 2.6 Illustration of the combustion process in a tube which is open at one end and closed at the other. (a) the ignition takes place at the open end, while (b) the ignition takes place at the closed end. 12

Fig. 2.7 Distribution of the temperature during a deflagration of a flammable mixture 14

Fig. 2.8 Overpressure as a function of flame speed for three different geometries. The relationships are based on calculations by use of a self-similar solution 16

Fig. 2.9 The generation of the turbulent flow field ahead of the flame front inside a channel with repeated obstacles 18

Fig. 2.10 Positive feedback loop causing the acceleration of the flame speed due to the presence of the turbulent flow field ahead the flame front 18

Fig. 2.11 A general event tree that shows typical accidental outcomes which may occur after the release of the flammable gas or vaporizing liquid into the atmosphere subsequently followed by the formation of the flammable gas or vapor cloud 22

Fig. 2.12 A view of the BP Texas city refinery after the explosion took place on 23rd March 2005 24

Fig. 2.13 A dramatic picture of the early stage of the Buncefiled smoke plume 24
Fig. 2.14 Illustration of three general shapes of the explosion blast wave as a function of time evaluated at a fixed location some distance to the center of explosion and the pressure is above ambient. (a) shock wave, (b) sonic compression wave and (c) rarefaction wave. 26
Fig. 2.15 Illustration of the flame propagation mechanism and the generation of pressure wave during detonation and deflagration of the flammable cloud. For both cases, the combustion reaction is initiated to the far away left 27
Fig. 2.16 A typical form of an explosion blast wave with a sudden shock front at a fixed time. In this figure, the development of pressure amplitude as a function of distance to the center of explosion (i.e. blast origin) is shown 28
Fig. 2.17 A typical form of the blast wave with a sudden shock front at a fixed location some distance from the center of explosion (the blast origin) 28
Fig. 2.18 A typical blast wave without having a shock front at a fixed location some distance from the blast origin 29
Fig. 2.19 Approximation to the positive impulse of blast waves by means of a triangular shape 30

Fig. 3.1 2,4,6-Trinitrotoluene (TNT) with the chemical formula $C_7H_5N_3O_6$ 33
Fig. 3.2 Representation of the TNT blast curves according to the Brode, Kingery-Bulmash, Kinney-Graham and Henrych correlation models 41
Fig. 3.3 The idealized hemispherical vapor cloud as the basis for the TNO Multi-Energy model 46
Fig. 3.4 The Multi-Energy blast curve for the scaled peak side-on overpressure as a function of the Sach's scaled distance 47
Fig. 3.5 The Multi-Energy blast curve for the scaled positive phase duration as a function of the Sach's scaled distance 48
Fig. 3.6 The TNO Multi-Energy blast curve family for the scaled overpressure 55
Fig. 3.7 The idealized spherical vapor cloud as the basis for the Baker-Strehlow-Tang model 56
Fig. 3.8 Scaled peak side-on overpressure as a function of the Sach's scaled distance for different flame speeds in terms of its Eulerian Mach number (M_f) 57
Fig. 3.9 Sach's scaled positive impulse as a function of the Sach's scaled distance for different flame speeds in terms of its Eulerian Mach number (M_f) 57
Fig. 3.10 Sach's scaled arrival time as a function of the Sach's scaled distance for different flame speeds in terms of its Eulerian Mach number (M_f) 58
Fig. 3.11 The Baker-Strehlow-Tang blast curve family for the scaled overpressure . . . 61

Fig. 4.1 Illustration of the initial configuration of the shock tube problem. The Riemann problem of the one-dimensional time-dependent Euler equations of gas dynamics is the generalization of this particular problem 74
Fig. 4.2 The generated wave structure after the removal of the thin diaphragm at time $t = 0$ for the shock tube problem illustrated in Fig. 4.1 76
Fig. 4.3 Possible Riemann waves configurations as the solution of the Riemann problem for the one-dimensional problem 77
Fig. 4.4 A complete structure of the Riemann wave solution for the shock tube problem initially illustrated by Fig 4.1 78
Fig. 4.5 Transformation of the shock tube and Riemann problem coordinate system as a basis for the sampling procedure. 82
Fig. 4.6 Procedure for determining the primitive variables at the sample point (x, t) where $x_L < x < x_R$ and $t > 0$ and the initial discontinuity is located at $x = x_0$. 83
Fig. 4.7 Illustration of four possible wave configurations for the evaluation of the sample point (x, t) 84
Fig. 4.8 Structure of the solution of the three-dimensional split Riemann problem in $x-$direction 87
Fig. 4.9 Initial configuration of Sod's shock tube problem 88
Fig. 4.10 Benchmark solutions of Sod's shock tube problem. In this figure, the physical primitive variables and specific internal energy at time $t = 0.015$ seconds after the break of the diaphragm are shown. 90
Fig. 4.11 Discretized one-dimensional domain which is presented in $x - t$ plane 92
Fig. 4.12 Discretization of the one-dimensional spatial domain in $x-t$ plane for a single time step 93
Fig. 4.13 Illustration of a piecewise constant distribution of the data $\mathbf{Q}$ at time level n 94
Fig. 4.14 The evolution of the solution of the conserved variables for the cell I_i from the time level n to the time level $n + 1$ using the Godunov numerical scheme. 95
Fig. 4.15 The local Riemann problem at the cell interfaces $i - \frac{1}{2}$ and $i + \frac{1}{2}$ in $x - t$ plane. 96
Fig. 4.16 Determination of the solution of the local Riemann problem in terms of primitive variables ($\mathbf{W}$) at the cell interface boundary 97
Fig. 4.17 Fictitious cells outside the computational domain for the one-dimensional case. 98
Fig. 4.18 Finite volume discretization of Cartesian domain (two dimensional case) . . 101
Fig. 4.19 General flow chart for the numerical simulation of the Euler equations of gas dynamics which is used in this thesis 102
Fig. 4.20 Exact and numerical solutions of Sod's shock tube problem at at time $t =$ 0.015 seconds after the break of the diaphragm 104
Fig. 4.21 Exact and numerical solutions of the tube problem case T1 at time $t = 0.15$ units 106

Fig. 4.22 Exact and numerical solutions of the tube problem case T2 at time $t = 0.012$ units . . . 107
Fig. 4.23 Exact and numerical solutions of the tube problem case T3 at time $t = 0.035$ units . . . 108
Fig. 4.24 Exact and numerical solutions of the tube problem case T4 at time $t = 0.035$ units . . . 109
Fig. 4.25 Initial configuration for a spherically symmetric wave motion. The fictitious balloon with a radius of r_0 is considered as the source of blast (driven section). 111
Fig. 4.26 Numerical simulation results for a spherically symmetric blast wave propagation. 112
Fig. 4.27 Blast overpressures (bar) with respect to the distance relative to the outer boundary of the spherical source for the test problem under consideration . . 113
Fig. 4.28 Initial conditions for the two-dimensional case of Euler equations of gas dynamics 115
Fig. 4.29 Simulation results at $t = 0.1$ units. . . . 116
Fig. 4.30 Simulation results at $t = 0.2$ units. . . . 117
Fig. 4.31 Simulation results at $t = 0.3$ units. . . . 118
Fig. 4.32 Initial conditions for the second test case of the two-dimensional Euler equations 119
Fig. 4.33 Simulation results for the pressure and temperature at $t = 0.004$ s after the burst . . . 120
Fig. 4.34 Simulation results for the pressure and temperature at $t = 0.008$ s after the burst . . . 121
Fig. 4.35 Simulation results for the pressure and temperature at $t = 0.012$ s after the burst . . . 122

Fig. 5.1 Propagation of uncertainty parameters through a model . . . 125
Fig. 5.2 Event tree for an instantaneous release of a pressurized gas or vaporizing liquid 127
Fig. 5.3 Event tree for a continuous release of a pressurized gas or vaporizing liquid . 127
Fig. 5.4 Event tree for a flammable liquid release . . . 128
Fig. 5.5 Event tree showing the probability of the ignition of the vapor cloud according to the result of a statistical analysis . . . 130
Fig. 5.6 Relationship between the damage probability P_d (%) and the probit variable Y 134
Fig. 5.7 The probability of the lung damage and the ear drum rupture due to the explosion blast wave overpressure. . . . 135
Fig. 5.8 Probability density function of the uniform distribution . . . 137
Fig. 5.9 Probability density function of the normal distribution . . . 137
Fig. 5.10 Probability density function of the log-normal distribution . . . 138
Fig. 5.11 Illustration of the wind distribution if no prior information is given. It is assumed that the wind is distributed uniformly to all directions. . . . 139
Fig. 5.12 The calculation area for the estimation of explosion risk using probabilistic approach for a single step of Monte Carlo simulation from M trials . . . 140

Fig. 5.13 The calculation of the individual risk based on the explosion blast overpressure versus stand-off distance relative to the initial release point using conservative method. The first peak: ignition location 1 about 55 m from the source, and the second peak: ignition location 2 about 550 m from the source 141
Fig. 5.14 The calculation of the individual risk based on the explosion blast overpressure versus stand-off distance relative to the initial release point using Monte-Carlo method for which the location of ignition is subject to uncertainty. 142
Fig. 5.15 Impression of large process vessel in the heat exchanger unit. 143
Fig. 5.16 Impression of connecting pipework in the heat exchanger unit. 143
Fig. 5.17 The maximum explosion overpressure of the propane cloud in the heat exchanger unit if the parameter of volume blockage ratio, flame path length and obstacles density are subject to uncertainty. 145
Fig. 5.18 Simulation results for the blast wave propagation due to an explosion in the heat exchanger unit 148

This page intentionally left blank

List of Tables

Table 2.1 Basic combustion properties of some gases or vaporizing liquids in air under atmospheric conditions 15
Table 2.2 Basic detonation properties of some common conventional high explosives . . 20
Table 2.3 Comparison of the minimum ignition energy (MIE) for a deflagration and detonation 21
Table 2.4 Detonation velocities of some flammable gases in air 21

Table 3.1 The ratio of the explosion energy of several common chemical explosives (α_e) 35
Table 3.2 Heat of combustion of several hydrocarbon fuel-air mixtures 36
Table 3.3 Typical explosion efficiencies for modeling vapor cloud or gas explosions and their conditions 37
Table 3.4 Stoichiometric concentrations and volumetric heat of combustions for common hydrocarbons and hydrogen assuming that the fuels are homogeneously and stoichiometrically mixed with air at atmospheric conditions 49
Table 3.5 Effect of confinement to the flame expansion 52
Table 3.6 Classification of the obstacle density 53
Table 3.7 Matrix for the qualitative selection of the initial blast strength of the flammable gas or vapor cloud for the use of the TNO Multi-Energy blast curve 53
Table 3.8 Parameters for the determination of the correlation for the maximum explosion overpressure of the vapor cloud 54
Table 3.9 Constants for Eq. (3.26) 55
Table 3.10 Matrix for the qualitative selection of the flame speed in terms of the Lagrangian Mach number (M_w) for the use of the Baker-Strehlow-Tang blast curve family 58
Table 3.11 The relationship between the Lagrangian Mach number, the Eulerian Mach number and the maximum explosion overpressure 60

Table 4.1 Important thermodynamic variables of air for solving the Euler equations . . 88
Table 4.2 Initial conditions of additional tube problems for testing the performance of the numerical Godunov solver 105

Table 4.3 Short summary of numerical solutions of additional tube problems and their wave solution characteristics 105

Table 5.1 Some statistical data of the release incident frequency 129
Table 5.2 Example of the database for the immediate ignition probability for stationary installations 130
Table 5.3 Typical scales of damage caused by different levels of blast peak overpressures 132
Table 5.4 Material properties and other required data for testing the procedure 138
Table 5.5 Distribution of the location of the ignition points 141
Table 5.6 Dimension of large process vessels and major supports in the heat exchanger unit 144
Table 5.7 Dimension of connecting pipes in the heat exchanger unit 144
Table 5.8 Specification of uncertain parameters for the determination of the maximum explosion over-pressure in the heat exchanger unit 145
Table 5.9 Statistical parameters for the maximum explosion overpressure (bar) 146
Table 5.10 Data for the estimation of blast overpressure outside the propane vapor cloud 146
Table 5.11 Estimated overpressure (bar) at various stand-off distances from the center of the vapor cloud 147

Table A.1 Constants used in Kingery-Bulmash polynomial equations for a free air burst 162
Table A.2 Constants used in Kingery-Bulmash polynomial equations for a surface air burst 163
Table B.1 Coefficients for Eq. (3.27) 164
Table B.2 Coefficients for Eq. (3.33) 166

List of Symbols and Abbreviations

Latin Letters

$\Delta\overline{p_s}$	The scaled peak overpressure, used in the Multi-Energy blast curve	-
$\Delta H_{c,\mathsf{f}}$	The heat of combustion of the flammable fuel	$\mathrm{kJ.kg^{-1}}$
$\Delta H_{c,\mathsf{vol}}$	Volumetric heat of combustion of the fuel in the flammable gas or vapor cloud	$\mathrm{J/m^3}$
$\Delta H_{d,\mathsf{ex}}$	The heat of detonation of the chemical explosive	$\mathrm{kJ.kg^{-1}}$
$\Delta H_{d,\mathsf{TNT}}$	The heat of detonation of the TNT charge	$\mathrm{kJ.kg^{-1}}$
Δp_s	The scaled overpressure, used in the TNT blast curves	-
$\mathbf{C}_{\mathsf{cfl}}$	Courant-Frederich-Lewy coefficient	-
$\mathbf{EF}$	TNT mass equivalent factor	-
$\mathcal{R}$	Universal molar gas constant	J/mol/K
$\overline{i_s}$	Dimensionless Sach's scaled positive impulse	-
$\overline{R}$	Dimensionless Sach's scaled distance	-
A	Pre-exponential factor of the *Arrhenius law*	
a	Correlation constant for the Kingery-Bulmash TNT blast model	
a_0	Speed of sound at ambient condition	m/s
b	Correlation constant for the Kingery-Bulmash TNT blast model	
c	Correlation constant for the Kingery-Bulmash TNT blast model	
c_s	Stoichiometric concentration of the flammable fuel in the gas or vapor cloud	vol.%
E_a	Activation energy of the reaction	J/mol
E_c	Explosion energy of the flammable gas or vapor cloud	J
f_{rel}	Release incident frequency	yr^{-1}

f_{VCE}	Frequency of the vapor cloud explosion	yr^{-1}
i_p	Positive impulse	Pa.s
i_s	Hopkinson's scaled impulse	$\text{Pa.s}^2.\text{kg}^{-1/3}$
k	Chemical reaction rate	
k_1	Constant of probit equation	
k_2	Constant of probit equation	
M_f	Langragian Mach number	-
M_w	Eulerian Mach number	-
P_d	Damage probability percentage	%
p_{dim}	Probability of a late/delayed ignition	-
p_{im}	Probability of an immediate ignition	-
p_{VCE}	Probability of the explosion given that the vapor cloud is ignited	-
p_{VCE}	Probability that a vapor cloud explosion will occur	-
R	The stand-off distance of the object of interest relative to the blast origin	m
R_0	The initial radius of a hemispherical gas or vapor cloud with a volume V_c	m
S_F	Flame speed	m/s
S_L	Laminar burning velocity	m/s
T	Temperature (in general)	^{0}C,K
u	x-component of velocity	
$U(z)$	Intermediate functions to be used for the Kingery-Bulmash TNT blast model	
u_u	Velocity of the unburned mixture	m/s
v	y-component of velocity	
V	Causative variable representing different impacts	
V_b	Volume of the burned mixture	m^3
V_c	Volume of the flammable gas or vapor cloud	m^3
V_u	Volume of the unburned mixture	m^3
w	z-component of velocity	
$W_{e,\mathsf{f}}$	The flammable mass of the gas or vapor cloud	kg
W_e	The given mass of the explosive material	kg
W_T	TNT equivalent mass	kg
Y	Probit variable	-
z	Hopkinson's scaled distance	$\text{m/kg}^{1/3}$

Greek Letters

α_{exp}	Expansion ratio of the combustion	-
α_e	Ratio of the explosion energy of the material to the TNT blast energy	-
β	Wave form parameter	-
η	Explosion efficiency factor	-
$\overline{\tau}_a$	Dimensionless Sach's scaled arrival time	-
$\overline{\tau}_d$	Dimensionless Sach's scaled positive phase duration	-
ϕ	Function for the TNT blast parameter of interest (the Kingery-Bulmash TNT blast model)	
ρ_b	Mass density of the burned mixture	kg/m^3
ρ_f	Vapor density of the flammable fuel in the gas or vapor cloud	kg/m^3
ρ_u	Mass density of the unburned mixture	kg/m^3
τ_d	Hopkinson's scaled positive phase duration	$s/kg^{1/3}$

Abbreviations

ANFO	Ammonium Nitrate Fuel Oil
BLEVE	Boiling Liquid Expanding Vapor Cloud Explosion
DDT	Deflagration-to-detonation transition
HMX	High-velocity Military Explosive, or High-Molecular-weight RDX
IVP	Initial Value Problem
LFL	Lower Flammability Limit
MERGE	Modeling and Experimental Research into Gas Explosions
PETN	Pentaerythritol tetranitrate
RDX	Research Department Explosive/1,3,5-Trinitroperhydro-1,3,5-triazine
TNO	Nederlandse Organisatie voor Toegepast Natuur-wetenschappelijk Onderzoek
TNT	Trinitrotoluene
UFL	Upper Flammability Limit
VCE	Vapor Cloud Explosion

This page intentionally left blank

Chapter 1

Introduction

1.1 The background, motivation and scope

An explosion is generally a challenging problem, especially for the chemical process industries. As one of major hazards, an explosion is considered as a complex phenomena involving many different aspects which may not be covered entirely by currently available knowledge. It is, however, important to understand the basic situation and mechanism of these phenomena in order to deal with the potential hazard which may affect human life and the environment.

In general, with respect to the chemical process industries, the assessment of risk, either qualitative or quantitative, including the potential of explosion hazards, basically attempts to answer three typical questions, namely '*What could go wrong*?', '*What consequences can be expected*?' and '*What is the expected frequency*?'. A hazard identification and analysis study may answer the question number one, while a consequences analysis and probability study which could describe further the potential outcomes for a particular hazard and its frequency may answer the second and the third question. Typical important stages in performing the engineering risk analysis, including a simplified relationship between safety analysis, risk assessment and risk management are depicted in Fig. 1.1 [1]. As shown in this figure, the risk assessment study can describe important contributions to the overall risk that an establishment or activity poses to the people, the environment or some other vulnerable part of society. This study is started by a basic step which includes the determination of hazards. As mentioned in the Murphy's law states, "if something can go wrong, sooner or later it will". Therefore, any possible hazards which may lead to any potential major accidents must first be properly defined [2, 3].

Furthermore, the prediction of hazard levels and potential damages to the vulnerable objects is very important for the safe design of a plant. It is generally known that there are three types of major industrial hazards, namely fires, explosions and the dispersion of toxic chemicals. These hazards occur not only at fixed site facilities, such as during the storage or manufacture, but also during transportation of the materials involved [5]. Fires and explosions, in fact, have been a major concern in safety for a long time, because when anyone of them or both occur, the consequences can be very severe [6].

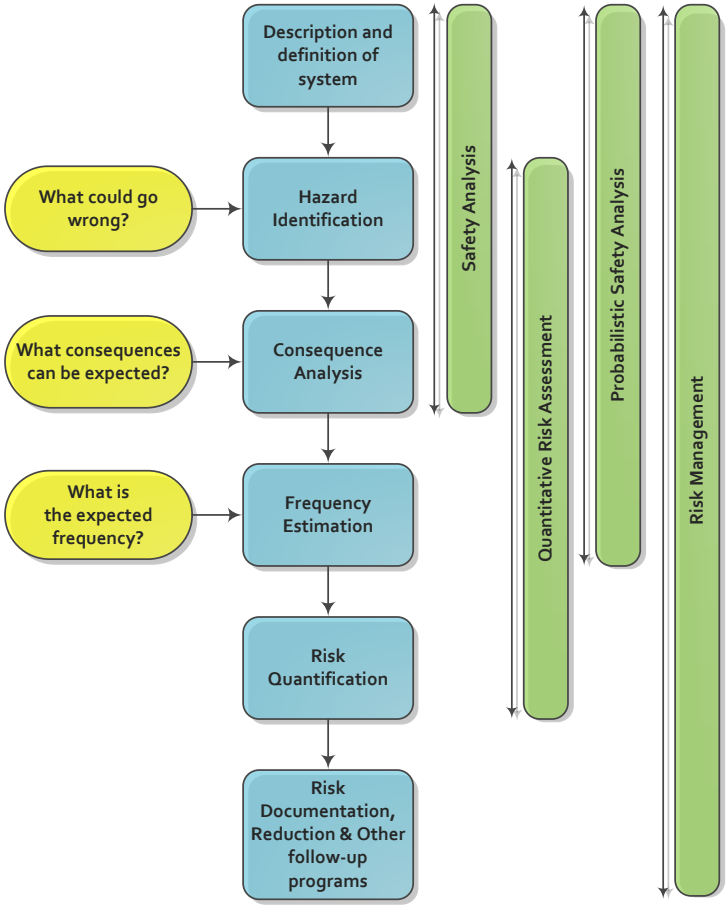

Figure 1.1. *Typical important stages in performing the engineering risk analysis [1, 4]*

Typical initiating events leading to the occurrences of these major hazards are the incidental release of a hazardous material (flammable/toxic) from its inventory or containment. This incident may be caused by any particular failure mechanism including the collapse or rupture of a tank, a process vessel or the rupture of the pipeline as well as the leak in a vessel or a hole in a pipeline. These failures can be followed, in the case of a volatile material, by its vaporization and dispersion [7]. Basically, any type of release incident, which might be instantaneous or continuous, could be succeeded by various sequential events depending on circumstances. These sequences may be related to process conditions of the material inventory or containment, the presence of one or more safety barriers, and the atmospheric (weather) conditions at the time of the release or other related factors. Each sequential path following the release may lead to a particular end scenario, which is known as accidental outcome. These outcomes may range from no or negligible consequence up to the possible three major accident categories as mentioned above [8, 9].

The three major hazard categories in the chemical process industries may still be broken down into numerous sub-categories. Each category has specific characteristics which may differ from one another. Therefore, in order to understand the possible outcome of a certain release incident, it is quite essential to properly define these sequences, which is typically done by using an event

tree. At the end, a detailed evaluation of each hazard scenario including the estimation of the potential risk to the vulnerable objects is required for taking appropriate actions to reduce their impacts. These impacts may include injury or fatality to the people, severe property damage or environmental damage. Several comprehensive measures can then be enacted to limit the likelihood of the accident. In general, these will form one of the bases for the appropriate selection of the safety integrity level (SIL).

With respect to the potential and the level of damage, explosions is considered to be the most serious safety problem in comparison to the other types of major hazard (i.e. fires or toxic dispersion). Explosion damage may not only affect the site of the explosion itself but also, according to the circumstances, may extend to much larger off-site surrounding areas. A statistical analysis to a numbers of accidents in the chemical process industries as reported in [10], has proved that explosions cause the most severe consequences, followed by fires and toxic dispersions. The same report has concluded that the probability of the accident decreases as the severity of the accident in terms of number of fatalities increases. However, for a given probability the number of fatalities for an explosion is generally higher. Another statistics study has mentioned the the average proportion of losses caused by explosions is about 67.7% against 30.2% by fires and 2.1% by toxic dispersions [11, 5]. In addition, according to circumstances, explosions may also lead to a fire and another secondary explosion. Therefore, an explosion is considered the most dangerous hazards that may occur in the chemical process industries. It should always be taken into account in the risk assessment study if any condition leading to its occurrence is present. In general, the prevention and mitigation of possible explosion have became a major priority the design and operation of process plants or other chemical installations [12, 13].

Perhaps, the most important feature of an explosion is the generation of the blast wave and damaging overpressure, which is the pressure rise above the ambient which may, at certain level, cause injury, fatality to the people, asset damage, or event escalation. The blast wave is actually the mechanical energy of the explosion that rapidly moves into the surrounding air away from the explosion origin which is the ignition point. The generation of overpressure is considered as the specific feature associated only to an explosion, which may distinguish it from a fire. The present study deals mainly with the treatment of the blast overpressure from a vapor cloud explosion. The work here has primary aimed to propose a methodology for treating the blast wave from a vapor cloud explosion by developing an efficient modeling for the blast wave propagation. Some important aspects from the empirical models are taken into account.

Another major challenge for a better prediction of the blast wave overpressure is the integration of uncertainties into the prediction methods. The use of such analyses, especially for a vapor cloud explosion is found very minimum. Currently available models do not seem to have applied these phenomena to the calculation of the blast parameters as well the assessment of vulnerability for risk studies. The treatment of uncertain parameters is actually essential for the quality and practical usability of the blast overpressure analysis. Therefore, when performing an analysis, a wide range of uncertainties will inevitably be introduced during the process.

1.2 Thesis objectives

A systematic review on the available calculation techniques for the prediction of the blast wave overpressure from vapor cloud explosions is to be addressed in the earlier stage of this thesis. A particular attention will be made to the most widely known models by means of empirical techniques. In addition, the focus of this work will turn to the development of an efficient computer program for the modeling of the blast wave propagation phenomena. The procedure for integrating the useful guidelines for estimating the maximum explosion overpressure into the modeling of the blast wave from an explosion becomes another prime goal of this thesis. At the end, it is expected that a methodology for incorporating uncertainties into the computational procedure involving the estimation of the blast overpressure can be proposed. The implementation of the procedure, for example, on the vulnerability study for the risk assessment is to be presented.

1.3 Thesis overview

The final report of this thesis consists of six chapters and several appendices. The chapters are further divided into several sections and subsections. Some of the subsections are also broken down further into several sub-subsections. These classifications have beeen systematically included into the numbering scheme as shown in the table of contents.

Chapter 1 describes the background, motivation and primary scope of the work carried out in this thesis. This chapter also covers the main and specific objectives of this thesis.

Chapter 2 presents a literature review of an explosion, in general, and vapor cloud explosions, in particular. The mechanism of the vapor cloud combustion including the difference between the detonation and deflagration is mentioned in this chapter. The important characteristics of the vapor cloud explosion and its typical consequences are presented. As the most important feature of an explosion, the blast wave phenomenon and its important properties is included in the discussion.

Chapter 3 presents the systematic review of the prediction methods of the blast wave parameters from vapor cloud explosions. The formulation, procedure of implementation, important characteristics, advantages and disadvantages of each of the models are described in much detail. The review also includes some critical points with respect to the use of the model for the work performed in this thesis.

Chapter 4 describes the modeling of the propagation of the blast wave. The procedure for solving the Euler equations of gas dynamics numerically, including the determination of the solution of the Riemann problem while dealing with discontinuity phenomena such as shock waves is presented in much better structure. The Godunov scheme on which the numerical solutions of the Euler equations has been based is introduced and implemented. The development of the blast solver for evaluating the behavior of the blast wave, including the interaction with

a certain object is included. The application for the one- and two-dimensional case is also demonstrated.

Chapter 5 describes the methodology for incorporating uncertainties into the prediction of the explosion and blast wave overpressure as well as into the vulnerability study for the risk assessment. The background of the mathematical treatment of uncertainty and method for presenting parameter uncertainty into the model is reviewed. The relevant aspects for the risk assessment study especially when the uncertainty is to be considered are mentioned. The illustration examples in several different situations including the application of the blast solver is also demonstrated.

Chapter 6 provides the conclusions and outlooks including future recommendations regarding the subject discussed in this thesis.

Chapter 2

Explosions in the Chemical Process Industries

2.1 The explosion phenomena

Basically, explosions can be defined in numerous ways. According to [14], an explosion is a sudden expansion of matter into a much larger volume than it formerly occupied. In [11] an explosion is defined as a rapid and violent release of energy for which the extent of its violence depends on the rate at which the energy is released. The rapid release of energy is considered to be the most essential feature of an explosion. If the energy is released gradually, explosion would not be expected.

In addition to the energy release rate, the violence of the explosion also depends on the mechanism by which the energy is dissipated following the release. There are several mechanisms for the energy from explosion being dissipated. The most important effect is the generation of blast leading to a massive over-pressurization. In [15] it is mentioned explicitly that an explosion is a release of energy that causes a blast. A blast is characterized by a transient change in the gas density, pressure and velocity of the air surrounding the explosion origin.

Other possible effects of an explosion include, among others, the generation of projectiles (missiles or debris), thermal radiation in case of thermal explosions as well as the inconvenience of acoustic energy leading to a noise of varying degrees of loudness. Each of them may cause different consequences to the surroundings which may affect people, environment or other properties. According to circumstances, explosions may directly or indirectly injure people, cause fatality, damage the structural buildings up to the demolition of the entire facilities or other valuable assets [16, 5].

In this thesis, the treatment of the pressure wave generated from explosions is the main interest. It has been understood that, in almost all explosion cases, the energy release from explosions would result in a rapid expansion of the surrounding gas and initiate a rapidly moving pressure wave carrying out a certain amount of explosion energy. In fact, while performing the safety and risk analysis, an explosion is always associated with the generation of overpressure that may cause

damage to the surroundings. Usually, the overpressure is considered to be the main property of pressure wave for characterizing the explosion effects. In the other words, the generation of damaging overpressure is quite important to determine whether or not an explosion needs to be included in a particular risk analysis.

2.2 Explosions in the chemical process industries

In general, explosions are typically distinguished based on the type of energy release. In fact, the energy source can be anything but has potential to generate violent reaction when initiated. Typical types of energy released from explosions may include physical, chemical or nuclear energy. Therefore, explosions may be classified into three different groups as depicted in Fig. 2.1. For the chemical process industries, explosions associated with the release of nuclear energy may be considered beyond of the scope of the discussion. In fact, the occurrence of a particular explosion

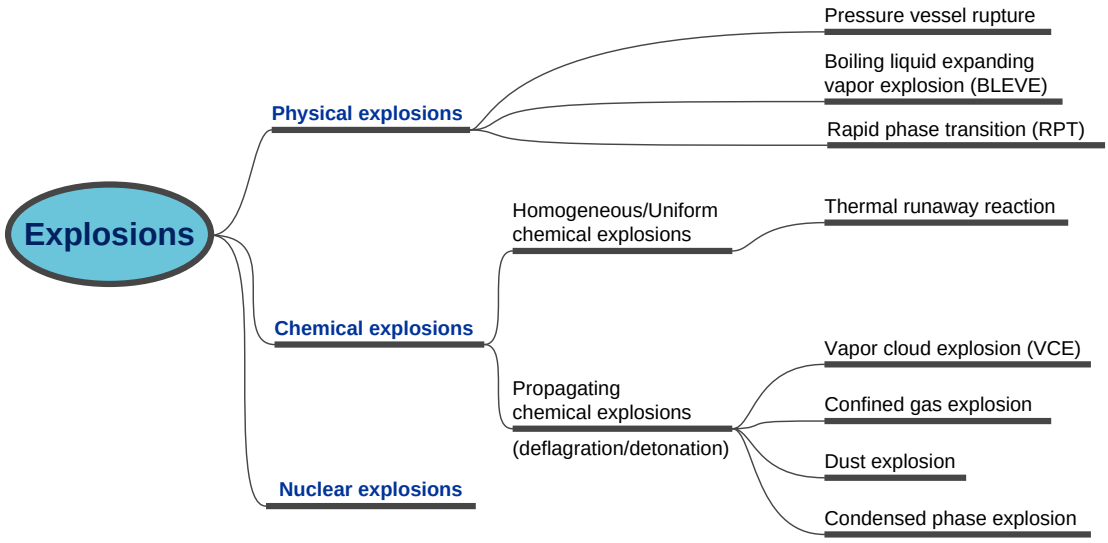

Figure 2.1. *Explosion types with respect to the type of energy release [16, 5]*

may not be associated with the release of single type of energy. A combination of both physical and chemical may also be possible according to the circumstances.

2.2.1 Physical explosions

The release of stored compression energy in a compressed gas which undergoes a sudden loss of containment is an example of physical explosions. In this case, chemical reactions are not to be expected. Such a release may lead to a rapid expansion of gas carrying out a large amount of explosion energy. This event is also known as a **pressure vessel rupture explosion**. The rupture of the vessel may occur due to a certain number of failure mechanisms, including mechanical defects, corrosion, heat exposure (external fire), cycling failure or other similar reasons.

Another typical example of a physical explosion which is also quite common to occur in the chemical process industries is the **BLEVE**, abbreviated from the **boiling liquid expanding vapor explosion**. This explosion is in fact a special case of a pressure vessel rupture in the sense that the pressure vessel that contains a liquefied gas stored underpressure and above its normal boiling point fails catastrophically due to similar reasons as stated before. The rupture of this vessel would result in a sudden flashing of the liquid into vapor which would expand rapidly to the surrounding. Strictly speaking, the BLEVE does not necessarily imply thermal effects. However, in many cases, the liquefied gas stored in the pressure vessel is typically a flammable material. Thus, once the pressure vessel fails, the expansion of the flammable vapor is expected. If this flammable vapor is ignited by a certain ignition source immediately after being release from the vessel, a fireball would occur following the physical explosion. Therefore, as usually happens, a BLEVE is also associated with the possibility of a fireball, making this accident to combine both the mechanical effects due to a gas expansion and thermal effects due to a fire.

Another typical example of a physical explosion as shown in Fig. 2.1 is a **rapid phase transition (RPT)**. This phenomenon is realized in liquefied natural gas (LNG) incidents in which LNG vaporizes violently upon coming in contact with water. During such explosions there is no combustion but rather a huge amount of energy is transferred in the form of heat from the room-temperature water to the LNG at a temperature difference of about 175 degree Celsius.

2.2.2 Chemical explosions

Chemical explosions are usually associated with the sudden release of chemical energy which is stored or generated from chemical reactions. These reactions may include rapid combustion process, decompositions or other rapid exothermic reactions. Chemical explosions can also be distinguished into two different groups, namely the **homogeneous chemical explosions** and the **propagating chemical explosions**. With respect to the homogeneous chemical explosions, the chemical reactions occur uniformly through space in a reaction mass. These explosions, in some literature, are also known as uniform chemical explosions. **Thermal runaway reactions** that occurs when the heat released by the chemical reaction exceeds the heat removal, is an example of these uniform chemical explosions.

Meanwhile, the propagating chemical explosions is always associated with chemical reactions that are initiated in a restricted part of the reaction mass and then spreads outwards. Thus, at a given later moment, these kinds of reaction would create three different regions. There is a region which has undergone the reaction (*a reacted zone*), a region which is not yet affected by the reaction (*an unreacted zone*) and, in between these two regions, there is a narrow zone within which the chemical reaction is taking place and the product of the chemical reaction at a high temperature is to be found. This interface zone which separates the cold unreacted mass from the hot reaction products is commonly known as the **reaction front**.

With respect to the propagation velocity of the reaction front relative to the unreacted mass immediately ahead the reaction front, the propagating chemical explosions can further be distin-

guished into **detonations** and **deflagrations**. In the case of detonations, the reaction front moves equal to or faster than the speed of sound in the unreacted mass. A typical example of detonation explosions is a condensed phase explosion involving conventional chemical explosive (e.g. TNT, C4, RDX, etc). Meanwhile, during deflagrations the reaction front moves at a speed less than the speed of sound in the unreacted mass. Typical examples of deflagration explosions include the **vapor cloud explosion** (**VCE**), **dust explosion**, and **confined gas explosion**.

In the following section, the mechanisms of explosion phenomena in the chemical process industries following the release of the flammable gases or vaporizing liquid is particularly mentioned in detail. As mentioned before, the outcomes following the release of the flammable gases or vaporizing liquid are not necessarily explosion. However, the main interest is the release incident leading to the formation of the vapor cloud. The different between two combustion modes, namely deflagration and detonation is firstly discussed.

2.3 Mechanisms of deflagration and detonation

Many chemical process industries frequently deals with an enormous inventory of hazardous substances, including the flammable gases and vaporizing liquids. Such fuels include non-liquefied flammable gases (hydrocarbon fuels with one or two carbon atoms e.g., methane, ethylene/ethene, acetylene/ethyne); liquefied gases under pressure (hydrocarbon fuels with three or four carbon atoms, e.g., propane, butane); and ordinary flammable liquids that are stored particularly at high temperatures and pressures (hydrocarbon fuels with five or more carbon atoms, e.g., cyclohexane, naphtha). With respect to the circumstances, typical consequences that can be expected following the release of these materials may include fires, explosions or atmospheric toxic dispersions. Figs. 2.2 and 2.3 are two typical diagrams showing the event sequences following the release incident of the pressurized gases and pressurized liquefied gas (vaporizing liquids).

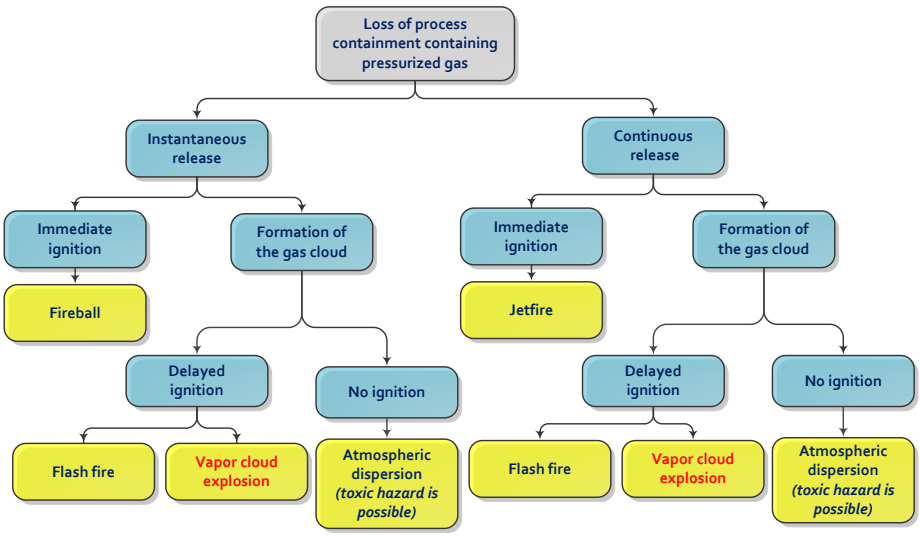

Figure 2.2. *Accidental sequences following the loss of process containment containing pressurized gases*

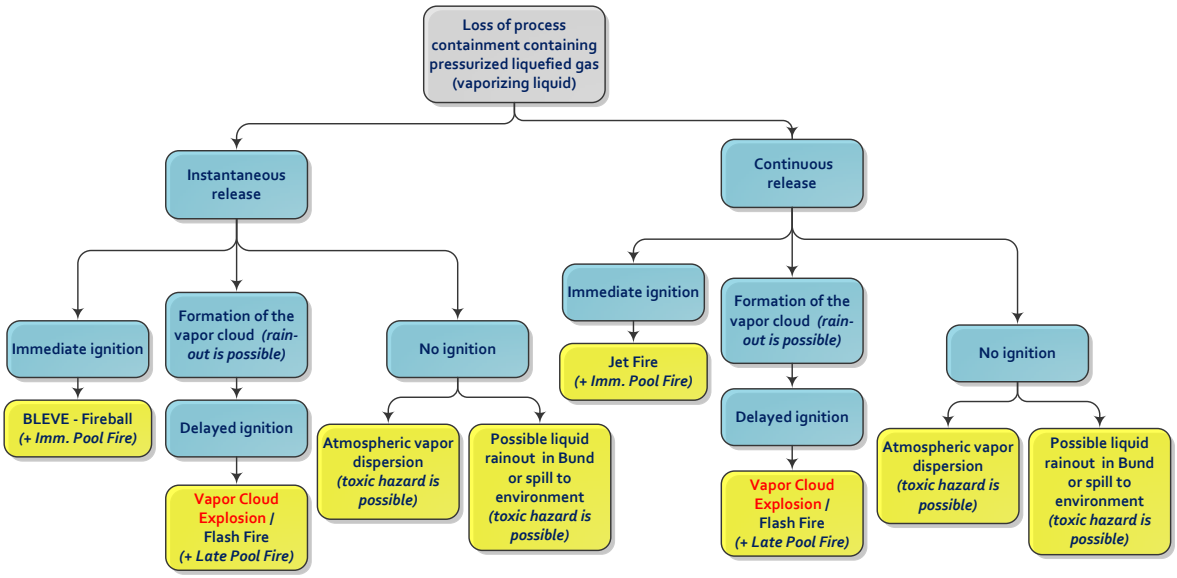

Figure 2.3. *Accidental sequences following the loss of process containment containing pressurized liquefied gases/vaporizing liquids. If a proportion of the vapor cloud rains out, a pool of liquid is created. Therefore, in addition to the specified effects shown in this diagram, the possible of pool fire may also be added to the specified accidental outcomes.*

In both figures, the flammable gases or vaporizing liquids may form a mixture with the surrounding atmospheric air. Such a mixture is known as the **gas or vapor cloud**. It has been understood that the formation of the gas or vapor cloud takes some time after the release incident and no immediate ignition is possible. If this gas or vapor cloud is explosive and subsequently ignited by a certain energetic ignition source that is able to initiate a rapid combustion reaction, explosion hazards may be expected. This means, in order to the explosion to occur, the formation of the gas or vapor cloud which is explosive is quite essential.

The determination whether or not a gas or vapor cloud is being explosive depends on the composition of the flammable material (fuel) in the cloud. This condition is known as the "explosion limits" or "flammability limits". The gas or vapor cloud is considered flammable if the concentration of the fuel in the cloud must be between the lower flammability limit (LFL) and the upper flammability limit (UFL). Fig. 2.4 illustrates the condition for the gas or vapor cloud being explosive. Some typical ranges of explosion limits for some hydrocarbon-air mixtures as well as hydrogen-air mixture in terms of the percentage volumetric amount of the fuel per volumetric amount of air at STP is depicted Fig. 2.5.

In the chemical process industries, the explosion of the explosive/flammable gas or vapor cloud is famously known as **vapor cloud explosions (VCEs)**. The accident history has concluded that VCEs are the major threat and the most dangerous hazard which may occur following the release incident of the flammable gases or vaporizing liquid. However, it has been well understood that the combustion of the flammable gas or vapor cloud would not necessarily give rise to the vapor cloud explosion. The combustion of the flammable gas or vapor cloud is basically only a deflagration and

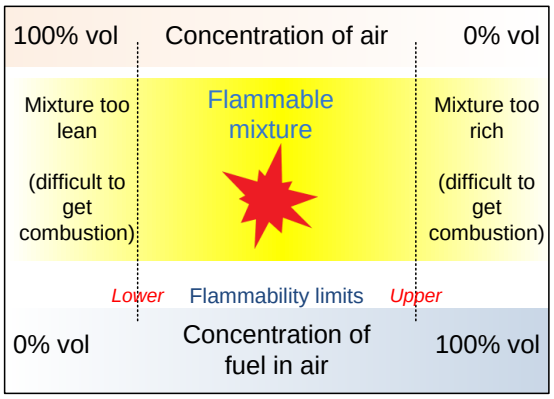

Figure 2.4. *Composition of the fuel in the cloud must be within the boundaries of the explosion limits in order to get explosive. Otherwise, explosion would hardly to occur.*

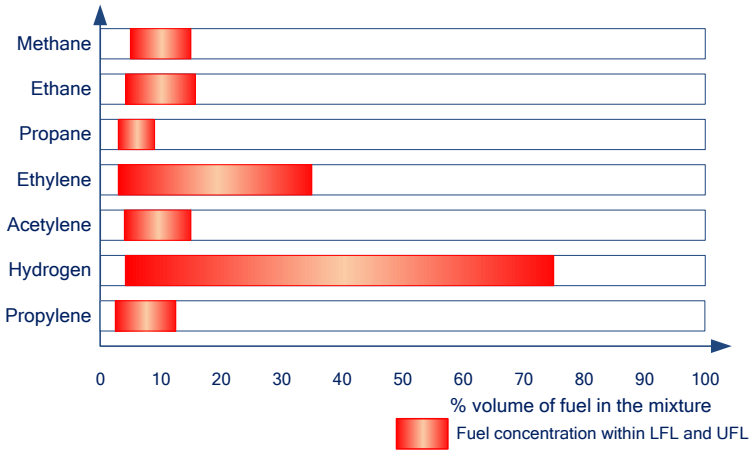

Figure 2.5. *Typical ranges of explosion limits for some hydrocarbon/hydrogen-air mixtures at 1 atm and $25^0 C$*

not an explosion. As mentioned before, explosions are always associated with the generation of damaging pressure wave. As for deflagration, no damaging overpressure would be expected. Thus, in the following the mechanism of deflagration that could generate damaging overpressure and its difference from detonation is described.

2.3.1 The premixed combustion

Deflagration and detonation ate two typical combustion modes. A combustion itself is defined as a process of heat release in exothermal reactions accompanied by the mass and heat transfer. A premixed combustion in sense that the fuel and oxidizer are essentially mixed prior to ignition is the most relevant mechanism for the explosion. In addition, the premixed combustion is also practically importance in engines or modern gas turbine [17].

The basic mechanism of premixed combustion is characterized by the propagation of the reaction front separating the unburned mixture from the fully burned mixture. The most distinctive feature of this kind of combustion is its ability to form a self-sustained reaction wave propagating with a

well-defined speed, which is either larger or much less than the speed of sound. Another remarkable property of a premixed combustion is the dependence of the chemical reaction rate on temperature, which is expressed by the *Arrhenius law* for the reaction rate [17]:

$$k = A \cdot \exp\left[-\frac{E_a}{\mathcal{R}T}\right] \tag{2.1}$$

where A is the pre-exponential factor, E_a is the apparent activation energy, $\mathcal{R}$ is the universal molar gas constant, valued 8.3143 J/mol/K and T is the absolute temperature. The activation energy of many reactions is typically large, so that the reaction rate at the room temperature may be taken as zero. In contrast, the increase of fuel temperature by factor of 2 or 3 may lead to an increase of the reaction rate by many orders of magnitude. In the case of a strongly exothermic reaction when a considerable energy release is involved, relatively slight increase of the temperature at some region ignites the reaction, which eventually extends over the whole gas [17, 18, 19].

Deflagration and detonation are two different regimes of premixed combustions. In both cases, there is a process in which the reaction front or the flame propagates spatially through the reaction mass. Basically, the main difference between deflagration and detonation depends on the propagation velocity of this reaction front relative to the unreacted mass immediately ahead the reaction front. The propagation velocity of the flame front relative to the unburned mass immediately ahead the flame is also known as the **burning velocity**. Another parameter to mention the propagation velocity of the flame is the flame speed. Both quantities are not similar but, in fact, are related each other. The **flame speed** is defined as propagation velocity of the flame relative to a stationary observer, such as the ground or another fixed frame [20]. The distinction between these two parameters can be described by mentioning the combustion process inside a tube that is open at one end and closed at the other as depicted in Fig. 2.6.

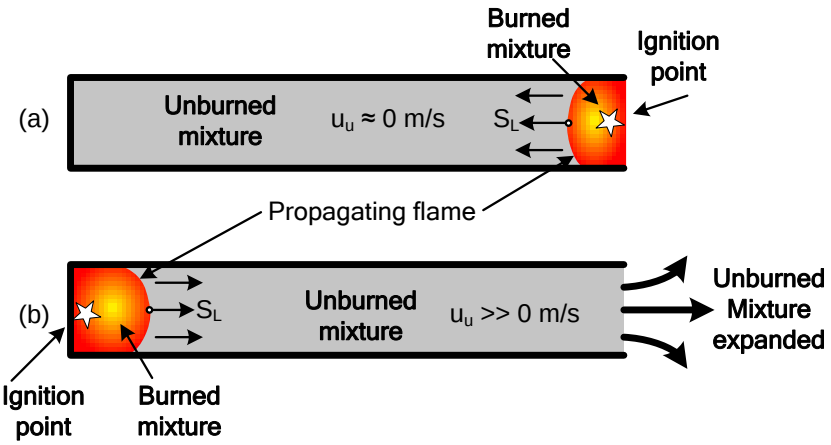

Figure 2.6. *Illustration of the combustion process in a tube which is open at one end and closed at the other. (a) the ignition takes place at the open end, while (b) the ignition takes place at the closed end.*

In this figure, both tubes are filled with the same flammable mixture of fuel and oxidizer. The

combustion is initiated once this mixture is ignited by a certain energetic ignition source. In the case that the ignition takes place at the open end, the flame propagates into the stagnant (stationary) unburned mixture. At this situation, the flame propagates at its burning velocity which normally takes place in a laminar region. Thus, this velocity is also called the **laminar burning velocity**, here denoted by S_L. If the velocity of the unburned mixture is denoted by u_u, in this particular case, $u_u = 0$. In fact, the flame speed is actually the sum of the burning velocity and the velocity of the unburned mixture. If the flame speed is denoted by S_F, thus

$$S_F = S_L + u_u \tag{2.2}$$

Therefore, for this first case, the flame speed S_F is considered similar to the laminar burning velocity S_L. The combustion product directly vent through the open end.

However, if the ignition takes place at the closed end, the combustion products would expand due the heat release from the reaction. This causes the unburned mixture to move at a velocity of $u_u \gg 0$. This means, this expansion creates a particular flow field in the the unburned mixture. Basically, the flame front itself would still propagates at its laminar burning velocity (S_L) relative to the unburned mixture immediately ahead the flame. However, the flame speed (S_F) is no longer equal to this laminar burning velocity but determined by Eq. 2.2.

In fact, the flame speed S_F is found to be proportional to the laminar burning velocity S_L. Such proportionality is represented by the **expansion ratio** defined as the ratio of the mass density ratio of the unburned mixture, denoted by ρ_u and the mass density of the burned mixture, denoted by ρ_b. This expansion ratio, denoted by α_{exp}, is given by the following equation:

$$\alpha_{\mathsf{exp}} = \frac{\rho_u}{\rho_b} = \frac{V_b}{V_u} \tag{2.3}$$

During an adiabatic combustion process of a stoichiometric hydrocarbon-air mixture, for example, the gas combustion products typically expand up to 8 times its initial volume. This means, $\alpha_{\mathsf{exp}} = 8$ [20, 21]. Taking into account this expansion ratio, the flame speed relates to the laminar burning velocity according to the following equation:

$$S_F = \alpha_{\mathsf{exp}} \cdot S_L \tag{2.4}$$

This means that the velocity of the unburned mixture is given by the following equation:

$$u_u = (\alpha_e - 1) \cdot S_L \tag{2.5}$$

2.3.2 Deflagration phenomena

Deflagration is a strongly subsonic combustion process in which the reaction front propagates at a speed less than the speed of sound in the unreacted mass immediately ahead the flame. In fact, the propagation of the flame during a deflagration is governed only by the ordinary transport

phenomena such as thermal heat conduction and molecular diffusion of heat and species. These ordinary transport processes are basically slow process making the flame to propagate also slow to the unburned mass ahead the flame.

The basic mechanism of deflagration can be described as follows. Suppose that a mixture of fuel and oxidizer has been formed, for example, the mixture of a flammable gas or vaporizing liquid with the atmospheric air (gas or vapor cloud) and it is explosive. If this mixture is ignited by a spark with an energy content of the order of as little as 1 mJ, before the cloud being diluted below its lower flammability limit (LFL), a deflagrative combustion will be initiated. In this case, a thin flame starts to propagate through the unburned mixture away from the ignition point. The products of this combustion reaction have larger temperature. The thermal conduction will transports the thermal energy from these hot combustion products (burned gas) to the cold unburned mixture. Fig. 2.7 shows the distribution of temperature across the reaction front during such a deflagration process. As a result of such transport process, the temperature of the unburned mixture close to

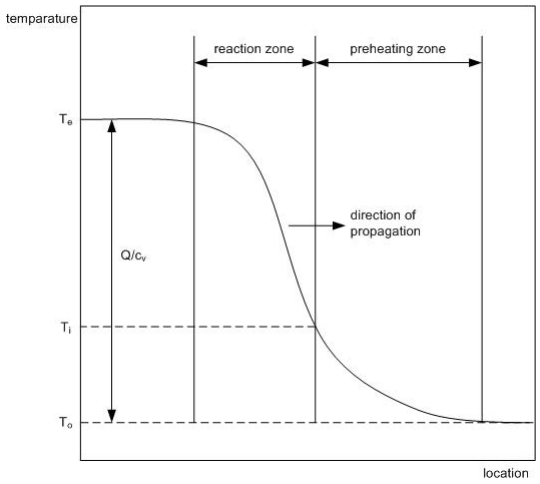

Figure 2.7. *Distribution of the temperature during a deflagration of a flammable mixture [22]*

the burned gas increases which causes the reaction in this zone to go faster until another portion of this cold unburned mixture is burned followed by the release of more energy. Again, this energy will be is transported by means of the thermal conduction process to the next layer of the cold unburned mixture resulting in the propagation of the reaction front. The reaction front is also known as the flame. This propagation process continues to make the flame survive so long until the whole part of the cold unburned mixture is burned. The thickness of the flame depends on thermal diffusivity and burning velocity. For stoichiometric fuel-air mixtures, the flame thickness is in the order of millimeter only. For example, in [23] the flame thickness of a stoichiometric methane-air flame at 1.0 atm is estimated only 0.175 mm.

Basically, the ordinary transport mechanisms such as the thermal conduction and molecular diffusion is a considerable low speed process. This is the main reason of why the flame advances into the cold unburned mixture at a slow burning velocity that normally takes place at a laminar region and significantly smaller than the speed of sound in the same medium. In some literature,

such deflagration phenomena is also known more specifically as a slow deflagration in order to distinguish it with a fast deflagration process which is going to discussed in the next section.

In fact, the laminar burning velocity of a certain fuel-air mixture is considered as a fundamental parameter whose value reflects the reactivity of such a mixture. For typical hydrocarbon-air mixture, such as methane-air or propane-air, the laminar burning velocities under atmospheric conditions are normally less than 1 m/s. However, for some fuels like acetylene and hydrogen, the laminar burning velocities of their mixtures with air under atmospheric conditions are significantly more than 1 m/s and higher than those of normal hydrocarbon air-mixtures. This means that hydrogen or acetylene is more reactive than normal hydrocarbon fuels. Furthermore, Table 2.1 further shows some more information of the basic combustion properties of some frequently handled gases or vaporizing liquids in the chemical process industries. These properties are valid if these fuels are mixed with air under atmospheric conditions.

Table 2.1. *Basic combustion properties of some gases or vaporizing liquids in air under atmospheric conditions [22, 24]*

Substances	Chemical formula	Flammability limits [vol. %]	Flash Point [°C]	Autoignition Temperature [°C]	Laminar Burning Velocity, S_L [m/s]
Methane	CH_4	5.0-15.0	-	595	0.448
Ethane	C_2H_6	3.0-15.5	-	515	0.476
Propane	C_3H_8	2.1-9.5	-	470	0.464
Ethylene	C_2H_4	2.7-34	-	425	0.735
Propylene	C_3H_6	2.0-11.7	-	455	0.512
Hydrogen	H_2	4.0-75.6	-	560	3.250
Acetone	$(CH_3)_2CO$	2.5-13.0	-19	540	0.444
Diethyl ether	$(C_2H_5)_2O$	1.7-36	-20	170	0.486
Acetylene	C_2H_2	1.5-100	-	305	1.550
Ethanol	C_2H_5OH	3.5-15	12	425	-
Toluene	C_7H_8	1.2-7.0	-	535	-
Cyclohexane	C_6H_{12}	1.2-8.3	-18	260	-
Hexane	C_6H_{14}	1.2-7.4	-15	240	-
Xylene	C_8H_{10}	1.0-7.6	30	465	-

According to [21, 25], if the reaction front propagates only at its laminar burning velocity, the flame speed is predicted only in the range 3.5 - 25 m/s. In general, with such low flame speeds, the generated overpressures will not be significant because the pressure build-up during deflagration processes depends strongly on the flame speed. Fig. 2.8 shows the graphical relationship between the generated flame speed and the generated overpressure. According to this figure, an overpressure in the order of hundred Pascals may still be expected from a slow deflagration. However, this is quite low to cause any danger or damage to the environment. For the risk analysis, such a low overpressure could simply be ignored. Therefore, slow deflagration is basically not to be defined as an explosion, but only as a fire. This kind of fire is also known as a vapor cloud fire or a flash fire. The main hazard typically dealing with a fire event is a thermal radiation or a direct flame contact.

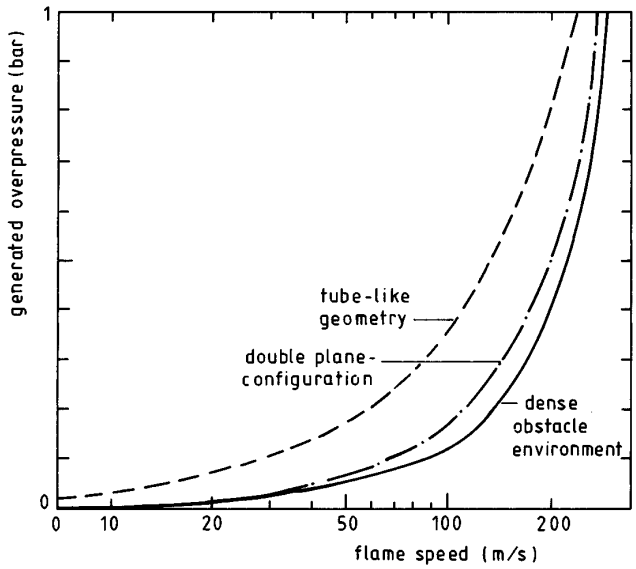

Figure 2.8. *Overpressure as a function of flame speed for three different geometries. The relationships are based on calculations by use of a self-similar solution [22]*

As mentioned previously, the generation of damaging overpressure is the basic feature to determine whether the combustion of flammable cloud is classified to be a fire or an explosion. The damaging overpressure from a deflagration will be expected if there is a mechanism for the generation of high flame speed. In the other word, during a deflagration process, the flame speed should be accelerated while propagates through the flammable cloud. This condition is basically influenced by the degree of confinement and congestion. This means that if a flammable cloud is ignited in a partially confined region with a certain level of congestion (obstacles), the flame front will be accelerated through its pathway in the flammable cloud. The burning velocity which is initially laminar may transit to the turbulent burning velocity and subsequently generate high flame speed. In this case, one can say that a slow deflagration has been transformed into a **fast deflagration** with a high potential to generate a damaging overpressure. This kind of fast or turbulent deflagration is no longer defined as a fire, but can now be considered as an explosion.

This means, with respect to the condition of confinement or congestion, a slow deflagration can be defined as a deflagration that takes place in a completely unconfined and uncongested region with no obstacles or obstructions present in the vicinity and this is actually a flash fire. Several experimental and theoretical studies, as reported in [26, 27, 28], have proved that damaging overpressure will not be expected if the deflagration of the flammable cloud is ignited in fully open environment.

Furthermore, the acceleration of the deflagration flame is basically associated with the wrinkling of the flame front. Such a condition may be initiated by either the intrinsic instability of the flame front or the external flow structure. The intrinsic instability of the flame front is actually a **hydrodynamic instability** which inherently occurs during the combustion process. This is also known as the **Darrieus-Landau instability**, named after G. Darrieus and Lev Landau, two

prominent physicists who have separately discovered this phenomenon [29, 30]. Basically, the main reason for this instability to occur is a thermal expansion across the flame front resulting from the coupling between flame and flow-field dynamics associated with the chemical heat release. If the deflagration of flammable cloud occurs in a completely unconfined and uncongested region, this hydrodynamic instability is, perhaps, being the only factor that causes the wrinkling of the flame front. In this particular case, the wrinkling of the flame front will not generate high flame speed since the effective burning velocity is expected not to be much higher than its laminar burning velocity. There will be no pressure build-up to be expected from this condition. Therefore, in this thesis, the wrinkling of the flame front due to the hydrodynamic instability will not be discussed at all. A little more detail study on this subject can be obtained further in some references, such as in [31].

The other mechanism that causes the wrinkling of the flame front leading to a high flame speed during deflagration is the generation of the turbulence flow field ahead the flame front. In general, there are two typical scenarios for which the turbulent flow field ahead the flame front can be generated [22]:

a. Turbulent flow field ahead the flame front can be generated if the flammable fuel is violently released, for instance a jet release or a catastrophic rupture of a vessel resulting in an explosively dispersed cloud. However, fast deflagration due to a jet release will not produce a significant flame speed and no damaging overpressures is expected. In [21], the maximum overpressures in jet combustions and explosively dispersed clouds observed experimentally are typically lower than 100 mbar. These overpressures are generally too low to create a serious danger to the environment.

b. Turbulent flow field ahead the flame front can also be generated by the interaction of the expansion flow ahead of the flame front with the boundaries. These boundaries are specified as either spatial configurations of obstacles or partial confinement of sufficient extent, whether or not obstructions were present.

In various chemical process plants or refineries, the second scenario is perhaps the most important mechanism because typical local areas in such places containing dense concentration of process equipments or other various obstacles such as pipework, process vessels, walls, etc. In the other word, the presence of confinement or obstacles may act as turbulent flow initiator once deflagration of the flammable vapor cloud is initiated in the area with such boundaries. The turbulent combustion in which the flame speed is accelerated will generate a damaging overpressure. The generation of turbulent flow field ahead the flame front due to the presence of obstacles in the area in which the flammable vapor cloud is engulfed can be illustrated by Fig. 2.9. In this figure, a turbulent flow field is generated due to repeated obstacles in a channel containing a flammable cloud. As the flame front expands toward the obstacles, the flow field is created due the expansion of the combustion product. Thus, due to the presence of obstacles , this flow field becomes turbulent which is generated around and behind the obstacles. The flame front, which is initially laminar,

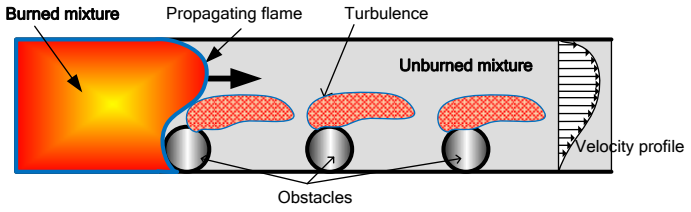

Figure 2.9. *The generation of the turbulent flow field ahead of the flame front inside a channel with repeated obstacles [20]*

encounters this turbulent flow field producing a turbulent flame. As a result, the flame consumes more of the unburned cloud per unit time and volume. The combustion process is intensified ans the expansion of combustion product becomes stronger. This process continuously enhances the flow turbulence and accelerates the flame. A positive feedback loop which is called **Schelkchkin** mechanism, as shown in Fig. 2.10 represents this flame acceleration mechanism.

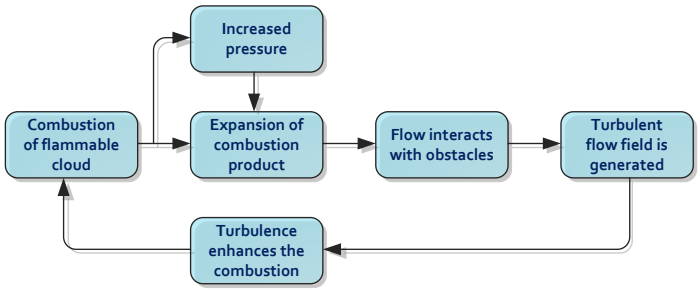

Figure 2.10. *Positive feedback loop causing the acceleration of the flame speed due to the presence of the turbulent flow field ahead the flame front [20]*

The flame front which encounters the turbulent flow while propagating away from the initial ignition point can be accelerated up to hundreds or thousand meters per second depending on the level of congestion. This condition can have a great potential to cause a significant damage to the surroundings [32, 33, 34]. It is important to mention that, if deflagrations occur in a confined but uncongested region, the flow field ahead the flame front may not be disturbed and the turbulence phenomena may not be encountered. Therefore, the flame will not be accelerated. However, in a confined region, the high flame speed may still be expected because the generation of overpressure does not depend on the generated flame speed.

2.3.3 Detonation phenomena

In contrast to a deflagration mode, a detonation is characterized by a supersonic combustion wave in which the flame front propagates at a speed equal or greater than the speed of sound relative to the unburned material immediately ahead the flame. The heat release from the reaction rapidly expands the combustion products and creates a shock wave. In this case, the propagation of the flame is no longer governed by the ordinary transport phenomena, but driven by the generated shock wave which compresses and heats the unburned material causing it to auto ignite and release

energy to sustain this compression wave. Both shock and combustion wave (reaction front) are, in fact, coincident or coupled together and propagating at the same speed. This means that a detonation is a self-sustaining process. Once this reaction has been initiated, it will continue to propagate at the same speed to its completion even through an unconfined or uncongested geometry [35].

Basically, detonation is a typical mode of combustion involving chemical explosives. A chemical explosive is a material which is normally in a state of metastable equilibrium, but which is capable of violent exothermic reaction [36]. A detonation of chemical explosive involves the rapid oxidation of the fuel element (hydrogen and carbon atoms) forming a part of explosive compound resulting in a sudden release of energy over a very short period of time, typically in the order of a few microseconds. The oxygen needed for this reaction is contained within the compound so that air is not necessary for the reaction to occur. During this process, the explosive breaks down and the component elements carbon and hydrogen react with the available oxygen. Basically, the propagation speed of the flame for such a reaction is supersonic and significantly greater than the burning velocity of a flammable fuel-air mixture in atmospheric air [37, 38, 39]. Since chemical explosives usually in the liquid and the solid phase, the detonation involving these materials are classified as condensed phase explosions.

Typical chemical explosives include conventional high and low explosive compounds as well as some other energetic substances. They have a general chemical formula $C_xH_yN_wO_z$ and are distinguished on the basis of their sensitivities and uses. Conventional high explosives, such as TNT, PETN, nitroglycerin (liquid), HMX or RDX, are the most sensitive materials. A detonation involving these materials is extremely a rapid event in which the energy would be released in a very short period of time. In contrast, low chemical explosives as well as other energetic substances, such as ammonium nitrate or sodium chlorate, are usually less sensitive materials but still have sufficient energy to decompose exothermally or to detonate. A detonation involving these materials would release the energy over a longer period of time, but still much shorter than the release energy rate of fast deflagration of a flammable cloud of hydrocarbon-air. Thus, a detonation involving low chemical explosives is considered less violent compared to a detonation of high chemical explosives [32, 40].

Furthermore, a detonation of a high chemical explosive can generate a flame speed up to 10 km/s leading to the generation of an extremely high overpressure. It is important to mention that the generation of such high overpressures does not require the presence of confinement or obstacles. In a very extreme condition, the explosion pressure may exceed 100 kbar, and may cause a completely catastrophic destruction over a large distance from the origin of the explosion [16]. For some common conventional high explosives, their basic detonation properties, such as the heat of detonation and detonation velocity, are shown in Table 2.2.

Furthermore, detonations may occur to the flammable cloud of fuel-air as well. As mentioned in the previous section, the basic combustion mode for a flammable cloud is deflagration, either the combustion takes place in the open environment or the area with obstacles or obstructions.

Table 2.2. *Basic detonation properties of some common conventional high explosives [41, 42]*

Explosive	Empirical/chemical formula	Density, ρ [g/cm^3]	Average heat of detonation, ΔH_D [kJ/kg]	Detonation velocity, D [m/s]
TNT	$C_7H_5N_3O_6$	1.60	4650	6800
RDX	$C_3H_6N_6O_6$	1.77	5370	7320
HMX	$C_4H_8N_8O_8$	1.89	5680	9110
Tetryl	$C_7H_5N_5O_3$	1.62	4510	7550
PETN	$C_5H_8N_4O_{12}$	1.76	6090	8260
CompB	(59.5% RDX + 39.5% TNT)	1.72	5210	7990
ANFO	(Ammonium Nitrate/Fuel Oil)	0.80	3720	4500

The flame can, however, be accelerated while propagates through the flammable cloud if the cloud engulfs the area with a certain degree of confinement or congestion. If the level of turbulence in the flow field ahead the flame is extremely high, the generated flame may extremely be accelerated causing the deflagration to transit to detonation. Such condition is also known as **DDT** (**Deflagration to Detonation Transition**). Thus, once detonation has occurred, turbulence is no longer necessary to maintain the propagating reaction since, detonation flame is able to propagate further even in unconfined or uncongested region [20, 22].

However, the DDT mechanism does not occur easily. Basically, an important requirement to achieve DDT is that the flammable part of the vapor cloud must be homogeneously mixed which are normally produced at laboratory scale, where the containers have somewhat restricted dimensions to ensure uniformity of temperature during heating. In reality, it is quite difficult to obtain such homogeneous mixtures since in the vapor cloud occupying an appreciable volume it is practically not possible to achieve uniformity of temperature. Under normal circumstances, a homogeneous vapor cloud rarely occurs. That means DDT may occur under a certain extreme condition only.

Several experimental works have been dedicated to the DDT phenomena, especially in those very reactive mixtures, such as near-stoichiometric acetylene-air, hydrogen-air or fuels with oxygen-enriched atmospheres [20]. In [43], an experiment of DTT involving fuel-air mixtures with moderate reactivity was reported. In this particular experiment, the deflagration of a propane-air mixture was initiated by a weak ignition source. The experimental study was performed in a large scale 50m^3 obstructed tube of a diameter of 2.5m and a length of 10m with one end closed and one open to the atmosphere. The result showed that the combustion can accelerate to a detonation in less than 10m, if sufficient confinement and obstructions are present.

In addition to the DDT condition, detonations of the flammable cloud of fuel-air mixture may also be possible due to a direct initiation of detonation by a considerably strong ignition source. This event is also known as **vapor cloud detonation**. Detonation of normal hydrocarbon-air mixtures, such as methane-air or propane-air, requires an initiation energy to the order of 10^6 Joules or more, which is comparable to the level of energy generated by a high explosive charge. As a comparison, the deflagration of these mixtures normally requires an ignition energy of approximately 10^{-4} Joules only. That means, under normal circumstances, a direct detonation is highly unlikely. The minimum ignition energy for moderate and high reactive fuels is typically much lower than that for

low reactive fuels. Table 2.3 illustrates the minimum ignition energy for deflagration and detonation for some typical hydrocarbon-air mixtures [22].

Table 2.3. *Comparison of the minimum ignition energy (MIE) for a deflagration and detonation [22]*

Gas mixture	MIE for a deflagration in Joules	MIE for a detonation in Joules
Methane-Air	0.28×10^{-3}	0.23×10^{9}
Propane-Air	0.25×10^{-3}	0.25×10^{7}
Acetylene-Air	0.7×10^{-5}	0.13×10^{3}

If a stoichiometric hydrocarbon-air mixture is detonated, the generation of detonation flame speed would be in the range of 1500-3000 m/s, which is much higher than the flame speed generated if the same material is burned in a deflagrative mode. Table 2.4 shows some typical values for detonation velocities of flammable hydrocarbon gases in air given by Stull [44]. Such high flame speed would create shock waves with overpressures in the range of 15-20 bar [16, 45].

Table 2.4. *Detonation velocities of some flammable gases in air [44]*

Gas	Velocity [m/s]
Methane	1540
Propane	1730
Ethyne (Acetylene)	1870
Hydrogen	3400

Finally, as a summary, Fig. 2.11 shows a general event tree following the formation of the vapor cloud due to the accidental release of the flammable gas or vaporizing liquid. In this case, all possible accidental outcomes according to the discussion in this section are presented. The possible blast wave effects are expected if the flammable cloud is ignited and the combustion process is enhanced in sense that the generated flame is accelerated while propagates through the flammable cloud. In the absence of the flame acceleration mechanism, the flammable cloud will burn only as a fire without generating damaging overpressure. In case that the flammable cloud is directly ignited by a strong ignition source or there is a transition from deflagration to detonation, a vapor cloud detonation may be expected. However, the latter event does rarely occur under normal circumstances.

2.3.4 Vapor cloud explosions in history

As stated earlier, the vapor cloud explosion is considered the most devastating and destructive event that may happen in typical chemical process and production plants. Since 1970s, when several devastating vapor cloud explosions occurred and caused significant damage to structures or building and injury or even fatality to people, a considerable degree of attention and research

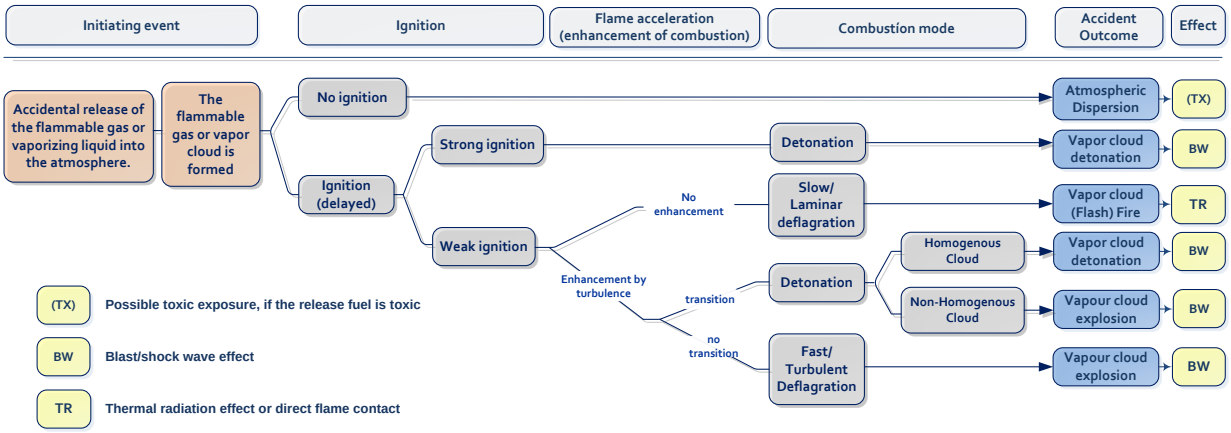

Figure 2.11. *A general event tree that shows typical accidental outcomes which may occur after the release of the flammable gas or vaporizing liquid into the atmosphere subsequently followed by the formation of the flammable gas or vapor cloud (modified from [22])*

effort has been focused on this subject [32]. In [46], a summary of over 200 vapor cloud explosions until the early 1990s is reported. According to this report, vapor cloud explosion hazards, although infrequent, represents a large share of the overall loss severity. Of the 10 largest property losses in the process industries, seven are due to vapor cloud explosions. A compilation of statistical data shows that vapor cloud explosion accidents do not only occur in the fixed industrial plant but also in transportation. In [20] is described that of the 100 largest losses that occurred in the hydrocarbon process industries for the period 1957-1986 vapor cloud explosions were the highest single cause of loss and were responsible for approximately 42% of the losses. Apart from these reports, there were many other vapor cloud explosions that occurred elsewhere in the world. Some accidents have been particularly influential in the development of major hazards controls around the world. In what follows, some notable past accidents are presented.

Flixborough, UK, 1974

Perhaps, best known accident occurred in June 1974, when the Nypro plant at Flixborough, UK exploded with a devastating results. The cause of the explosion was an uncontrolled release of about 30 tons of cyclohexane due to the failure of a pipe. A few minutes after the leakage started, the cyclohexane cloud ignited and a violent explosion occurred. The fires burned for over a week. This explosion is estimated to be equivalent to some 16 tons of TNT. 28 people were killed and 36 were injured on site. Outside the plant, 53 persons were reported injured and 1821 houses as well as 167 shops suffered damage. This accident was not, however, the first major vapor cloud explosion. Two major explosions with destructive of human life had occurred earlier in Ludwigshafen, Germany in 1943 and 1948. Both accidents resulted respectively in 57 and 207 fatalities [11, 20, 47].

Beek, the Netherlands, 1975

A further serious vapor cloud explosion incident occurred in a naphtha cracker installation located at Beek in The Netherlands in November 1975. The explosion due to an escape of propylene, apparently from brittle fracture of a feed drum on a depropanizer, gave rise to a vapor cloud explosion which resulted in 14 fatalities. This accident destroyed the installation, resulted in severe damage in the direct surroundings of the installation and window breakage up to 4.5 km from the installation [11, 48].

Piper Alpha, North Sea, 1988

Another remarkable accident was the explosion and fire at the Piper Alpha offshore platform in July 1988. Piper Alpha is later known as the "Flixborough accident" of the off-shore industry. At Piper Alpha a rather small gas explosion in a compressor module caused fires which subsequently resulted in a rupture of the riser. The main part of the platform burned down. At the time of the disaster 226 people were on the platform; 167 died leaving 59 survivors. From this incident it can be learned that a gas explosion can easily result in domino effects and loss of control. Installations should be designed to avoid such domino effects. Until now, Piper Alpha remains the largest offshore loss in history [20, 49].

BP Texas, USA, 2005

On March 23, 2005, a series of explosions and fires at BP Texas City refinery killed 15 people and injured 170. The Texas City refinery is BPs largest oil refinery with an ability to produce about 11 million gallons of gasoline per day. The incident occurred in the isomerization unit (ISOM) during the starting up when a raffinate splitter tower was overfilled and overheated. The ISOM converts low-octane blending feeds into higher-octane components for blending to unleaded regular gasoline. When liquid subsequently filled the overhead line, the relief valves opened. Hydrocarbon flowed to the blowdown drum and stack and overwhelmed it, resulting in liquids carrying over out of the top of the stack, flowing down the stack, accumulating on the ground. A vapor cloud was formed and ignited by a contractor's pickup truck as the engine was left running causing a vapor cloud explosion. All of the fatalities occurred in or near office trailers located close to the blowdown drum. Houses were damaged as far away as three-quarters of a mile from the refinery [50].

Buncefield, UK, 2005

Most recently, a vapor cloud explosion is believed to have occurred at Buncefield Oil Storage Depot, Hemel Hempstead, Hertfordshire, UK, in November 2005. The explosion generated significant blast pressures in the surroundings. The damage caused by this explosion resulted in further loss of containment and the subsequent fires involved a number of fuel storage tanks on the site. Fortunately, there were no fatalities, but 43 people were injured and widespread damage occurred to both commercial and residential properties in the vicinity.

Figure 2.12. *A view of the BP Texas city refinery after the explosion took place on 23rd March 2005 [51]*

Figure 2.13. *A dramatic picture of the early stage of the Buncefiled smoke plume [52]*

The explosion was a consequence of the spillage of 300 tons of unleaded winter-grade gasoline at 15^0C following the overfilling of one of the storage tanks on the site. Winter gasoline is approximately composed by 10%C_4, 17%C_5, 16%C_6, and 57%C_{10} by weight [53, 54]. The overfilling of a tank led to fuel starting to overflow. The protection system which should have shut off the supply did not operate and continued pumping. This led to the fuel cascading down the side of the tank leading to the rapid formation of a rich fuel/air mixture that collected in the bund. A large vapor cloud was formed which found an ignition source resulting in a violent explosion. This was followed by the further explosions and a large fire that engulfed over 20 storage tanks.

In fact, Buncefield is not the first incident where overfilling of a gasoline storage tank has resulted in a drifting vapor cloud and vapor cloud explosion. Other similar accidents which significant impacts were [55]:

- Newark, New Jersey, 1983: Overfilling of a storage tank resulted in a spillage of up to 265 ton of gasoline into a bund. A vapor cloud 450 m to 600 m long and 60-90 m wide was formed. The explosion caused significant damage on site, including damage to storage tanks in the order of hundred of meters from the point of release, and glass breakage out to a distance of 5.6 km
- Naples, Italy, 1985: Overfilling of a gasoline storage tank resulted in a spillage of about 700 ton into a bunded area. The explosion resulted in serious damage to structures within 100 m and glass breakage out to km
- Saint Herblain, France, 1991: A release of gasoline from a section of pipe inside a bund produced a vapor cloud. Ignition of the vapor cloud then caused extensive damage
- Sri Racha, Laem Chabang, Thailand, 1999: Overfilling of a gasoline storage tank resulted in an explosion causing damage to nearby buildings.

2.4 Explosion blast phenomena

As mentioned above, the formation of the pressure wave which moves rapidly from the center of an explosion is the main interest of this thesis. For many chemical process and production plants, much of the damage from an explosion is done by this moving pressure wave because this wave may carry some or all release energy from the explosion. It is important to mention that, in the detonation of chemical explosives, almost one hundred percent of the energy release is converted into the blast energy. This conversion is, in fact, not completely efficient because some part of them may go to other types of energy such as thermal radiations [56]. For the deflagration of hydrocarbon-air mixture under atmospheric conditions, the maximum theoretical conversion for the blast energy (the expansion of the combustion products), is approximately 40%. In practice, it is however much lower [57, 21]. Therefore, a proper knowledge and a better understanding of the characteristics and dynamics of the pressure wave from an explosion is extremely important in order to ensure the safe design of process installations as well as to protect the surrounding areas from any possible undesired impact [16, 58].

Fundamentally, the explosion pressure wave is a highly transient parameter which rises and falls during the course of the explosion [59]. Generally speaking, the pressure wave propagating in air which is set in motion due to a sudden release of energy during an explosion is commonly known as a **blast wave** [14, 60]. Both chemical and physical explosions which are associated with the rapid expansion of gas may give rise to a blast. As introduced before, this expansion may come from a compressed gas that undergoes a sudden loss of containment or a high-temperature expansion of gas combustion products resulting from a rapid combustion process.

The magnitude and shape of the blast wave mainly depends on the nature of the energy release and on the distance of the object from the center of an explosion. The physical properties of an explosion source will determine the characteristics of the blast wave. Fig. 2.14 illustrates three general shapes of the explosion blast waves as a function of time evaluated at a fixed location some distance to the center of explosion and the pressure is above ambient. In this figure, the propagating blast wave can be in the form of (i) a shock wave followed by a rarefaction wave, (ii) a shock wave followed by a sonic compression wave and a rarefaction wave, or (iii) a sonic compression wave followed by a rarefaction wave.

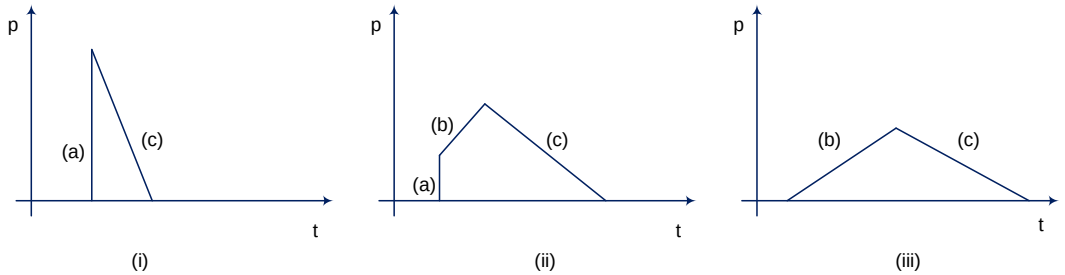

Figure 2.14. *Illustration of three general shapes of the explosion blast wave as a function of time evaluated at a fixed location some distance to the center of explosion and the pressure is above ambient. (a) shock wave, (b) sonic compression wave and (c) rarefaction wave. This figure is modified from [20]*

It can be seen that, before the arrival of the blast wave at the location under consideration, the pressure in the system is still at normal pressure (ambient). For the blast wave in category (i), the pressure increases or jumps up instantaneously to its maximum value due to a strong supersonic compression wave. This fully developed compression blast wave of large amplitude is called a **shock wave** or a **shock front**. This shock wave propagates at supersonic velocity relative to the gas immediately ahead the shock front across with the mass density, particle velocity and pressure of the gas change drastically. In general, the blast front is defined as the leading edge of the blast wave as it moves into undisturbed ambient air. The thickness of a shock front is of the order of the mean free path and may be treated as a *discontinuity* [20]. Since the shock wave may propagate at a velocity of more than ten times the speed of sound, it can surely displace the medium by creating a destructive wind [45]. In fact, the speed of sound basically limits the velocity with which the liberated energy release from the combustion reaction can be transported in the form of pressure waves away into the surrounding area. The sound waves itself propagate at a velocity of about 331

m/s at 0^0C in dry air (near 0% humidity) and without displacement of the medium. The blast wave of this first category is typically associated with detonations of chemical explosive (condensed phase explosions) or bursting of a pressure vessel containing a compressed/pressurized gas (physical explosions).

Meanwhile, the blast wave in category (iii) is typically associated with a deflagration of the flammable cloud. If the flammable cloud is ignited in the open environment, the pressure increases gradually and smoothly to reach its maximum value without having an extreme sudden shock front. It takes much longer time until reaching the peak value which is definitely much lower than that of the blast wave from a detonation. The blast front propagates only at sonic velocity relative to the undisturbed gas ahead the blast wave. It is important to mention here that the deflagration combustion wave propagates at subsonic velocity relative to the unburned mixture immediately ahead the flame. The illustration of the blast wave formation from both detonation and deflagration mechanism is depicted in Fig. 2.15.

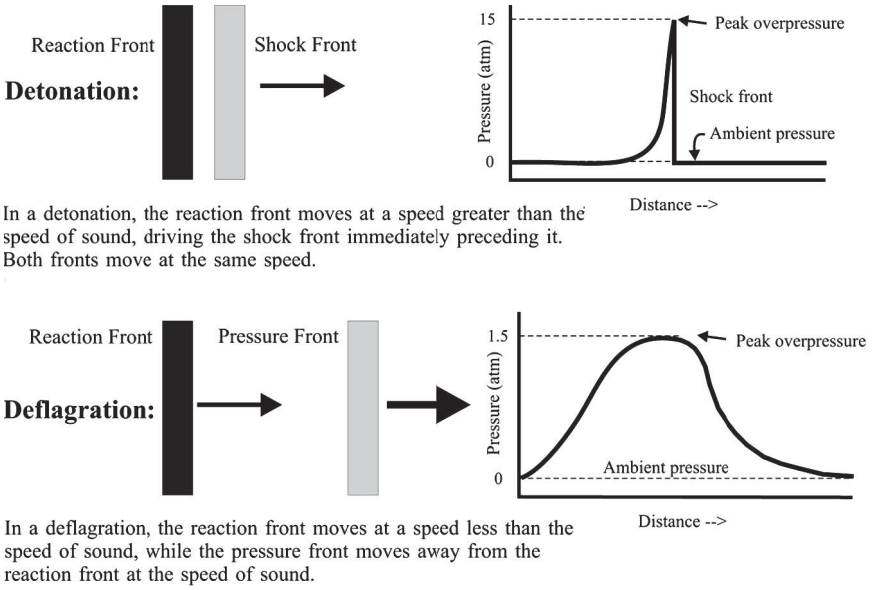

Figure 2.15. *Illustration of the flame propagation mechanism and the generation of pressure wave during detonation and deflagration of the flammable cloud. For both cases, the combustion reaction is initiated to the far away left [16].*

In the case that the deflagration flame is accelerated while it propagates through the flammable cloud, the combustion process will be intensified which produces high burning velocity thus high flame speed. As a result, the pressure front moves much faster with a high pressure amplitude. This means, if the such flame acceleration mechanism occurs, the blast wave could be initially in the form of category (iii), but then it can be shocking up and end as category (i) while it continues to propagate away from the center of explosion (blast origin). As mentioned in the previous chapter, the deflagration in the chemical process industries typically occurs in the congested area causing the flame to accelerate and transit to turbulent combustion with high burning velocity and high flame speed.

Fig. 2.16 shows in much detail the typical form of an explosion blast wave with a sudden shock front as a function of distance to the blast origin at a certain fixed time. If standing at a fixed

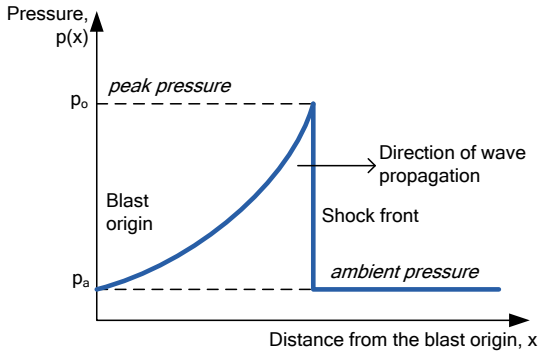

Figure 2.16. *A typical form of an explosion blast wave with a sudden shock front at a fixed time. In this figure, the development of pressure amplitude as a function of distance to the center of explosion (i.e. blast origin) is shown [16]*

location some distance from the center of explosion (the blast origin), the typical shape of a blast wave with a sudden shock front as a function of time is shown in Fig. 2.17. Meanwhile, Fig. 2.18 shows the typical blast wave from deflagration as a function of time at a fixed location some distance from the center of explosion. The center of explosion is assumed as the origin of the blast wave. In those figures, p_a represents the **ambient pressure** for which the atmospheric pressure

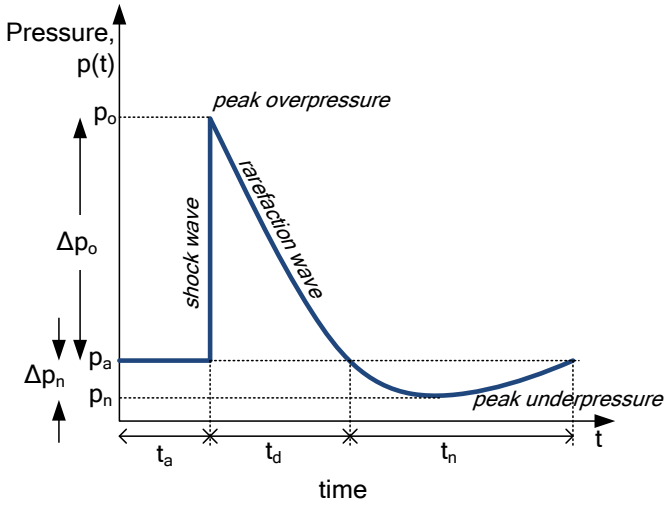

Figure 2.17. *A typical form of the blast wave with a sudden shock front at a fixed location some distance from the center of explosion (the blast origin) [16]*

is mostly assumed, and p_o is the **absolute peak pressure** that is reached by the blast wave. In Figs. 2.16 and 2.17, p_o is the absolute peak pressure at the shock front. The difference between the absolute peak pressure and the ambient pressure is called the **peak overpressure**, denoted by Δp_o. Thus,

$$\Delta p_o = p_o - p_a \tag{2.6}$$

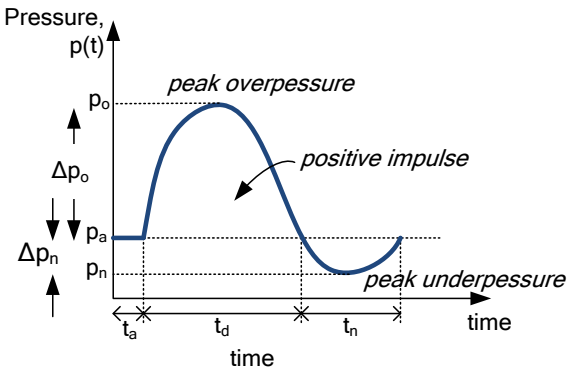

Figure 2.18. *A typical blast wave without having a shock front at a fixed location some distance from the blast origin, modified from [61]*

Furthermore, as shown in Fig. 2.16, there exists a small but finite time, t_a, before the shock front travels from the center of explosion to the location under consideration. This particular time is called the **arrival time** at which the peak shock overpressure Δp_o can be observed. Soon afterward, the pressure amplitude decreases gradually to reach the ambient pressure at time $t = t_a + t_d$. The variable t_d is called the **positive phase duration**, which is defined as the period under which the blast pressure above the ambient.

Thus, as the blast wave expands continuously outward its origin, the pressure amplitude falls below ambient and eventually reach its minimum point. The minimum reached point under ambient is called the **absolute peak negative pressure**, denoted by p_n. The difference between the absolute peak negative pressure and the ambient pressure is called the **peak underpressure**, denoted by Δp_n. The period under which the blast pressure below ambient is called the **negative phase duration**, denoted by t_n. The blast wind then reverses its direction and flows toward the blast origin as required to conserve mass. Eventually, the pressure amplitude is settling back to ambient as the blast wave passes by.

The assessment of damage from explosions is typically associated with the positive period of the blast wave. According to the circumstances, potential damaging during the negative phase should also be taken into account. However, for the chemical process industries, the negative period of the blast wave is less important and not to be discussed in this thesis. Most probably, the underpressure period would be considered important while analyzing the damage from a nuclear explosion, because during such an explosion the blast wave could have an extremely high overpressure with a really sharp shock front.

With respect to the analysis of risk from an explosion, in addition to the peak overpressure (Δp_o) and the positive phase duration (t_d), the so-called **positive impulse**, denoted by i_p, is also used quite often particularly for assessing the possible damage to structural buildings. This parameter is defined as the area under the pressure-time curve during the positive period (the overpressure period) and describes the change of momentum during this positive phase having a dimension of pressure-time product. Therefore, the positive impulse is the integral of pressure as a

function of time during the positive phase duration as given by the following equation:

$$i_p = \int_{t_a}^{t_a+t_d} p(t)dt \tag{2.7}$$

Here, $p(t)$ is the function of pressure-time history during the positive phase and t is time. In fact, there are several equations which can be used to describe the pressure-time history during the positive phase duration. A widely used one is the modified *Friedlander wave equation* which assumes the ideal blast wave, as shown in Fig. 2.17. In this case, the decay of pressure after reaching the peak overpressure is approximated exponentially. The modified *Friedlander wave equation* is based on the Sedov-Taylor blast wave self-similar solution and expressed as follows [37, 62]:

$$p(t) = p_a + \Delta p_o \left[1 - \left(\frac{t}{t_d}\right)\right] \exp\left(-\frac{\beta t}{t_d}\right) \tag{2.8}$$

where β is a wave form parameter that describes the rate at which the pressure decreases after reaching its peak value. In [63], an approximation of the pressure-time profile during the positive phase to a triangular shape is introduced. Thus, the pressure-time history for both types of blast wave can be illustrated by Fig. 2.19. Using this approximation, the positive impulse is simply given

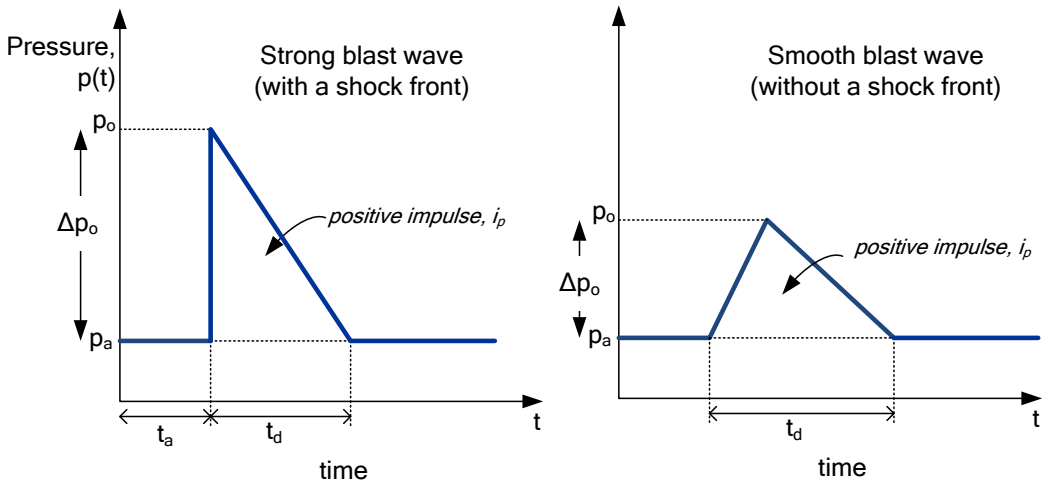

Figure 2.19. *Approximation to the positive impulse of blast waves by means of a triangular shape*

by:

$$i_p \approx \frac{\Delta p_o \cdot t_d}{2} \tag{2.9}$$

Chapter 3

Estimation of the Blast Wave Parameters by means of Empirical Techniques

The prediction of the blast wave properties either for detonation or deflagration blast wave is extremely important for safety considerations of process plants. With respect to the chemical process facilities including the transportation process, the vapor cloud explosion becomes a concern because, when occurred, it has a potential to generate damaging levels of overpressure and causes human injury, death, or event escalation. The state-of-the-art for the prediction of overpressures resulting from a vapor cloud explosion falls generally into two broad categories of models, namely **simplified empirical models** and the **advanced computational fluid dynamics (CFD) models**.

CFD models actually calculate the overpressure field by solving the Navier-Stokes equations numerically and incorporating different sub-models to account for turbulence and combustion reactions. Results are often strongly dependent on the location and strength of the ignition point, the location and composition of the flammable cloud throughout its volume, and the location and configuration of any obstacles or obstructions within the cloud. The time required for calculating the overpressure resulting from a single ignition point; a single cloud geometry or location can be significant. Given the number of combinations of ignition points and cloud geometries (e.g., changes in wind direction or wind speed) that can influence a given flammable release, it is generally prohibitive to use CFD models for the risk assessment or building siting purposes [64]. Therefore, the empirical models are still very popular for the consequence analysis.

In fact, regardless of which models being used for solving a particular problem, the prediction results are quite important for assessing the type and level of damage from an explosion to the vulnerable objects. As stated before, these objects of interest may include people, structures and the environment. As the blast wave propagates away from its origin, the most important parameters include the **peak side-on overpressure** (Δp_o), **positive phase duration** (t_d) and **positive**

impulse (i_p). In this chapter, however, the procedure for the prediction of blast parameters by means of the empirical techniques are further described.

In general, the empirical models are considered the most simplified tool for predicting the properties of the explosion blast wave. These models can be implemented to the blast wave from both detonation or deflagration. The empirical technique is essentially based on the analysis of corresponding experimental data or has been developed from the numerical analysis of physical parameters relationships. Therefore, the use of these models are generally simple, easy to be implemented and enable one to carry out fast calculations. However, according to the circumstances, it is quite common to add several conservative assumptions and simplifications in order to use these model.

With respect to the prediction of the blast overpressure of a vapor cloud explosion, three empirical models are still quite famous in use. These three models are classified into two general groups. One model is based on the characteristic of the TNT charge blast, which is commonly known as the **TNT equivalent model**, and two other models are based on the characteristics of the fuel-air charge blast. These two models are **TNO Multi-Energy model** and the **Baker-Strehlow-Tang model**.

The TNT equivalent model is generally good for the prediction of the parameters from detonation blasts, such as the detonation of chemical explosives and other similar cases. However, to a certain extent, this model has also been implemented for non detonative blasts (deflagrative blasts). The vapor cloud explosion has also been predicted using this model. However, for the latter case, the user must be very careful because there are some conservative assumptions which must be taken into consideration and these may lead to significant simplifications of the analysis giving inaccurate prediction outcomes. In a short sentence, the TNT equivalent model is very limited to a particular range of application only. At the beginning of this chapter, the procedure for the use of this model is discussed in much detail.

Meanwhile, the models based on the characteristics of the fuel-air charge blast has been explicitly dedicated for the prediction of the parameters from the deflagration blast waves. Both the TNO Multi-Energy and Baker-Strehlow-Tang models are very popular to the prediction of the blast wave from a vapor cloud explosion. The second part of this chapter is designed to describe the procedure for the use of these two models in detail.

3.1 The TNT equivalent model

3.1.1 The TNT equivalent concept

The TNT equivalent method was developed based on the analysis of the blast data from the TNT (Trinitrotoluene) charge detonation. This model is, in fact, the most widely known classical empirical model for the prediction of the blast wave parameter. Historically, TNT or **2,4,6-Trinitrotoluene** (see Fig. 3.1) with the chemical formula $C_7H_5N_3O_6$ is one of the first explosives to be widely and reliably manufactured. It was firstly prepared in 1863 by Wilbrand while its

isomer was firstly discovered in 1870 by Beilstein and Kuhlberg. Later, a pure TNT was prepared by Hepp in 1880 and its structure determined by Claus and Becker in 1883. It was not until 1891 after Hauserman manufactured this material in industrial quantities [42]. Since then TNT has been required for high explosive shell fillings [65]. It can be loaded into shells by casting as well as pressing. This material can be cast easily as a sphere or hemisphere, and reliably detonated, without containment [66]. TNT is later recognized as the most important blasting charge either as commercial explosives or for military purposes.

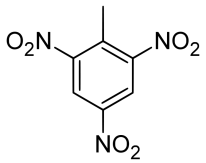

Figure 3.1. *2,4,6-Trinitrotoluene (TNT) with the chemical formula* $C_7H_5N_3O_6$

Due to its frequently use, there is a large amount of the blast data from the detonation of the TNT in comparison to the other chemical explosives. This situation has made the TNT to be used as a standard reference for explosion blast analysis [67, 68]. A model was developed based on this data in order to predict the blast effects from other explosive material. This model is later called the TNT equivalent model. In fact, this model uses a conservative assumption that the characteristics of blast waves from explosion of different types of explosive materials are basically comparable to the blast wave generated from the TNT charge detonation. In the other word, there is an attempt to equate the blast wave effects generated from different types of explosive materials with those produced by an equivalent mass of TNT charge [69, 70].

It is, however, quite important to mention that the TNT blast is a detonation blast and not a deflagration. The detonation typically produces a high overpressure blast wave due to the generation of a shock. Therefore, the TNT equivalent model is practically good for the prediction of the properties of detonation blast wave only. It is generally recommended that the blast wave generated from other types of conventional chemical explosives are to be directly estimated by this model. During its later development, the blast waves from the direct detonations of the flammable gas or vapor cloud as well as the bursting of pressure vessel, which probably have the similar blast wave behavior to the TNT charge, may also be predicted by this model.

Due its simplicity, the application of the TNT equivalent model was then extended to the non-detonative blast case. The blast parameters from the deflagration of the flammable gas or vapor cloud, or the vapor cloud explosion has also been predicted using this model. However, the use of the TNT equivalent model for this particular case is considered a very conservative approach because the physical properties of deflagration wave are significantly different from those of detonation wave. Therefore, some conservative assumptions should be made while using this model for the vapor cloud explosion analysis.

3.1.2 Important procedures

3.1.2.1 Determination of the TNT equivalent mass

Perhaps, the most important procedure for the TNT equivalent model is only to determine the TNT equivalent mass for the explosive material under consideration. This feature has made this model quite simple and generally easy. The TNT equivalent mass, which is here denoted by W_T, is defined as the mass of the TNT charge that would give rise to the same blast effect as the given mass of the explosive material under consideration [39]. The general formula to determine this quantity is given by the following equation [32]:

$$W_T = \mathbf{EF} \times W_e \tag{3.1}$$

Here, W_e is the given mass of the explosive material under consideration in kg and **EF** is the dimensionless TNT mass equivalent factor. The procedure for the determination of the explosive mass of the material is given as follows:

- For the chemical explosive, W_e is taken as the whole mass of the material without any restriction. In this case, the whole mass of the material basically contributes to the generation of the blast wave.
- For the flammable gas or vapor cloud, W_e is actually the mass of the flammable material within the explosion limits, which is also called the flammable mass. As mentioned before, if the concentration of the flammable material in the vapor cloud above the upper limit or below the lower limit, the vapor cloud is not explosive. Therefore, the result of the dispersion analysis is required for this particular case [57]. However, for the worst case scenario and, if no dispersion analysis is made, it could still be assumed that the total amount of flammable material released from the inventory contributes to the generation of the blast.

The TNT mass equivalent factor (**EF**) is determined by another two important variables, namely (1) the ratio of the explosion energy of the material relative of the explosion energy of the TNT charge, denoted by α_e and (2) the explosion efficiency as the portion of the explosion energy of the explosive material under consideration being converted to generate the blast wave (the blast energy), denoted by η. Thus, **EF** is expressed by the following equation:

$$\mathbf{EF} = \eta \times \alpha_e \tag{3.2}$$

The procedures for the determination of these two variables (α_e and η) are mentioned in the following:

- For the chemical explosive other than the TNT charge,
  - The explosion energy of the material is the heat of detonation of the chemical explosive,

denoted by $\Delta H_{d,\mathsf{ex}}$. Thus, α_e is given by:

$$\alpha_e = \frac{\Delta H_{d,\mathsf{ex}}}{\Delta H_{d,\mathsf{TNT}}} \tag{3.3}$$

The heat of detonation of TNT charge (corresponding also to the explosion energy of the TNT) itself typically between 4190 kJ/kg and 4650 kJ/kg as indicated in [21, 32]. While calculated from Table 2.2, Typical values of α_e for several common chemical explosives is shown in Table 3.1 assuming that the explosion energy of TNT is 4650 kJ/kg.

Table 3.1. *The ratio of the explosion energy of several common chemical explosives (α_e)*

Chemical explosives	α_e	Chemical explosives	α_e
RDX	1.154	2,4 Dinitrotoluene	0.77
HMX	1.221	Ammonium nitrate	0.56
Nitroglycerin	1.481	Cyclohexanone peroxide	0.19
PETN	1.309	Sodium chlorate	0.15
Pentolite	1.129		

- It is quite common to take a conservative assumption that the whole explosion energy of any chemical explosive is converted to generate of blast wave. This means, by default, the explosion efficiency of any chemical explosive is always equal to unity ($\eta = 1$). This assumption is conservative and, however, not always true, because the detonation process itself may not be completely efficient. In reality, the entire energy set free by the detonation would not be completely converted into the generation of blast waves. Some fraction of this energy may be released in other non blast wave forms, such as thermal radiation [56, 68].

- Finally, the TNT equivalent mass for any chemical explosive is given by the following equation:

$$W_T = \frac{\Delta H_{d,\mathsf{ex}}}{\Delta H_{d,\mathsf{TNT}}} \times W_{e,\mathsf{ex}} \tag{3.4}$$

where $W_{e,\mathsf{ex}}$ is the given mass of the explosive material in kg.

- For the flammable gas or vapor cloud

  - It is assumed that the heat of combustion of the flammable fuel (gas or vaporizing liquid) in the gas or vapor cloud, denoted by $\Delta H_{c,\mathsf{f}}$, is the explosion energy of the flammable gas or vapor cloud. Thus, α_e is given by:

$$\alpha_e = \frac{\Delta H_{c,\mathsf{f}}}{\Delta H_{d,\mathsf{TNT}}} \tag{3.5}$$

Table 3.2 shows typical values of the heat of combustion of several common hydrocarbon fuel-air mixtures.

Table 3.2. *Heat of combustion of several hydrocarbon fuel-air mixtures [71]*

Fuel	Heat of combustion [kJ/kg]	Fuel	Heat of combustion [kJ/kg]
Methane	50030	n-Pentane	44980
Ethane	47490	n-Hexane	44750
Propane	46360	Propene	45790
Ethene	47170	Propylene	45790
n-Butane	45720	Acetylene	48220
n-Heptane	44560	Hydrogen	130800

– The ratio of the explosion energy of the flammable gas or vapor cloud which is the heat release from the combustion reaction being converted to the generation of the blast wave is typically much lower than 1 ($\eta \ll 1$). For instance, the maximum theoretical explosion efficiency of the flammable cloud of hydrocarbon-air mixture under atmospheric conditions is approximately 40%, although in practice it is always much lower [57]. In fact, the explosion efficiency for the flammable gas or vapor cloud is difficult to be determined and remains one of uncertain parameters. However, according to experiences, this value is most estimated varying between 1% to 15% [33]. The true value for a specific case is unknown and not calculable. During the analysis using the TNT equivalent model, this value must be provided by the user. There are several references providing typical values of the explosion efficiency for different conditions of the vapor cloud in the chemical process industries [11, 21, 72]. These values are summarized in Table 3.3

– Finally, the TNT equivalent mass for the flammable gas or vapor cloud is given by the following equation:

$$W_T = \eta \times \frac{\Delta H_{c,\mathsf{f}}}{\Delta H_{d,\mathsf{TNT}}} \times W_{e,\mathsf{f}} \tag{3.6}$$

where $W_{e,\mathsf{f}}$ is the estimated flammable mass of the vapor cloud in kg.

3.1.2.2 TNT blast curves

Once the TNT equivalent mass (W_T) has been determined, the next procedure is read the blast parameters of interest from a TNT blast curve. Typically, the TNT blast curve is a 2D plot relating the blast parameters with the stand-off distance relative to the center of the explosion (the origin of the blast wave). In literature, there are available several TNT blast curves for different circumstances. Most of them were compiled from the analysis of TNT blast data (experimental

Table 3.3. *Typical explosion efficiencies for modeling vapor cloud or gas explosions and their conditions*

Method		**Scenario/Remarks**	$\eta(\%)$
Source: **Lees** [11] and **CCPS/AIChE** [22]			
Brasie and Simpson	-	Near fied	2.0
	-	Far field	5.0
Advisory Committee on Major Hazards (ACMH)	-	Typical value for predictive purposes	3.0
Exxon	-	Open terrain	3.0
	-	Partially confined and obstructed terrain	10.0
Eichler and Napadensky	-	Symmetric cloud (max)	2.0
	-	Asymmetric cloud (max)	up to 40.0
Prugh	-	Mass of vapor cloud = 100 kg	2.0
	-	Mass of vapor cloud = 10^6 kg	up to 70.0
British Gas (Investigation by Harris and Wickens)	-	Mass in obstructed region only	20.0
Health Safety Executive UK	-	Low reactivity (e.g. methane)	3.0
	-	Medium reactivity (e.g. propene oxide)	6.0
	-	Very reactive gases (e.g. ethene oxide)	10.0
Factory Mutual Research Corporation	-	Low reactive materials	5.0
	-	Moderately reactive materials	10.0
	-	Highly reactive materials	15.0
Industrial Risk Insurers			2.0
Source: **TNO** [21] and **Van den Berg et al.** [72]			
First version CPR-14E	-	Upper limit for predictive purpose	10.0
Lannoy et al.		Statistical analysis over 23 accidents:	
	-	Median observed value	3.0
	-	Mean value (covering 60% cases)	4.0
French Authority Safety Rule	-	Recommendation for safety purpose	10.0
French Chemical Industry	-	Recommendation for safety purpose	4.0

result or similar sources). Some models have been developed by solving mathematical relationships of physical parameters involved. The latter technique is sometimes called the semi-empirical blast curve. In the following, four models for the TNT blast curve, which are typically found and have been recognized widely, are presented.

One of the first attempts to develop the TNT blast curve was based on the numerical calculation by a US nuclear physicist Harold L. Brode [73, 74]. He developed a semi-empirical correlation model

for the TNT blast. The **Brode's equations** are a set of equations for the prediction of the peak overpressure of the TNT spherical blast as a function of stand-off distance to the blast origin. The stand-off distance to the center of the explosion is given in terms of the scaled quantity governed by so-called the **Hopkinson's scaling law**. This variable is called the scaled distance and denoted by z and based on the cube root of the mass of the TNT or, in general, the TNT equivalent mass. Thus,

$$z = \frac{R}{\sqrt[3]{W_T}} \tag{3.7}$$

Here, R is the stand-off distance of the object of interest relative to the blast origin in m and W_T is the TNT equivalent mass in kg. Thus, the scaled distance z has a dimension $\mathrm{m/kg^{1/3}}$.

Brode's equations are made up of two equations for two different zones distinguished with respect to the blast overpressure. The expression of the Brode's equations are:

$$\Delta p_o(z) = \begin{cases} \dfrac{0.1567}{z^3} + 1 & \text{for} \quad \Delta p_o > 10 \text{ bar (near field)} \\ \dfrac{0.269}{z} + \dfrac{0.119}{z^2} + \dfrac{0.137}{z^3} - 0.019 & \text{for} \quad 0.1 < \Delta p_o < 10 \text{ bar (far field)} \end{cases} \tag{3.8}$$

Unfortunately, Brode's equations are not available for the other important blast parameters, such as positive impulse or positive phase duration. In addition, there is no equation if the blast overpressure falls beyond the range mentioned above. Therefore, the prediction of the blast overpressure beyond the given range is hard to do and generally not recommended.

Another widely accepted TNT blast curve is the one developed by **Charlie Kingery** and **Gerry Bulmash**. These two researchers had collected the experimental data from literally hundreds of references on TNT detonation as mentioned on their 1984 report [11, 75]. These data were then analyzed and compiled in order to develop correlations for the several important blast parameters.

The correlations for the blast parameters which are the fits to the experimental data, according to Kingery and Bulmash, can be made in the form of 8th-order and 11th-order polynomial equations presenting the relation of the blast parameter as a function of the stand-off distance to the blast origin. This distance is given again in terms of its scaled quantity according to the Hopkinson's law. The 8th-order polynomial equations are the model for the TNT spherical blast, while the 11th-order equations are for the hemispherical blast model. The blast parameters to be predicted by this model include the peak side-on overpressure (Δp_o), positive impulse (i_p), arrival time (t_a) and positive phase duration (i_p).

In general, for a particular parameter represented by $\phi(z)$, the Kingery-Bulmash equations are expressed by the following equation:

$$\log \phi(z) = \sum_{i=0}^{n} c_i \cdot U(z)^i \tag{3.9}$$

Here, $\phi(z)$ is the blast wave parameter function of interest, c is a correlation constant and n is the polynomial order. The intermediate function $U(z)$ is determined by the following formula:

$$U(z) = a + b \cdot \log(z) \tag{3.10}$$

where a and b are another correlation constants. All constants of the equations can be found further in Appendix A. The Kingery and Bulmash equations are unfortunately valid only for a limited range of the Hopkinson's scaled distance. For a spherical model, this model is to be used only for $0.0531 \leq z \leq 40$, while for the hemispherical model, this model is considered valid within the range of $0.0674 \leq z \leq 40$. The use of these models beyond these given ranges are generally not recommended.

Another semi-empirical model for the TNT blast curve has also been developed by **Josef Henrych** [62]. He proposed a set of equations for a TNT spherical blast. This model is able to predict the peak side-on overpressure for three different zones, namely near, middle and far zone, specified by the range of the Hopkinson's scaled distance (z). The Henrych's equations are written as follows:

$$\Delta p_o(z) = \begin{cases} \dfrac{14.072}{z} + \dfrac{5.540}{z^2} - \dfrac{0.357}{z^3} + \dfrac{0.00625}{z^4} & \text{for} \quad 0.05 < z \leq 0.3 \\ \dfrac{6.194}{z} - \dfrac{0.326}{z^2} + \dfrac{2.132}{z^3} & \text{for} \quad 0.3 < z \leq 1 \\ \dfrac{0.662}{z} + \dfrac{4.05}{z^2} + \dfrac{3.288}{z^3} & \text{for} \quad 1 < z < 10 \end{cases} \tag{3.11}$$

Here, the peak side-on overpressure $\Delta p_o(z)$ is in bar. The use of this model is also limited by the range of the scaled distance. No equation was defined for the estimation of the peak overpressure beyond the given range.

Another TNT blast model which is considered more flexible and can be applicable for any range of scaled distance is the one from **Kinney and Graham**. The two researchers had developed a set of equations for the prediction of the TNT spherical blast parameters which are the fits to the experimental data. These equations are able to predict the peak side-on overpressure (Δp_o), positive impulse (i_p) and positive phase duration (t_d) [76]. Unlike the other three model mentioned above, the presentation of the blast parameters in this model are given in terms of their scaled quantities for the peak side-on overpressure and the positive phase duration. Meanwhile, the positive impulse remains unscaled.

The scaling of the peak overpressure, here denoted by Δp_s, is not based on the cube root of the explosive mass, but only the ratio of the peak (side-on) overpressure relative to the absolute ambient pressure. Thus,

$$\Delta p_s = \frac{\Delta p_o}{p_a} \tag{3.12}$$

Here, p_a is the absolute ambient pressure whose the atmospheric pressure is usually taken into account. Δp_s is a dimensionless parameter.

Meanwhile, the scaling of the positive phase duration, here denoted by τ_d is based on the cube-root of the TNT equivalent mass according to the Hopkinson's scaling law. Thus,

$$\tau_d = \frac{t_d}{\sqrt[3]{W_T}} \tag{3.13}$$

which means that the scaled positive phase duration is not a unitless variable but has a dimension $\mathrm{s/kg^{1/3}}$.

The expression of the Kinney-Graham equations of the TNT spherical blast parameters are written as in the following [77]:

$$\Delta p_s(z) = \frac{808\left[1+\left(\frac{z}{4.50}\right)^2\right]}{\sqrt{\left[1+\left(\frac{z}{0.048}\right)^2\right]\left[1+\left(\frac{z}{0.32}\right)^2\right]\left[1+\left(\frac{z}{1.35}\right)^2\right]}} \tag{3.14}$$

$$i_p(z) = \frac{0.067\sqrt{1+\left(\frac{z}{0.23}\right)^4}}{z^2\sqrt{1+\left(\frac{z}{1.55}\right)^3}} \tag{3.15}$$

$$\tau_d(z) = \frac{980\left[1+\left(\frac{z}{0.54}\right)^{10}\right]}{\left[1+\left(\frac{z}{0.02}\right)^3\right]\left[1+\left(\frac{z}{0.74}\right)^6\right]\sqrt{\left[1+\left(\frac{z}{6.9}\right)^2\right]}} \tag{3.16}$$

In some other cases, a TNT blast curve for the positive impulse may also be found. This parameter may be presented in its original form or in its scaled form. In the case of the positive impulse is estimated using the TNT equivalent model by reading the appropriate TNT blast curve and it is given in its scaled form, the Hopkinson's scaling law is also applicable in this case. The expression of the **Hopkinson's scaled positive impulse**, denoted by i_s, is written as follows:

$$i_s = \frac{i_p}{\sqrt[3]{W_T}}\Delta p_o \cdot t_d \tag{3.17}$$

This parameter is not a unitless variable but has a dimension $\mathrm{N^2s^2/(m^4kg^{1/3})}$. However, according to the previous chapter, the positive impulse may also estimated from the peak overpressure and the positive phase duration using the triangle rule approach. Therefore, once the latter two variables have been determined, the positive impulse can be estimated accordingly.

Fig. 3.2 shows the TNT blast curves which are generated by employing the four equations presented above. In this figure, only the relation of the peak side-on overpressure Δp_o (bar) as a function of the scaled distance (z) for a TNT spherical blast is presented. As seen in this figure,

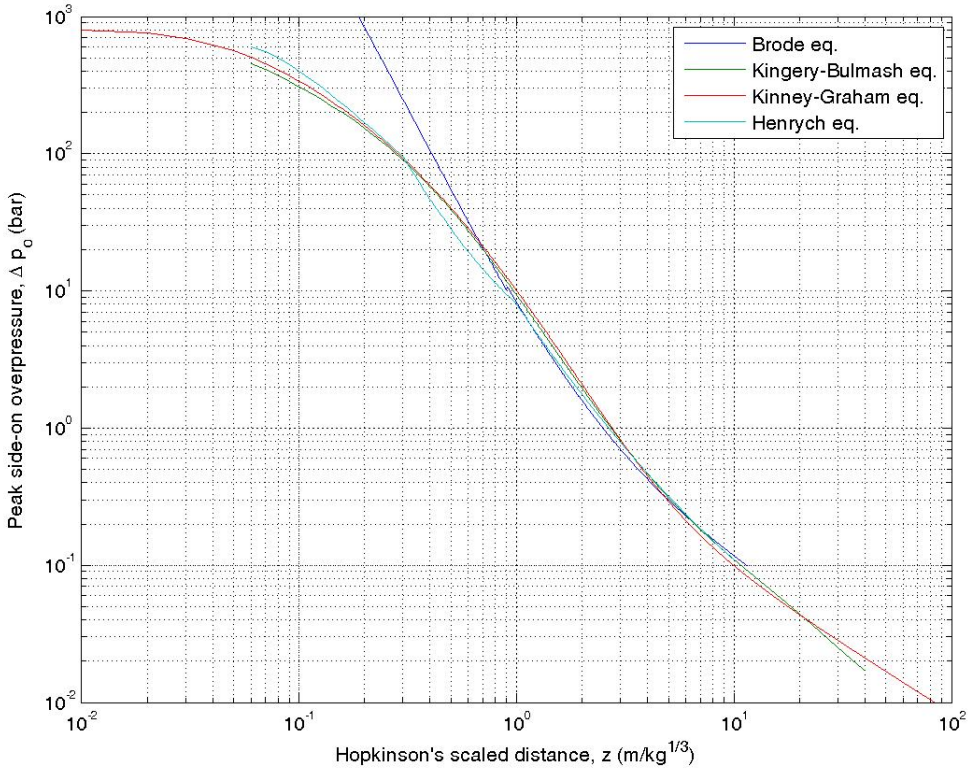

Figure 3.2. *Representation of the TNT blast curves according to the Brode, Kingery-Bulmash, Kinney-Graham and Henrych correlation models. In this figure, only the peak side-on overpressure (Δp_o, bar) of the TNT spherical blast model as a function of the Hopkinson's scaled distance (z, m/kg$^{1/3}$) is shown. If necessary, the atmospheric pressure of 1 atm is assumed*

Brode's equations estimate that the peak side-on overpressure of a spherical blast is much higher for the scaled distance approximately smaller 0.7. For a scaled distance higher than 0.7 up to 10, these four models give almost the same prediction result. However, as introduced above, it is found to be more convenient to use the Kinney-Graham equations due to its unrestricted scaled distance range application. For the computer application in this thesis, unless indicated otherwise, the Kinney-Graham equations are applied for the prediction of the blast parameters if the TNT equivalent model is to be implemented.

3.1.2.3 Important consideration for the application of the TNT equivalent model for the blast analysis of vapor cloud explosions

As mentioned above, the vapor cloud explosion blast may also be predicted using the TNT equivalent models. However, the prediction result form this model is considered very conservative especially in the near field. The shape of the blast and the magnitude of the overpressure from a vapor cloud explosion are basically not the same to those from the TNT charge or other chemical explosive materials. Some conservative assumptions, such as the selection of the explosion efficiency and

the procedure for the determination of the quantity of flammable mass in the vapor cloud could, could be proposed in order to make the TNT equivalent model being useful for analyzing the vapor cloud explosion blast.

Another important point which must also be considered is that the vapor clouds are most likely exploded near to the surface of earth or not too far from the ground. Therefore, the blasts from vapor cloud explosions should always be modeled as hemispherical blasts instead of spherical blasts. The effect of ground surface reflection to the blast prediction must be taken into account. Once the TNT equivalent mass for the flammable mass in the vapor cloud has been determined, this flammable mass should be assumed in its hemispherical volume. The blast parameters of interest are to be read from the TNT blast curve. However, the relevant blast curve for the vapor cloud explosion should be the blast curve representing the TNT hemispherical blast. If the blast curve of the TNT is given for the spherical blast, some important modifications should be made. In order to deal with this problem, Smith and Hetherington [56] suggest that the modification should be made to the explosive mass, which means the flammable mass of the vapor cloud. A reflection factor, denoted here by k, is used to account for the ground reflection giving the initial given mass which is previously assumed as hemispherical mass being a spherical one. The reflection factor of 2 is typically assumed for a perfect reflection [11]. The reflection factor is to be multiplied to the flammable mass of the vapor cloud. Therefore, once the TNT equivalent mass has been determined, the calculation of the scaled distance according to Eq. (3.7) should use the modified equivalent mass. The bigger the explosive mass, the smaller the scaled distance (z) giving the higher the overpressure which should normally be expected for a hemispherical explosive mass.

In [78], another procedure is mentioned. The modification should be made to the final prediction of the blast parameters. For example, for the blast overpressure, the hemispherical effect would make this parameter to be multiplied with the corresponding reflection factor. Such modification is found simple since no modification to the explosive mass should be in the calculation process. While using this procedure, the expression for the Kinney and Graham equations model will get a little change. It is only by inserting additional factor k into the the equation to account for the hemispherical blast wave. Thus, the blast overpressure for the vapor cloud with a scaled distance z from the initial blast point accounting for the initial hemispherical mass is given by the following equation:

$$\Delta p_s(z) = \frac{k \cdot 808 \left[1 + \left(\frac{z}{4.50}\right)^2\right]}{\sqrt{\left[1 + \left(\frac{z}{0.048}\right)^2\right]\left[1 + \left(\frac{z}{0.32}\right)^2\right]\left[1 + \left(\frac{z}{1.35}\right)^2\right]}} \tag{3.18}$$

Again, the reflected factor of 2 may also be assumed for a perfect reflection. In practice, a factor is often lower than this value due to the fact that the energy released in the explosion is not only dissipated in the production of blast, but also leaving the system as thermal losses and etc [57]. In [79], the factor of 1.6 is used in order to normalize the initial blast curve from Marshall which has been used since many years as indicated [22].

3.2 The TNO Multi-Energy model

3.2.1 Critical points with regard to the TNT equivalent model for the vapor cloud explosion analysis

In fact, according to [80], the maximum overpressure in a vapor cloud explosion is a complicated function of different factors. These factors are actually the initial and boundary conditions of the vapor cloud explosion. The initial conditions are specified as follows:

- The fuel type in the gas or vapor cloud represented by the reactivity of the fuel involved. The more reactive the material, the higher the overpressure.
- The initiation of the vapor cloud explosion with respect to the location and the strength of the ignition source.

Meanwhile, the boundary conditions are as follows:

- The degree of the confinement which determines the possible dimension of the flame expansion following the ignition.
- The obstacle configuration which determines the density of obstacle, the size of the obstacles and the area or volume blockage ratio which reduces the free volume to which the vapor cloud may expand.
- The scale in sense that the higher the overpressure in the experiments as the scale increases.

Unfortunately, none of these factors is taken into account while using the TNT equivalent model, except probably for the fuel reactivity which is used for the estimation of the explosion efficiency. The TNT equivalent model takes into account only the whole mass of the explosive material and assumes the explosion efficiency for the determination of any blast parameter. No other factor is taken into consideration. It is absolutely acceptable since for the detonation mode to which the TNT equivalent model is addressed does not consider whether or not the confinement or congestion is present in the vicinity. Therefore, the TNT equivalent model is recommended for high explosive materials.

The consideration whether the blast wave is a detonation or a deflagration blast is ignored in the TNT equivalent model. The deflagration blast must also be assumed to have similar behaviors as the detonation blast if this model is implemented. This assumption is unfortunately not true. The vapor cloud explosion remains a deflagration process for which the flame is accelerated. It will not be a detonation except for the reason mentioned previously in the past chapter. Detonation of the flammable vapor cloud would probably occur if there is a transition from deflagration due to a very extreme flame acceleration or if there is a direct initiation of detonation by a extremely strong ignition source. Neither of these processes would occur in normal circumstances.

In fact, the main problem which may arise while using the TNT equivalent model for the vapor cloud explosion is the over-estimation of the blast overpressure in the near field. With respect to the physics of a detonation, this combustion mode generates an initially intense blast wave with

a strong shock front close to the blast center, across which there will be large changes of entropy. Consequently, less energy is available as the blast expands to lower overpressure at some distance from the blast origin. In contrast, deflagration produces smooth blast waves, a longer positive phase duration resulting in a larger positive impulse and with initially smaller changes of entropy. Thus, there will be more energy available as the blast propagates at greater distances. It means that although the detonation of a TNT charge and the rapid combustion of a flammable gas or vapor cloud may release the same amount of energy, the shape of the blast wave produces by a deflagration does not necessary resemble that from a detonation. Therefore, by default, the TNT equivalent model tends to over-estimate near field overpressure from vapor cloud explosions. Van den Berg et al. [72] has recommended that the TNT equivalent model should only be used for the assessment of blast effects at the far-field where the peak overpressure level is less than 30 kPa. In this case, the distinction between detonation and deflagration blasts quite smaller in comparison to those at the near field. A deflagration blast wave can then be assumed to be closely resemble the blast effect from a TNT detonation. In the other words, the shape of blast wave is assumed to be nearly independent of its source at far field [81, 82].

Although there are several critical points to the TNT equivalent model, including also the determination of the explosion efficiency η, which is unfortunately highly empirical and uncertain, this model remains widely used until now. However, for a better and satisfied result especially for the vapor cloud explosion, the following two models, the TNO Multi-Energy and the Baker-Strehlow-Tang model, should be taken into account. In this section, the TNO Multi-Energy is presented.

3.2.2 The Multi-Energy concept

The **TNO Multi-Energy model** is another widely used empirical model which uses the blast curve for the estimation of the properties of vapor explosion explosion blast waves. In general, this model is based on the fact that the vapor cloud explosion is not a detonation with an extremely high overpressure, but also remains only a deflagration which may give rise to a certain level of overpressure typically lower than the detonation overpressure but still sufficient to cause certain dangers to the vulnerable objects in the surroundings (e.g., people or building). The generation of blast overpressure in the vapor cloud explosion definitely depends on several conditions and circumstances with respect to the location or area in which the vapor cloud engulfs.

As mentioned in the previous chapter, the generation of blast overpressure in the vapor cloud explosion extremely depends on whether the propagation flame speed during the deflagration of the vapor cloud is accelerated or not. This mechanism is determined by the existence of process boundaries which is engulfed by the flammable gas or vapor cloud. The combustion of the flammable vapor cloud in the fully open areas (unconfined) would produce a lower overpressure or even none at all. As stated before, the unconfined part tends to burn out slowly as a fire without generating overpressure. This outcome is usually called a flash fire.

Basically, the TNO Multi-Energy model is implemented to estimate the blast overpressure from

a vapor cloud explosion. This model can also be named an "*equivalent*" model for any vapor cloud explosion. It takes into account the influence of process boundaries, including the degree of confinement, the level of congestion and the characteristics of the fuel in the vapor cloud, for the determination of the blast parameters. Therefore, the TNO Multi-Energy model is more realistic than the TNT equivalent model, especially when dealing with the blast wave from deflagrations.

Historically, the TNO Multi-Energy model is a revised version of the initial TNO blast model as described in [83, 84]. TNO is the Netherlands organization for applied scientific research (in Dutch, *Nederlandse Organisatie voor Toegepast Natuurwetenschappelijk Onderzoek*). The development of this model is described, among others, in [72, 85, 86]. The procedure for its implementation is mentioned in much detail in the revised version of the TNO Yellow Book [21]. In recent years, there are some considerable improvements to the procedure of this model as indicated in [87, 88].

The TNO Multi-Energy model is essentially based on the concept of the **Multi-Energy**. Initially, the TNO blast model had assumed that the whole flammable gas or vapor cloud contributes to the blast wave and to the generation of blast overpressures. At a glance, this assumption does not have any difference from the basic assumption of the TNT equivalent model. In this sense, the two models have considered a single explosion and take into account the total mass of the explosive material. However, as mentioned above, in the case of vapor cloud explosion the unconfined part of the flammable gas or vapor cloud would not make a serious contribution to the generation of blast overpressure.

Later on, the initial concept of TNO blast model is revised and replaced by the Multi-Energy concept. According to this new concept, the violence of a vapor cloud explosion depends on the size and the initial strength of the portion of the flammable gas or vapor clouds which are partially confined or congested by the process boundaries. This means that the Multi-Energy concept assumes that the blast overpressure would develop only in those parts of the flammable gas or vapor cloud that are located in partially confined or congested areas. Therefore, the portion of the flammable gas or vapor cloud which is confined and congested is also called the *blast source*. If the flammable gas or vapor cloud which is confined but expands within the unobstructed area which does not include any kind of obstacles, the initial blast strength of the vapor cloud once it is ignited would be quite low. However, if such flammable gas or vapor cloud expands within the area with high density of obstacles, such as process equipments, walls, and buildings, a higher initial blast strength should be assigned, because the cloud could expands only into the free space in between obstacles causing the expansion flow following the ignition to be intensified.

3.2.3 Important procedures

Like the TNT equivalent model, the TNO Multi-Energy model also determines the blast parameters of interest using the blast curves that relate the blast parameter as a function of distance from the explosion origin. It is important to mention that the explosion of the vapor cloud is based on a ground explosion of hemispherical vapor cloud as shown in Fig. 3.3. $\Delta p_{o,\max}$ is assumed to be the maximum overpressure that can be attained in the vapor cloud. For the analysis for the vapor

cloud explosion, it is typically assumed that this value is constant along the radius of the vapor cloud. Therefore, the generation of the family of blast curves usually assumes different flame speeds which are specified to be constant during the explosion.

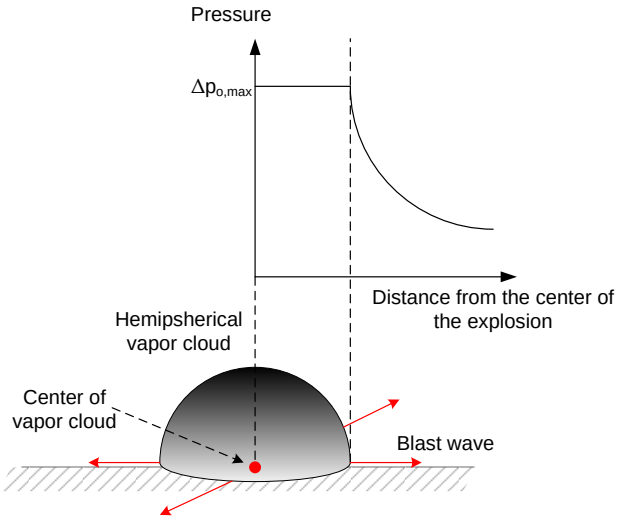

Figure 3.3. *The idealized hemispherical vapor cloud as the basis for the TNO Multi-Energy model [89]*

The TNO Multi-Energy model consists of a family of blast curve for peak overpressure, positive phase duration and dynamic pressure versus distance. Figs. 3.4 and 3.5 show two sets of the TNO Multi-Energy blast curve family for the first two parameters. As mentioned earlier, these curves provide the scaled peak side-on overpressure and scaled positive phase duration as a function of scaled distance of the object of interest relative to the initial point of explosion (blast origin). Unlike the TNT blast curves, the scaling of the blast parameters, except for the peak side-on overpressure (Δp_o), is not based on the Hopkinson's blast scaling law, but refers to the so-called **Sach's blast scaling law** instead.

The use of the Sach's blast scaling law would make all blast parameters to be scaled fully non-dimensionally. For this purpose, other important parameters for characterizing the explosion blast, such as the volumetric explosion energy of the flammable gas or vapor cloud, denoted by E_c; the ambient pressure, denoted by p_a; as well as the speed of sound at the ambient condition, denoted by a_0 must be taken into account. Since the energy of explosion is also taken into consideration, the Sach's scaled parameters are also known as the combustion energy-scaled parameters in some literatures.

The expressions of the Sach's scaling law for the blast parameters involved in the TNO Multi-Energy blast curves are as follows:

- **Sach's scaled distance** or the combustion energy-scaled distance, denoted by $\overline{R}$

$$\overline{R} = R\sqrt[3]{\frac{p_a}{E_c}} \tag{3.19}$$

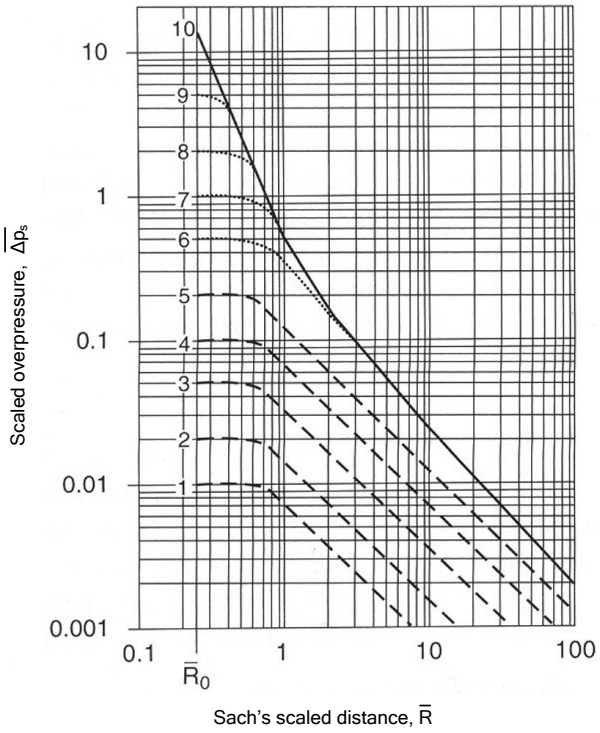

Figure 3.4. *The Multi-Energy blast curve for the scaled peak side-on overpressure as a function of the Sach's scaled distance [87]*

- **Sach's scaled positive phase duration**, denoted by $\overline{\tau}_d$

$$\overline{\tau}_d = t_d \times a_0 \sqrt[3]{\frac{p_a}{E_c}} \tag{3.20}$$

where R is the stand-off distance of the object of interest to the blast origin in m. Variables E_c, p_a and a_0 are given in J, Pa and m/s respectively. Therefore, both $\overline{R}$ and $\overline{\tau}_d$ are unitless parameters.

Meanwhile, the scaled peak side-on overpressure is presented in a similar manner to Eq. (3.12). In order to distinguish it from the Hopkinson's scaled overpressure, the scaled peak overpressure for the TNO Multi-Energy blast curve is denoted by $\Delta\overline{p_s}$ and defined by the following equation:

$$\Delta\overline{p_s} = \frac{\Delta p_o}{p_a} \tag{3.21}$$

The family of the TNO Multi-Energy blast curves consists of 10 different curves parameterized by the initial strength of the blast source. This initial strength (1-10) must be selected according to the circumstances. The higher the number, the stronger the blast source. A strong blast which corresponds to a shock wave is represented by solid lines level number 10. While, low-strength blast waves are indicated by dashed lines that may steepen into strong wave curve in the far field.

In addition to the selection of the blast strength, the volumetric explosion energy of the vapor cloud (E_c) must also be determined, as written in Eq. (3.19) before the prediction of the blast

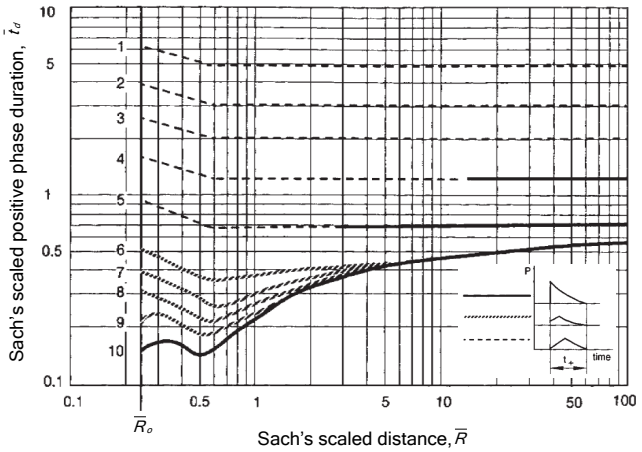

Figure 3.5. *The Multi-Energy blast curve for the scaled positive phase duration as a function of the Sach's scaled distance [16]*

parameter of interest is performed. In the following, the key procedure for the determination of these important two variables, i.e. the size of the blast source in terms of the volume of the vapor cloud in the obstructed region to determine the volumetric explosion energy of vapor cloud; and the initial strength of the blast source, is presented.

3.2.3.1 Determination of the size of the blast source

The procedure for the determination of the size of the blast source is generally done in the following two main steps:

1. The total volume of the flammable gas or vapor cloud is estimated initially by considering the quantity of flammable material (the flammable mass) in the vapor cloud assuming that no obstruction or congestion is present in the vicinity. This variable is denoted by V_c. It is assumed that the vapor cloud is filled with the fuel-air charge mixture homogeneously at its stoichiometric concentration. Thus, the total volume of the flammable gas or vapor cloud is determined by the following equation:

$$V_c = \frac{W_{e,\mathrm{f}}}{\rho_f \times c_s} \tag{3.22}$$

where $W_{e,\mathrm{f}}$ is the flammable mass of the vapor cloud in kg, ρ_f is the vapor density of the flammable fuel in the gas or vapor cloud in kg/m^3 and c_s is the stoichiometric concentration of the flammable fuel in the gas or vapor cloud in % volume. The total volume of the cloud V_c is given in m^3. Typical stoichiometric concentration of some common hydrocarbon fuel-air mixture at atmospheric condition can be found in Table 3.4. Actually, if the dispersion analysis is performed, the total volume of the vapor cloud can be estimated by taking into account only the cloud within the explosion limits and the flammable mass is also limited into these limits. In case of pool evaporation one could multiply the evaporation rate by a

Table 3.4. *Stoichiometric concentrations and volumetric heat of combustions for common hydrocarbons and hydrogen assuming that the fuels are homogeneously and stoichiometrically mixed with air at atmospheric conditions [21]*

Gas or vapor	Stoichiometric concentration, c_s vol.%	Volumetric heat of combustion, $\Delta H_{c,\text{vol}}$ MJ/m^3
Methane	9.5	3.23
Ethane	5.6	3.39
Propane	4.0	3.46
Ethene	6.5	3.64
Butane	3.1	3.48
Propene	4.4	3.59
Cyclohexane	2.3	3.85
Hydrogen	29.5	3.01

certain time period to come up with a mass quantity. However, as mentioned before, for the worst case scenario and safe approach it could be assumed that the flammable mass is the whole released mass from the inventory and the total volume is estimated from this mass.

2. Once the total volume of the flammable gas or vapor cloud has been estimated, the free volume in the obstructed region, denoted by V_r, is to be determined. In order to obtain this free volume, the total volume of the available obstacles in the obstructed region is deducted from the total volume of the obstructed region itself. If the total volume of the obstructed region is V_{or} and the total volume of the obstacles is V_{ob}, thus $V_r = V_{or} - V_{ob}$. Furthermore, the total volume of the flammable gas or vapor cloud is to be compared with the free volume in the obstructed region. If the volume of the flammable gas or vapor cloud (V_c) is larger than the free volume of the obstructed region (V_r), a high initial blast strength would be assigned to the portion of the flammable gas or vapor cloud with the size equal to the free volume of the obstructed region, while a low initial blast strength would be assigned to the remaining cloud. On the contrary, if V_c is smaller than V_r, the whole portion of the flammable gas or vapor cloud would be assigned with a certain high initial blast strength and the remaining free space of the obstructed region would not be taken into account.

In order to determine whether a particular obstacle belongs to an obstructed region or not, two empirical conditions were proposed as indicated in [85, 21]. These two conditions which must be satisfied by an obstacle to be included into an obstructed region are:

1. The distance of the outer boundary of the obstructed region and the outer boundary of the new obstacle is smaller than 25 meters.
2. The distance from the center of a new obstacle to the center of the previous considered obstacle is smaller than 10 times of d_1 or 1.5 times of d_2. Both d_1 and d_2 are defined as follows:

    - d_1 is the smallest dimension oriented in a plane perpendicular to the direction of the flame propagation.

- d_2 is the dimension of the obstacle parallel to the direction of the flame propagation.

Since typical structures in a potentially hazardous area like an industrial site may be considered as being composed of basic geometrical shapes, such cylinder with length l_c and diameter d_c; boxes with dimensions b_1, b_2 and b_3; or sphere with diameter d_s, the variable d_1 could be l_c or d_c if the new obstacle is a cylinder; or the smallest between b_1, b_2 or b_3 if it is a box; or d_s if it is a sphere. An obstructed region itself would be defined as a box that contains all satisfied obstacles in the region. The volume of the obstructed region to be considered is its free volume, denoted by V_r, which is defined as the volume of the box after excluding the space occupied by the obstacles. If necessary, multiple boxes could also be introduced according to the circumstances.

Once an appropriate volume of the flammable gas or vapor cloud has been determined, it is then assumed that the flammable gas or vapor cloud is in its stochiometrically hemispherical volume. Thus, the initial radius of this hemispherical flammable gas or vapor cloud, denoted by R_0, is given by the following equation:

$$R_0 = \sqrt[3]{\frac{3V_c}{2\pi}} \tag{3.23}$$

From here, the volumetric explosion energy of the blast source (E_c) can be calculated by multiplying the volume of hemispherical gas or vapor cloud (V_c) with the volumetric heat of combustion of the fuel ($\Delta H_{c,\mathsf{vol}}$, see Table 3.4). Thus,

$$E_c = V_c \times \Delta H_{c,\mathsf{vol}} \tag{3.24}$$

In fact, the volumetric heat of combustion of the fuel which is stoichiometrically mixed with air is calculated from the specific heat of combustion of the fuel (ΔH_c), the density of the fuel (ρ_f) and the stoichiometric concentration of the fuel in air (c_s) as given by the following equation:

$$\Delta H_{c,\mathsf{vol}} = \Delta H_c \times \rho_f \times c_s \tag{3.25}$$

where ΔH_c is given in J/kg, ρ_f in kg/m^3, c_s in % volume and $\Delta H_{c,\mathsf{vol}}$ in J/m^3.

3.2.3.2 Determination of the initial strength of the blast source

The safe and most conservative estimate for the initial strength of the blast source which corresponds to the flammable gas or vapor cloud in the obstructed region leading to the possible generation of a shock wave can be made by assuming the maximum strength of 10. According to Figs. 3.4 and 3.5, for the peak side-on overpressure below about 0.5 bar, no significant difference is shown for source strengths ranging from 7 to 10 [22]. The curves for blast source strengths of 7 to 9 may steepen into a blast strength 10 at the Sach's scaled distance of approximately 1, while for blast strength 6 at the Sach's scaled distance of approximately 2. The blast resulting from the unobstructed parts of the flammable gas or vapor cloud can be modeled by assuming a low

initial strength. For example, for extended and quiescent parts, the minimum strength of 1 may be assumed, and for more non-quiescent parts, which are in low intensity turbulent motion, for instance due to the momentum of a fuel release, a blast strength of 3 can be assigned.

In fact, there is a qualitative procedure for the determination of the initial blast strength of the vapor cloud. As mentioned earlier in this section, there are several factors which must be taken into account for the generation of the explosion overpressures. This particular procedure attempts to develop a relationship between these parameters qualitatively. Therefore, each factor is to be divided into several categories covering typical situations for the vapor cloud explosion. In this case, there are three factors to be taken into account, namely the flame expansion type represented the degree of confinement; the reactivity of the fuel represented the type of the fuel in the material; and the obstacle density represented the configuration of the obstacles in the obstructed region. The categorization of these factors are mentioned as follows:

(i) **Dimension of the flame expansion**, which can be in 1-D, 2-D and 3-D expansion.
The degree of confinement of the flammable gas or vapor cloud determines the number of dimension in which the flame may expand. This is not the dimension of the vapor cloud or the region engulfed by the vapor cloud [16].

- 3-D expansion means that there is a free flame expansion in an unconfined volume. The flame is free to expand spherically or hemispherically from a point ignition. The overall flame surface increases with the square of the distance from the point of the ignition source. According to the circumstances, the flame acceleration and the level overpressure are relatively the lowest one.
- 2-D expansion means that there is a cylindrical flame between two plates, the overall flame surface area is proportional to the distance from the ignition point. Consequently, deformation of the flame surface will have a stronger effect and generates higher overpressures.
- 1-D expansion is used for examples for planar flames propagating in pipes. In this case, the projected flame surface area is constant. This configuration is however rarely encountered in actual plants. According to [87], in many realistic situations the expansion of the flame during vapor cloud explosion is typically in 2D or 3D only.

The classification of the effect of the confinement to the flame expansion is further shown in Table. 3.5

(ii) **The reactivity of the fuel in the flammable gas or vapor cloud**
The fuel reactivity is a term used to describe the propensity of a flame to accelerate in a vapor cloud explosion for a given fuel. The reactivity of the materials is divided into three categories, namely **low**, **medium**, and **high reactivity**. It is generally accepted that materials having a laminar or fundamental burning velocity greater than 0.75 m/s are considered high reactive

Table 3.5. *Effect of confinement to the flame expansion [16]*

Flame expansion	Description	Geometry
3-D	Unconfined volume, almost completely free expansion	
2-D	Platform carrying process equipment; space beneath cars; open-sided multistory buildings	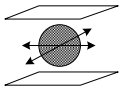
1-D	Tunnel, corridors, or sewage systems	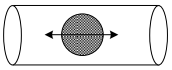

materials, while those having a laminar burning velocity below 0.4 m/s are considered low reactive materials. Other materials which do not meet this criterion are considered medium reactive materials.

In accordance with the TNO recommendations [90], methane and carbon monoxide are the only materials regarded as low reactive materials. While, hydrogen, acetylene, ethylene, ethylene oxide, and propylene oxide are typical examples of highly reactive materials. The classification of a flammable fuel consisting of more than one fuel (mixture) should be based on the concentration of each fuel. Thus, the reactivity of the mixed fuel can be is considered to be the same to the reactivity of the fuel with a highest composition in a conservative approach.

(iii) **The obstacle density**

The level of obstruction is represented by the obstacles density in the obstructed area engulfed by the flammable gas or vapor cloud. The classification of the obstacle density is **low**, **medium** and **high** density. Basically, this classification is based on the area blockage ratio and pitch. The area blockage ratio is defined as the ratio of the area blocked by obstacles to the total cross-section area. The pitch is defined as the distance between successive obstacles or obstacle rows. Low obstacle density was defined as having an area blockage ratio of less than 10%, while high obstacle density provides an area blockage ratio of 40% or greater, and everything else is considered medium [91]. This classification is further illustrated in Table 3.6.

The combination of each category is realized in a matrix shown in Table 3.7. This is the matrix to be used for the selection of the initial blast strength of the vapor cloud explosion qualitatively. It is important to mention that the intervention of the user for the selection of these strengths is still required similar to the selection of the explosion efficiency in the TNT equivalent model.

Recently, an attempt to develop a quantitative procedure for the selection of the initial strength

Table 3.6. *Classification of the obstacle density [16]*

Type	Obstacle Area Blockage Ratio per Plane	Pitch for Obstacle Layers	Geometry
Low	Less than 10%	One or two layers of obstacles	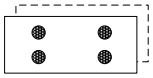
Medium	Between 10% and 40%	Two or three layers of obstacles	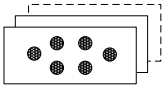
High	Greater than 40%	Three or more fairly closely spaced obstacles layers	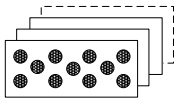

Table 3.7. *Matrix for the qualitative of the initial blast strength of the flammable gas or vapor cloud for the use of the TNO Multi-Energy blast curve [92]*

		Obstacle density		
Dimension	Reactivity	High	Medium	Low
1-D Expansion	High	10	10	10
	Medium	9-10	9	7-8
	Low	9-10	7-8	4-5
2-D Expansion	High	9	7-8	6
	Medium	7-8	6-7	2-3
	Low	6	5-6	1-2
3-D Expansion	High	6	3	1
	Medium	3-4	2	1
	Low	3	2	1

of the blast source, especially for a realistic situation has been made [87, 80]. This new guideline aims to develop a set of correlations for the determination of the maximum explosion overpressures of the vapor cloud which is denoted by $\Delta p_{o,\max}$ in Fig. 3.3. With respect to the TNO Multi-Energy blast curve, $\Delta p_{o,\max}$ is the overpressure for any scaled distance equal or smaller than $\overline{R}_0$ (see Fig. 3.4 and 3.5). Therefore, once $\Delta p_{o,\max}$ has been determined, it is then possible to determine which the blast strength level has to follow while using the TNO blast curve family. It is important to mention that $\Delta p_{o,\max}$ is considered to be constant during the explosion or until the combustion of the vapor cloud is complete.

As mentioned above, $\Delta p_{o,\max}$ depends on several parameters which could still be broken down into several categories. In addition to the three parameters above, the strength and location of the ignition source and the size of the obstacles are also taken into account. However, some of them were treated quantitatively. The obstacle density and fuel type in the vapor cloud, which were previously treated qualitatively, are now treated quantitatively by introducing new variables.

The volume blockage ratio (VBR) was used instead of the area blockage ratio (ABR). The degree of confinement remains treated qualitatively as well as the strength of the ignition source. The remaining factors are to be treated quantitatively. Table 3.8 shows the treatment of the parameters for the determination of the correlation for the maximum explosion overpressure in the vapor cloud.

Table 3.8. *Parameters for the determination of the correlation for the maximum explosion overpressure of the vapor cloud [87]*

Approach	**Parameter**		
Qualitative	Strength of ignition source	a. Low energy b. High energy	
	Degree of confinement (Dimension of flame expansion)	a. 3-D flame expansion b. 2-D flame expansion c. 1-D flame expansion	
Quantitative	Obstacle density (Level of congestion)	Volume blockage ratio Notation: VBR	-
	Fuel type in the cloud (fuel reactivity)	Laminar burning velocity Notation: S_L	m/s
	Location of the ignition in the vapor cloud	Length of the flame path Notation: L_p	m
	Obstacle size (scale of experiment)	Typical average diameter Notation: D	m

According to [80], the determination of the correlation for the maximum explosion overpressure was based on the dataset from MERGE (Modeling and Experiment Research into Gas Explosions) experiments. The data available for low energy ignition (spark) in explosion experiment with obstacles without confinement (3-D) and between parallel planes (2-D) were used for the evaluation. It was found that the four quantitative variables in Table 3.8 are related to the maximum explosion overpressure ($\Delta p_{o,\max}$) for 2-D and 3-D flame expansion according to the following equation:

$$\Delta p_{o,\max} = a \cdot \left[\frac{\mathsf{VBR} \cdot L_p}{D}\right]^b \cdot S_L^c \cdot D^d \tag{3.26}$$

where $\Delta p_{o,\max}$ is given in bar. It is important to mention that D is the typical average obstacle diameter for the whole obstructed region. This parameter is also proportional to the scale of the experiment; L_p accounts for the location of ignition or the maximum distance covered by the flame. Constants a, b, c and d for these correlations can be found further in Table 3.9.

Table 3.9. *Constants for Eq. (3.26)*

Conditions	a	b	c	d
No confinement (open, 3-D)	0.84	2.75	2.7	0.7
Confinement between parallel plates (2-D)	3.38	2.25	2.7	0.7

3.2.3.3 Fitted equations of the TNO Multi-Energy blast curve family

In the following the equations that fit the TNO Multi-Energy blast curve family for the overpressure as given in [21] are presented. These equations could predict the blast overpressure at any distance from the initial blast source especially for the computer application. For each level of the initial blast strength in the TNO Multi-Energy blast curve family, the fitted equation is generally given by the following expression:

$$y = a \cdot x^b + 10^{-b \cdot \log x - c} \tag{3.27}$$

where y is the vertical axis of the blast curve representing the scaled overpressure $\Delta\overline{p}_s$ and x is the horizontal axis of the curve representing the energy (Sach's) scaled distance ($\overline{R}$). These equations are combined from the fitted equations given in [93] and the proposed equations given in [94].

The coefficients required for Eq. (3.27) for different blast strength level and different ranges of x are given in Appendix B. The range of x-axis starts from about 0.23 corresponding to $\overline{R}$. The value of $\Delta\overline{p}_s$ for any $\overline{R} < 0.233$ is to be determined by Eq. (3.26). The maximum range of x is 100 as indicated in the original curve. It is, therefore, not recommended to use these equations for the scaled distance ($\overline{R}$) greater than 100. Fig. 3.6 shows the TNO Multi-Energy blast curve family generated with these equations.

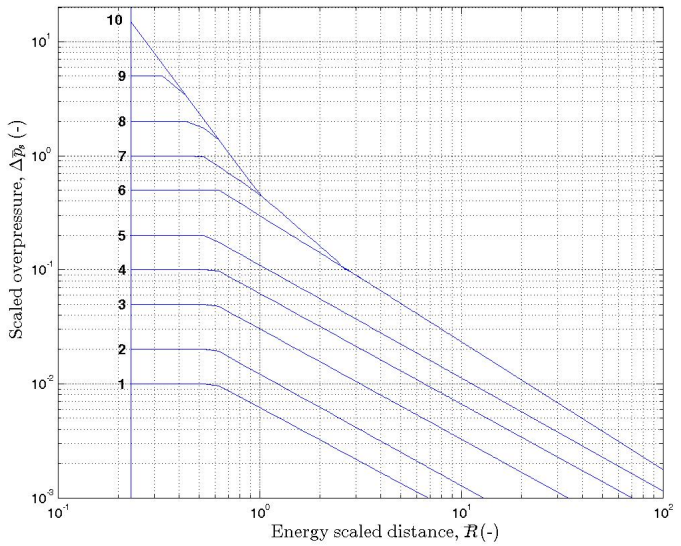

Figure 3.6. *The TNO Multi-Energy blast curve family for the scaled overpressure generated with Eq. (3.27)*

3.3 The Baker-Strehlow-Tang model

3.3.1 The basic concept of the Baker-Strehlow-Tang

The Baker-Strehlow-Tang model is another empirical model which also uses the blast curve for the estimation of the properties of explosion blast waves. This model is actually an extended blast model developed from the Strehlow approach which selects blast curves based on flame speed [91]. The original work of Strehlow et.al [95] had experienced several considerable improvement as mentioned in [69, 88]. Basically, the Baker-Strehlow-Tang model has similarities to the TNO Multi-Energy model as both of them are based on the premise that a vapor cloud explosion can occur only within that portion of a flammable gas or vapor cloud that is congested or partially confined. This means that both models recognize the effect of the obstacles and confinement to the flame expansion flow field resulting in higher intensities of a vapor cloud explosion.

Unlike the TNO Multi-Energy blast curve, the Baker-Strehlow-Tang blast curve family is parameterized by the flame speed in terms of its Mach number. The blast curve family for the peak overpressure, positive impulse and the arrival time are shown in Figs. 3.8 - 3.10. These curves were derived from detailed numerical simulations of idealized free-air (spherical) explosion scenario with a fuel-air charge at stoichiometric concentration filling the sphere as shown in Fig. 3.7. The

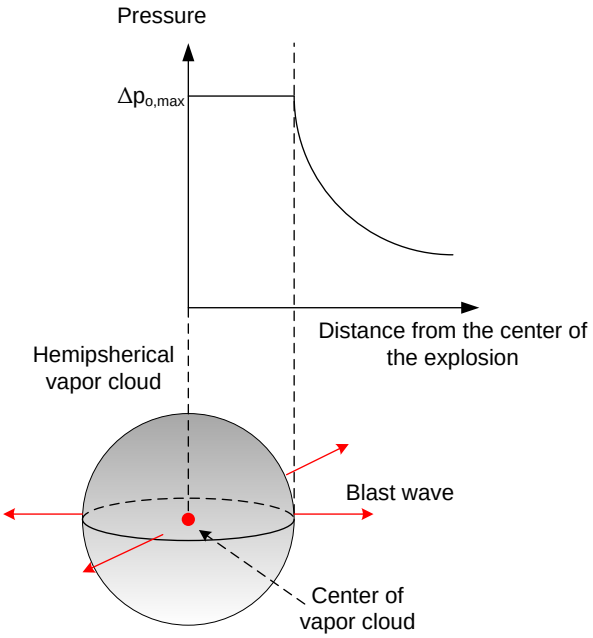

Figure 3.7. *The idealized spherical vapor cloud as the basis for the Baker-Strehlow-Tang model [89]*

procedure for the determination of the cloud sizes including the treatment of the obstructed regions in order to obtain the volumetric explosion energy of the vapor cloud is, however, still similar to the TNO Multi-Energy model. The blast parameters are also presented in their scaled forms and the Sach's scaling law is also still in use. Sach's scaled parameters for the positive impulse and the time arrival are are non-dimensionalized variables and given by the following equation:

- **Sach's scaled positive impulse**:

$$\overline{i_s} = i_p \times \frac{a_0}{p_a} \times \sqrt[3]{\frac{p_a}{E_c}} \tag{3.28}$$

- **Sach's scaled arrival time**:

$$\overline{\tau}_a = t_a \times a_0 \sqrt[3]{\frac{p_a}{E_c}} \tag{3.29}$$

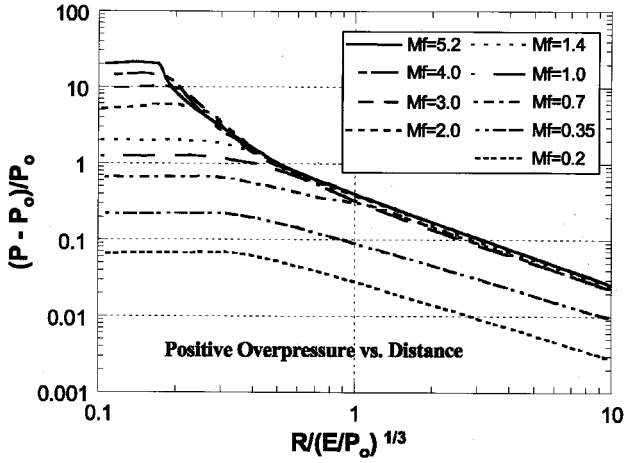

Figure 3.8. *Scaled peak side-on overpressure as a function of the Sach's scaled distance for different flame speeds in terms of its Eulerian Mach number (M_f) [69]*

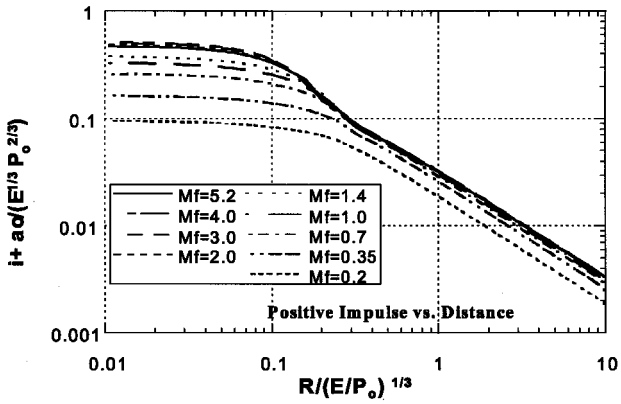

Figure 3.9. *Sach's scaled positive impulse as a function of the Sach's scaled distance for different flame speeds in terms of its Eulerian Mach number (M_f) [69]*

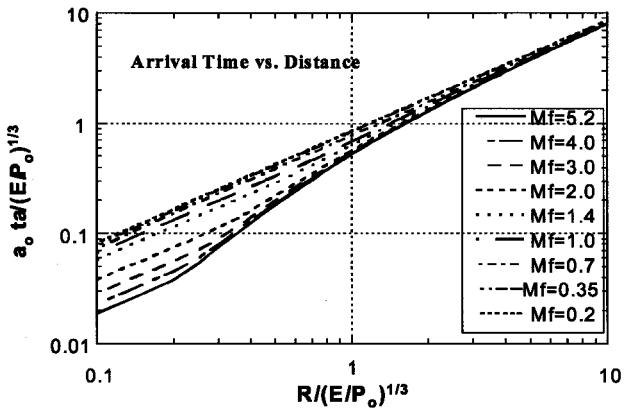

Figure 3.10. *Sach's scaled arrival time as a function of the Sach's scaled distance for different flame speeds in terms of its Eulerian Mach number (M_f) [69]*

3.3.2 The important procedures

3.3.2.1 Determination of the flame Mach number

Similar to the TNO Multi-Energy model, there is a qualitative method for the determination of the flame speed which is realized in a matrix combining three different factors that influence the generation of the maximum explosion overpressure of the vapor cloud. As mentioned in [96], the combination of the flame expansion geometry, the obstacles density and the reactivity of the fuel determines also the flame propagation speed of the deflagration of the flammable vapor cloud. The categorization of the parameters are similar to the TNO Multi-Energy model. The matrix for the selection of the flame speed is shown in Table 3.10. In this case, the flame speeds are given in terms of their Lagrangian Mach number (M_w), which is the velocity of heat addition in the numerical calculation in a Lagrangian coordinate system (moving system).

Table 3.10. *Matrix for the qualitative selection of the flame speed in terms of the Lagrangian Mach number (M_w) for the use of the Baker-Strehlow-Tang blast curve family [16, 88]*

		Obstacle Density		
Dimension	Reactivity	High	Medium	Low
2-D Expansion	High	DDT	DDT	0.59
	Medium	1.6	0.66	0.47
	Low	0.66	0.47	0.079
2.5-D Expansion	High	DDT	DDT	0.47
	Medium	1.0	0.55	0.29
	Low	0.50	0.35	0.053
3-D Expansion	High	DDT	DDT	0.36
	Medium	0.50	0.44	0.11
	Low	0.34	0.23	0.026

Note: $M_w = 5.2$ is assumed for DDT

In Table 3.10, a new flame expansion dimension labeled by 2.5-D is included. This new di-

mension is associated with the situation in the confinement which is not totally 3-D or 2-D. For instance, the confinement is made up of either a frangile panel or by a nearly solid confining plane. Typical example for this dimension is the pipe rack where the pipe are almost touching. The Mach numbers for the 2.5-D expansion are simply obtained by taking an arithmetic average between the corresponding 2-D and 3-D expansion Mach number for the same obstacles and fuel reactivity [88].

The 1-D expansion type is not to be used any longer in the new Baker-Strehlow-Tang model because the maximum flame speed achieved in true 1-D expansion conditions (i.e., a pipe) is a function of the length-to-diameter ratio of the pipe in addition to pipe geometry, fuel reactivity, and congestion level. Many fuels are able to undergo a DDT in a 1-D expansion geometry if the combination of length-to-diameter ratio and obstacle density are sufficiently high [88].

Recently, the Baker-Strehlow-Tang blast curve family have been updated was reported in [69]. The new blast curve is parameterized by the Eulerian Mach number, denoted by M_f, instead of the Lagrangian Mach number (M_w). The Eulerian Mach number (M_f) represents the flame speed measured in the experiments relative to a fixed observer (Eulerian coordinate system). The relationship between the Lagrangian and Eulerian Mach number is generally given by the following equation:

$$M_f = \sqrt[3]{\frac{\rho_u}{\rho_b}} \times M_w \tag{3.30}$$

where ρ_u and ρ_b are the density of the gas ahead (unburnt) and behind (burnt) of the flame. This relation is invalid if the M_f value approaches unity.

Furthermore, for supersonic flames, $M_f = M_w$. Meanwhile, for the near sonic flames, the relationship between M_w and M_f was established by using the approximate equation for the apparent flame Mach number and the overpressure at the flame front. Assuming an expansion ratio of 7 for stoichiometric mixtures of commonly used hydrocarbon-air mixtures and a specific heat ratio of 1.40 (ambient air), the equation for the determination of the Eulerian Mach number (M_f) is derived from the acoustic theory as given by the following equation:

$$\frac{p_{o,\max} - p_a}{p_a} = \frac{\Delta p_{o,\max}}{p_a} = 2.4 \times \frac{M_f^2}{1 + M_f} \tag{3.31}$$

where $p_{o,\max}$ is the absolute maximum explosion pressure of the vapor cloud at the flame front, while $\Delta p_{o,\max}$ is the maximum explosion overpressure at the same position. p_a is the ambient pressure for which the atmospheric pressure is typically assumed. Therefore, in order to convert M_w to M_f in this case, the maximum explosion overpressure for a range of values of M_w is first determined and M_f is then calculated from Eq. (3.31). Table 3.11 presents the relationship between the Lagrangian Mach number, the Eulerian Mach number and the maximum explosion overpressure.

An attempt to develop a quantitative method for the estimation of flame speed in terms of the Eulerian Mach number has been proposed in [64]. This method is actually related with the set of correlations for the determination of the maximum explosion overpressure of the vapor cloud

Table 3.11. *The relationship between the Lagrangian Mach number, the Eulerian Mach number and the maximum explosion overpressure [69]*

Lagrangian Mach number M_w	Eulerian Mach number M_f	Maximum overpressure $P_{\max}$ (bar)
0.035	0.07	0.010
0.074	0.12	0.028
0.125	0.19	0.070
0.250	0.35	0.218
0.500	0.70	0.680
0.750	1.00	1.240
1.000	1.40	2.000
2.000	2.00	5.000

developed for the selection of the initial blast strength of the TNO Multi-Energy model (see Eq. (3.26)). Combining this equation to Eq. (3.31), the Eulerian Mach number ($M_f > 0$) can now be estimated by solving the following equation:

$$\frac{M_f^2}{1+M_f} = \frac{a}{2.4 \cdot p_a} \times \frac{\mathsf{VBR} \cdot {L_p}^b}{D} \cdot S_L^c \cdot D^d \tag{3.32}$$

where VBR, L_p, S_L and D are the same variables as defined previously in Eq. (3.26). Table 3.9 is also applicable for selecting appropriate constants a, b, c and d for two typical problems of vapor cloud explosions in the process industries.

3.3.2.2 Fitted equations for the Baker-Strehlow-Tang blast curve family

In the following the equations that fit the Baker-Strehlow-Tang blast curve family for the determination of the blast overpressure are presented. In fact, these equations are actually useful for the computer application. For each level of the flame speed, the Baker-Strehlow-Tang blast curve can be approximated by the following expression:

$$y = a + y_1 + y_2 \tag{3.33}$$

where:

$$\log y_1 = b \cdot (\log x)^6 + c \cdot (\log x)^5 + d \cdot (\log x)^4 + e \cdot (\log x)^3 + f \cdot (\log x)^2 + g \cdot (\log x) + h$$

$$\log y_2 = p \cdot (\log x) + q$$

where y is the vertical axis of the blast curve representing the scaled overpressure $\Delta\overline{p}_s$ and x is the horizontal axis of the curve representing the energy (Sach's) scaled distance ($\overline{R}$). All required coefficients of Eq. (3.33) for different defined flame speeds and different ranges of x can further be found in Appendix B of this thesis. This main source of information for these correlation is actually extracted from the technical documentation of the DNV PHAST software package version

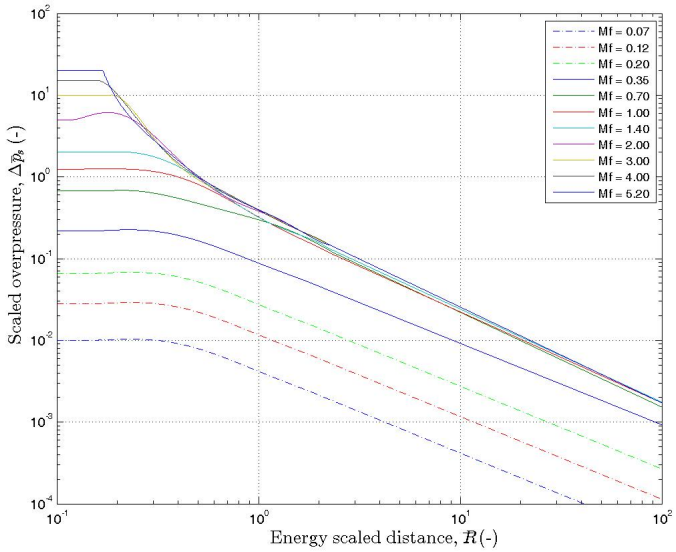

Figure 3.11. *The Baker-Strehlow-Tang blast curve family for the scaled overpressure generated with Eq. (3.33)*

6.7 [97]. Thus, Fig. 3.11 shows the Baker-Strehlow-Tang blast curve for the scaled overpressure if Eq. (3.33) is implemented.

Chapter 4

Modeling of the Propagation of the Blast Waves

4.1 Governing equations of the blast wave propagation

During explosion processes involving various explosive materials as well as the rapid combustion of the flammable vapor cloud, especially if occuring in the congested region, complex motions of the gas behind the shock wave would arise. This phenomenon has been introduced previously as the blast propagation phenomenon. In fact, blast wave propagations can be studied experimentally by means of models or theoretically by means of the investigation of mathematical problems using equations of gas dynamics. These equations deal with compressible inviscid flows. In this chapter the fundamental theoretical approach for studying this phenomenon is considered.

Generally, the flows of fluids are governed by the conservation laws of physics. These laws provide the structures of fluid mechanics and involve three fundamental physical quantities which are neither created nor destroyed, but are only redistributed or, excepting mass, converted from one form to another. The three quantities are [98]:

- the mass of fluid which is conserved
- the rate of change of momentum which equals the sum of the forces on a fluid particle and is described by Newton's second law, and
- the rate of change of energy which is equal to the sum of the rate of heat addition and to the rate of work done on a fluid particle. This particular quantity is described by the first law of thermodynamics.

The mathematical statement of the conservation laws is a set of time-dependent nonlinear partial differential equations which is called the **Navier-Stokes equations**. The equations were formulated independently by the French physicist C.L.M.H. Navier (1785- 1836) in 1822 and the British mathematician and physicist G.G. Stokes (1819-1903) in 1845 [99]. Basically, the Navier-Stokes equations could describe the full range of fluid dynamics including compressible or incompressible flows, viscous or non-viscous flows, laminar or turbulent flows and other related phenomena.

Gas dynamics theory itself deals with compressible flows, which means that the effects of body forces, viscous stresses and heat flux are neglected. Thus, the original Navier-Stokes equations are modified by dropping the fluid viscosity and heat flux terms and reduced to the so-called **Euler equations**. This modification leads to a hyperbolic non-linear equations system which admits discontinuous solutions, such as shock waves and contact discontinuities. The original Navier-Stokes equations themselves actually involve second-order derivatives making the equations parabolic and having smooth solutions for all times. The procedures for solving the Euler equations are treated in this chapter.

In order to solve the Euler equations, it is important first to understand that there are two sets of variables to be chosen to describe the fluid flow under consideration. These are either the **primitive variables** or the **conserved variables**. In general, for a multi-dimensional case of Euler equations in Cartesian coordinate system, there are four independent variables, namely three spatial coordinates (x, y, z directions) and one temporal (t). The primitive variables are actually five dependent variables which are the functions of all four independent variables. These variables are the **mass density**, denoted by $\rho(x, y, z, t)$); **pressure** $p(x, y, z, t)$ and three components of the **particle velocities** for each spatial directions. These velocities components are $u(x, y, z, t)$ for x-direction, $v(x, y, z, t)$ for y direction and $w(x, y, z, t)$ for z direction. They can further be represented only by a single vector $\mathbf{u} = [u, v, w]^T$.

Meanwhile, the conserved variables represent the **conserved mass**, **conserved momentum** and **conserved energy**. Each variable is respectively represented by ρ, $\rho\mathbf{u}$ and E. The variable E itself is actually the **total energy per unit volume** which may be broken down into the internal and kinetic energy per unit volume. In fact, as mentioned later, both primitive and conserved variables are related to each other by simple algebraic equations.

4.1.1 The general expression of the Euler equations system

Suppose that $\phi(x, y, z, t)$ is a scalar field function. The rate of change ϕ with time by an observer moving with the fluid velocity $\mathbf{u} = (u, v, w)$ can be expressed by

$$\frac{D\phi}{Dt} = \frac{\partial\phi}{\partial t} + \mathbf{u} \cdot \nabla\phi \tag{4.1}$$

This term is called the substantial derivative or material derivative. The first term on the right hand side denotes the partial derivative of ϕ with respect to time and represents the local rate of change of ϕ with time. Meanwhile, the second term represents the convective rate of change.

Furthermore, if the integration of ϕ over a control volume V enclosed by a piece-wise smooth boundary surface A that moves with the material under consideration is denoted with Ψ and expressed by the following equation

$$\Psi(t) = \iiint_V \phi(x, y, z, t)\ dV \tag{4.2}$$

Then, the substantial derivative of $\Psi(t)$ can be written as follows:

$$\frac{D\Psi}{Dt} = \iiint_V \frac{\partial \phi}{\partial t}\, dV + \iint_A (\mathbf{n} \cdot \phi \mathbf{u})\, dA \tag{4.3}$$

where $\mathbf{n} = (n_1, n_2, n_3)$ is the outward pointing unit vector normal to the surface A. If the variable ϕ in Eq. (4.3) respectively replaced with the conserved variables of the Euler equations, the integral form of the multi-dimensional time-dependent **Euler equations** for an arbitrary control volume V is generally written as follows:

$$\iiint_V \frac{\partial \rho}{\partial t}\, dV + \iint_A \mathbf{n} \cdot (\rho \mathbf{u})\, dA = 0 \tag{4.4}$$

$$\iiint_V \frac{\partial}{\partial t}(\rho \mathbf{u})\, dV + \iint_A \left[\mathbf{u}(\mathbf{n} \cdot \rho \mathbf{u}) + p\mathbf{n}\right]\, dA = 0 \tag{4.5}$$

$$\iiint_V \frac{\partial E}{\partial t}\, dV + \iint_A \mathbf{n} \cdot [E + p]\mathbf{u}\, dA = 0 \tag{4.6}$$

Furthermore, if V is a fixed control volume independent of time t, the first term on the right hand side of Eq. (4.3) can also be modified as follows:

$$\iiint_V \frac{\partial \phi}{\partial t}\, dV = \frac{d}{dt} \iiint_V \phi\, dV \tag{4.7}$$

Thus, modifying Eqs. (4.4)-(4.6) with Eq. (4.7) for each right hand side term, the multi-dimensional Euler equations can also be written as follows:

$$\frac{d}{dt} \iiint_V \rho\, dV + \iint_A \mathbf{n} \cdot (\rho \mathbf{u})\, dA = 0 \tag{4.8}$$

$$\frac{d}{dt} \iiint_V (\rho \mathbf{u})\, dV + \iint_A \left[\mathbf{u}(\mathbf{n} \cdot \rho \mathbf{u}) + p\mathbf{n}\right]\, dA = 0 \tag{4.9}$$

$$\frac{d}{dt} \iiint_V E\, dV + \iint_A \mathbf{n} \cdot [E + p]\mathbf{u}\, dA = 0 \tag{4.10}$$

where ρ is the mass density in $\mathrm{kg/m^3}$, $\mathbf{u}$ is the particle velocity in m/s, p is the pressure in Pa, and E is the total energy per unit volume in $\mathrm{J/m^3}$. As mentioned above, E is actually defined as the sum of the internal energy per unit volume, denoted by ρe and the kinetic energy per unit volume, expressed by $\frac{1}{2}\rho|\mathbf{u}|^2$. Thus,

$$E = \rho \left(e + \frac{1}{2}|\mathbf{u}|^2 \right) \tag{4.11}$$

where

$$\frac{1}{2}|\mathbf{u}|^2 = \frac{1}{2}|\mathbf{u}\cdot\mathbf{u}| \tag{4.12}$$

The variables e and $\frac{1}{2}|\mathbf{u}|^2$ are the specific internal and kinetic energy given in J/kg.

4.1.2 The Euler equations system in the differential form

The integral form of the Euler equations system as given in Eqs. (4.4)-(4.6) can be transformed into the differential forms. In this particular case, the surface integral in those equations should be transformed to a volumetric integral form by applying Gauss's theorem. This theorem states that for any differentiable vector field $\Phi = (\phi_1, \phi_2, \phi_3)$ and a volume V with smooth bounding surface A the following identity holds

$$\iint_A (\mathbf{n}\cdot\Phi)\ dA = \iiint_V \nabla\cdot\Phi\ dV \tag{4.13}$$

Therefore, when Gauss's theorem is applied to the second term of all Eqs. (4.4)-(4.6), the differential form of the multi-dimensional time-dependent Euler equations system will be obtained. This system of equations is now expressed as follows:

$$\frac{\partial\rho}{\partial t} + \nabla\cdot(\rho\mathbf{u}) = 0 \tag{4.14}$$

$$\frac{\partial}{\partial t}(\rho\mathbf{u}) + \nabla\cdot(\rho\mathbf{u}\otimes\mathbf{u} + p\mathsf{I}) = 0 \tag{4.15}$$

$$\frac{\partial E}{\partial t} + \nabla\cdot\ ([E+p]\mathbf{u}) = 0 \tag{4.16}$$

Here ∇ is the *nabla* operator representing the gradient column vector and $\mathbf{u}\otimes\mathbf{u}$ is the tensor product of particle velocity. I is the identity unit tensor which is defined as follows:

$$\mathsf{I} = \begin{pmatrix} 1 & 0 & 0 \\ 0 & 1 & 0 \\ 0 & 0 & 1 \end{pmatrix}$$

As mentioned before, the Euler equations are the reduced form of the Navier-Stokes equations which express the conservation laws of physics. Eq. (4.14) expresses **continuity** or **mass conservation** equation. The first term on the left-hand side of the equation describes the rate of the density change with time, while the second term describes the net flow of mass out of the element across its boundaries, also known as the convective term.

Eq. (4.15) is the **momentum conservation** equation. Basically, the conservation of momentum states that momentum changes are due to one of three factors, namely: redistribution, conversion of momentum to or from energy, and forces. In a multi-dimensional coordinates system, such as Cartesian coordinates, this equation comprises further three sub-equations because

the tensor product $\mathbf{u} \otimes \mathbf{u}$, where $\mathbf{u} = [u, v, w]^T$, is written in its complete form by the following equation:

$$\mathbf{u} \otimes \mathbf{u} = \begin{pmatrix} u^2 & uv & uw \\ uv & v^2 & vw \\ uw & vw & w^2 \end{pmatrix}$$

Meanwhile, Eq. (4.16) is the expression of the **energy conservation** equation, which represents the energy balance based on the first law of thermodynamics.

Furthermore, Eqs. (4.14) - (4.16) can be expressed more comfortably in an alternative compact divergence form as the following:

$$\frac{\partial \mathbf{Q}}{\partial t} + \nabla \cdot \mathsf{H} = 0 \tag{4.17}$$

where $\mathbf{Q}$ is called the column vector of the conserved variables, given by:

$$\mathbf{Q} = [\rho, \rho u, \rho v, \rho w, E]^T \tag{4.18}$$

and H is the tensor of fluxes of the conserved variables in the x, y and z directions, written as follows:

$$\mathsf{H} = \begin{bmatrix} \rho u & \rho u^2 + p & \rho uv & \rho uw & (E+p)u \\ \rho v & \rho uv & \rho v^2 + p & \rho vw & (E+p)v \\ \rho w & \rho uw & \rho vw & \rho w^2 + p & (E+p)w \end{bmatrix} \tag{4.19}$$

The tensor H can also be alternatively replaced by defining three column vectors of fluxes of the conserved variables (conserved fluxes). Each column vector is regarded as a function of the conserved variables vector $\mathbf{Q}$. For Cartesian coordinates, they are denoted by $\mathbf{F}(\mathbf{Q})$, $\mathbf{G}(\mathbf{Q})$ and $\mathbf{H}(\mathbf{Q})$ for x, y and z directions respectively. The expressions of the three column vector of the conserved fluxes are given as follows:

$$\mathbf{F}(\mathbf{Q}) = [\rho u, \rho u^2 + p, \rho uv, \rho uw, (E+p)u]^T \tag{4.20}$$

$$\mathbf{G}(\mathbf{Q}) = [\rho v, \rho uv, \rho v^2 + p, \rho vw, (E+p)v]^T \tag{4.21}$$

$$\mathbf{H}(\mathbf{Q}) = [\rho w, \rho uw, \rho vw, \rho w^2 + p, (E+p)w]^T \tag{4.22}$$

Therefore, the differential form of the multi-dimensional time-dependent Euler equations may also be written as follows:

$$\frac{\partial}{\partial t}\mathbf{Q} + \frac{\partial}{\partial x}\mathbf{F}(\mathbf{Q}) + \frac{\partial}{\partial y}\mathbf{G}(\mathbf{Q}) + \frac{\partial}{\partial z}\mathbf{H}(\mathbf{Q}) = 0 \tag{4.23}$$

In this case, no source term is present, i.e. $\mathbf{S}(\mathbf{Q}) = 0$. Thus, Eq. (4.17) is a homogeneous system of equations. If the source terms are taken into account, this equation is no longer a homogeneous

equations system. In fact, the source terms can be split into two parts: geometrical source terms which arise in the case of non-Cartesian coordinates, and physical source terms such as radiative heating and cooling, gravitation, etc. The inhomogeneous system of the multi-dimensional time-dependent Euler equations is then expressed generally in a compact form as follows:

$$\frac{\partial \mathbf{Q}}{\partial t} + \nabla \cdot \mathsf{H} = \mathbf{S}(\mathbf{Q}) \tag{4.24}$$

Usually, $\mathbf{S}(\mathbf{Q})$ is a prescribed algebraic function of the flow variables and usually does not involve derivatives of these variables, although at certain circumstances, there are some exceptions.

As mentioned before, depending on the interest of the analysis, the fluid flow under consideration can be described by means of their **conserved variables** or **primitive variables**. The primitive variables are represented by the column vector $\mathbf{W}$. For Cartesian coordinates, this vector is:

$$\mathbf{W} = [\rho, u, v, w, p]^T \tag{4.25}$$

Analytical solutions of the Euler equations are available only for some simple cases, such as the Sod's shock tube problem. In much more complex circumstances, numerical schemes for solving the equations need to be developed [100]. The numerical solutions of the Euler equations can be developed using several schemes of the finite volume method. In this thesis, the **Godunov scheme** which has first-order accuracy is applied. In order to implement the Godunov scheme, the initial value problem of the Euler equations, which is commonly known as the **Riemann problem** is required. As shown later in this thesis, the Godunov scheme implements the exact Riemann solver for solving numerical fluxes at cell interface boundaries.

4.1.3 Thermodynamic considerations

In all cases of the Euler equations, the number of unknown variables exceeds the number of equations by one. This means that the Euler equations only are insufficient to completely described the physical process involved [101]. A closure condition or an additional equation is required in order to guarantee a solution for all unknown variables. This condition is provided by an appropriate thermodynamic equation of state relating two or more basic quantities within the medium.

In the previous discussion, some basic quantities have been introduced. These include the mass density ρ, pressure p and specific internal energy e. In this section, the relation of these quantities with other basic quantities, such as temperature, denoted by T, and the specific entropy, denoted by s are shown.

4.1.3.1 Equation of state of ideal gases

The system of gas which is considered throughout this thesis is assumed to be in its local chemical and thermodynamic equilibrium. This gas can be completely described by two basic variables, namely *pressure* p and *specific volume* v. The latter variable is actually the reciprocal of the *mass*

density as $v = 1/\rho$. The state function of this gas can be described by a curve in the $p - v$ plane, each characterized by a variable temperature T. Therefore, such a system is also known as $p - v - T$ system [101, 102]. The best way to relate these basic variables is through the so-called **thermodynamic equation of state**, where $T = T(p, v) = T(p, \rho)$, or $p = p(T, v) = p(T, \rho)$. For **thermally ideal gases**, the corresponding thermal equation of state is expressed as follows:

$$p = \rho RT \tag{4.26}$$

where the pressure p is in Pa, and the temperature T in K. The constant R is called the specific gas constant given in J/kg/K which depends on the specific type of the gas under consideration. This equation of state can further be modified as the following:

$$p = \frac{n \cdot M_w}{V} RT, \tag{4.27}$$

since

$$\rho = \frac{m}{V} = \frac{n \cdot M_w}{V}$$

where m is the mass of the gas in kg, V the volume of the gas system in m^3, n the amount of gas in volume V in kilomoles (kmol), and M_w the molecular weight of the gas in kg/kmol.

The multiplication of the specific gas constant and molecular weight gives the universal gas constant, denoted by $\mathcal{R}$, thus

$$\mathcal{R} = R \cdot M_w \tag{4.28}$$

This variable, as introduced shortly in Chapter 2, has the value of 8.134 J/mol/K valid for any kind of gas. Using this equation, the equation of state as given in Eq. (4.27) is expressed generally as:

$$p \cdot V = n \cdot \mathcal{R} \cdot T \tag{4.29}$$

The specific internal energy (e) plays an important role in the **First Law of Thermodynamics**. In general, for a non-adiabatic system the change of specific internal energy (de) in a process is given by the following equation:

$$\begin{aligned} \Delta e &= \Delta Q - \Delta W \\ &= \Delta Q - p \cdot \Delta V \end{aligned} \tag{4.30}$$

where ΔQ is the heat transferred to the system and ΔW is the work done by the system. The sign may be change if the condition changes. Meanwhile, the relation of the specific internal energy (e) with the two previous basic variables, pressure p and specific volume v is also given by the so-called

specific enthalpy. This variable is denoted by h and defined by the following equation:

$$h = e + p \cdot v = e + \frac{p}{\rho} \tag{4.31}$$

With the addition of the specific kinetic energy $\frac{1}{2}|\mathbf{u}|^2$ into Eq. (4.31), the so-called **total enthalpy** is obtained. This variable is denoted by H and written as follows:

$$H = h + \frac{1}{2}|\mathbf{u}|^2 = e + \frac{p}{\rho} + \frac{1}{2}|\mathbf{u}|^2 = \frac{E + p}{\rho} \tag{4.32}$$

where both h and H are given in J/kg.

Furthermore, the system's **entropy** is involved in the **Second Law of Thermodynamics**. The entropy measures the disorder in the system, and indicates the degree to which the internal energy is available for doing useful work. The greater the entropy, the less available the energy. The **specific entropy**, s is defined by the following relation:

$$Tds = de + pdv \tag{4.33}$$

In order to fully describe the physical process involved in the phenomenon of blast wave propagation, several other variables are also considered important quantities. These include the **specific heat capacities**, denoted by c, the **speed of sound** in the gas a, **specific heat ratio**, denoted by γ and **Mach number** denoted by M.

The **specific heat capacity** is defined as the ratio between the heat added to the system dQ and the change of temperature dT, meaning that $c = dQ/dT$. Two specific heat capacities are distinguished; the **specific heat capacity at constant pressure**, denoted by c_p and the **specific heat capacity at constant volume**, denoted by c_v. Considering that a process is at a constant pressure, Eq. (4.30) may be written as:

$$dQ = de + pdv = de + d(pv) = d(e + pv) = dh \tag{4.34}$$

which means that the **specific heat capacity at constant pressure** c_p is defined as:

$$c_p = \left(\frac{\partial h}{\partial T}\right)_p \qquad \text{or} \qquad c_p = T\left(\frac{\partial s}{\partial T}\right)_p \tag{4.35}$$

Meanwhile, for a process at a constant volume, Eq. (4.30) becomes:

$$dQ = de + pdv = de \tag{4.36}$$

which means that the **specific heat capacity at constant volume** c_v is defined as:

$$c_v = \left(\frac{\partial e}{\partial T}\right)_v \qquad \text{or} \qquad c_v = T\left(\frac{\partial s}{\partial T}\right)_v \tag{4.37}$$

Furthermore, there exists a general expression to relate both specific heat capacities:

$$c_p = c_v + \frac{\alpha^2 T v}{\beta} \tag{4.38}$$

where α is the volume expansivity (expansion coefficient) in $^\circ\mathrm{C}^{-1}$ and β the isothermal compressibility in m^2/N. Both of them are respectively defined as follows:

$$\alpha = \frac{1}{v}\left(\frac{\partial v}{\partial T}\right)_p \qquad \text{and} \qquad \beta = -\frac{1}{v}\left(\frac{\partial v}{\partial p}\right)_T \tag{4.39}$$

In addition, the **ratio of these specific heat capacities**, denoted by γ, is defined as:

$$\gamma = \frac{c_p}{c_v} \tag{4.40}$$

which means that γ is dimensionless quantity, while both specific heat capacities c_p and c_v, in SI units, are given in J/kg/K.

Furthermore, there is another equation of state which relates the specific entropy s with the pressure p and mass density ρ. For thermally ideal gases, this equation of state is given by:

$$s = c_v \ln\left(\frac{p}{\rho^\gamma}\right) + C = c_v \ln p - c_p \ln \rho + C \tag{4.41}$$

In this case, the exact value of the additive constant C is usually unobtainable. Under normal circumstances, this constant is considered not important because we only deal with entropy differences.

Another important variable is the **speed of sound** in gas denoted by a. When the gas treated in this problem is assumed to be an ideal gas, this variable may be expressed as [103]

$$a^2 = \frac{\gamma\, p}{\rho} = \gamma R T \tag{4.42}$$

In SI units, the variable a is given in m/s. For certain purposes, the **Mach number**, denoted by M, is also necessary. This variable is defined as a ratio between the absolute value of the gas particle velocity $|\mathbf{u}|$ and the speed of sound in the gas a. Thus,

$$M = \frac{|\mathbf{u}|}{a} \tag{4.43}$$

which means that the Mach number M is a dimensionless quantity. Supersonic waves or flows have $M > 1$, which is true for detonations or shock waves. Subsonic waves or flows have $M < 1$, which is true for most deflagration flames.

4.1.3.2 Thermodynamic considerations for a polytropic gas

In this thesis, the modeling of the blast wave propagation in air assumes that air behaves as an ideal gas with a constant ratio of specific heat capacity ($\gamma = C$). In fact, for a thermally ideal gas, Eq. (4.26) is the equation of state which relates the temperature T to the pressure p and the mass density ρ. Thus, when the thermally ideal gas is assumed, it follows that the internal energy e is a function of temperature alone, which means that $e = e(T)$. In this case, the internal energy e can simply be proportional to the temperature T according to the following equation:

$$e = c_v \cdot T \tag{4.44}$$

and when the specific heat capacity at constant volume c_v is assumed to be a constant, one speaks of a **calorically ideal gas** or **polytropic gas**. For this kind of gas, the specific heat capacity at constant pressure c_p is also a constant, so that Eq. (4.35) yields,

$$h = c_p \cdot T \tag{4.45}$$

which means that the specific enthalpy h is also proportional to the temperature. Since both the specific heat capacities are constants, the specific heat capacity ratio γ according to Eq. 4.40) is also a constant and also known as the **polytropic index**. This is among the basic features of the polytropic gas.

Furthermore, the volume expansivity α and the isothermal compressibility β for the ideal gas according to Eq. (4.39) are respectively given by:

$$\alpha = \frac{1}{v}\left(\frac{\partial v}{\partial T}\right)_p = \frac{1}{T} \qquad \text{and} \qquad \beta = -\frac{1}{v}\left(\frac{\partial v}{\partial p}\right)_T = \frac{1}{p} \tag{4.46}$$

This means, according to Eq. (4.38), the relationship between both specific heat capacities and the gas constant can be established as given by the following equation:

$$c_p = c_v + R \tag{4.47}$$

By applying Eq. (4.40) to Eq. (4.47), both specific heat capacities can be expressed as follows:

$$c_p = \frac{\gamma R}{\gamma - 1} \qquad \text{and} \qquad c_v = \frac{R}{\gamma - 1} \tag{4.48}$$

The values of c_v, c_p and γ can be predicted by the law of equipartition of energy in the kinetic molecular theory of gases. According to this theory, both specific heat capacities c_v and c_p as well as the ratio γ can be calculated by the following equation:

$$c_v = \frac{\alpha_f}{2}R, \qquad c_p = \big(1 + \frac{\alpha_f}{2}\big)R \qquad \text{and} \qquad \gamma = \frac{\alpha_f + 2}{\alpha_f} \tag{4.49}$$

where α_f is the number of active degrees of freedom. For example, ideal monoatomic gases typically have three degrees of freedom ($\alpha_f = 3$) contributed only from the translational motion. By the equipartition principle the total energy of the molecule is equally distributed among the degrees of freedom. Thus, $c_v = \frac{3}{2}R$ while $c_p = \frac{5}{2}R$ and the specific heat ratio $\gamma = 1.67$.

For diatomic molecules, two rotational degrees of freedom are added, corresponding to the rotation about two perpendicular axes through the center of the molecule. Therefore, $\alpha_f = 5$, the specific heat capacities and its ratio are respectively given by $c_v = \frac{5}{2}R$, $c_p = \frac{7}{2}R$ and $\gamma = 1.40$. In general, polyatomic molecules have 3 translational, 3 rotational degrees of freedom and a certain number of vibrational modes. Typically, the specific heat ratio γ for these molecules are predicted around 1.33.

Finally, by applying both Eqs. (4.26) and (4.48) to Eq. (4.44), the specific internal energy e can now be expressed as

$$e = \frac{pv}{\gamma - 1} = \frac{p}{\rho(\gamma - 1)} \tag{4.50}$$

and the total energy per unit volume E according to Eq. (4.11) can be written as follows:

$$E = \frac{p}{\gamma - 1} + \frac{1}{2}\rho|\mathbf{u}|^2 \tag{4.51}$$

4.2 The Riemann Problem for the Euler equations

4.2.1 Introduction to the Riemann problem and the exact Riemann solver

The Riemann problem has played a central role both in the theoretical analysis of systems of hyperbolic conservation laws and in the development and implementation of practical numerical solutions for such systems. It is a fundamental tool for studying the interaction between waves. In the context of solving the Euler equations, the Riemann problem is the initial value problem (IVP) under a very particular initial condition which consists in a jump in the variables between two states, with a uniform distribution on the left of the discontinuity and another still uniform but possibly different distribution on the right, to infinity. In this thesis, as shown later, both distribution of both initial data states are assumed uniform distributions.

In general, the solution of the Riemann problem is computed by what is called the Riemann solver. In what follows, the procedure for developing an exact Riemann solver for the one-dimensional time-dependent Euler equations of gas dynamics assuming that the gas is ideal is presented. However, it is only the most important points to be mentioned here. The full detailed procedure which may include also other type of Riemann solvers can be found in some recommended references and publications, such as [101], [104], [105] and [106].

The Riemann problem for the one-dimensional time-dependent Euler equations of gas dynamics

is actually the following initial value problem:

$$\text{PDEs:} \qquad \frac{\partial}{\partial t}\mathbf{Q}(x,t) + \frac{\partial}{\partial x}\mathbf{F}\left(\mathbf{Q}(x,t)\right) = 0 \tag{4.52}$$

$$\text{ICs:} \qquad \mathbf{Q}(x,0) = \mathbf{Q}^0(x) = \begin{cases} \mathbf{Q}_\mathsf{L}, & \text{if } x < 0 \\ \mathbf{Q}_\mathsf{R}, & \text{if } x > 0 \end{cases} \tag{4.53}$$

where $\mathbf{Q}$ is the vector of the conserved variables and $\mathbf{F}\left(\mathbf{Q}\right)$ is the vector of the conserved fluxes. Therefore, expanding both vectors with all their components as mentioned in the previous section, the partial differential equations for the Riemann problem of the one-dimensional time-dependent Euler equations are completely written as follows:

$$\text{PDEs:} \qquad \frac{\partial}{\partial t}\underbrace{\begin{pmatrix} \rho \\ \rho u \\ E \end{pmatrix}}_{\mathbf{Q}(x,t)} + \frac{\partial}{\partial x}\underbrace{\begin{pmatrix} \rho u \\ \rho u^2 + p \\ (E+p)u \end{pmatrix}}_{\mathbf{F}(\mathbf{Q}(x,t))} = 0$$

According to this equation, the motion of the gas is assumed to have a non-zero velocity in the x-direction only. Therefore, the domain of interest in the $x-t$ plane is a set of points (x,t) where $-\infty < x < \infty$ and $t > 0$. As written in Eq. (4.53), the initial discontinuity of the Riemann problem is located at $x = 0$ separating two initial constant data states which are denoted by $\mathbf{Q}_\mathsf{L}$ and $\mathbf{Q}_\mathsf{R}$. Both subscripts L and R indicate the data states to the left and the right with respect to the position of the initial discontinuity ($x = 0$).

The solution of the Riemann problem with two initial constant data states $\mathbf{Q}_\mathsf{L}$ and $\mathbf{Q}_\mathsf{R}$ is generally written as $\mathbf{RP}(\mathbf{Q}_\mathsf{L}, \mathbf{Q}_\mathsf{R})$. It is a self-similar solution in sense that if $u(x,t)$ is a solution of this problem, then $u(\alpha x, \alpha t)$ is also the solution, whatever α. The concept of self-similar solution actually means that the solution only depends on x/t and is therefore constant on the half-lines which cross $(0,0)$ [107].

As introduced before, the Euler equations are to be solved numerically using the Godunov scheme. In order to develop the scheme, the Riemann problem is required. In this thesis, the Riemann problem is solved in terms of the physical primitive variables represented by the column vector $\mathbf{W}$ instead of the the vector of conserved variables represented by the column vector $\mathbf{Q}$. The initial conditions of the Riemann problem should also be expressed in terms of the column vector of the physical primitive variables. This expression is written as follows:

$$\text{ICs:} \qquad \mathbf{W}(x,0) = \mathbf{W}^0(x) = \begin{cases} \mathbf{W}_\mathsf{L} = [\rho_\mathsf{L}, u_\mathsf{L}, p_\mathsf{L}]^\mathsf{T}, & \text{if } x < 0 \\ \mathbf{W}_\mathsf{R} = [\rho_\mathsf{R}, u_\mathsf{R}, p_\mathsf{R}]^\mathsf{T}, & \text{if } x > 0 \end{cases} \tag{4.54}$$

Physically, the Riemann problem for the one-dimensional time-dependent Euler equations of gas dynamic is a slight generalization of the solution of the **shock tube problem** in the sense

that two gases under two different conditions fill in two regions of the tube separating by a thin diaphragm some where in the middle of the tube. Fig. 4.1 illustrates the shock tube problem with a length L. In this figure, the axial position of the initial discontinuity, i.e. the axial position of the thin diaphragm, is at $x = x_0$. The main interest is to determine the gas state in terms of either physical primitive or conserved variables for any point (x, t) where $t > 0$.

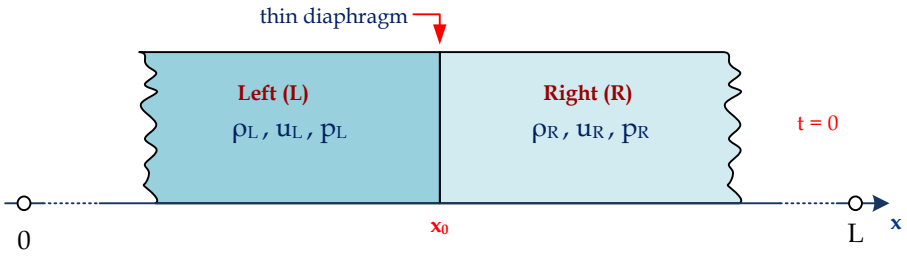

Figure 4.1. *Illustration of the initial configuration of the shock tube problem. The Riemann problem of the one-dimensional time-dependent Euler equations of gas dynamics is the generalization of this particular problem. A thin diaphragm in the middle of the tube acts as a boundary separating the two gases under two different conditions in terms of mass density, velocity and pressure.*

The main interest of this problem is to determine the state variables of the gas inside the tube once the thin diaphragm is removed. It is important to mention that the state variables of the gas are represented by the physical primitive variables. It has been understood that the removal or rupture of the thin diaphragm at $x = x_0$ at time $t = 0$ will initiate a process to naturally equalize the pressure. This generates a nearly centered wave system which typically consists of **two non-linear waves** and a **contact discontinuity**. Depending on the initial constant data states of the gas occupying the tube, i.e. $\mathbf{Q}_\mathsf{L}$ and $\mathbf{Q}_\mathsf{R}$ or $\mathbf{W}_\mathsf{L}$ and $\mathbf{W}_\mathsf{R}$, the two non-linear waves can be either the **shock wave (compression wave)**, the **rarefaction wave (expansion wave)**, or a combination of both of them.

In general, the contact discontinuity and shock wave are two types of singularities which can propagate through the gas. In the case of the contact discontinuity, the pressure p and particle velocity u remain continuous across this wave, but the mass density ρ as well as other quantities depending on it, e.g, the specific internal energy e, are discontinuous (jump) across this wave. In contrast, for the shock wave, all those quantities are discontinuous (jump) across the shock front. The jump in value across the shock front is governed by the **Rankine-Hugoniot conditions** relating the gas state ahead and behind the shock front. Meanwhile, in the case of the rarefaction (expansion) wave, smooth (continuous) solutions for all physical variables involved are expected across the wave because the expansion from a high-density to a low-density material does not take place instantaneously [101, 106].

4.2.2 Hyperbolic properties of the Euler equations of gas dynamics

The conservative formulation of the one-dimensional time-dependent Euler equations is expressed according to Eq. (4.52). This formulation can also be expressed in a slightly different form by

modifying the spatial partial derivative of the equation in the way written below:

$$\frac{\partial}{\partial t}\mathbf{Q}(x,t) + \mathbf{A}\frac{\partial}{\partial x}\mathbf{Q}(x,t) = 0 \tag{4.55}$$

Thus, a preposition factor $\mathbf{A}$ is introduced here. This factor represents the first derivative of the conserved fluxes with respect to the conserved variables. This means that:

$$\mathbf{A} = \frac{\partial \mathbf{F}(\mathbf{Q})}{\partial \mathbf{Q}} \tag{4.56}$$

By taking into account all physical variables defined in the previous discussion and assuming that the gas treated in this case is the ideal gas with a constant ratio of specific heats (γ = constant), $\mathbf{A}$ would form a 3×3 **Jacobian matrix** expressed as follows:

$$\mathbf{A} = \begin{pmatrix} 0 & 1 & 0 \\ 1/2(\gamma-3)u^2 & (3-\gamma)u & \gamma - 1 \\ 1/2(\gamma-1)u^3 - uH & H - (\gamma-1)u^2 & \gamma u \end{pmatrix} \tag{4.57}$$

As mentioned before, H is the total enthalpy according to Eq. (4.32). Furthermore, it can be shown that the matrix $\mathbf{A}$ is diagonalizable having three real eigenvalues:

$$\lambda_1 = u - a, \qquad \lambda_2 = u, \qquad \lambda_3 = u + a, \tag{4.58}$$

which correspond to the following three eigenvectors:

$$\mathbf{K}^{(1)} = \begin{pmatrix} 1 \\ u-a \\ H - au \end{pmatrix}, \quad \mathbf{K}^{(2)} = \begin{pmatrix} 1 \\ u \\ 1/2\ u^2 \end{pmatrix}, \quad \mathbf{K}^{(3)} = \begin{pmatrix} 1 \\ u+a \\ H + au \end{pmatrix} \tag{4.59}$$

Here a is the speed of sound in the gas formulated by Eq. (4.42). Since, the Jacobian matrix $\mathbf{A}$ is in fact not a constant and shown to be diagonalizable with three real eigenvalues, Eq. (4.52) is a hyperbolic equation system. For solving this equations, it is important to know that the solution waves which typically consists of two non-linear waves and a contact discontinuity are characterized by the three eigenvalues given above.

4.2.3 Basis structure of the Riemann waves

In order to understand the basic structure of the Riemann waves, the shock tube problem illustrated by Fig. 4.1 is here considered. The initial conditions is given in terms of primitive variables according to Eq. (4.54). If considered that $p_{\mathsf{L}} > p_{\mathsf{R}}$, the structure of the waves generated immediately after the removal of the thin diaphragm at time $t = 0$ can be illustrated by Fig. 4.2.

As shown in this figure, the generated wave structures in the tube separate the gas, from left to right, into five different states. The gas from the left of the diaphragm (at high pressure)

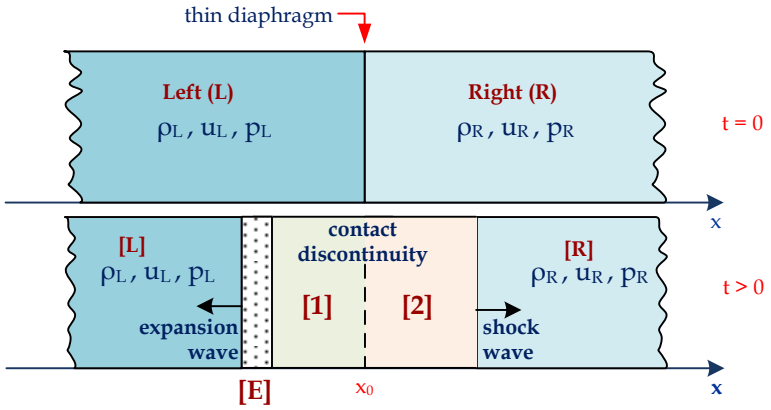

Figure 4.2. *The generated wave structure after the removal of the thin diaphragm at time $t = 0$ for the shock tube problem illustrated in Fig. 4.1 if the initial condition is governed by Eq. (4.54) in the sense that $p_L > p_R$.*

expands through a rarefaction wave and flows into the right region, pushing the gas of this part. The rarefaction is a continuous process and takes place inside a well-defined region (the expansion fan) that propagates to the left (region [E]) for which the width of the expansion fan grows in time. The compression of the low-pressure gas generates a shock wave propagating to the right. The expanded gas (region '[1]') is separated from the compressed gas (region '[2]') by a contact discontinuity, which can be regarded as a fictitious membrane traveling to the right at constant speed.

In fact, there are four possible configurations of the Riemann wave solutions depending on the initial condition of the Riemann problem. These configurations, as shown in $x-t$ plane in Fig. 4.3, represent the general solution of the Riemann problem. The rarefaction wave is usually represented by a pair of rays, while the shock wave is depicted by a single, solid line. The middle wave is always a contact surface discontinuity wave and indicated by a dash line.

For the particular shock tube problem as illustrated by Fig. 4.2, the structure of the Riemann waves in $x-t$ plane is similar to case (a) in Fig. 4.3. The Riemann problem is actually to determine the gas state in all generated regions after the removal of the thin diaphragm. As mentioned before, with respect to the Godunov scheme later, the state of the gas is characterized by the physical primitive variables, represented by the column vector of $\mathbf{W} = [\rho, u, p]^{\mathsf{T}}$. The complete structure of the Riemann wave solution for the shock tube problem in Fig. 4.2 is depicted in Fig. 4.4.

The left and right state in Fig. 4.4, represented by $\mathbf{W}_{\mathsf{L}}$ and $\mathbf{W}_{\mathsf{R}}$ respectively, are actually the given initial condition of the shock tube problem. For the general Riemann problem, this condition remain the same. Therefore, the other remaining states are now to be determined. In what follows, the procedure for determining these remaining unknown states is particularly presented.

The region in between two non-linear waves, as indicated by ('[1]') and ('[2]') in Fig. 4.2, is also known as the **star region**. Therefore, an additional subscript $(*)$ is added to any state variables of the gas falling into this region. In general, this region can be divided into two sub-regions which are always separated by a contact discontinuity wave. The sub-region to the left side of

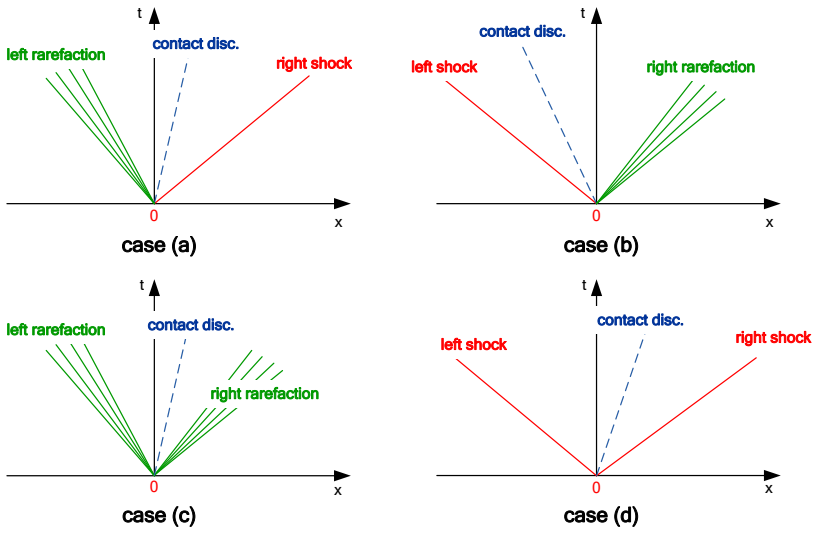

Figure 4.3. *Possible Riemann waves configurations as the solution of the Riemann problem for the one-dimensional problem. Case:*
(a) left rarefaction wave, contact discontinuity wave, right shock wave.
(b) left shock wave, contact discontinuity wave, right rarefaction wave.
(c) left rarefaction wave, contact discontinuity wave, right rarefaction wave.
(d) left shock wave, contact discontinuity wave, right shock wave.

the contact discontinuity is called the **star left region** specifically denoted by additional subscript ($*\mathsf{L}$), while the other sub-region to the right side is called the **star right region** specifically denoted by additional subscript ($*\mathsf{R}$). Meanwhile, the state variables of the gas in the expansion wave ('E') which are also not yet known are denoted by the additional subscript F (Expansion fan).

In order to determine the state variables of the gas in the star region, it is important to remember again that both pressure and particle velocity remain constant across the contact discontinuity wave which means that:

$$\begin{aligned} p_{*\mathsf{L}} &= p_{*\mathsf{R}} = p_* \\ u_{*\mathsf{L}} &= u_{*\mathsf{R}} = u_* \end{aligned} \tag{4.60}$$

However, mass densities of the gas across of this contact wave are jump discontinuously. This means that,

$$\rho_{*\mathsf{L}} \neq \rho_{*\mathsf{R}} \tag{4.61}$$

This causes any variable that depends on the mass density, such as the specific internal energy (e), temperature (T), speed of sound (a) as well as specific entropy (s) to be discontinuous (jump) across this contact discontinuity wave. Therefore, the procedure for determining the state variables of the gas in the star region is developed based on the constancy of both pressure and particle velocity across the contact discontinuity wave.

The general procedure mentioned in the following takes is valid for both star regions (left and

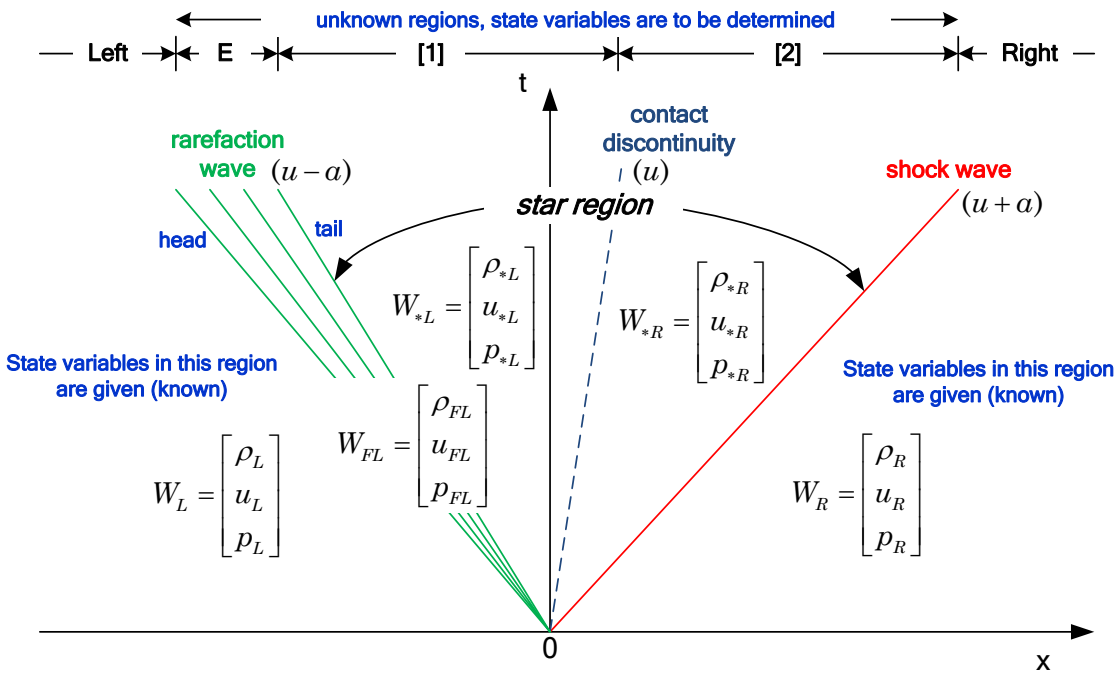

Figure 4.4. *A complete structure of the Riemann wave solution for the shock tube problem initially illustrated by Fig 4.1 with the initial conditions given by Eq. (4.54) in the sense that $p_L > p_R$. The situation inside the tube is depicted in Fig. 4.2. In this figure, it is shown also the head and tail of the rarefaction wave.*

right). Therefore, it is introduced a temporary new rule. A new subscript '0' is used first to indicate the state variables which are given which means to any state variables ahead or behind the star region. Meanwhile, both subscripts (*L) and (*R) are temporarily simplified to subscript $(*)$ only. Thus, the procedure for determining the mass densities of the gas in the two sub-star regions are as follows:

1. If the star region and the region behind or ahead of it (the given or known region) is connected by a **shock wave**, the jump in mass density across the shock wave is governed by the **Rankine-Hugoniot conditions**. According to this condition, the mass density behind the shock wave (ρ_*) is related to the mass density ahead the shock wave (ρ_0) as the function of the ratio of the pressure behind the shock wave (p_*) and ahead of the shock wave (p_0). Assuming that the gas treated in this case is ideal with a constant ratio of specific heats ($\gamma =$ constant, polytropic gas), the expression of the ratio of the mass density behind and ahead the shock wave is given by the following equation [35, 101]:

$$\frac{\rho_*}{\rho_0} = \frac{\left(\frac{\gamma-1}{\gamma+1}\right) + \left(\frac{p_*}{p_0}\right)}{\left(\frac{\gamma-1}{\gamma+1}\right)\left(\frac{p_*}{p_0}\right) + 1} \tag{4.62}$$

2. If the star region is connected to the region behind or ahead of it by a rarefaction wave, the

mass density of the star region is solved by means of the Poisson adiabatic equation (isentropic expansion process). In general, the Poisson adiabatic equation is written as follows [101]:

$$p = C\rho^{\gamma} \tag{4.63}$$

where C is a constant. The rarefaction wave is always moving toward the given region. Therefore, for both regions behind and ahead the rarefaction wave, the expression of the Poisson adiabatic equation is expressed as follows:

$$p_* = C\rho_*^{\gamma}, \quad \text{for the region behind the rarefaction wave} \tag{4.64}$$

$$p_0 = C\rho_0^{\gamma}, \quad \text{for the region ahead the rarefaction wave} \tag{4.65}$$

Manipulating both Eqs. (4.65) and (4.64), the ratio between the mass density behind and ahead the rarefaction wave can be determined by the following equation [101]:

$$\frac{\rho_*}{\rho_0} = \left(\frac{p_*}{p_0}\right)^{1/\gamma} \tag{4.66}$$

According to both Eqs. (4.62) and (4.66), the ratio of the mass density behind and ahead the non-linear wave is actually parameterized only by the ratio of both pressures behind and ahead the respected wave (p_* and p_0). Therefore, in the case of ideal gas with a constant ratio of specific heats, the mass density of the star region for all cases can be written in an alternative compact form as follows:

$$\rho_*\left(\gamma, \frac{p_*}{p_0}\right) = \begin{cases} \rho_0 \left[\dfrac{\frac{\gamma-1}{\gamma+1} + \frac{p_*}{p_0}}{\frac{\gamma-1}{\gamma+1}\cdot\frac{p_*}{p_0} + 1}\right], & \text{if} \quad \frac{p_*}{p_0} \geq 1, \quad \text{(across a shock wave)} \\ \rho_0 \left(\frac{p_*}{p_0}\right)^{1/\gamma}, & \text{if} \quad 0 < \frac{p_*}{p_0} < 1, \quad \text{(across a rarefaction wave)} \end{cases} \tag{4.67}$$

The implementation of Eq. (4.67) implies that the pressure in the star region (p_*) should be defined first. In fact, this variable can be determined by solving the following algebraic equation:

$$f(p_*, \mathbf{W}_\mathsf{L}, \mathbf{W}_\mathsf{R}) \equiv f_\mathsf{L}(p_*, \mathbf{W}_\mathsf{L}) + f_\mathsf{R}(p_*, \mathbf{W}_\mathsf{R}) + \Delta u = 0 \tag{4.68}$$

where $\Delta u = u_\mathsf{R} - u_\mathsf{L}$.

Both functions $f_\mathsf{L}(p_*, \mathbf{W}_\mathsf{L})$ and $f_\mathsf{R}(p_*, \mathbf{W}_\mathsf{R})$ are defined by the following equations:

$$f_\mathsf{L}(p_*, \mathbf{W}_\mathsf{L}) = a_\mathsf{L} \cdot \mathsf{v}_w\left(\gamma, \frac{p_*}{p_\mathsf{L}}\right), \qquad \text{and} \qquad f_\mathsf{R}(p_*, \mathbf{W}_\mathsf{R}) = a_\mathsf{R} \cdot \mathsf{v}_w\left(\gamma, \frac{p_*}{p_\mathsf{R}}\right) \tag{4.69}$$

where a_L and a_L are the speed of sound in respective gas which, according to Eq. (4.42), are

calculated by the following formula:

$$a_{\mathsf{L}} = \sqrt{\gamma \frac{p_{\mathsf{L}}}{\rho_{\mathsf{L}}}} \qquad \text{and} \qquad a_{\mathsf{R}} = \sqrt{\gamma \frac{p_{\mathsf{R}}}{\rho_{\mathsf{R}}}} \tag{4.70}$$

Meanwhile, both functions $\mathsf{v}_w\left(\gamma, \frac{p_*}{p_{\mathsf{L}}}\right)$ and $\mathsf{v}_w\left(\gamma, \frac{p_*}{p_{\mathsf{R}}}\right)$ are again determined from either the Rankine-Hugoniot condition in case of shock or the Poisson adiabatic equation in case of rarefaction. In general, function $\mathsf{v}_w\left(\gamma, \frac{p_*}{p_0}\right)$ is given by the following equation:

$$\mathsf{v}_w\left(\gamma, \frac{p_*}{p_0}\right) = \begin{cases} \dfrac{\frac{p_*}{p_0} - 1}{\sqrt{\gamma\left(\frac{p_*}{p_0}\frac{\gamma+1}{2} + \frac{\gamma-1}{2}\right)}}, & \text{if} \quad \frac{p_*}{p_0} \geq 1, \quad \text{(shock wave)} \\ \\ \frac{2}{\gamma-1}\left(\frac{p_*}{p_0}^{\frac{\gamma-1}{2\gamma}} - 1\right), & \text{if} \quad 0 < \frac{p_*}{p_0} < 1, \quad \text{(rarefaction wave)} \end{cases} \tag{4.71}$$

Furthermore, the solution of the ordinary algebraic Eq. (4.68) is obtained by applying the **Newton-Raphson** iteration rule. This procedure is written in general as follows:

$$p_{*,(i)} = p_{*,(i-1)} - \frac{f(p_{*,(i-1)}, \mathbf{W}_{\mathsf{L}}, \mathbf{W}_{\mathsf{R}})}{f'(p_{*,(i-1)}, \mathbf{W}_{\mathsf{L}}, \mathbf{W}_{\mathsf{R}})} \tag{4.72}$$

where $p_{*,(i)}$ is the i-th iterate ($i = 1, 2, 3, ...$). This iteration is stopped whenever:

$$\frac{|p_{*,(i)} - p_{*,(i-1)}|}{\frac{1}{2}\left[p_{*,(i)} + p_{*,(i-1)}\right]} \tag{4.73}$$

is less than a prescribed small tolerance, typically 10^{-6}. Once this condition has been fulfilled, the value of p_* is obtained. In order to execute the Newton-Raphson iteration procedure, the first derivative of Eq. (4.68) is required. It is given by the following equation:

$$f'(p_*, \mathbf{W}_{\mathsf{L}}, \mathbf{W}_{\mathsf{R}}) = a_{\mathsf{L}} \cdot \frac{d}{dp_*}\left[\mathsf{v}_w\left(\gamma, \frac{p_*}{p_{\mathsf{L}}}\right)\right] + a_{\mathsf{R}} \cdot \frac{d}{dp_*}\left[\mathsf{v}_w\left(\gamma, \frac{p_*}{p_{\mathsf{R}}}\right)\right] \tag{4.74}$$

Meanwhile, the first derivative of Eq. (4.71) with respect to the pressure p_* is given by

$$\frac{d}{dp_*}\left[\mathsf{v}_w\left(\gamma, \frac{p_*}{p_0}\right)\right] = \begin{cases} \dfrac{1}{p_0\sqrt{\gamma(Ap_* + B)}}\left[1 - \dfrac{A}{2}\left(\dfrac{p_* - p_0}{Ap_* + B}\right)\right], & \text{if} \quad \frac{p_*}{p_0} > 1 \\ \\ \dfrac{1}{\gamma p_0}\left(\dfrac{p_*}{p_0}\right)^{-\frac{\gamma+1}{2\gamma}}, & \text{if} \quad 0 < \frac{p_*}{p_0} \leq 1 \end{cases} \tag{4.75}$$

with

$$A = \frac{\gamma + 1}{2p_*} \qquad \text{and} \qquad B = \frac{\gamma - 1}{2}$$

In addition, it is important to mention that the Newton-Raphson procedure requires an initial value of p_* for running the iteration. This means that, for the very first iteration ($i = 1$), the value of $p_{*,(0)}$ must be made available. As recommended in [101], the initial guess value of the pressure in the star region can be obtained directly from a linearized relation of given primitive variables (initial conditions). Such linearized relation is expressed by the following equation:

$$p_{\mathsf{pv}} = \frac{1}{2}(p_{\mathsf{R}} + p_{\mathsf{L}}) - \frac{1}{8}(u_{\mathsf{R}} - u_{\mathsf{L}})(\rho_{\mathsf{R}} + \rho_{\mathsf{L}})(a_{\mathsf{R}} + a_{\mathsf{L}}) \tag{4.76}$$

And, the initial guess value of $p_{*,(0)}$ is obtained from the condition that:

$$p_{*,(0)} = \max(\text{tolerance}, p_{\mathsf{pv}}) \tag{4.77}$$

Once the initial guess value of p_* has been obtained, the iterative Newton-Raphson procedure can be executed to determine the desired value of the star region pressure (p_*). Up to this point, the pressure and mass density of the star region have been determined. The particle velocity (u_*) in this region is determined by solving the following simple algebraic equation:

$$u_* = \frac{1}{2}\left[u_{\mathsf{L}} + u_{\mathsf{R}} + f_{\mathsf{R}}(p_*, \mathbf{W}_{\mathsf{R}}) - f_{\mathsf{L}}(p_*, \mathbf{W}_{\mathsf{L}})\right] \tag{4.78}$$

4.2.4 Sampling procedure

In the following, the procedure for determining the state of the gas at any point within the domain of interest is described. In [101], this procedure is called the sampling procedure in which the exact solution of the Riemann problem serves as a basis of the calculation. Suppose that the physical domain of the shock tube problem is $x := [0, L]$, this procedure will determine the state of the gas at any point (x, t) where $t > 0$. The initial discontinuity is located at $x = x_0 = L/2$.

In order to guarantee self-similarity within the problem, the axial position of this initial discontinuity should be transformed to $x' = 0$, where x' represents the axial position in the Riemann problem coordinate system. Such transformation is illustrated by Fig. 4.5 and governed by the following equation:

$$x' = x - \frac{L}{2} \tag{4.79}$$

As mentioned before, the middle wave (*wave-2*) is always a contact discontinuity wave. While, *wave-1* and *wave-3* are the two possible non-linear waves, which may be either shock waves or rarefaction waves or both may be a shock and a rarefaction wave. As shown in Fig. 4.5, velocities of each wave system are denoted by s_1, s_2 and s_3. s_2 is the velocity of the middle wave. If the speed required to reach point x' at time t on the Riemann problem coordinate system is given by:

$$s'(x', t) = \frac{x'}{t} = \frac{x - \frac{L}{2}}{t} \tag{4.80}$$

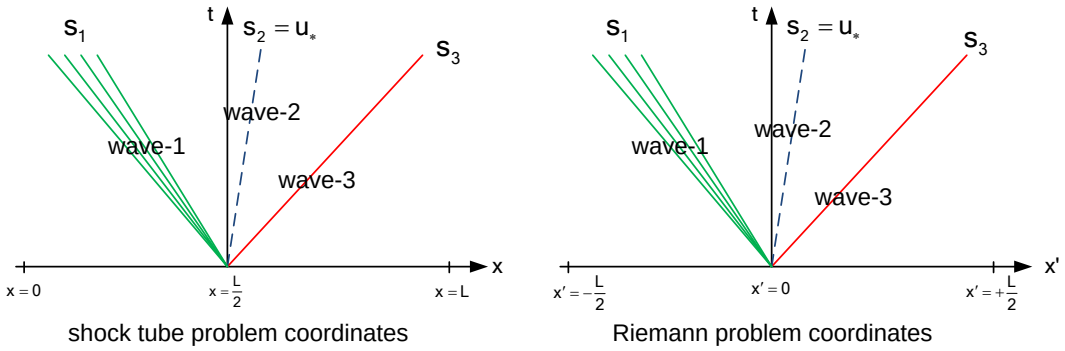

Figure 4.5. *Transformation of the shock tube and Riemann problem coordinate system as a basis for the sampling procedure.*

the state of the gas at any sample point (x,t) in terms of primitive variables which is represented by the column vector $\mathbf{W}(x,t)$ is determined by comparing the speed $s'(x',t)$ to the speeds of the Riemann wave.

Since the speed of the middle wave (*wave-2*), as described previously, is always u_*, the comparison of $s'(x',t)$ to u_* will determine whether the sample point (x,t) is positioned to the left or to the right of the contact discontinuity. This condition is specified by the following decision procedure as illustrated by Fig. 4.6:

- if the speed $s'(x',t) = \frac{x'}{t} < u_*$, the sample point (x,t) is located left of the contact discontinuity, or
- if the speed $s'(x',t) = \frac{x'}{t} > u_*$, the sample point (x,t) lies right of the contact discontinuity.

Furthermore, for each condition, there are two possible wave configurations with respect to the type of non-linear wave which can be illustrated by Fig. 4.7. With respect to the initial conditions of the Riemann problem, the type of left and right non-linear wave is determined by the ratio of the pressures in the star region (p_*) and the pressure in the known region (p_L or p_R).

As indicated by Fig. 4.7, for each condition, the primitive variables of the gas at a sample point (x,t) can be easily determined by comparing the speed of the sample point $s'(x',t)$ to the speed of the non-linear wave. Prior to describe the complete procedure for determining the entire solution of the Riemann problem, it is necessary to mention that if the non-linear wave is a rarefaction wave, the speed of the head and the tail of the rarefaction wave must be taken into account. This means that the sample point may be located inside the expansion region (indicated by the green area in Fig. 4.7). In this case, the determination of the primitive variables at that sample point requires a special procedure as mentioned in [101]. Finally, the complete procedure for determining the primitive variables at any sample point (x,t), where $x_\mathsf{L} < x < x_\mathsf{R}$ and the initial discontinuity is at $x = x_0$, is summarized as follows:

I. **Right wave**,
   which means that the sample point (x,t) lies right of the contact wave.
   The condition is: $s'(x',t) = \dfrac{x'}{t} = \dfrac{x - x_0}{t} > u_*$

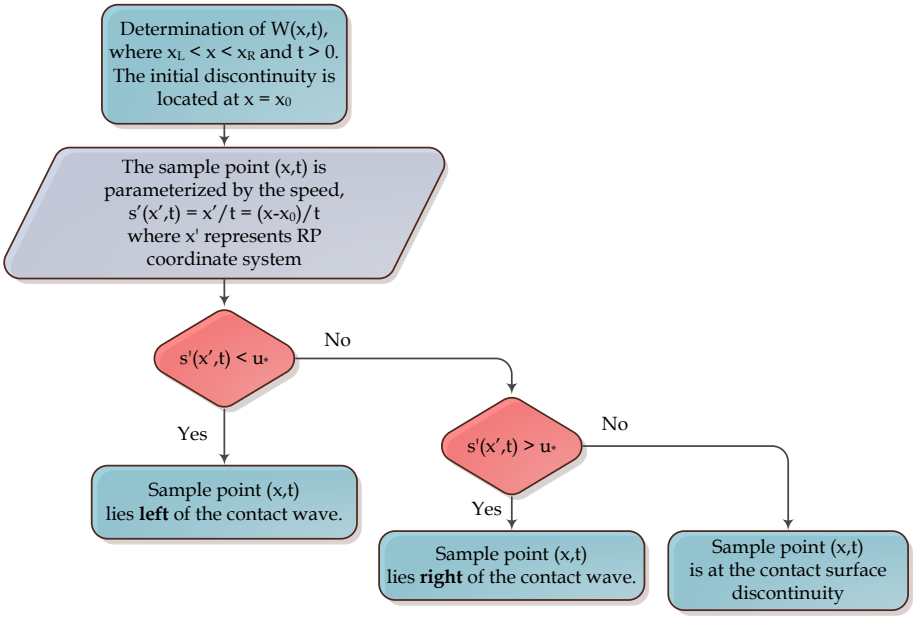

Figure 4.6. *Procedure for determining the primitive variables at the sample point (x,t) where $x_L < x < x_R$ and $t > 0$ and the initial discontinuity is located at $x = x_0$.*

- if $p_* > p_{\mathsf{R}}$, the right wave is a **shock wave**.
  Calculation of the shock wave velocity, denoted by s_{R}:

$$s_{\mathsf{R}} = u_{\mathsf{R}} + a_{\mathsf{R}} \cdot \sqrt{\frac{\gamma+1}{2\gamma}\frac{p_*}{p_{\mathsf{R}}} + \frac{\gamma-1}{2\gamma}} \tag{4.81}$$

  where

$$a_{\mathsf{R}} = \sqrt{\gamma \frac{p_{\mathsf{R}}}{\rho_{\mathsf{R}}}}$$

  Thus, $\mathbf{W}(x,t)$ is:

$$[\rho, u, p]^{\mathsf{T}}(x,t) = \begin{cases} \mathbf{W}_{\mathsf{R}} = [\rho_{\mathsf{R}}, u_{\mathsf{R}}, p_{\mathsf{R}}]^{\mathsf{T}}, & \text{for} \quad s'(x',t) > s_{\mathsf{R}} \\ \mathbf{W}_{*\mathsf{R}} = [\rho_{*\mathsf{R}}, u_*, p_*]^{\mathsf{T}}, & \text{for} \quad u_* < s'(x',t) < s_{\mathsf{R}} \end{cases} \tag{4.82}$$

- if $p_* \leq p_{\mathsf{R}}$, the right wave is a **rarefaction wave**.
  Calculation of the speed of the head and tail of the rarefaction wave:

$$s_{\mathsf{HR}} = u_{\mathsf{R}} + a_{\mathsf{R}}, \qquad \text{and} \qquad s_{\mathsf{TR}} = u_* + a_{*\mathsf{R}} \tag{4.83}$$

  where

$$a_{*\mathsf{R}} = \sqrt{\gamma \frac{p_*}{\rho_{*\mathsf{R}}}}$$

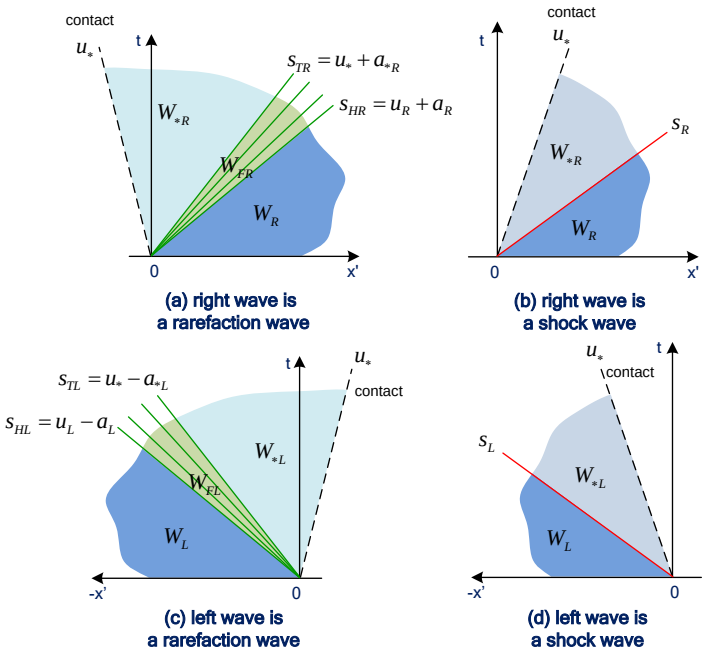

Figure 4.7. *Illustration of four possible wave configurations for the evaluation of the sample point (x,t). Case (a) and (b) are for the right wave, while case (c) and (d) are for the left wave. Subscripts H and T indicates the head and tail of the rarefaction wave.*

Thus, $\mathbf{W}(x,t)$ is:

$$[\rho,u,p]^{\mathsf{T}}(x,t) = \begin{cases} \mathbf{W}_{\mathsf{R}} = [\rho_{\mathsf{R}},u_{\mathsf{R}},p_{\mathsf{R}}]^{\mathsf{T}}, & \text{for} \quad s'(x',t) \geq s_{\mathsf{HR}} \\ \mathbf{W}_{\mathsf{FR}} = [\rho_{\mathsf{FR}}(x,t),u_{\mathsf{FR}}(x,t),p_{\mathsf{FR}}(x,t)]^{\mathsf{T}}, & \text{for} \quad s_{\mathsf{TR}} < s'(x',t) < s_{\mathsf{HR}} \\ \mathbf{W}_{*\mathsf{R}} = [\rho_{*\mathsf{R}},u_*,p_*]^{\mathsf{T}}, & \text{for} \quad u_* < s'(x',t) \leq s_{\mathsf{TR}} \end{cases} \tag{4.84}$$

where the solution inside the rarefaction wave is:

$$\rho_{\mathsf{FR}}(x,t) = \rho_{\mathsf{R}}\left[\frac{2}{\gamma+1} - \frac{\gamma-1}{(\gamma+1)a_{\mathsf{R}}}(u_{\mathsf{R}} - \frac{x'}{t})\right]^{\frac{2}{\gamma-1}} \tag{4.85}$$

$$u_{\mathsf{FR}}(x,t) = \frac{2}{\gamma+1}\left[-a_{\mathsf{R}} + \frac{\gamma-1}{2}u_{\mathsf{R}} + \frac{x'}{t}\right] \tag{4.86}$$

$$p_{\mathsf{FR}}(x,t) = p_{\mathsf{R}}\left[\frac{2}{\gamma+1} - \frac{\gamma-1}{(\gamma+1)a_{\mathsf{R}}}(u_{\mathsf{R}} - \frac{x'}{t})\right]^{\frac{2\gamma}{\gamma-1}} \tag{4.87}$$

II. **Left wave**,

which means that the sample point (x,t) lies left of the contact wave.

The condition is: $s'(x',t) = \dfrac{x'}{t} = \dfrac{x-x_0}{t} < u_*$

- if $p_* > p_{\mathsf{L}}$, the left wave is a **shock wave**.

Calculation of the shock wave velocity, denoted by s_{L}:

$$s_{\mathsf{L}} = u_{\mathsf{L}} - a_{\mathsf{L}} \cdot \sqrt{\frac{\gamma+1}{2\gamma}\frac{p_*}{p_{\mathsf{L}}} + \frac{\gamma-1}{2\gamma}} \tag{4.88}$$

where

$$a_{\mathsf{L}} = \sqrt{\gamma\frac{p_{\mathsf{L}}}{\rho_{\mathsf{L}}}}$$

Thus, $\mathbf{W}(x,t)$ is:

$$[\rho, u, p]^{\mathsf{T}}(x,t) = \begin{cases} \mathbf{W}_{\mathsf{L}} = [\rho_{\mathsf{L}}, u_{\mathsf{L}}, p_{\mathsf{L}}]^{\mathsf{T}}, & \text{for} \quad s'(x',t) < s_{\mathsf{L}} \\ \mathbf{W}_{*\mathsf{L}} = [\rho_{*\mathsf{L}}, u_*, p_*]^{\mathsf{T}}, & \text{for} \quad s_{\mathsf{L}} < s'(x',t) < u_* \end{cases} \tag{4.89}$$

- if $p_* \leq p_{\mathsf{L}}$, the left wave is a **rarefaction wave**.
  Calculation of the speed of the head and tail of the rarefaction wave:

$$s_{\mathsf{HL}} = u_{\mathsf{L}} - a_{\mathsf{L}} \qquad \text{and} \qquad s_{\mathsf{TL}} = u_* - a_{*\mathsf{L}} \tag{4.90}$$

where

$$a_{*\mathsf{L}} = \sqrt{\gamma\frac{p_*}{\rho_{*\mathsf{L}}}}$$

Thus, $\mathbf{W}(x,t)$ is:

$$[\rho, u, p]^{\mathsf{T}}(x,t) = \begin{cases} \mathbf{W}_{\mathsf{L}} = [\rho_{\mathsf{L}}, u_{\mathsf{L}}, p_{\mathsf{L}}]^{\mathsf{T}}, & \text{for} \quad s'(x',t) \leq s_{\mathsf{HL}} \\ \mathbf{W}_{\mathsf{FL}} = [\rho_{\mathsf{FL}}(x,t), u_{\mathsf{FL}}(x,t), p_{\mathsf{FL}}(x,t)]^{\mathsf{T}}, & \text{for} \quad s_{\mathsf{HL}} < s'(x',t) < s_{\mathsf{TL}} \\ \mathbf{W}_{*\mathsf{L}} = [(\rho_{*\mathsf{L}}, u_*, p_*]^{\mathsf{T}}, & \text{for} \quad s_{\mathsf{TL}} \leq s'(x',t) < u_* \end{cases} \tag{4.91}$$

where the solution inside the rarefaction wave is:

$$\rho_{\mathsf{FL}}(x,t) = \rho_{\mathsf{L}}\left[\frac{2}{\gamma+1} + \frac{\gamma-1}{(\gamma+1)a_{\mathsf{L}}}(u_{\mathsf{L}} - \frac{x'}{t})\right]^{\frac{2}{\gamma-1}} \tag{4.92}$$

$$u_{\mathsf{FL}}(x,t) = \frac{2}{\gamma+1}\left[a_{\mathsf{L}} + \frac{\gamma-1}{2}u_{\mathsf{L}} + \frac{x'}{t}\right] \tag{4.93}$$

$$p_{\mathsf{FL}}(x,t) = p_{\mathsf{L}}\left[\frac{2}{\gamma+1} + \frac{\gamma-1}{(\gamma+1)a_{\mathsf{L}}}(u_{\mathsf{L}} - \frac{x'}{t})\right]^{\frac{2\gamma}{\gamma-1}} \tag{4.94}$$

The complete procedures for determining the exact solution to the Riemann problem for the one-dimensional Euler equations, or also known as the exact Riemann solver has been implemented in a MATLAB® program. This programming language was chosen because it is a scientific computing language which supports a comprehensive environment for numerical simulation with integrated visualization, powerful scripting framework and fast algorithms implementation. Several references, such as [108, 109, 110] contain a comprehensive practical guide for using this programming language for various problems of science and engineering, including fluid dynamics problems.

4.2.5 Important remarks to solve the multi-dimensional Riemann problem using the exact Riemann solver

When solving numerically the two or three dimensional Euler equations of gas dynamics by the upwind method, as mentioned later in the next section (numerical solution using the Godunov scheme), the solution of splitting Riemann problems are required. For a three dimensional Euler equations, the corresponding x-splitting Riemann problem is the following initial value problem:

$$\text{PDEs:} \qquad \frac{\partial}{\partial t}\mathbf{Q}(x,y,z,t) + \frac{\partial}{\partial x}\mathbf{F}\left(\mathbf{Q}(x,y,z,t)\right) = 0 \tag{4.95}$$

$$\text{ICs:} \qquad \mathbf{Q}(x,y,z,0) = \mathbf{Q}^0(x,y,z) = \begin{cases} \mathbf{Q}_\mathsf{L}, & \text{if } x < 0 \\ \mathbf{Q}_\mathsf{R}, & \text{if } x > 0 \end{cases}$$

where

$$\mathbf{Q} = \begin{bmatrix} \rho \\ \rho u \\ \rho v \\ \rho w \\ E \end{bmatrix}, \qquad \mathbf{F}(\mathbf{Q}) = \begin{bmatrix} \rho u \\ \rho u^2 + p \\ \rho uv \\ \rho uw \\ (E+p)u \end{bmatrix} \tag{4.96}$$

and the total energy E is now given by the following equation:

$$E = \frac{p}{\gamma - 1} + \frac{1}{2}\rho\left(u^2 + v^2 + w^2\right) \tag{4.97}$$

As mentioned before, the Riemann problem is to be solved in terms of primitive physical variables which requires also the primitive variables as the main input. This means that the conserved variables should be transformed into their primitive variables before the Riemann solver is used. The structure of the similarity solution of the x-splitting Riemann problem is generally depicted in Fig. 4.8. Both pressure and normal velocity u remain constant in the star region, across the middle wave. The most important point deals with the determination of the tangential velocity component v and w. According to the properties and characteristics of the Riemann wave, these tangential velocities remain constant across the non-linear wave irrespective of their type. This means, for

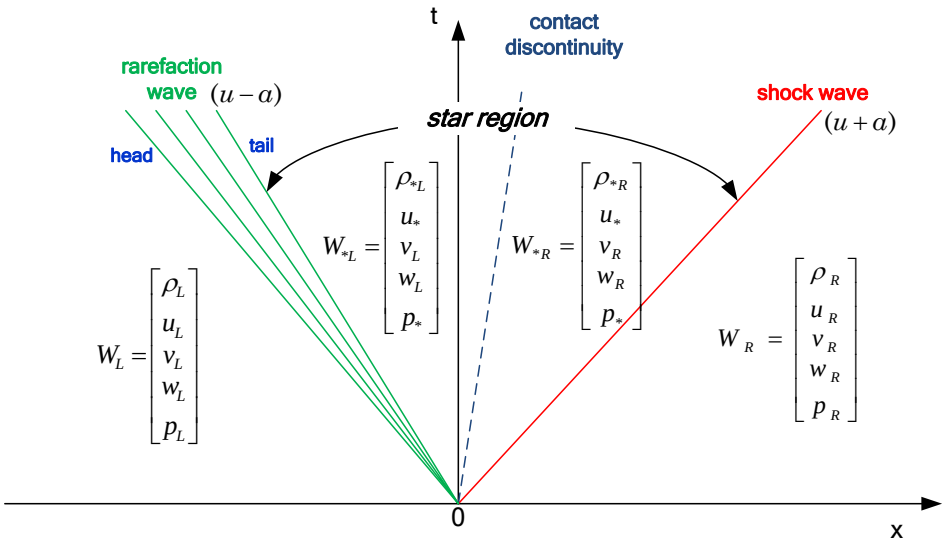

Figure 4.8. *Structure of the solution of the three-dimensional split Riemann problem in $x-$direction*

example, the tangential velocity vector at the cell interface boundary in Fig. 4.8 is given by:

$$U_t = [0, v_L, w_L] \tag{4.98}$$

Therefore, the solution of the splitting Riemann problem of three dimensional case is fundamentally similar to the procedure for solving the one-dimensional case, except for the treatment of the tangential velocity vector. Such simple behavior of the tangential velocity vector is sometimes incorrectly modeled by some approximate Riemann solvers [101]. Thus, the numerical method for the one or multi-dimensional case of the Euler equations of gas dynamics by means of the Godunov scheme, as shown in a later section, implements the exact Riemann solver. The general computational flow for the determination of the solution of the Riemann problem using the exact Riemann solver is given in Appendix C

4.2.6 Testing the exact Riemann solver: The benchmark solution of Sod's shock tube problem

In what follows, the benchmark solution of the well-known Sod's shock tube problem is presented. This particular problem is to be solved using the procedure previously presented, that is by means of the exact Riemann solver. In fact, Sod's shock tube problem is a special case of the shock tube problem, which is named after **Gary A. Sod** who first introduced this problem in 1978 [111]. For many numerical analyses of gas and other fluid dynamics problems, Sod's shock tube problem is considered as a benchmark and also as a standard reference to test the ability of various algorithms for solving fluid dynamics problems, especially when the phenomena of shock waves are encountered. The main reason is that the analytical solution of Sod's shock tube problem is widely known.

The initial configuration of Sod's shock tube problem is similar to Fig. 4.1. In this particular problem, the gases occupying the region to the left and to the right of the diaphragm are initially assumed at rest. This means that the initial velocity is set to zero along the tube domain ($u_{\mathsf{L}} = u_{\mathsf{R}} = 0$). The other initial quantities such as pressures and mass densities are not zero and discontinuous across the diaphragm. The left region to the diaphragm is occupied by a high pressure and high density gas, and the right hand region by a low pressure and low density gas. For the following test, it is assumed that the tube has a physical domain of $x = [0, 20]$ m. The thin diaphragm is located right in the middle of the tube at $x = 10.0$ m. This diaphragm then separates the following two initial constant data states which is considered as the initial condition of the Riemann problem:

$$\mathbf{W}(x,0) = \mathbf{W}^0(x) = \begin{cases} \mathbf{W}_{\mathsf{L}} = [\rho_{\mathsf{L}}, u_{\mathsf{L}}, p_{\mathsf{L}}]^{\mathsf{T}} = [1.0, 0.0, 1.0 \times 10^5], & \text{if } x < 10.0 \text{ m} \\ \mathbf{W}_{\mathsf{R}} = [\rho_{\mathsf{R}}, u_{\mathsf{R}}, p_{\mathsf{R}}]^{T} = [0.125, 0.0, 0.1 \times 10^5], & \text{if } x > 10.0 \text{ m} \end{cases} \tag{4.99}$$

Here ρ, u and p are the primitive variables respectively given in kg/m^3, m/s and Pa. Fig. 4.9 illustrates again the initial configuration of Sod's shock tube problem.

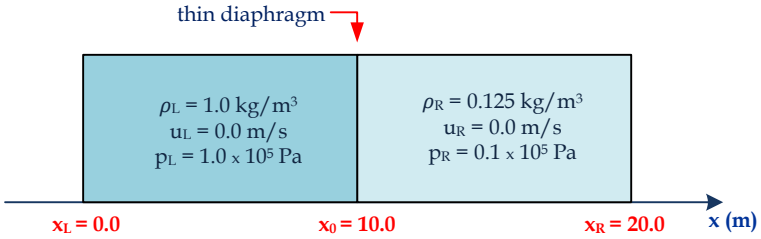

Figure 4.9. *Initial configuration of Sod's shock tube problem*

The gas occupying the tube is assumed to be air which is treated as an ideal gas with a constant ratio of specific heats (polytropic gas). For this particular case, $\gamma = 1.40$ has been assumed. Table 4.1 shows other important thermodynamic variables which are also required actually for determining the solutions of Sod's shock tube problem other than the primitive variables using the exact Riemann solver.

Table 4.1. *Important thermodynamic variables of air for solving the Euler equations*

Variables	Equation	Numeric value	Unit
Molecular weight, $M_{w,\text{air}}$	-	28.94	kg/kmol
Specific gas constant, R_{air}	Eq. (4.28)	287.28	J/kg/K
Specific heat at constant pressure, $c_{p,\text{air}}$	Eq. (4.48)	1.005×10^3	J/kg/K
Specific heat at constant volume, $c_{v,\text{air}}$	Eq. (4.48)	0.718×10^3	J/kg/K

By using the Newton-Raphson iteration method, the pressure and particle velocity around the middle of the tube after the removal of the diaphragm (i.e. variables in the star region) are $p_* = 0.3031$ bar and $u_* = 293.29$ m/s respectively. The mass densities in this region are

$\rho_{*L} = 0.4263$ kg/m^3 for the left of the contact wave and $\rho_{*R} = 0.2656$ kg/m^3 for the right of the contact wave.

The primitive variables, including the specific internal energy at 3000 equally spatial points throughout the tube at time $t = 0.015$ seconds after the break of the diaphragm are depicted in Fig. 4.10. From these figures, it can be seen that the benchmark solutions of Sod's shock tube problem consists of a left rarefaction wave, contact wave and right shock wave which agree with the data and plots published in [101, 112]. The exact Riemann solver which was developed for solving the Riemann problem in this thesis is now used for developing the numerical solutions of the Euler equations of gas dynamics.

4.3 Numerical solutions of the Euler equations using the finite volume method: The Godunov scheme

As mentioned in the previous section, the exact analytical solutions of the Euler equations are available only for some simple cases, such as Sod's shock tube problem. In much more complex circumstances, a numerical scheme for solving the equations needs to be developed [100]. Since the Euler equations of gas dynamics admit discontinuous solutions, these equations are good to be solved using finite volume techniques. The underlying philosophy is to solve conservation laws over volumes, while dealing with essentially discontinuous variables. In this case, the more fundamental integral form involving integrals over control volumes and their boundaries is required. Using this technique, the continuous and discontinuous profiles can be treated in the same way, without a need for particular treatments for the shocks or contact discontinuities. In addition, a continuous flow can also be considered as a particular case of a discontinuous flow.

With respect to the finite volume techniques, the discretized domains are naturally defined as computational cells. In [113], several finite volume schemes which can be applied for solving the Euler equations are discussed. In this thesis, the Godunov scheme is used. As mentioned previously, the Riemann problem is the key ingredient of developing the numerical solution of the Euler equations using the Godunov scheme. The Riemann problem is solved in terms of the exact Riemann solver. It is necessary to mention that the Godunov numerical scheme which is implemented with exact Riemann solver provides only first-order accuracy.

Basically, the Godunov scheme is an upwind numerical method. In this context, as mentioned before, the exact Riemann solver is employed for computing numerical fluxes of mass, momentum, and energy at the cell interface between two neighboring computational cells. This computation is performed for the entire computational domain [106] at every time level. An efficient numerical scheme for solving the one-dimensional Euler equations serves as the basis for developing the modeling of the multi-dimensional cases. In this thesis, the development of the numerical modeling for the one-dimensional case is presented in much detail. Important steps for the numerical simulation are discussed. In later section, important consideration for solving the two as well as the three dimensional cases are also described.

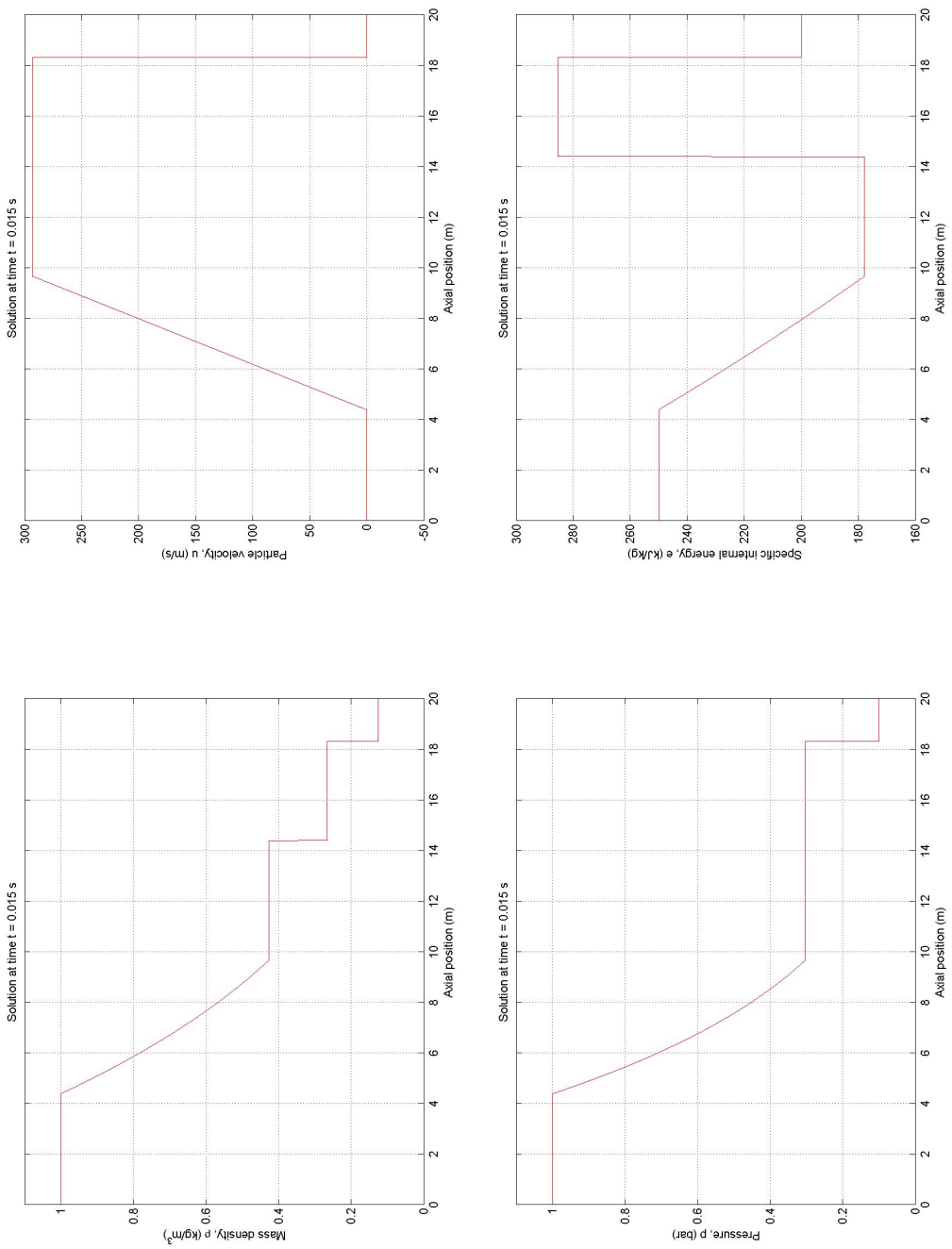

Figure 4.10. *Benchmark solutions of Sod's shock tube problem. In this figure, the physical primitive variables and specific internal energy at time* $t = 0.015$ *seconds after the break of the diaphragm are shown.*

4.3.1 The initial boundary value problem of the one-dimensional Euler equations

In this section, the problem of interest is to develop a procedure for solving of the following initial boundary value problem of the one-dimensional time-dependent Euler equations of gas dynamics numerically. Again, these equations are written in general as follows:

$$\text{PDEs:} \qquad \frac{\partial}{\partial t}\mathbf{Q}(x,t) + \frac{\partial}{\partial x}\mathbf{F}(\mathbf{Q}(x,t)) = 0 \tag{4.100}$$

with the following initial conditions:

$$\text{ICs:} \qquad \mathbf{Q}(x,0) = \mathbf{Q}^{(0)}(x)$$

and the boundary conditions:

$$\text{BCs:} \qquad \mathbf{Q}(0,t) = \mathbf{Q}_L(t), \qquad \text{and} \qquad \mathbf{Q}(L,t) = \mathbf{Q}_R(t)$$

where $\mathbf{Q}$ is the column vector of conserved variables; $\mathbf{F}(\mathbf{Q})$ is the column vector of conserved fluxes; $\mathbf{Q}^{(0)}(x)$ is the piecewise constant distribution of initial data at time $t = 0$ which can also be calculated from the primitive variables in case the initial conditions are given in those variables. $[0, L]$ is the spatial boundary conditions and computational domain. The state of the gas at these boundaries are assumed to be represented by $\mathbf{Q}_L(t)$ and $\mathbf{Q}_R(t)$ [101, 114]. The condition of the boundary may be specified as a reflective or transmissive type based on the problem under consideration.

4.3.2 The discretization of the spatial and temporal domain

Unlike in the classical finite difference method, the discretization of the spatial domain in the finite volume technique is done in terms of **computational cells**. Fig. 4.11 illustrates a discretized $x - t$ mesh configuration if the length of the spatial domain is L. There is a uniform spatial mesh for which the spatial domain is discretized into M computational cells. Each computational cell, denoted by $I_i = [x_{i-\frac{1}{2}}, x_{i+\frac{1}{2}}]$, where $i = 1, 2, 3, ..., M$ is the cell index, has a regular size of cell (width) $\Delta x = {}^{L}/_{M}$.

The computational cell I_i is bounded by faces $i - \frac{1}{2}$ and $i + \frac{1}{2}$ which are positioned at:

$$x_{i-\frac{1}{2}} = (i-1)\cdot\Delta x, \qquad x_{i+\frac{1}{2}} = i\cdot\Delta x \tag{4.101}$$

and, the center of the cell I_i is located at:

$$x_i = (i - \frac{1}{2})\cdot\Delta x \tag{4.102}$$

For this particular case, the left space boundary is at $x_{\frac{1}{2}} = 0$, while the right one is located at $x_{M+\frac{1}{2}} = L$.

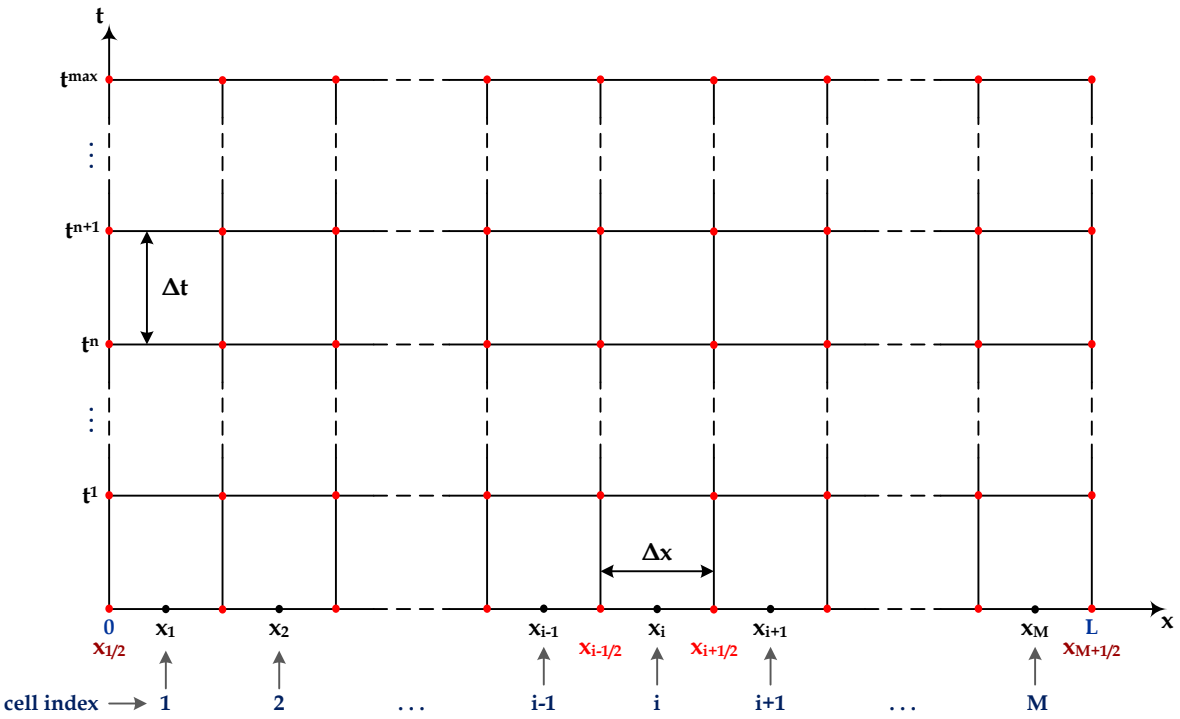

Figure 4.11. *Discretized one-dimensional domain which is presented in $x-t$ plane. In actual simulation, the one-dimensional computational cell is represented only by a line for which the interface between two computational cells is represented only by a point.*

Meanwhile, the discretization of the temporal domain is, in fact, not uniform. The **computational time step**, denoted by Δt is determined by the following equation:

$$\Delta t = \frac{\mathbf{C}_{\text{cfl}} \cdot \Delta x}{s^n_{\max}} \tag{4.103}$$

The subscript n denotes the time level. The coefficient $\mathbf{C}_{\text{cfl}}$ is called a **Courant-Frederich-Lewy** number which must satisfies the following condition,

$$0 < \mathbf{C}_{\text{cfl}} < 1 \tag{4.104}$$

The variable $s^n_{\max}$ is the maximum wave speed present throughout the spatial domain during time level n.

4.3.3 The discretization of the Euler equations

The conservative form of the Euler equations is particularly important when dealing with the problem admitting shocks or other discontinuities in the solution [101, 114]. Fig. 4.12 shows the discretization of the spatial domain $[0, L]$ for a time step $[t^n, t^{n+1}]$.

The development of the numerical scheme for Eq. (4.100) begins with the integration of the equation for a specific control volume $V_i = I_i \times [t^n, t^{n+1}] = [x_{i-\frac{1}{2}}, x_{i+\frac{1}{2}}] \times [t^n, t^{n+1}]$ in the domain

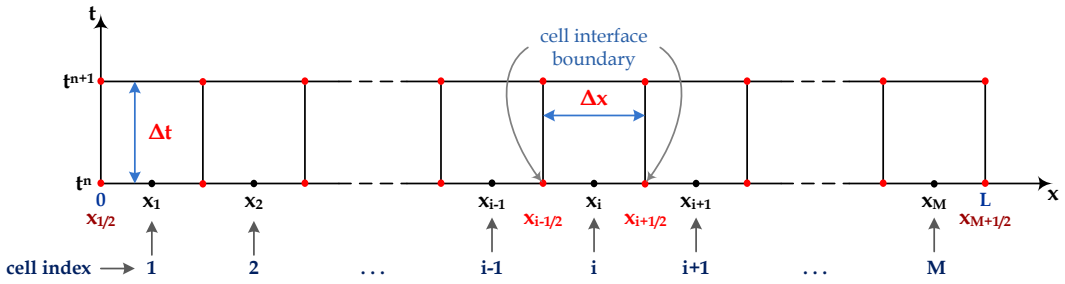

Figure 4.12. *Discretization of the one-dimensional spatial domain in $x-t$ plane for a single time step*

of interest. Firstly, Eq. (4.100) is integrated with respect to the space over I_i as follows:

$$\int_{x_{i-\frac{1}{2}}}^{x_{i+\frac{1}{2}}} \frac{\partial}{\partial t}\mathbf{Q}(x,t)\ dx = -\int_{x_{i-\frac{1}{2}}}^{x_{i+\frac{1}{2}}} \frac{\partial}{\partial x}\mathbf{F}(\mathbf{Q}(x,t))dx \tag{4.105}$$

The Gauss theorem can be applied to the left hand side of this equation, thus

$$\int_{x_{i-\frac{1}{2}}}^{x_{i+\frac{1}{2}}} \frac{\partial}{\partial t}\mathbf{Q}(x,t)\ dx = \frac{d}{dt}\int_{x_{i-\frac{1}{2}}}^{x_{i+\frac{1}{2}}} \mathbf{Q}(x,t)\ dx \tag{4.106}$$

While, the right hand side is expanding according to the following rule:

$$\int_{x_{i-\frac{1}{2}}}^{x_{i+\frac{1}{2}}} \frac{\partial}{\partial x}\mathbf{F}(\mathbf{Q}(x,t))dx = \mathbf{F}(\mathbf{Q}(x_{i-\frac{1}{2}},t)) - \mathbf{F}(\mathbf{Q}(x_{i+\frac{1}{2}},t)) \tag{4.107}$$

This will modify Eq. (4.105) to give:

$$\frac{d}{dt}\int_{x_{i-\frac{1}{2}}}^{x_{i+\frac{1}{2}}} \mathbf{Q}(x,t)\ dx = \mathbf{F}(\mathbf{Q}(x_{i-\frac{1}{2}},t)) - \mathbf{F}(\mathbf{Q}(x_{i+\frac{1}{2}},t)) \tag{4.108}$$

Thus, Eq. (4.108) is further integrated with respect to the time between t^n and t^{n+1}, with $t^n < t^{n+1}$ as written as follows:

$$\int_{x_{i-\frac{1}{2}}}^{x_{i+\frac{1}{2}}} \mathbf{Q}(x,t^{n+1})\ dx - \int_{x_{i-\frac{1}{2}}}^{x_{i+\frac{1}{2}}} \mathbf{Q}(x,t^{n})\ dx = \int_{t^n}^{t^{n+1}} \mathbf{F}(\mathbf{Q}(x_{i-\frac{1}{2}},t))\ dt - \int_{t^n}^{t^{n+1}} \mathbf{F}(\mathbf{Q}(x_{i+\frac{1}{2}},t))\ dt \tag{4.109}$$

This last form is in fact the basic integral formulation for developing the numerical scheme of the one-dimensional time dependent Euler equations using the finite volume technique.

With respect to the Godunov scheme, two new quantities are introduced to Eq. (4.109). First, the Godunov scheme assumes a piece-wise constant distribution of the data as illustrated by Fig. 4.13 which is realized by defining the cell average of the conserved variables assigned to each

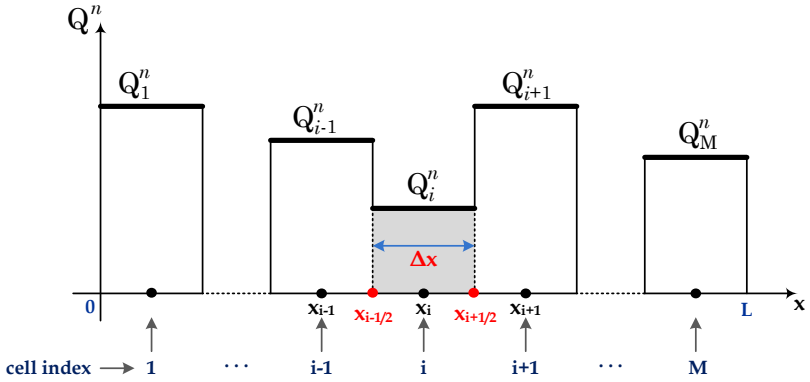

Figure 4.13. *Illustration of a piecewise constant distribution of the data* $\mathbf{Q}$ *at time level* n

computational cells. Thus,

$$\mathbf{Q}_i^n = \frac{1}{\Delta x} \int_{x_{i-\frac{1}{2}}}^{x_{i+\frac{1}{2}}} \mathbf{Q}(x, t^n)\, dx \tag{4.110}$$

Second, in order to determine the evolution of the solution to the next time level, the time average of the conserved fluxes at cell interface boundaries is introduced. This quantity is generally defined by the following equation:

$$\mathbf{F}_{i\pm\frac{1}{2}} = \frac{1}{\Delta t} \int_{t^n}^{t^{n+1}} \mathbf{F}(\mathbf{Q}(x_{i\pm\frac{1}{2}}, t))\, dt \tag{4.111}$$

Furthermore, Eq. (4.109) is to be modified by dividing all terms with Δx and manipulating the right hand side in order to obtain the following expression:

$$\begin{aligned} \frac{1}{\Delta x} \int_{x_{i-\frac{1}{2}}}^{x_{i+\frac{1}{2}}} \mathbf{Q}(x, t^{n+1})\, dx &= \frac{1}{\Delta x} \int_{x_{i-\frac{1}{2}}}^{x_{i+\frac{1}{2}}} \mathbf{Q}(x, t^n)\, dx \\ &+ \frac{\Delta t}{\Delta x} \left[\frac{1}{\Delta t} \int_{t^n}^{t^{n+1}} \mathbf{F}(\mathbf{Q}(x_{i-\frac{1}{2}}, t))\, dt - \frac{1}{\Delta t} \int_{t^n}^{t^{n+1}} \mathbf{F}(\mathbf{Q}(x_{i+\frac{1}{2}}, t))\, dt \right] \end{aligned} \tag{4.112}$$

Thus, applying the two new quantities introduced above, the Godunov numerical scheme of the

one dimensional time-dependent Euler equations is written as follows:

$$\mathbf{Q}_i^{n+1} = \mathbf{Q}_i^n + \frac{\Delta t}{\Delta x}\left[\mathbf{F}_{i-\frac{1}{2}} - \mathbf{F}_{i+\frac{1}{2}}\right] \tag{4.113}$$

This equation indicates that the solution of $\mathbf{Q}_i^{n+1}$ is determined by the conserved variables $\mathbf{Q}_i^n$ and the net flux through a cell I_i where $\mathbf{F}_{i-\frac{1}{2}}$ represents the conserved fluxes entering the cell through cell interface $i-\frac{1}{2}$ and $\mathbf{F}_{i+\frac{1}{2}}$ represents the conserved fluxes leaving the cell through cell interface $i+\frac{1}{2}$ as depicted in Fig. 4.14. Therefore, it is important to mention the procedure for determining the numerical conserved fluxes at the cell interface boundaries. This procedure is discussed in the next section.

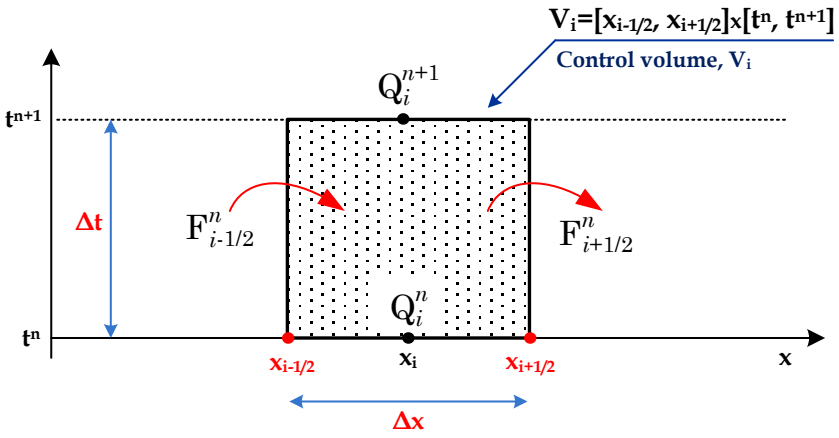

Figure 4.14. *The evolution of the solution of the conserved variables for the cell I_i from the time level n to the time level $n+1$ using the Godunov numerical scheme.*

4.3.4 Determination of the numerical fluxes at the cell interface boundaries: the local Riemann problem

In the context of the Godunov numerical scheme, the numerical fluxes of conserved variables at the cell interface boundaries are determined by the exact Riemann solver. According to Eq. (4.20), the fluxes of conserved variables at the cell interface boundaries for the one-dimensional time-dependent Euler equations are represented by the following column vector:

$$\mathbf{F}_{i\pm\frac{1}{2}} = [\rho u, \rho u^2 + p, (E+p)u]^T_{i\pm\frac{1}{2}} \tag{4.114}$$

In this case, the solutions for the primitive variables (ρ, u and p) at each cell interface are evaluated by solving the local Riemann problem at the interfaces boundaries.

The information to solve the local Riemann problem is provided by the data of each pair of cells within the computational domain. Thus, the local Riemann problem at the cell interfaces $i-\frac{1}{2}$ and $i+\frac{1}{2}$ for a given time level n, as depicted in Fig. 4.15, is denoted by $\mathbf{RP}(\mathbf{Q}_{i-1}, \mathbf{Q}_i)$ and $\mathbf{RP}(\mathbf{Q}_i, \mathbf{Q}_{i+1})$ respectively. The solution of the Riemann problem $\mathbf{RP}(\mathbf{Q}_{i-1}, \mathbf{Q}_i)$ is the solution of

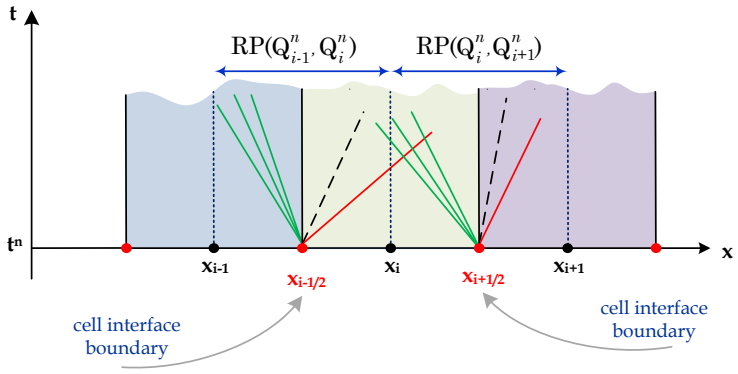

Figure 4.15. *The local Riemann problem at the cell interfaces* $i - \frac{1}{2}$ *and* $i + \frac{1}{2}$ *in* $x - t$ *plane.*

the following initial value problem:

$$\text{PDEs:} \qquad \frac{\partial}{\partial t}\mathbf{Q} + \frac{\partial}{\partial x}\mathbf{F}(\mathbf{Q}) = 0 \tag{4.115}$$

with the following initial conditions in terms of the primitive variables:

$$\text{ICs:} \qquad \mathbf{W}(x, t^n) = \mathbf{W}_i^n = \begin{cases} \mathbf{W}_{i-1}, & x < 0 \\ \mathbf{W}_i, & x > 0 \end{cases}$$

In this equation, variable x represents the axial position in the local Riemann problem coordinate system. This means that the axial position of the cell interface $x_{i-\frac{1}{2}}$ from the initial physical domain is transformed into $x = 0$ in the local Riemann problem coordinate system.

For the Godunov scheme, the sampling procedure is performed at the cell interface only for the special value of $s'(x'/t) = 0$. Refer to the previous section about the algorithm for the exact Riemann solver, if $s'(x'/t) < u_*$ the sample point was located left of the contact wave. For the Godunov scheme, this condition is analogous to $u_* > 0$ for which the cell interface boundary is now regarded as the sample point. Similarly, $u_* > 0$ indicates that the sample point is located right of the contact wave. For $\mathbf{RP}(\mathbf{Q}_{i-1}, \mathbf{Q}_i)$, u_* is the particle velocity in the star region which is obtained after calculating the star region pressure (p_*) around the cell interface boundary $i - \frac{1}{2}$ using the Newton-Raphson iteration method considering two initial constant data states $\mathbf{W}_{i-1}$ and $\mathbf{W}_i$. With respect to this condition, there are five different cases to evaluate the solution of $\mathbf{W}_{i\pm\frac{1}{2}}$ as shown in Fig. 4.16.

In order to solve the exact Riemann problem for the whole computational domain, the following considerations need to be taken into account:

- The computational time step Δt is determined according to Eq. (4.103). As mentioned previously, $s^n_{\max}$ is the maximum wave speed present throughout the computational domain at time level n. This means that no wave present in the solution of all local Riemann problems travels more than a distance Δx in time step Δt. This value is usually taken from the result of the local Riemann problem at the cell interface boundary. For the time-dependent

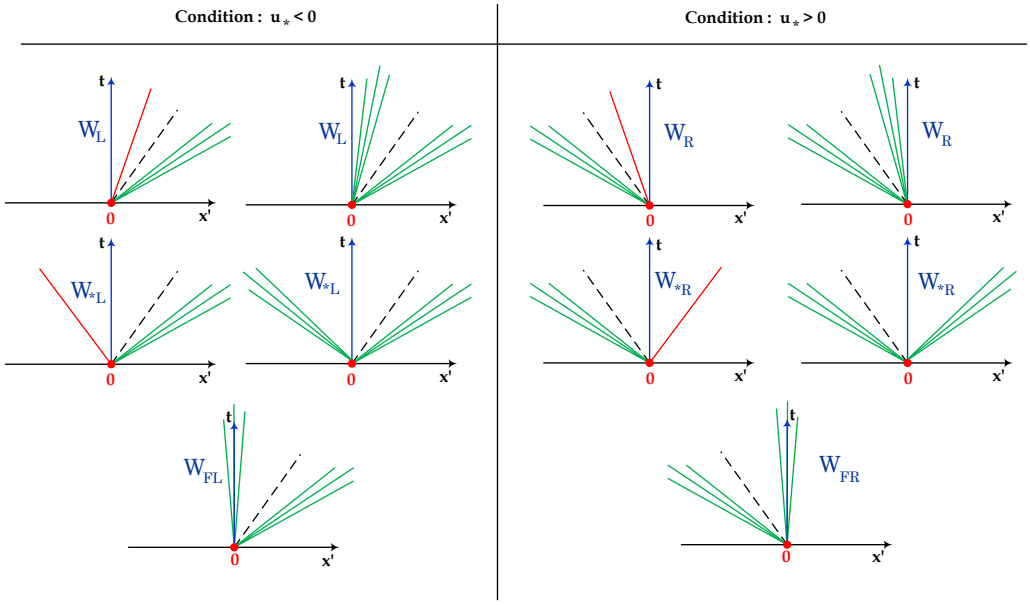

Figure 4.16. *Determination of the solution of the local Riemann problem in terms of primitive variables (**W**) at the cell interface boundary. The condition is parameterized by the particle velocity in the star region u_*. The result is required for evaluating the numerical fluxes for the Godunov scheme.*

Euler equations, a popular estimation of $s^n_{\max}$, which may be extended to multidimensional problems, is given by the following equation:

$$s^n_{\max} = \max_i \{|u^n_i| + a^n_i\} \tag{4.116}$$

where u^n_i and a^n_i are the normal velocity and the speed of sound at the cell I_i at time level n. In addition, the $\mathbf{C}_{\mathsf{cfl}}$ controls the stability and efficiency of the computation. In [101], $\mathbf{C}_{\mathsf{cfl}} = 0.9$ is practically recommended. A more conservative choice may be advisable, especially if there are uncertainties in the estimation of $s^n_{\max}$.

- Fig. 4.12 shows the discretization of the spatial domain $[0, L]$ into M uniform computational cells of length Δx. According to the Godunov scheme Eq. (4.113), numerical fluxes $\mathbf{F}_{\frac{1}{2}}$ and $\mathbf{F}_{M+\frac{1}{2}}$ are required. However, in order to obtain these numerical fluxes, the constant data states for cells I_0, denoted and I_{M+1} are additionally defined. Both cells are called **fictitious cells**. Therefore, numerical flux $\mathbf{F}_{\frac{1}{2}}$ is calculated after $\mathbf{W}_{\frac{1}{2}}$ is obtained as the solution of the local Riemann problem $\mathbf{RP}(\mathbf{Q}_0, \mathbf{Q}_1)$. Similarly, numerical flux $\mathbf{F}_{M+\frac{1}{2}}$ is calculated after $\mathbf{W}_{M+\frac{1}{2}}$ is obtained as the solution of the local Riemann problem $\mathbf{RP}(\mathbf{Q}_M, \mathbf{Q}_{M+1})$. The addition of fictitious cells into the physical domain $[0, L]$ is depicted in Fig. 4.17.

With respect to the boundary conditions, the attachment of fictitious cells to each boundary cell slightly increases the total number of the computational cells but, as a compensation, all the cell interface boundary are now internal and can be treated uniformly to simplify the computation.

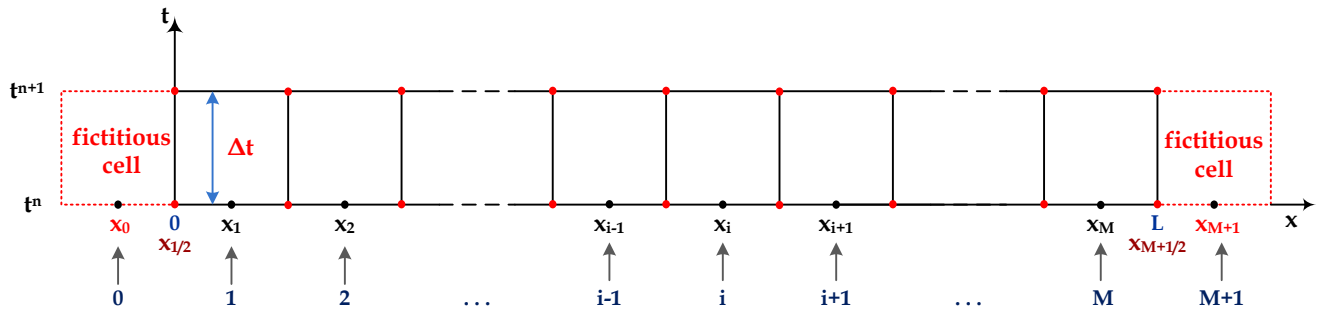

Figure 4.17. *Fictitious cells outside the computational domain for the one-dimensional case.*

The data for the fictitious cell can be defined independently adapted to the boundary condition of the problem without changing the state of other given variables.

When the boundary physically consists of a fixed, reflective impermeable wall, the physical situation for each computational time step is correctly modeled by the state of the fictitious cells $\mathbf{Q}_{\mathsf{FC}}$ which is defined from the known state of the boundary cell $\mathbf{Q}_{\mathsf{BC}}$ such that:

$$\begin{bmatrix} \rho \\ \rho u \\ E \end{bmatrix}_{i=\mathsf{FC}} = \begin{bmatrix} \rho \\ -\rho u \\ E \end{bmatrix}_{i=\mathsf{BC}}, \qquad \text{where } \mathsf{BC} = \{1, M\},\ \mathsf{FC} = \{0, M+1\} \tag{4.117}$$

Meanwhile, transmissive, or transparent boundaries attempt to numerically reproduce boundaries that allow the physical passage of waves without any effect of them. Thus, the state of the fictitious cell $\mathbf{Q}_{\mathsf{FC}}$ is defined as follows:

$$\begin{bmatrix} \rho \\ \rho u \\ E \end{bmatrix}^n_{i=\mathsf{FC}} = \begin{bmatrix} \rho \\ \rho u \\ E \end{bmatrix}^n_{i=\mathsf{BC}}, \qquad \text{where } \mathsf{BC} = \{1, M\},\ \mathsf{FC} = \{0, M+1\} \tag{4.118}$$

The transmissive boundary is also known as open-end boundary condition or non-reflecting boundary condition.

4.3.5 Numerical solutions of the non-homogeneous equations: the integration of the source terms

So far, the homogeneous Euler equations of gas dynamics have been solved numerically. The numerical scheme for such equations has been developed using the Godunov scheme for which the exact Riemann solver is implemented. As mentioned in Section 4.1, if the source term is taken into account, the Euler equations of gas dynamics is no longer homogeneous. The procedure for solving the inhomogeneous Euler equations are the main interest in the following discussion.

While considering the one-dimensional case, the inhomogeneous Euler equations of gas dynamics

is written in general as follows:

$$\frac{\partial}{\partial t}\mathbf{Q} + \frac{\partial}{\partial x}\mathbf{F}(\mathbf{Q}) = \mathbf{S}(\mathbf{Q}) \tag{4.119}$$

where $\mathbf{S}(\mathbf{Q})$ is the source or forcing term. The vector $\mathsf{S}(\mathbf{Q})$ can be split into two parts, namely geometrical source terms which arise in the case of non-Cartesian coordinates, and physical source terms, such as radiative heating, cooling and gravitation, etc. Usually, $\mathbf{S}(\mathbf{Q})$ is a prescribed algebraic function of the flow variables and does not involve derivatives of these, but there are some exceptions which are not discussed here.

Inhomogeneous Euler equations of gas dynamics arise naturally in many problems of practical interest. A whole class of inhomogeneous systems are derived when reducing the spatial dimensionality of multidimensional problems. For example, under the assumption of spherically or cylindrically symmetric flow, the two or three dimensional Euler equations become a one-dimensional system with the presence of geometrical source term.

In order to solve Eq. (4.119), the splitting method is used. It means that the homogeneous part of the equations and the source term integration are solved separately and one after another. Thus, Eq. (4.119) can be splitted in two equations as follows:

$$\frac{\partial}{\partial t}\mathbf{Q} + \frac{\partial}{\partial x}\mathbf{F}(\mathbf{Q}) = 0 \tag{4.120}$$

$$\frac{\partial}{\partial t}\mathbf{Q} - \mathsf{S}(\mathbf{Q}) = 0 \tag{4.121}$$

As mentioned previously, Eq. (4.120) is solved using the Godunov numerical scheme. Eq. (4.121) governs only the source term and is a system of ordinary differential equations. This equation can be solved using various numerical scheme. Considering the same control volume I_i and a time step $[t^n, t^{n+1}]$ from the previous numerical discretization of the Godunov scheme procedure, the integral form of Eq. (4.121) is written as follows:

$$\int_{x_{i-\frac{1}{2}}}^{x_{i+\frac{1}{2}}} \left[\mathbf{Q}(x, t^{n+1}) - \mathbf{Q}(x, t^n)\right]\, dx = \int_{x_{i-\frac{1}{2}}}^{x_{i+\frac{1}{2}}} \int_{t^n}^{t^{n+1}} \mathsf{S}(\mathbf{Q}(x,t))\, dx\, dt \tag{4.122}$$

Dividing all terms by Δx, the general form for solving the source term numerically is:

$$\frac{1}{\Delta x}\left[\int_{x_{i-\frac{1}{2}}}^{x_{i+\frac{1}{2}}} \mathbf{Q}(x, t^{n+1})\, dx - \int_{x_{i-\frac{1}{2}}}^{x_{i+\frac{1}{2}}} \mathbf{Q}(x, t^n)\, dx\right] = \frac{1}{\Delta x}\int_{x_{i-\frac{1}{2}}}^{x_{i+\frac{1}{2}}} \int_{t^n}^{t^{n+1}} \mathsf{S}(\mathbf{Q}(x,t))\, dt \tag{4.123}$$

Various numerical methods are possible for solving this equation depending on the way the integral is evaluated. In this thesis, the Backward Euler method which is first order accurate is used. Therefore, the complete numerical scheme for the one-dimensional heterogeneous Euler equations

is written as follows:

$$\mathbf{Q}_i^{n+1} = \mathbf{Q}_i^n + \Delta t \cdot \mathsf{S}(\mathbf{Q}_i^{n+1}) \tag{4.124}$$

where

$$\mathsf{S}_i^{n+1} \approx \frac{1}{\Delta x}\frac{1}{\Delta t}\int\limits_{x_{i-\frac{1}{2}}}^{x_{i+\frac{1}{2}}}\int\limits_{t^n}^{t^{n+1}} \mathsf{S}(\mathbf{Q}(x,t))\; dt \tag{4.125}$$

4.3.6 The procedure for solving the multi-dimensional time-dependent Euler equations of gas dynamics

For solving the multidimensional problem of Euler equations of gas dynamics, the unsplit finite volume Godunov scheme has been implemented in this thesis. It is important to mention that the local Riemann problem at each computational cell interface is solved using the exact Riemann solver which may be treated as a split Riemann problem for each direction. The main advantage of using the unsplit Godunov scheme is that the solution can be obtained in a single computational time step because all flux contributions are simultaneously taken into account at the same time.

In the following, the procedure for the two-dimensional problem in Cartesian coordinates system is presented. This procedure can be extended to the three dimensional case without changing their fundamental steps. As mentioned earlier in this chapter, the homogeneous time-dependent two-dimensional Euler equations is written in general as follows:

$$\frac{d}{dt}\mathbf{Q} + \frac{d}{dx}\mathbf{F}(\mathbf{Q}) + \frac{d}{dy}\mathbf{G}(\mathbf{Q}) = 0 \tag{4.126}$$

In order to solve this equation, it is assumed that the boundaries of the computational domain are aligned with the coordinate directions x and y. In this thesis, the two dimensional problem is solved using the structured mesh for which the computational cell $I_{i,j}$ has a dimension of $\Delta x \times \Delta y$ as depicted in Fig. 4.18. Indexes i and j represents the computational cell index in x- and y-direction within the computational domain. The cell-averaged conserved variables ($\mathbf{Q}_{i,j}$) is assigned to the center of the cell. At each cell interface, the numerical conserved fluxes are to be determined by solving the local Riemann problem.

Furthermore, the cell-averaged conserved variables ($\mathbf{Q}_{i,j}$) in cell $I_{i,j}$ at time level n is updated to time level $n+1$ by a single step implementing the Godunov scheme as given by the following equation:

$$\mathbf{Q}_{i,j}^{n+1} = \mathbf{Q}_{i,j}^n + \frac{\Delta t}{\Delta x}\left[\mathbf{F}_{i-\frac{1}{2},j} - \mathbf{F}_{i+\frac{1}{2},j}\right] + \frac{\Delta t}{\Delta x}\left[\mathbf{G}_{i,j-\frac{1}{2}} - \mathbf{G}_{i,j+\frac{1}{2}}\right] \tag{4.127}$$

where the computational time step (Δt) is computed using Eq. 4.103 for which the CFL condition and the maximum wave speed at the whole cell interfaces are taken into account. As mentioned

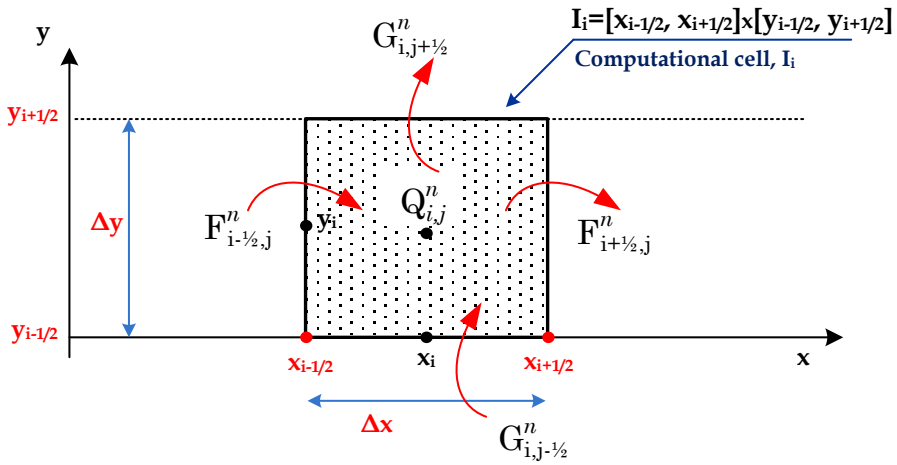

Figure 4.18. *Finite volume discretization of Cartesian domain (two dimensional case). A computational cell $I_{i,j}$ has four interfaces with the corresponding neighboring cells at which the numerical fluxes are to be determined by solving the local Riemann solver.*

before, the maximum wave speed is computed from the result of the local Riemann problem at the cell interface boundary. It is the normal velocity to be taken into account. Thus,

$$s^n_{\max} = \max_k \left\{ |u^n_{n,k}| + a^n_k \right\} \tag{4.128}$$

where k represents the index of the cell interface boundary.

With respect to the boundary conditions and the state of fictitious cells, it is important to mention that, for a two dimensional case especially in Cartesian domain, there will be four boundary conditions to be treated in order to update the state of the gas in the fictitious cells. In this thesis, these boundaries are labeled by the north (BCN), east (BCE), south (BCS) and west (BCW) boundary. There will be no special treatment for updating the state of the fictitious cell while dealing with the transmissive boundary because the state of fictitious cells simply equal to the state of the corresponding boundary. However, for the reflective boundary, it is important to check the direction of the normal particle velocity, since the state component involving the normal velocity should be corrected with the corresponding boundary condition. Finally, the general flow chart for numerical computation of the Euler equations of gas dynamics using the Godunov scheme is shown in Fig. 4.19.

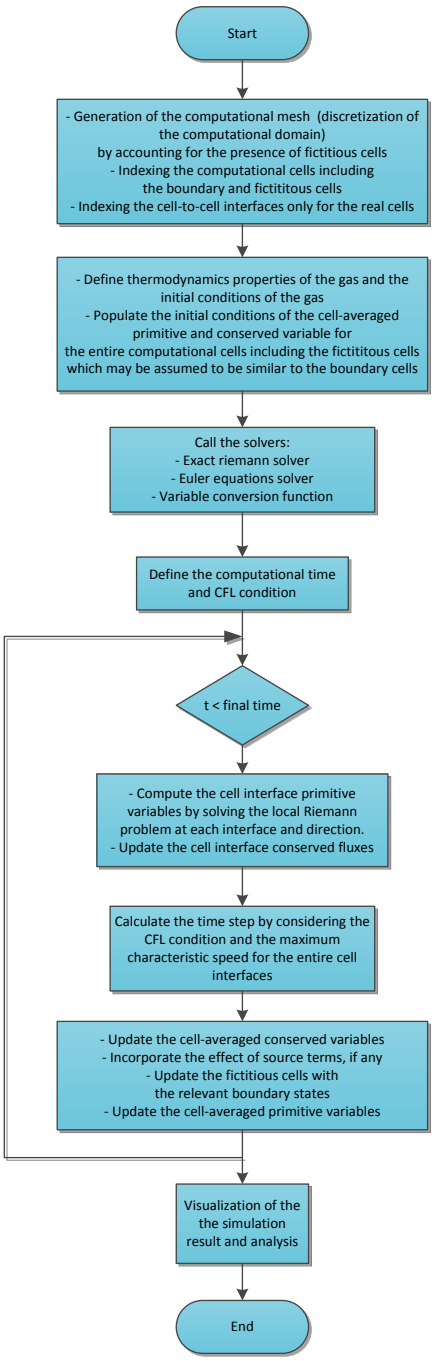

Figure 4.19. *General flow chart for the numerical simulation of the Euler equations of gas dynamics which is used in this thesis. The evolution of the states is solved using the upwind Godunov scheme which implements the exact Riemann solver to determine the solution of the local Riemann problem at the cell interface. The individual processes in the flow chart are not shown in detail.*

4.4 Implementation of the solver for simulating the blast wave propagation

4.4.1 One-dimensional case in Cartesian coordinates system: The shock tube problem

4.4.1.1 Sod's shock tube problem

In this section, the numerical solutions of several shock tube problems using the Godunov scheme solver are demonstrated. With respect to Sod's shock tube problem, their numerical solutions are to be compared with the benchmark solutions as presented previously in section 4.2.6. The benchmark of Sod's shock tube problem consists of a left rarefaction wave, contact wave and right shock wave. The spatial domain of the problem remains unchanged. And, similar to the previous case, it is assumed that the tube is filled with air which is treated as an ideal gas with a constant ratio of specific heat. The other input parameters and conditions are also unchanged including that tube length is 20 m and the initial discontinuity is located at $x = 10$ m. Thus, the initial conditions of the problem is also similar to Eq. (4.99).

The numerical simulation for this particular problem has been performed using a structured (uniform) mesh with 400 computational cells. Both boundary conditions of the tube were assumed to be transmissive boundaries, which means no reflection at the spatial boundary is considered. As recommended previously, the CFL coefficient of 0.9 was taken into account. The numerical solutions at a time $t = 0.015$ s after the break of the diaphragm were evaluated. These solutions were presented in Figs. 4.20. In this figure, both the exact and numerical solutions of all primitive variables for Sod's shock tube problem are shown. In addition, the temperature development along the tube up to the time under consideration is also shown. This figure has shown that the numerical solutions implementing the Godunov scheme with the exact Riemann solver agree with their respective exact solutions. It can also be seen that the numerical solutions has smeared somehow at the shock and contact discontinuity point, as well as at the head and tail of the rarefaction wave. Such spreading of shock waves may seem unsatisfactory, but it is actually quite typical for numerical solutions using the first order scheme. In fact, as mentioned in some literatures, implementing other types of first order upwind method would spread a shock wave even more than the Godunov scheme [101]. Therefore, the Godunov scheme has been chosen in this thesis for solving the Euler equations of gas dynamics numerically.

4.4.1.2 Testing some other recommended wave propagation problem in tube

As suggested in [101], four other examples of tube problems may also be used for testing the performance of the numerical computer code which has been developed. These four problems are different to Sod's shock tube problem which can be seen from their respective initial conditions. In fact, the aim of these tests is to further check the ability of the developed computer code to solve problem with different wave characteristics. Similar to Sod's shock tube problem, numerical solutions of these additional problems are also to be compared with their known benchmark (exact)

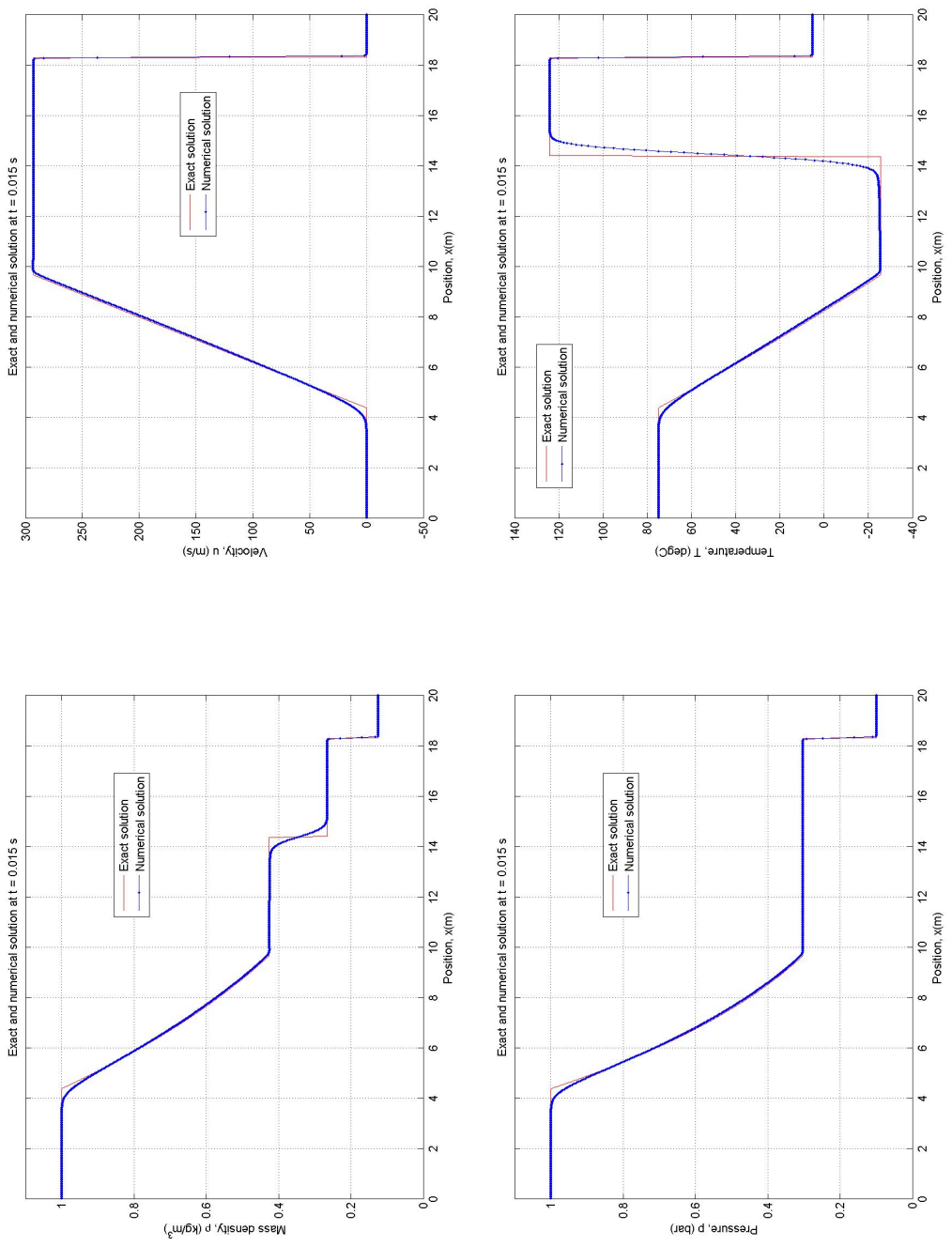

Figure 4.20. *Exact and numerical solutions of Sod's shock tube problem at at time $t = 0.015$ seconds after the break of the diaphragm. The numerical solutions are obtained using the Godunov scheme.*

solutions.

Table 4.2 shows initial conditions of these four additional tube problems [101]. For all cases, both the left and right spatial boundary of the tube are assumed to be transmissive boundary, thus no reflection wave is to be simulated.

Table 4.2. *Initial conditions of additional tube problems for testing the performance of the numerical Godunov solver. All primitive variables given in terms of its non-dimensional quantities [101]*

Case	Left to the diaphragm			Right to the diaphragm			Computational time
	ρ_{L}	u_{L}	p_{L}	ρ_{R}	u_{R}	p_{R}	(units)
T1	1.0	-2.0	0.4	1.0	2.0	0.4	0.15
T2	1.0	0.0	1000.0	1.0	0.0	0.01	0.012
T3	1.0	0.0	0.01	1.0	0.0	100.0	0.035
T4	5.99924	19.5975	460.894	5.99242	-6.19633	46.0950	0.035

In order to perform the numerical simulation of these problems, the spatial domain has been divided into 300 uniform computational cells. It is assumed that $x = [0.0, 1.0]$ for which the initial discontinuity is positioned at the middle of the tube, i.e. at $x = 0.5$. The gas filling the tube is air to be treated as an ideal gas with a constant ratio of specific heats (a polytropic gas with a constant γ). In this case, a polytropic index $\gamma = 1.40$ has been assumed for all cases.

The numerical simulation results for all cases are shown in Figs. 4.21 to 4.24. The respective exact solutions of each problem are also shown in the same figure. In general, it can be seen once again that both numerical and exact solutions are in good agreement with their respective exact solutions. Table 4.3 gives a short summary of the numerical simulations. Important parameters for the star region once the diaphragm is broken as well as the characteristics of the wave solutions are given. Upon completing these simulations, it can be concluded that the Godunov scheme which is implemented with the exact Riemann solver is reliable enough for simulating the motions of the gas in different conditions. The implementation of the developed computer code based on this scheme has shown the ability of the scheme to accurately predict the location and physical parameters of each wave at different conditions. Actually, these are the features particularly important for modeling the blast wave propagation.

Table 4.3. *Short summary of numerical solutions of additional tube problems and their wave solution characteristics*

Case	Star region variables				Wave pattern
	p_*	u_*	$\rho_{*\mathsf{L}}$	$\rho_{*\mathsf{R}}$	characteristics
T1	0.00189	0.0000	0.02185	0.02185	Two strong expansion waves
T2	460.894	19.597	0.57506	5.99924	Left expansion, contact, right shock
T3	46.0950	-6.1870	5.92514	0.57562	Left shock, contact, right expansion
T4	1691.64	8.6898	14.2824	31.0426	Two shock waves

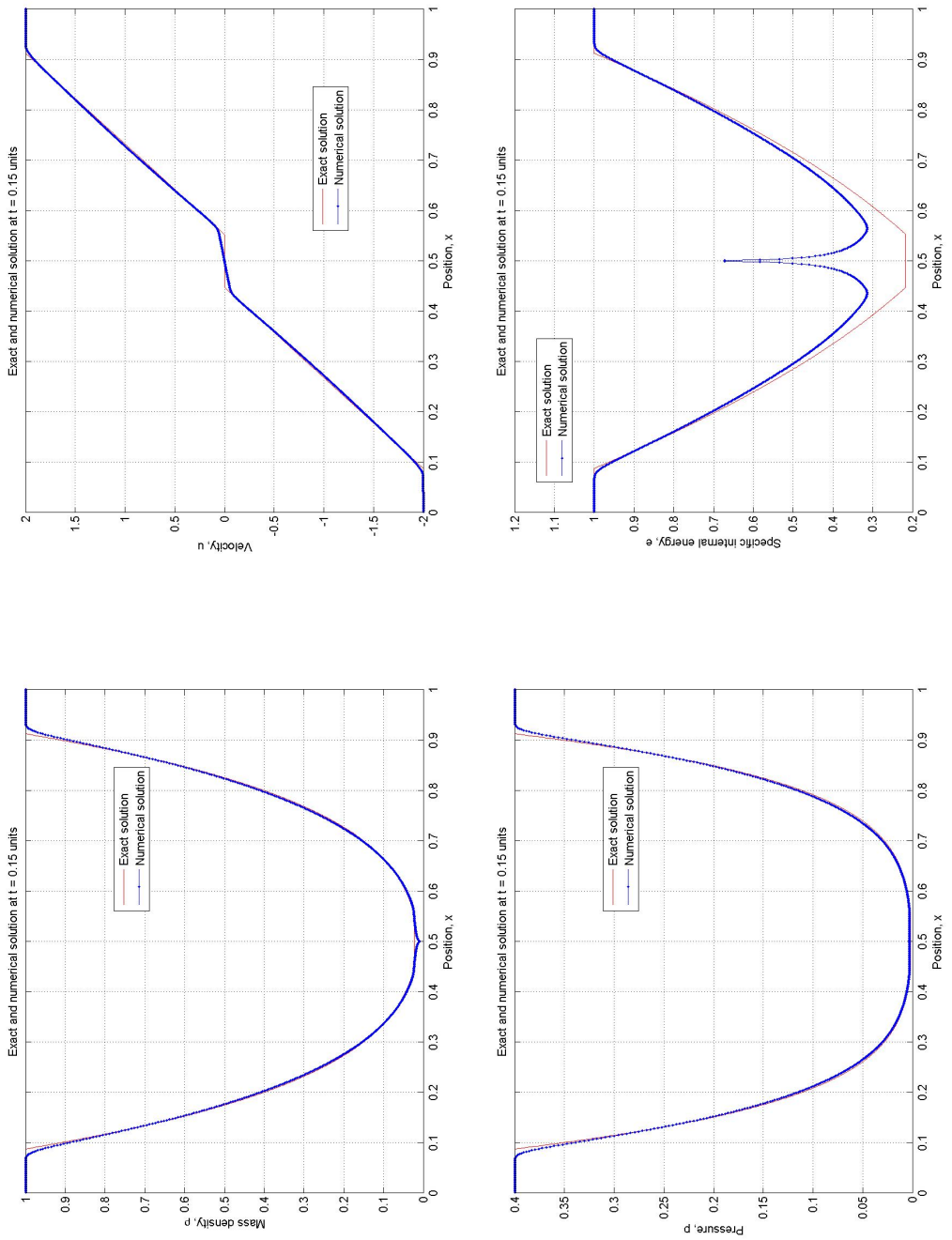

Figure 4.21. *Exact and numerical solutions of the tube problem case T1 at time $t = 0.15$ units. All variables are in their scaled (non-dimensional) form. This figure shows the profile of basic primitive variables including the specific internal energy.*

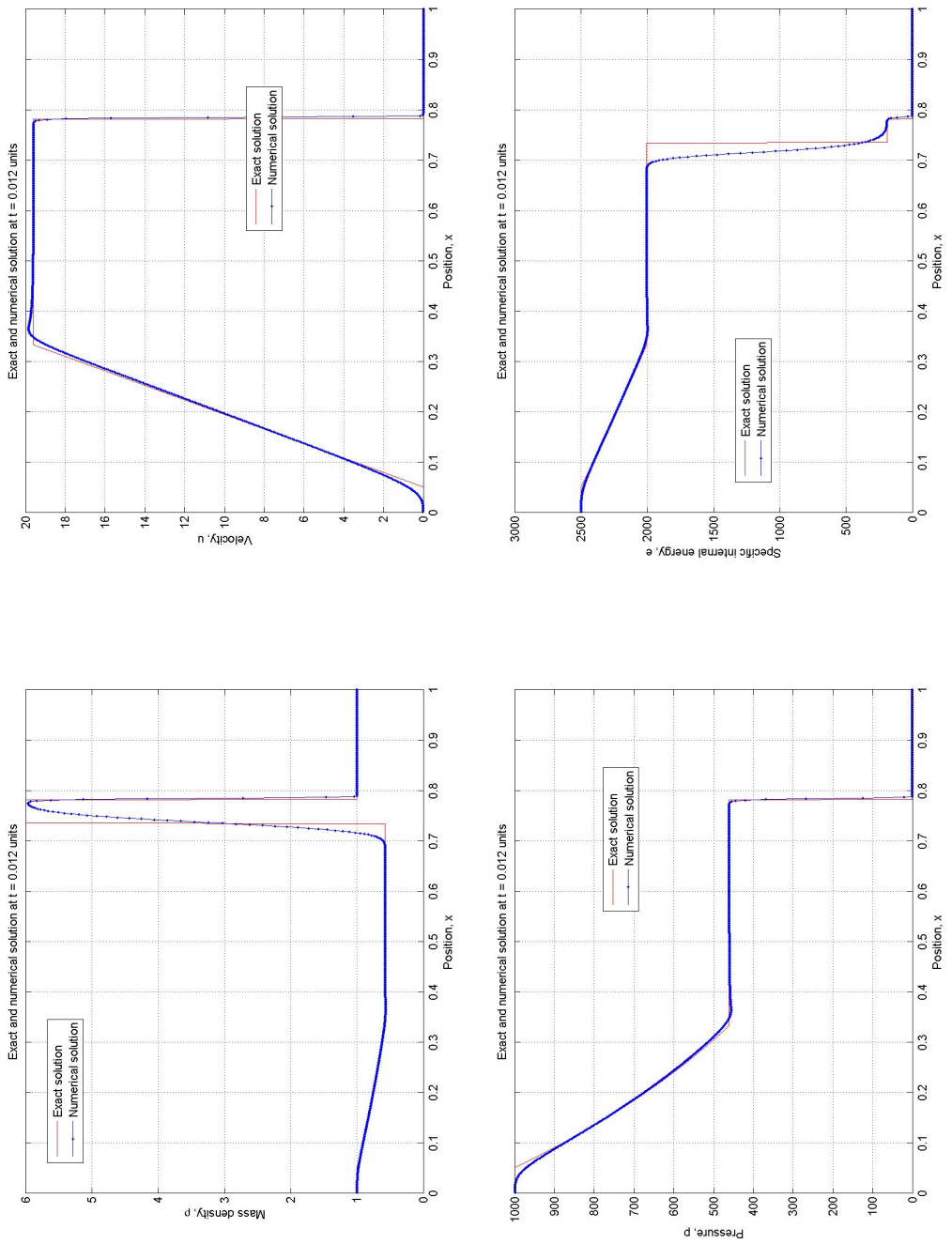

Figure 4.22. *Exact and numerical solutions of the tube problem case T2 at time $t = 0.012$ units. All variables are in their scaled (non-dimensional) form. This figure shows the profile of basic primitive variables including the specific internal energy.*

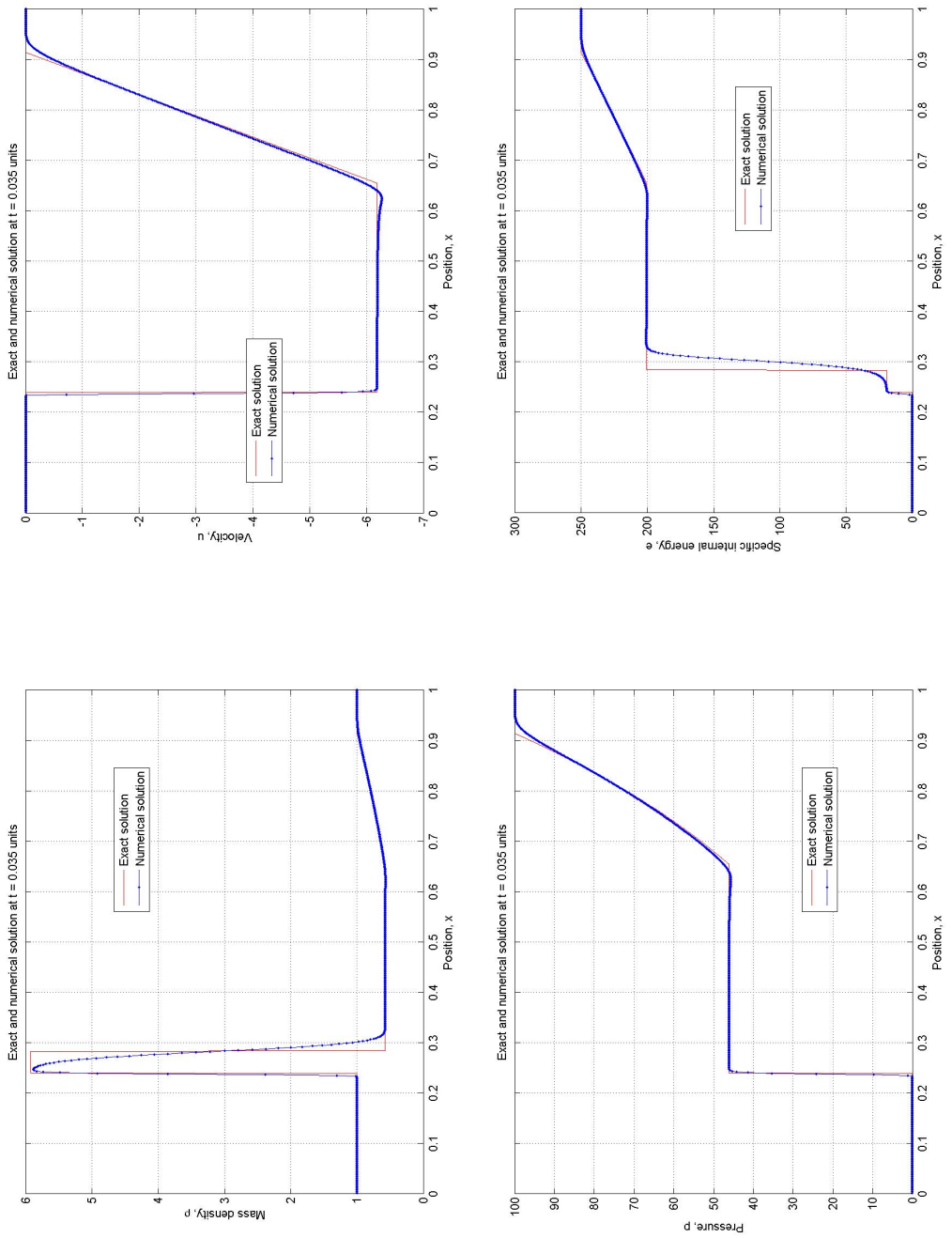

Figure 4.23. *Exact and numerical solutions of the tube problem case T3 at time $t = 0.035$ units. All variables are in their scaled (non-dimensional) form. This figure shows the profile of basic primitive variables including the specific internal energy.*

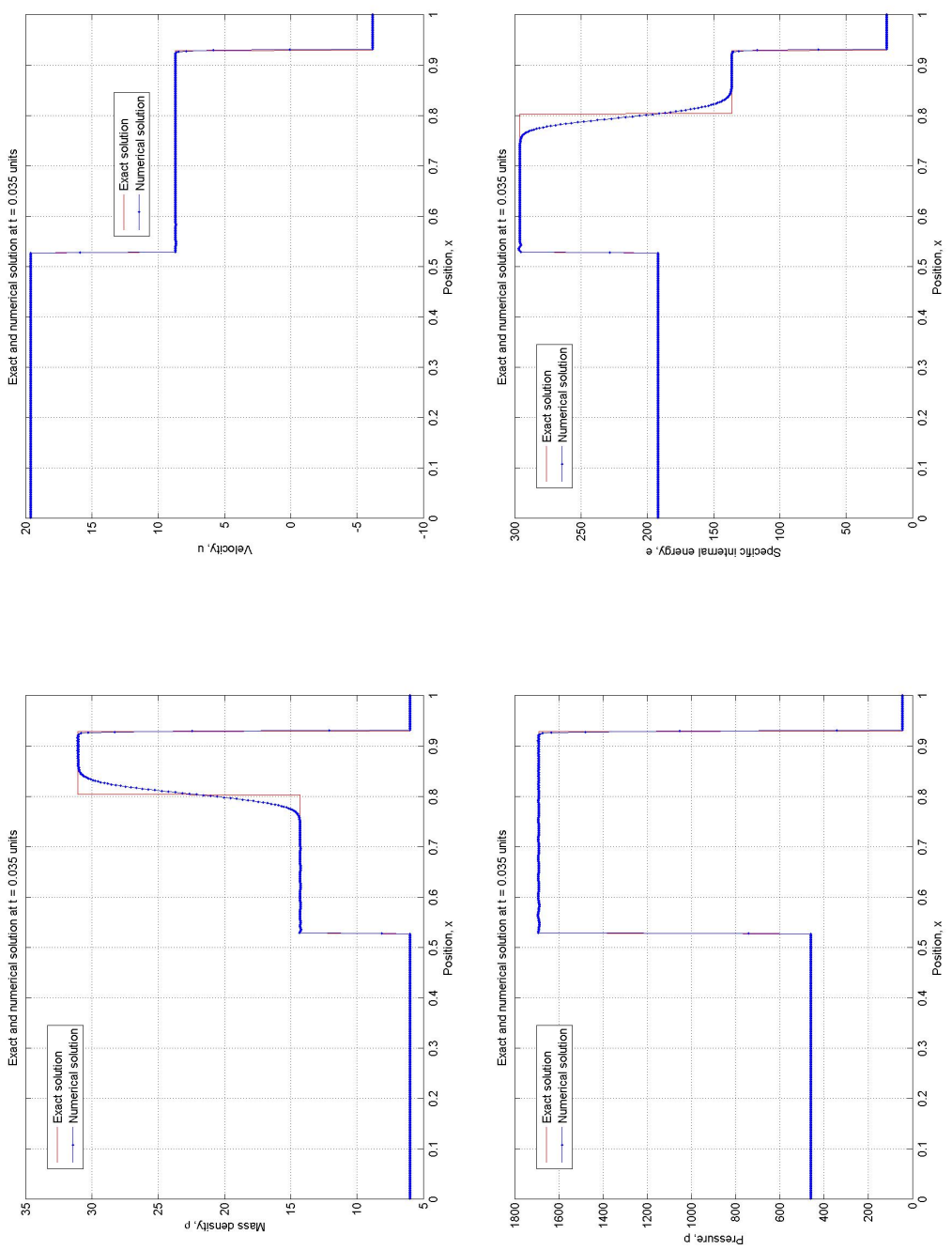

Figure 4.24. *Exact and numerical solutions of the tube problem case T4 at time $t = 0.035$ units. All variables are in their scaled (non-dimensional) form. This figure shows the profile of basic primitive variables including the specific internal energy.*

4.4.2 One-dimensional case in spherical coordinates system: The spherically symmetric wave motion

Spherically symmetric wave motion arises not only in the theory of explosion wave in air but also in water or other media. In these particular situations, a multidimensional Euler equation in spherical coordinates can be reduced essentially to a one dimensional Euler equations by considering the presence of a geometric source term (represented by vector $\mathbf{S}(\mathbf{Q})$). This source term is actually to account for the second and third spatial dimensions. Therefore, in general, a symmetric wave motion is governed by the following equations:

$$\frac{\partial}{\partial t}\mathbf{Q} + \frac{\partial}{\partial r}\mathbf{F}(\mathbf{Q}) = \mathbf{S}(\mathbf{Q}) \tag{4.129}$$

where:

$$\mathbf{Q} = \begin{bmatrix} \rho \\ \rho u \\ E \end{bmatrix}, \quad \mathbf{F}(\mathbf{Q}) = \begin{bmatrix} \rho u \\ \rho u^2 + p \\ (E+p)u \end{bmatrix}, \quad \mathbf{S}(\mathbf{Q}) = -\frac{\alpha}{r}\begin{bmatrix} \rho u \\ \rho u^2 \\ (E+p)u \end{bmatrix} \tag{4.130}$$

It is important to mention here that the column vector $\mathbf{S}(\mathbf{Q})$ represents only the geometric source term which means no physical source term is to be considered. α is the coefficient for updating the spatial dimension, in the sense that if the coefficient $\alpha = 0$, Eq. (4.129) describes a one-dimensional flow in plane geometry. Thus, it is similar to the governing equations of the wave motions in the tube, or one-dimensional in Cartesian coordinates system. Furthermore, if the coefficient $\alpha = 1$, Eq. (4.129) governs a cylindrically symmetric wave motion which is considered a two-dimensional symmetric flow. Meanwhile, if the coefficient $\alpha = 2$, Eq. (4.129) solves a spherically symmetric wave motion which is considered a three-dimensional symmetric flow.

Fig. 4.25 illustrates the initial configuration (condition) for a spherically symmetric blast wave motion. The domain of interest in $r - t$ plane is any set point of (r, t) where $0 \leq r \leq L$ and $t > 0$. In this case, a sphere with a radius of r_0 is considered as a blast source, which means that it is the driven section of the gas motion. Since the spatial boundary of this sphere at $r = r_0$ just a fictitious membrane separating two different gases with two different conditions (inside and outside the sphere), this sphere can also be considered as a fictitious balloon. Therefore, the fictitious membrane in this problem plays the same role of the diaphragm in the case of Sod's shock or other previous tube problems. As the source of the blast, the balloon has extreme initial conditions with respect to its surrounding gas. These conditions may be characterized in terms of high density, high pressure, or high temperature. It can also be assumed that the gas either inside or outside the balloon is initially at its rest or defined by a certain velocity to a particular direction with respect to r.

In what follows, the modeling of such spherical blast wave propagation implementing the Godunov numerical scheme previously presented is demonstrated. In this case, the fictitious sphere is filled with a high density air, and its surrounding (outside of the sphere) is considered a normal atmospheric air. Both gas systems are treated as ideal gases with a constant γ of $= 1.40$. The

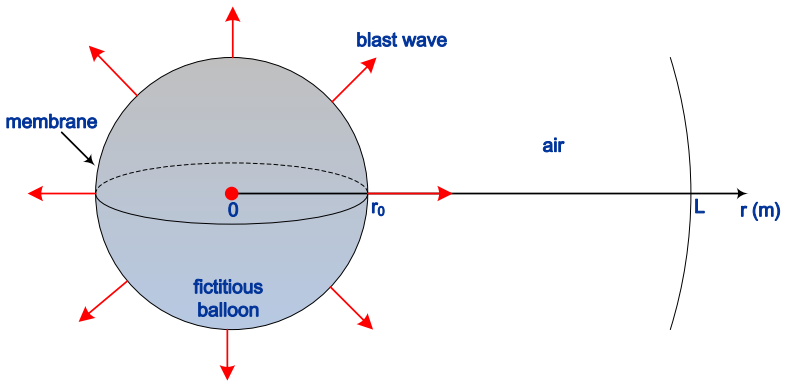

Figure 4.25. *Initial configuration for a spherically symmetric wave motion. The fictitious balloon with a radius of r_0 is considered as the source of blast (driven section).*

radius of the sphere is 1 m. The initial pressure of the gas inside the sphere is 10 bar (gauge, overpressure). The gas is initially at its rest everywhere ($u = 0$). Therefore, the initial conditions for this spherically symmetric blast wave propagation are given by the following equations,

$$\mathbf{Q}(r,0) = \mathbf{Q}^0(r) = [\rho, u, p]^T = \begin{cases} \left[1.86, 0.0, 1 \times 10^6\right]^T, & \text{for} \quad r < r_0 \\ \left[1.204, 0.0, 1.01325 \times 10^5\right]^T, & \text{for} \quad r > r_0 \end{cases} \tag{4.131}$$

In this case, ρ, u and p are given in kg/m^3, m/s and Pa respectively. Other necessary information related to the thermodynamics of air can be obtained from Table 4.1.

The numerical modeling was performed based on Eq. (4.129) with $\alpha = 2$. This simulation will evaluate basic variables including density, particle velocity, pressure and temperature of the gas at various distances relative to the center of the sphere at different times after the burst of the fictitious membrane. With respect to the initial conditions of Eq. (4.131), it is fully understood that the shock wave would travel outwards and a rarefaction wave would travel inwards the sphere.

The numerical simulation results for this particular problem are depicted in Fig. 4.26. It can be seen that there is reflection due to the rarefaction (expansion) wave which travels inside the sphere towards its centre. The magnitude of the shock wave which travel outwards decreases with respect to the distance relative to the center of the source. After 10 ms, the blast wave overpressure of about 0.175 bar is estimated at the distance of about 5 m from the blast source. A complete result of blast overpressure (bar) versus distance is shown in Fig. 4.27.

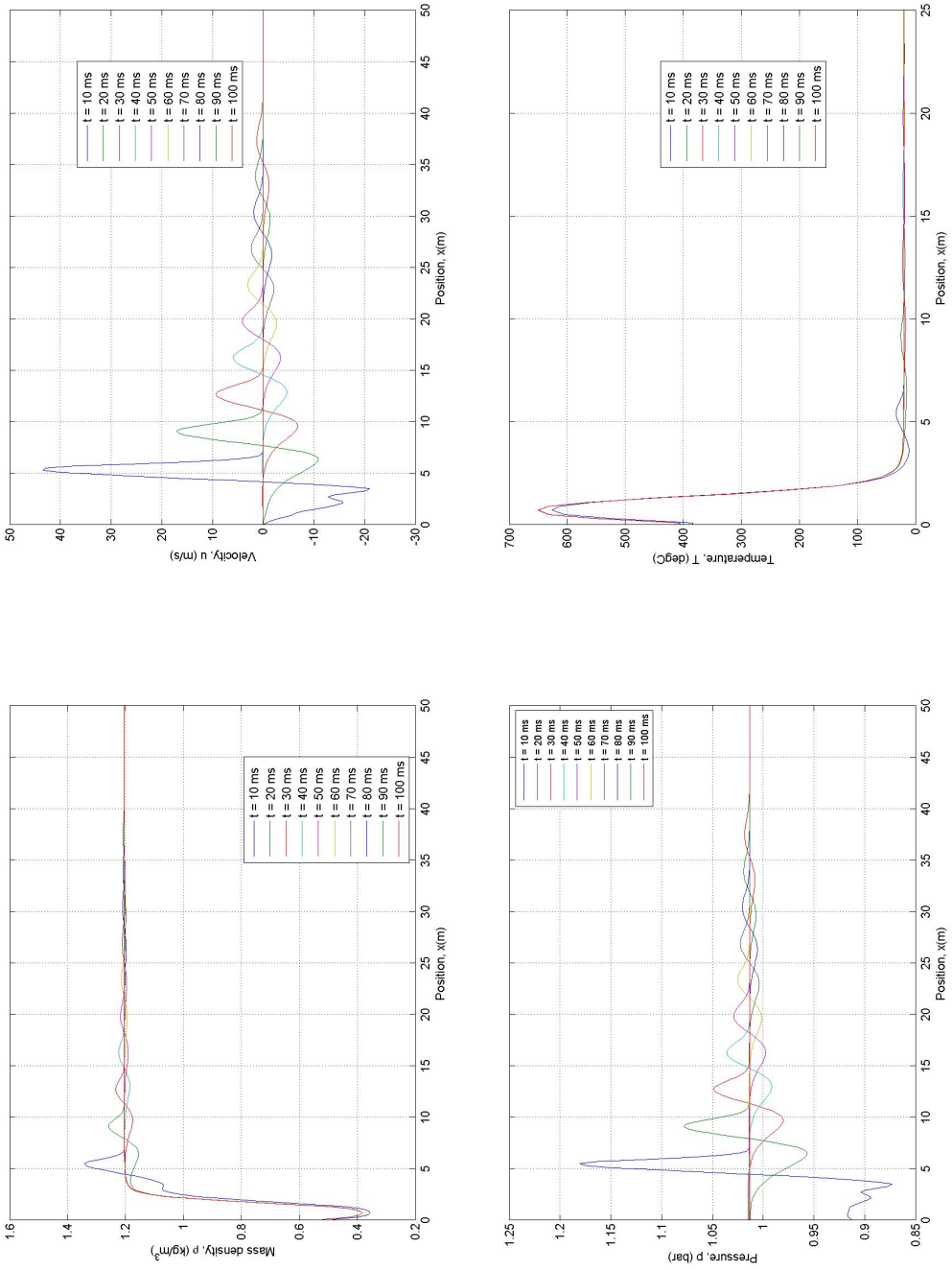

Figure 4.26. *Numerical simulation results for a spherically symmetric blast wave propagation.*

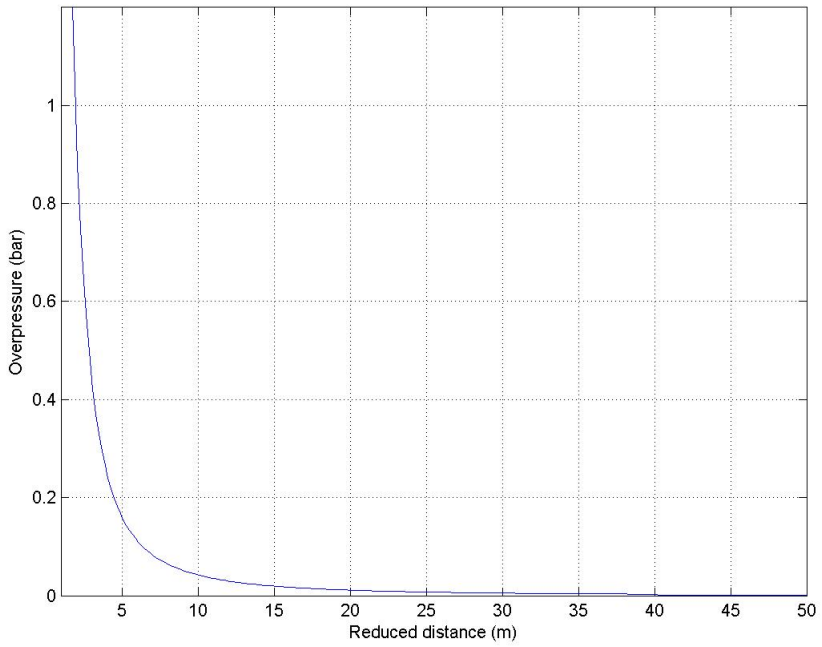

Figure 4.27. *Blast overpressures (bar) with respect to the distance relative to the outer boundary of the spherical source for the test problem under consideration*

4.4.3 Two-dimensional cases in Cartesian coordinates system

4.4.3.1 Test case I

In what follows, the treatment of the two dimensional Euler equations in a Cartesian coordinate system is demonstrated. In general, this problem is governed by Eq. (4.126). First, the following example is considered. In this case, the blast wave propagation in a square domain of $[0,1]\times[0,1]$ is simulated and evaluated. Initially, this spatial domain is virtually divided into four uniform regions. Each region is characterized by different properties of the gas. In this case, different conditions of gas are defined and they are treated as ideal gases with a constant γ of 1.40. Furthermore, the initial conditions of the problem under consideration describing the properties of the gas in each region and expressed in terms of their non-dimensional values are as follows:

$$(\rho,u,v,p)(x,y,0)=\begin{cases}(0.8,0.1,0.0,0.4), & \text{if } x<0.5 \text{ and } y<0.5\\ (0.5313,0.1,0.7276,0.4), & \text{if } x>0.5 \text{ and } y<0.5\\ (0.5313,0.8276,0.0,0.4), & \text{if } x<0.5 \text{ and } y>0.5\\ (1.0,0.1,0.0,1.0), & \text{if } x>0.5 \text{ and } y>0.5\end{cases} \tag{4.132}$$

Fig. 4.28 illustrates these conditions in $x-y$ plane. For this particular simulation, all spatial boundaries are assumed the transmissive.

In order to perform the simulation, a structured mesh of 40000 cells (200×200) computational

cells was generated. A CFL condition of 0.5 was chosen. Figs. 4.29-4.31 show the results of this simulation. In this case, the development of pressure and density at various computational times is shown. It can be seen that the shock wave moves from the top right of the domain to the top left as well as from the top right to the bottom right. Meanwhile, a contact discontinuity wave moves from the top left to the bottom left as well as from the bottom right to the bottom left. In general, these results are in good agreement with a similar test described in [115].

4.4.3.2 Test case II

In the second case, the blast wave propagation in a square domain in which the blast source is localized at a certain position within the domain is treated. It is assumed that the spatial domain under consideration is a square domain with dimension of 10×10 m. This domain is realized in the $x-y$ plane for which $x := [0, 10]$ m and $y := [0, 10]$ m. The source of the blast is identified as a circular region with initial radius of 1 m centered at $(x, y) = (1, 1)$. This source is a high pressure and high density gas separated from the outside surrounding gases by a fictitious membrane at the initial time of the simulation. The surrounding gas is assumed to be a normal atmospheric air.

Furthermore, the initial condition of this particular problem is given as follows:

$$(\rho, u, v, p)(x, y, 0) = \begin{cases} (1.68, 0, 0, 10 \times 10^5), & \text{for a circular source} \\ & \text{centered at } (x, y) = (1, 1) \\ (1.20, 0, 0, 1.01 \times 10^5), & \text{otherwise} \end{cases} \tag{4.133}$$

In this case, variables ρ, u, v and p are given in kg/m^3, m/s, m/s and Pa. These conditions are illustrated in Fig. 4.32.

It is assumed that both the gas localized inside the source and the surrounding gas are air to be treated as ideal gases with a constant γ of 1.40. In addition, no physical boundary within the domain under consideration is defined. This means that all four spatial boundaries are assumed to be transmissive. Further propagation of the blast wave outside the computational domain is not considered.

In order to perform the simulation, the spatial domain is discretized into 90000 uniform cells (300×300). To ensure the stability of the computation, a CFL condition of 0.5 has been chosen. The computation was run up to 12 ms. The results of this simulation are shown in Figs. 4.33 - 4.35. The pressure and temperature at any point within the domain for various computational times are shown. The shock wave moves outwards the source symmetrically for which the magnitude of blast overpressure decreases by time. It is shown that, at $t = 6$ ms, the shock wave has reached at a distance of about 6 m from the center of blast source with a temperature estimated in the range of of $250 - 300^0$C.

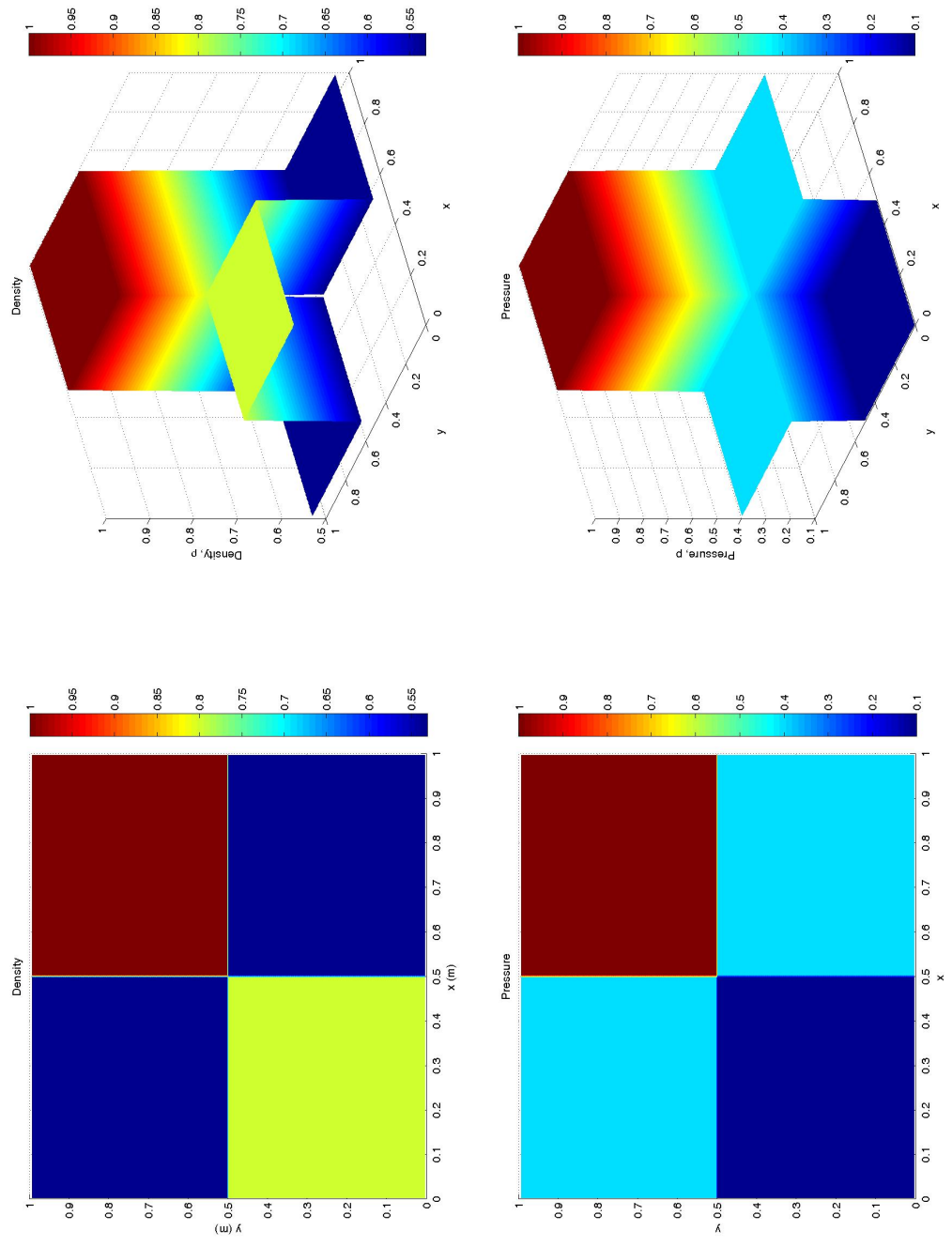

Figure 4.28. *Initial conditions for the two-dimensional case of Euler equations of gas dynamics according to Eq. (4.132).*

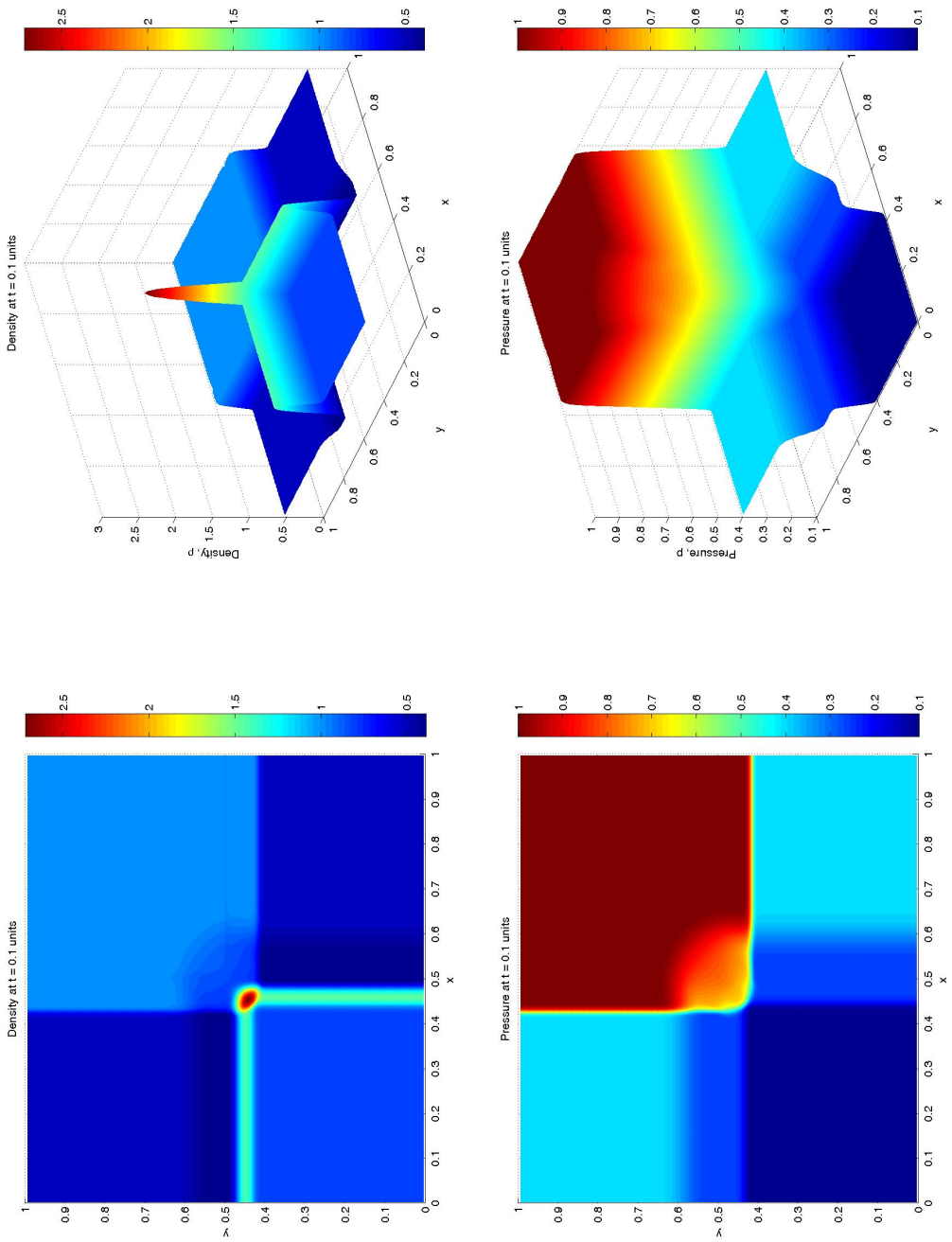

Figure 4.29. *Simulation results at $t = 0.1$ units.*

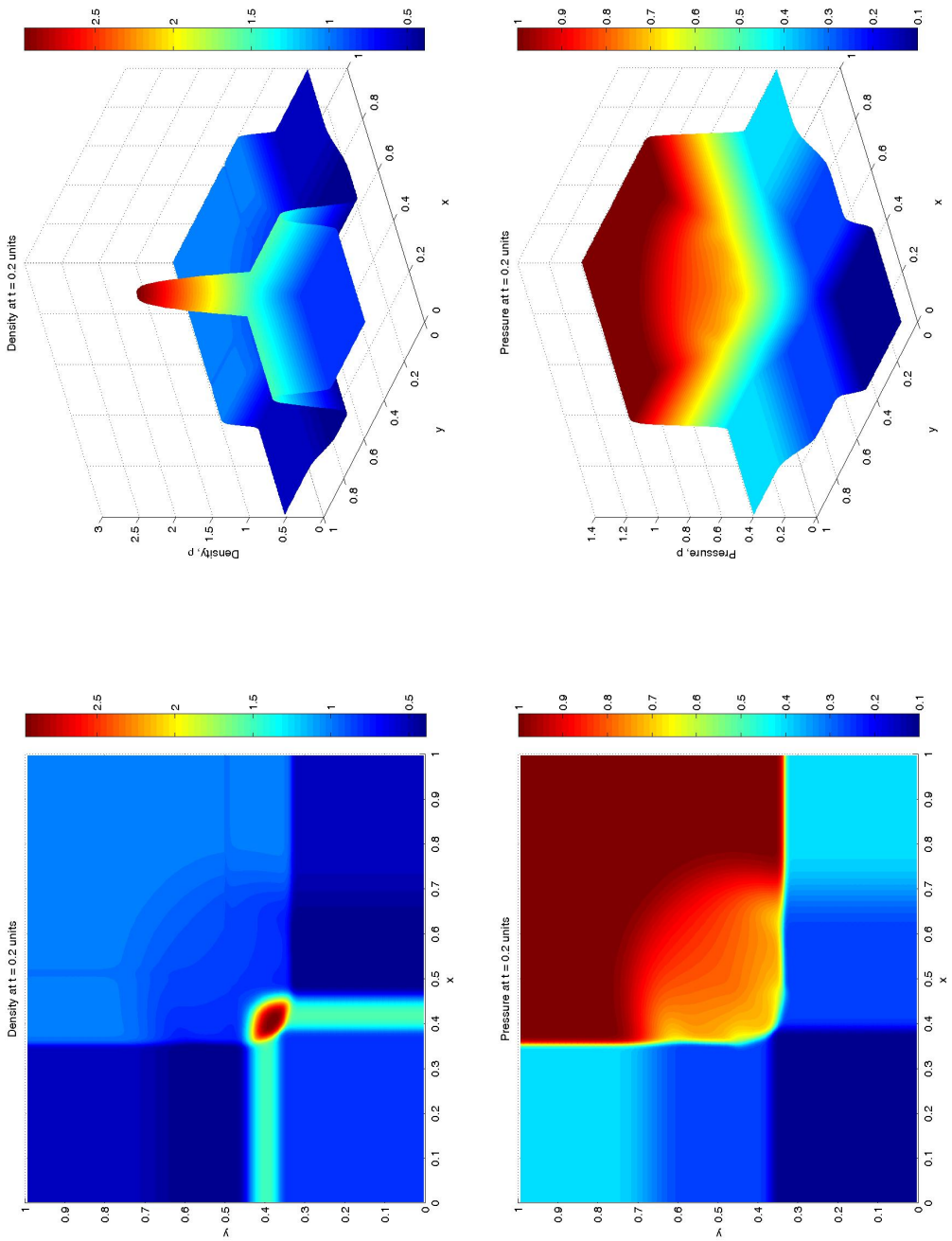

Figure 4.30. *Simulation results at $t = 0.2$ units.*

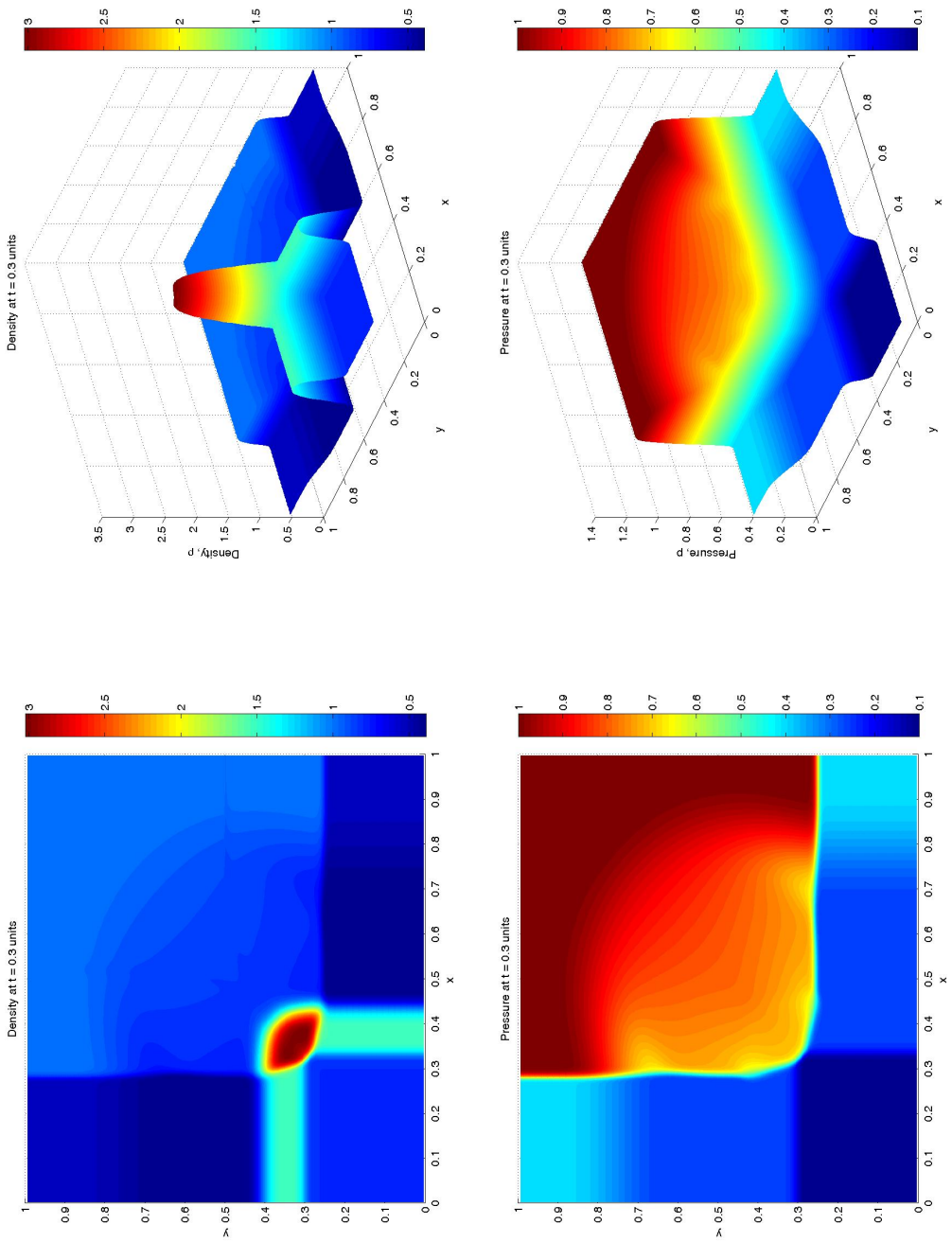

Figure 4.31. *Simulation results at $t = 0.3$ units.*

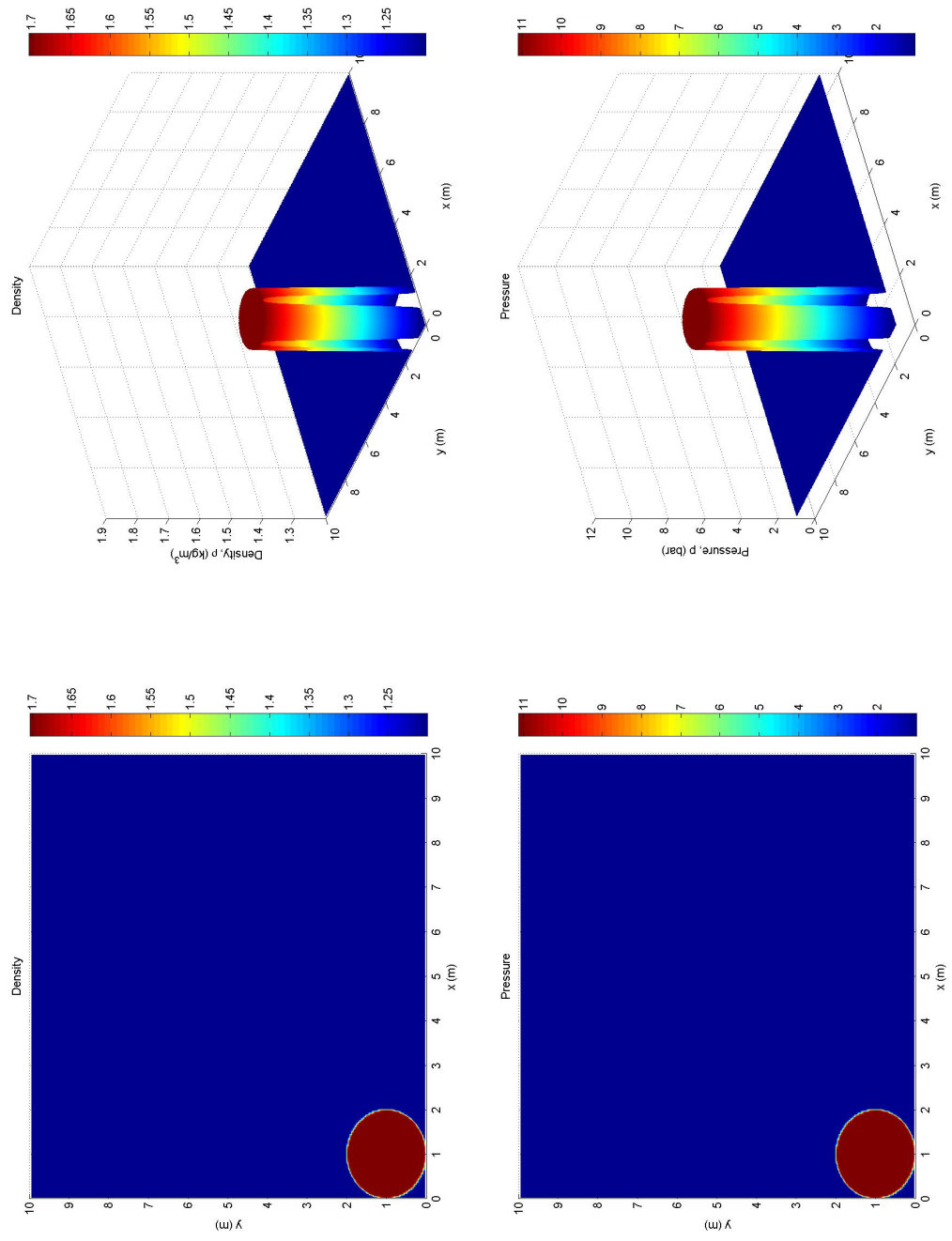

Figure 4.32. *Initial conditions for the second test case of the two-dimensional Euler equations according to Eq. (4.133). The blast source is regarded as a circle with an initial radius of 1 m centered at $(x, y) = (1, 1)$ of the local coordinate system*

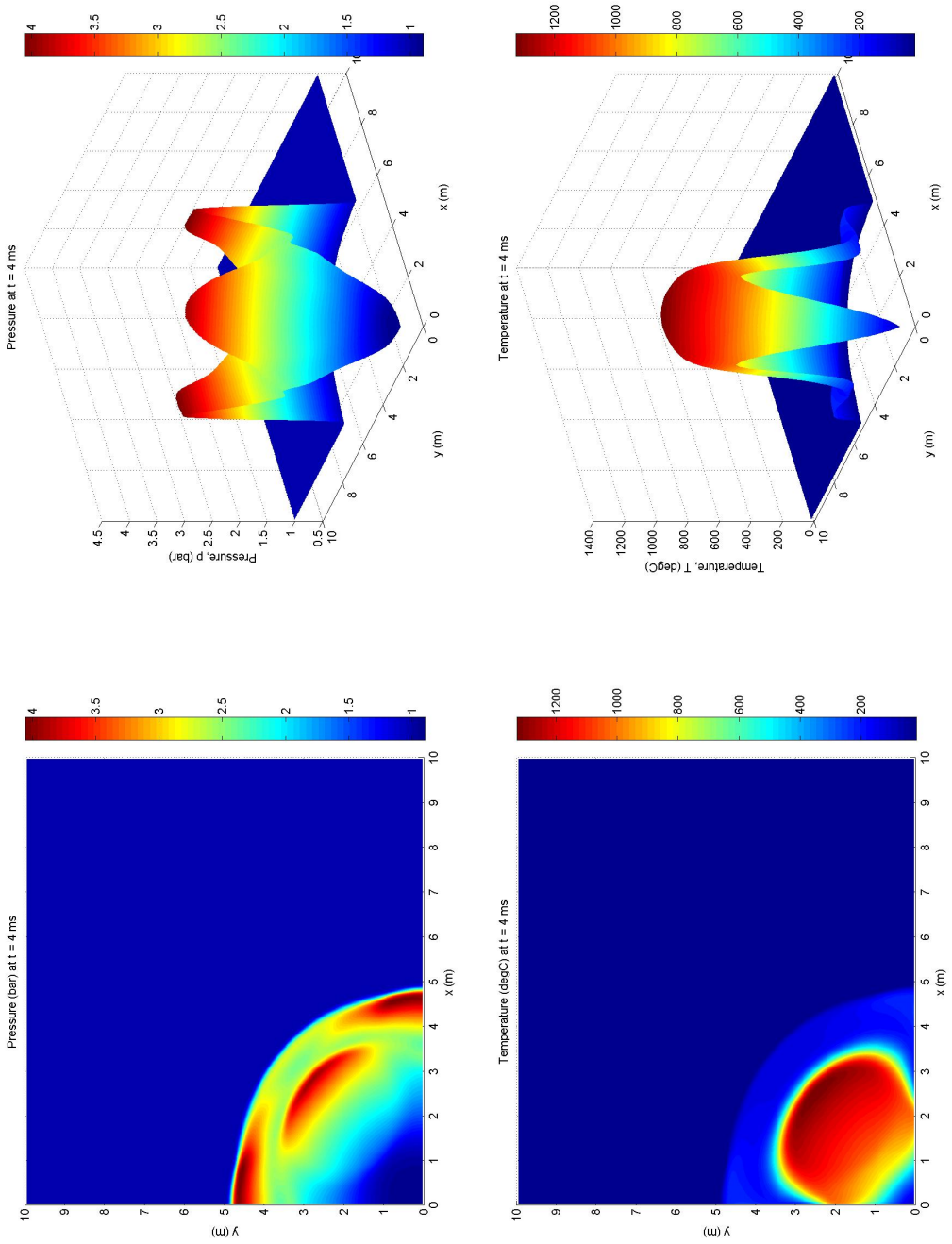

Figure 4.33. *Simulation results for the pressure and temperature at* $t = 0.004$ *s after the burst*

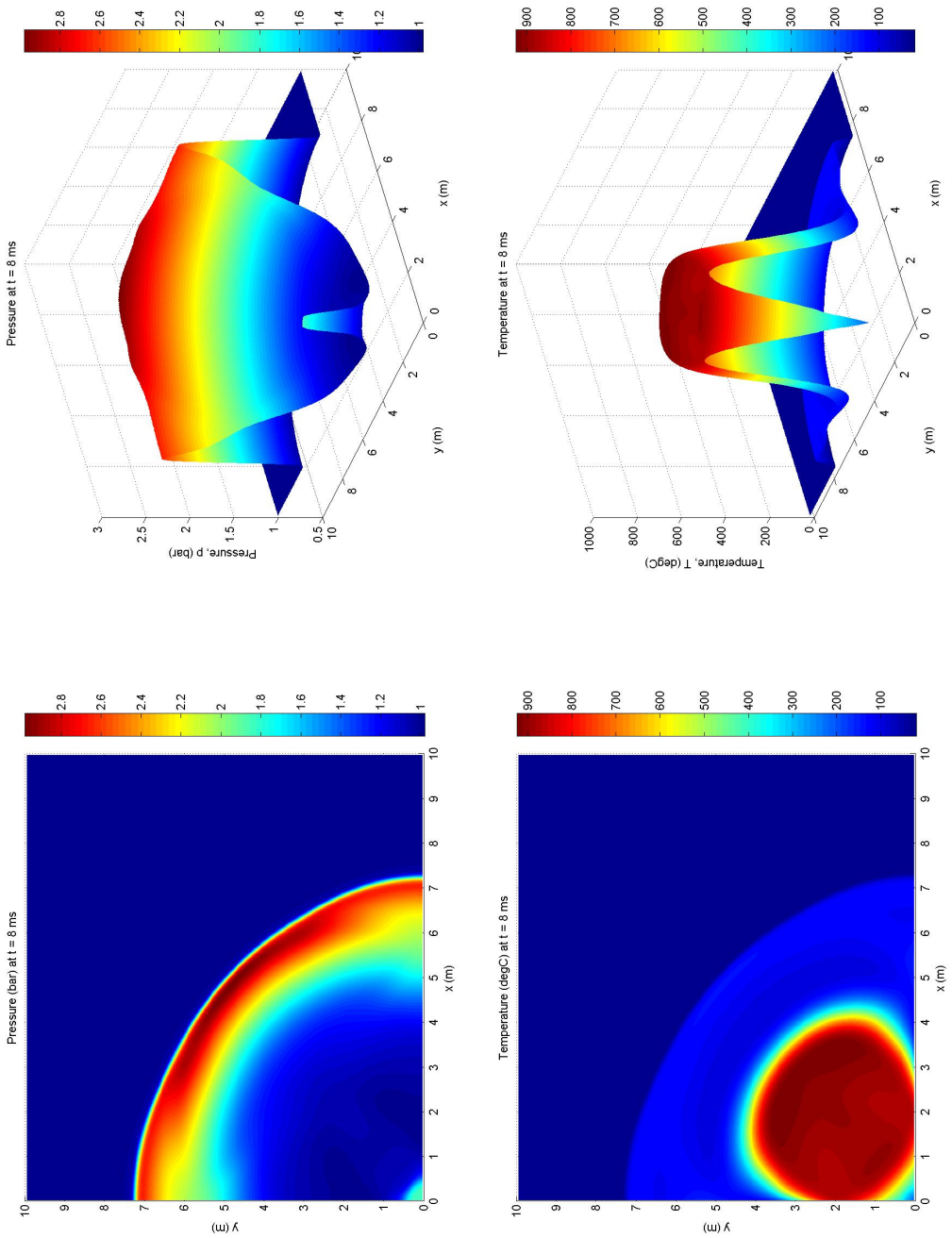

Figure 4.34. *Simulation results for the pressure and temperature at $t = 0.008$ s after the burst*

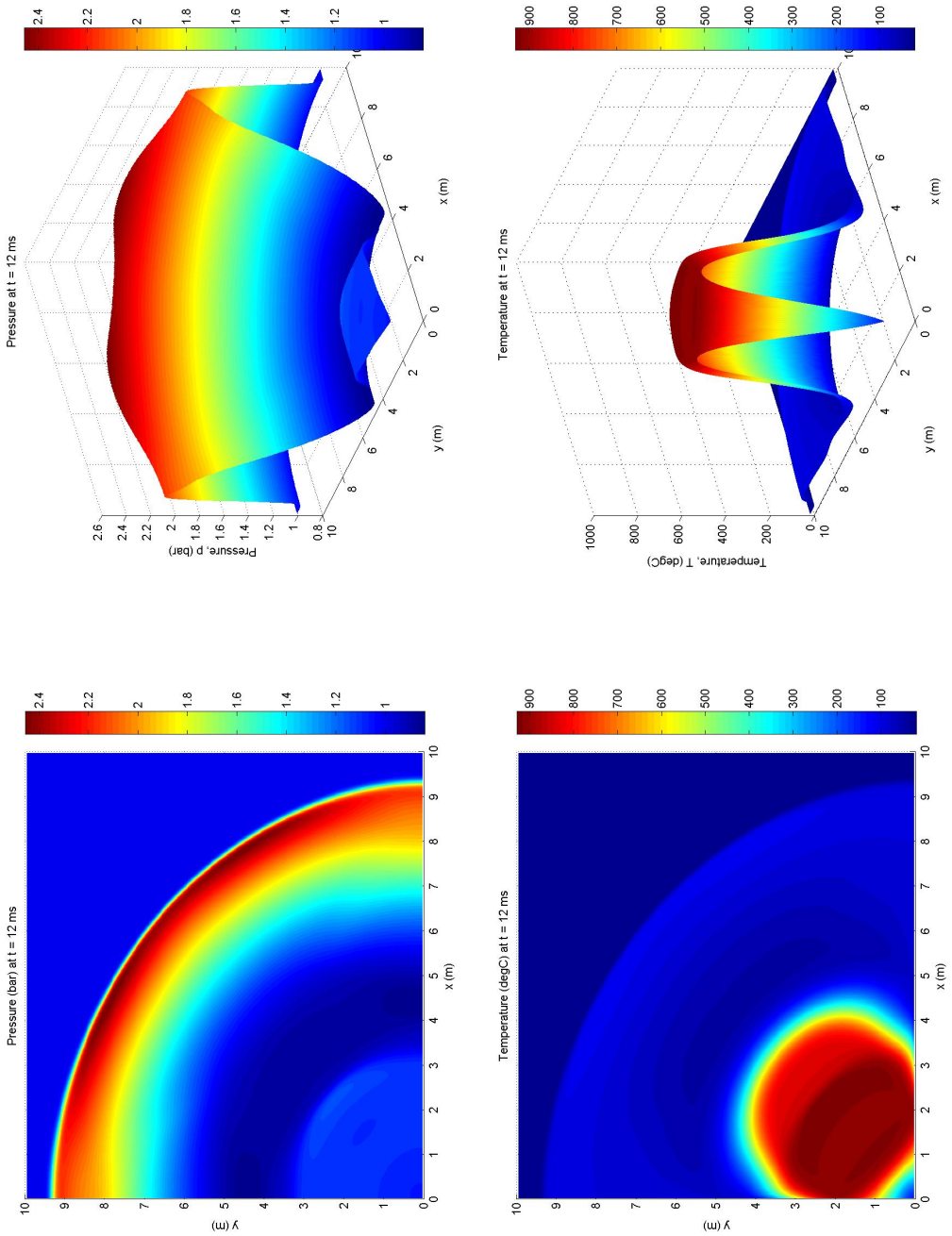

Figure 4.35. *Simulation results for the pressure and temperature at* $t = 0.012$ *s after the burst*

Chapter 5

Uncertainties and the Calculation of the Blast Overpressure and Explosion Risk

5.1 Mathematical treatment of uncertainties

5.1.1 Introduction

Data uncertainties are present in any engineering calculation. Their impact may be particularly important if they concern the safety aspects of industrial installations. There are many definitions of uncertainty. Perhaps the simplest and most complete is that "Uncertainty is a general concept that reflects our lack or sureness about something or someone, ranging from just short of complete sureness to an almost complete lack of conviction about an outcome [116].

In order to help understand the concept of uncertainty, and to be able to treat uncertainties in a structured manner, many attempts have been made to characterize classes of uncertainty and the underlying source of uncertainty [117]. At a fundamental level, two major groups of uncertainty are recognized in the literature. On the one hand there is the **aleatory**, or **stochastic uncertainty** which arises because of natural, unpredictable variation in the performance of the system under study. This type of uncertainty cannot be reduced. The knowledge of experts cannot reduce this uncertainty although their knowledge may be useful in quantifying this uncertainty. The second group is the **epistemic** or **knowledge uncertainty** which arises due to a lack of knowledge about fundamental phenomena or the behavior of the system that is conceptually resolvable. Therefore, this uncertainty could, in principle, be removed by further research.

In general, the discussion mentioned in this chapter mainly deals with the treatment of the epistemic uncertainty. With respect to this type of uncertainty, the following three classes can be further distinguished [118]:

- *Parameter uncertainty*
  It is introduced when the values of the parameters used in the models are not accurately known. It is often dealt with by assigning probability distributions to the uncertain parameters, representing the analyst's knowledge about them.

- *Model uncertainty*
  This uncertainty arises from the fact that any model, conceptual or mathematical, will inevitably be a simplification of the reality which the model is designed to represent.

- *Completeness uncertainty*
  This uncertainty originates from the fact that not all contributions to risk are addressed in the risk analysis models. For example, it will not be feasible to cover all possible initiating events in a quantitative risk analysis.

Knowing the sources of uncertainty involved in the analysis plays an important role in the overall handling of uncertainty. Different kinds of uncertainty call for different methods of treatment. If one knows why there are uncertainties and what kinds of uncertainty are involved, one has a better chance of finding the right methods for reducing them. Furthermore, the present treatment is about parameter uncertainties. Their impact on the calculation of the explosion risk is to be presented. This does not, of course, imply that the modeling or completeness uncertainties should not be addressed in this context.

Basically, not accounting for uncertainties in engineering calculations may lead to errors. At the level of study results without indication of uncertainties may be the cause of wrong conclusions. Uncertainties have to be propagated through the entire calculation and hence be reflected in the final result. At the end, some advantages arising from taking into account parameter uncertainties are as follows [119]:

(a). The information base becomes broader

(b). If the input data for treating a problem differ in quality, they are correctly combined. Their differing contents of information is reflected in the final result of the calculation

(c). The meaning of safety factors becomes evident; safety reserves are shown

(d). The credibility of results increases

(e). Indications are obtained as to the areas where models and data have to be refined

5.1.2 Methods of representing and evaluating the uncertainty

By far, the most common approach used to represent parameter uncertainties is to use the probability distributions. Some uncertain parameters involved in engineering calculations are normally treated as unknown fixed quantities. In order to account for uncertainties a different statistical viewpoint is taken. The quantities are no longer considered to be fixed but their behavior is assumed to be random due to one or several of the causes of uncertainty mentioned above. Random variables are treated by probability distributions, whose parameters are estimated on the basis of experimental results or, in default of these, occasionally fixed by an expert.

According to the circumstance of input data availability, several probability distributions are quite common to represent the stochastic behavior of technical parameters, among others: **normal**, **uniform**, **log-normal**, **truncated normal**, **Weibull**, **inverse Gauss**, **log-logistic**, **Gamma** or

inverse Gamma [120, 121]. If several probability distributions were to be considered the data would be fitted with each of them using, for example, the minimal value of the squared differences between measured and fitted values as the criterion for the choice of the most adequate distribution [122].

5.1.3 Techniques for the propagation and evaluation of uncertainty

There are various methods for performing uncertainty analysis. The method chosen for the implementation of uncertainty in the calculation of the explosion risk in this chapter is the standard Monte Carlo simulation method. This method is also known as the basic Monte Carlo method to distinguish it from the various modified Monte Carlo methods which have been developed to reduce the computational expense. These efficiency improvements, which are known as variance reduction techniques, include among others the importance sampling method and the Latin Hypercube sampling method.

The procedure for the standard Monte Carlo method for the treatment of uncertainty involves in general three steps:

1. The generation of a value for each uncertain parameter by randomly sampling the known or assumed probability density function
2. The propagation of the uncertain variables through the model function as schematically shown in Fig. 5.1.
3. The simulation process is repeated M times by generating a new set of random quantities as under 1.

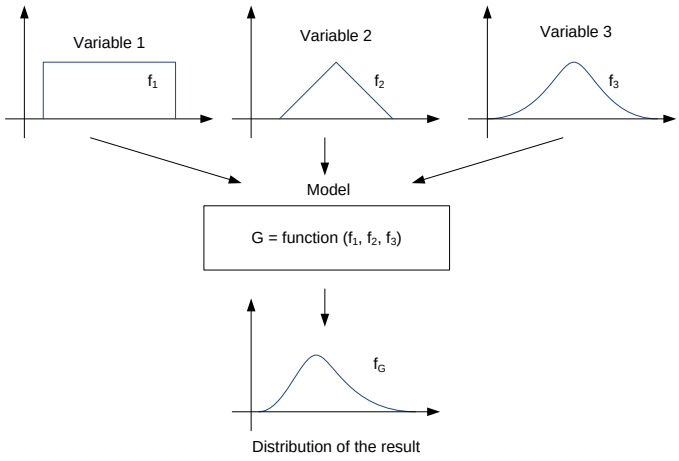

Figure 5.1. *Propagation of uncertainty parameters through a model. The parameter uncertainty is specified as the probability density function [117]*

4. The statistical analysis of the output data set to define the distribution of the output. The evaluation of the uncertainties impact to the output can be represented by presenting the

statistical parameters of the final results. These may include an expected value with some upper and lower bound, an expected value and both upper and lower centiles of the underlying distribution.

5.2 Relevant aspects for the risk assessment

5.2.1 Event trees for representing typical events following the release incident

In this section, the procedure to account for parameter uncertainties in the estimation of the risk, especially the risk from an explosion is presented. The determination of risk in the chemical process industries, especially to the people, also known as the individual risk, depends on the type of the accident which is encountered.

As mentioned earlier in this thesis, undesired accidents in the chemical process industries are typically initiated by certain release incidents and followed by several sequences leading to the a particular outcome. These sequences are usually represented by an event tree showing possible outcomes following a certain release incident. In general two general types of release incidents can be distinguished, namely the instantaneous release, such as the catastrophic rupture of the vessel or the complete rupture of the pipeline, or the continuous release, such as the leak from the vessel or the pipeline, the discharge through a relief valve or rupture disk. There are many types of accidental outcomes possible from each type of release incident, which may include the groups of fire, explosion or atmospheric toxic dispersion. However, in this thesis, the estimation of risk focuses only on the effect from an explosion. A typical impact to be considered is the explosion overpressure which can be estimated using both empirical models or the computational models of gas dynamics, as explained above.

Typical event trees following the release of a pressurized flammable gas or vaporizing liquid for the instantaneous and continuous event are shown in Figs. 5.2 and 5.3. Meanwhile, the event tree for the release of a flammable liquid is depicted in Fig. 5.4. Accidental outcomes with blue color are relevant only for the two-phase release. If a proportion of the cloud rains out, a pool of liquid may be created. In addition to the specified effects in the event tree, a pool fire may also be possible. If appropriate, this event should be added to the event tree.

The branches in the event tree actually indicate the possibility of a particular event to occur to which a conditional probability for its occurrence may be attached. f_{rel} represents the frequency of the release incident usually given its expected annual frequency. This data can be taken from many available accidental databases. Table 5.1 shows some typical values of release incident frequencies taken from several references.

In addition, some other databases may give different values which may be relevant for a specific problem under consideration. For example, the frequencies of loss of containment for pipeline failure with different sizes of diameter according to HSE is lying between 4×10^{-8} and 1×10^{-6} per m per year [124]. While, according to purple book they are lying between 3×10^{-8} and 5×10^{-6} per m per year [125].

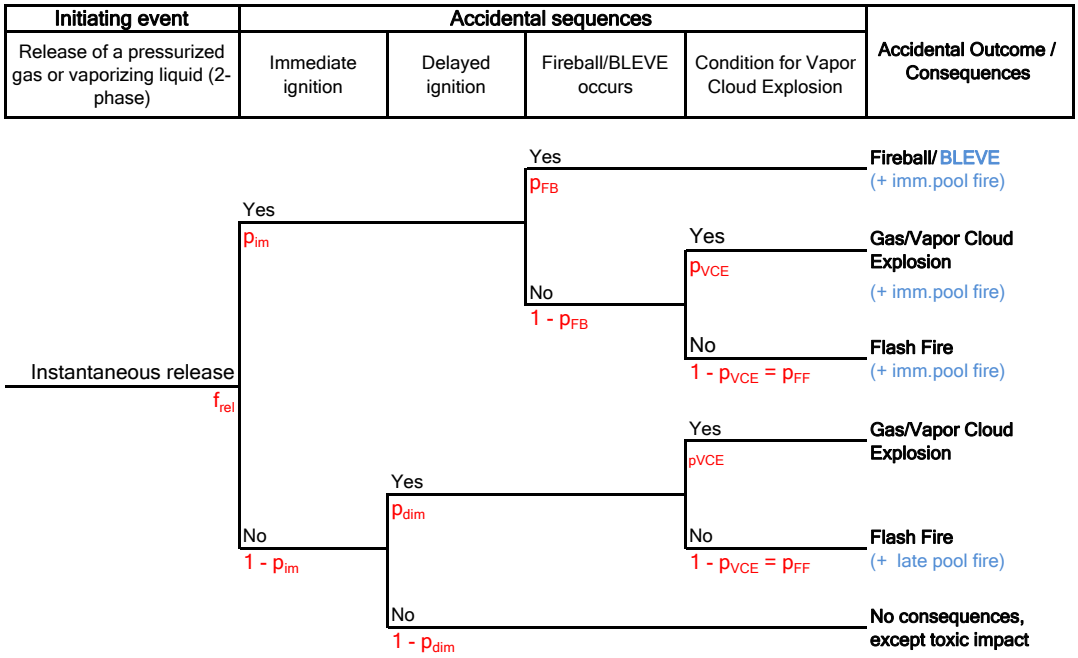

Figure 5.2. *Event tree for an instantaneous release of a pressurized gas or vaporizing liquid*

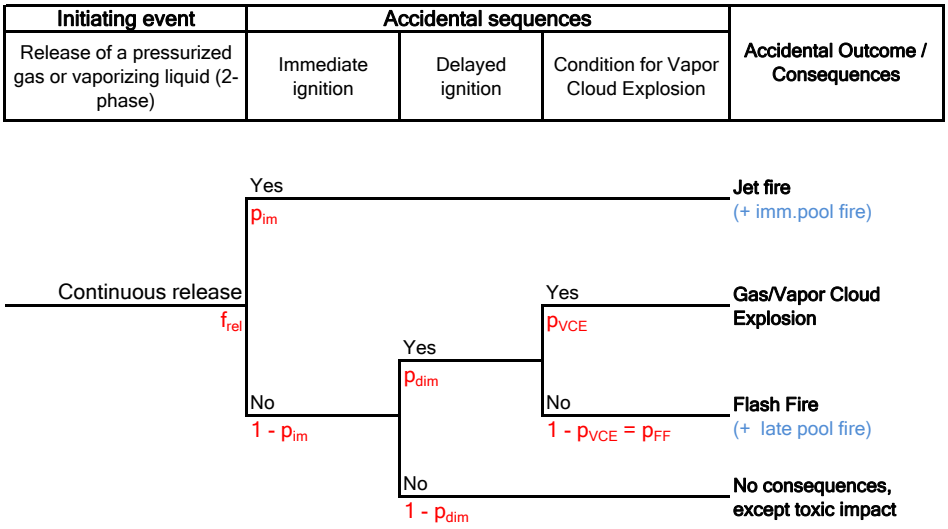

Figure 5.3. *Event tree for a continuous release of a pressurized gas or vaporizing liquid*

Since the released material could be immediately ignited by a certain ignition source soon after the release or at some moment after the release incident, p_{im} and p_{dim} are used to represent the probability of these two ignition sequential types. There are few data from which the probability of immediate ignition can be estimated. Hence for the purpose of the risk analysis it is quite common to propose a number of simplification. Table 5.2 shows typical values of the immediate ignition probability for stationary installations recommended by the Bevi Risk Assessment manual [123]. The probability of immediate ignition for the liquid release is in between 0.01 and 0.065 as

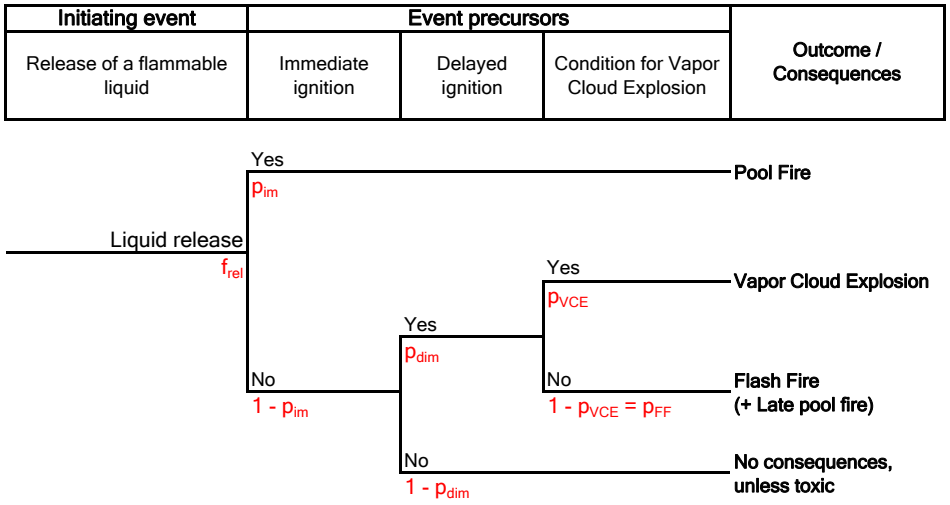

Figure 5.4. *Event tree for a flammable liquid release*

mentioned from the same source. The delayed ignition is usually assumed to be the complementary of the immediate ignition given that the toxic dispersion is not taken into account.

Furthermore, as mentioned in the previous chapter, the outcome of delayed ignition could be an explosion only if the released material, particularly gas or vapor, has formed a flammable mixture with the atmospheric air (gas or vapor cloud). However, if the condition to the vapor cloud explosion is not possible, the flash fire may be the outcome of the ignition of the vapor cloud. The frequencies that these two events would occur giving the vapor cloud is ignited are represented by F_{VCE} and F_{FF}. In the Bevi Risk Assessment manual, a default value of 0.4 is used.

In what follows, the treatment of parameter uncertainty is limited by two primary criteria. Firstly, there was a release of flammable gas or vaporizing liquid, and secondly, the ignition took place at some moment after the release. Therefore, vapor clouds that were not ignited or accidents where the ignition took place at the same time as the release are excluded from the analysis. The outcome to be considered is only the vapor cloud explosion which results in a certain degree of overpressure. Taking into account all probabilities or frequency of the occurrence of a particular accidental outcome, the probability that a vapor cloud explosion will occur following a particular type of release incident is given by:

$$p_{\mathsf{VCE}} = (1 - p_{\mathsf{im}}) \times p_{\mathsf{dim}} \times p_{\mathsf{VCE}} \tag{5.1}$$

and, by inclusion of the frequency of the release incident, the frequency of the vapor cloud explosion is given by:

$$f_{\mathsf{VCE}} = f_{\mathsf{rel}} \times p_{\mathsf{VCE}} \tag{5.2}$$

Table 5.1. *Some statistical data of the release incident frequency*

Failure description/scenario	frequency (yr^{-1})	Source
Pressurized storage tanks for gases and liquefied pressurized gases		
- Aboveground (inst. release of entire contents)	5×10^{-7}	[123]
- Underground (inst. release of entire contents)	5×10^{-7}	[123]
Gas containers		
- Instantaneous release of entire contents	5×10^{-6}	[123]
Failure of pipelines		
- Rupture in the pipeline (average)	4.6×10^{-7}	[123]
- Leak with an effective diameter up to 50 mm (average)	2.5×10^{-6}	[123]
Reactor & process vessels		
- Instantaneous release of entire contents	5×10^{-6}	[123]
Pressurized tank (catastrophic failure)	3×10^{-6}	[11]
Cold storage tank (catastrophic failure)	5×10^{-6}	[11]
Ammonia storage	6×10^{-4}	[11]
Atmospheric tank	3×10^{-5}	[11]
Loss of containment according to HSE		
- Catastrophic tank failure	5×10^{-6}	[124]
- Major tank failure	1×10^{-4}	[124]
- Minor tank failure	2.5×10^{-3}	[124]
- Pump	3.5×10^{-5}	[124]
Loss of containment according to Purple book		
- Atmospheric tank (instantaneous release of entire contents)	5×10^{-6}	[125]
- Pump, catastrophic failure	1×10^{-4}	[125]
- Pump, leak with an effective diameter up to 50 mm	5×10^{-4}	[125]
Overfilling of the tank per tank per year		
- Average value from the Lastfire report	4×10^{-4}	[124]
- Average value from Chevron	5.74×10^{-3}	[124]

However, when no information about the release incident is provided and other event tree paths are not to be considered giving that only the vapor cloud which has formed following the release is to be taken into account, the empirical investigation can be used for developing an event tree. In this case, the event tree is dealing only with the vapor cloud, the ignition and the accidental outcome. As mentioned before, the outcome of the ignition of the vapor cloud is either a vapor cloud explosion or a flash fire.

In what follows, the statistical study as reported in [126] is presented. The study has been focused on the accidental release of a combustible gas or vaporizing liquid leading to the formation of the flammable gas or vapor cloud. In the summary of the study, it was mentioned that a slightly more than 60% of the vapor cloud were ignited within 100 m from the initial release point. In [127, 128], the probability of 61% was chosen. In addition, only 20% of the cases did the cloud drift more than 1 km before ignition took place.

Table 5.2. *Example of the database for the immediate ignition probability for stationary installations [123]*

Description	Probability of immediate ignition, p_{im}
Low reactive materials	
- release mass: < 1000 kg	0.02
- release mass: $1000 - 10000$ kg	0.04
- release mass: > 10000 kg	0.09
Medium and high reactive materials	
- release mass < 1000 kg	0.2
- release mass $1000 - 10000$ kg	0.5
- release mass > 10000 kg	0.7

Another statistical conclusion was dealing with the probability of whether a vapor cloud explosion or a fire would occur once the vapor cloud is ignited. Regardless of the surroundings, in nearly 60% of the outcome of the ignition of the vapor cloud were the vapor cloud explosion that produces a significant overpressure. This means that it is about 40% of the cases resulting in a fire without giving rise to the overpressure. Therefore, an event tree can also be created relevant to result of statistical analysis as depicted in Fig. 5.5. With respect to this figure, the probability of a vapor

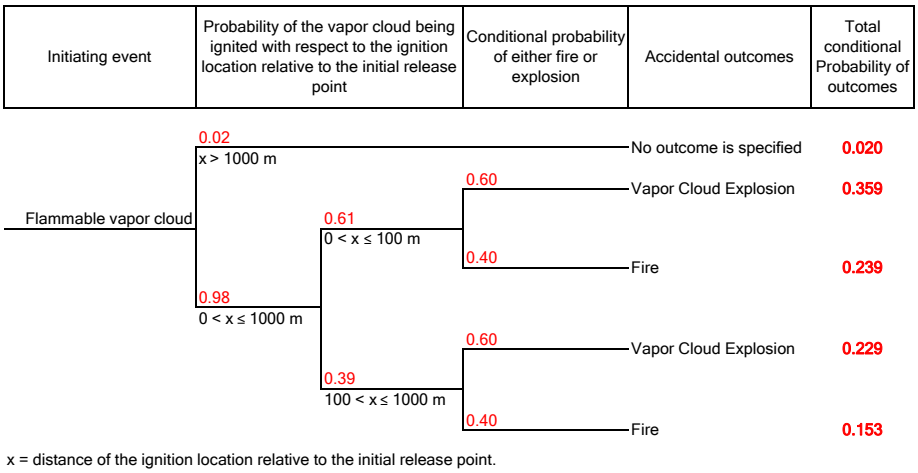

Figure 5.5. *Event tree showing the probability of the ignition of the vapor cloud according to the result of a statistical analysis as reported in [126]*

cloud explosion p_{VCE} is about 58.8% which means that the vapor cloud explosion is slightly more likely than the flash fire if the vapor cloud is ignited. The probability of the vapor cloud explosion if the vapor cloud is ignited at the distance up to 100 m and between 100 m and 1 km is also in general always greater than that of the flash fire.

5.2.2 Vulnerability models for assessing the damage of the blast wave

The primary effect of the explosion to be taken into account is the blast overpressure. As mentioned earlier in this thesis, there are, at least, three most important and dangerous blast parameters which are chiefly responsible for damage to either human beings, structures and environmental elements. These are namely the the **peak side-on overpressure** (Δp_o), **positive phase duration** (t_d) and **positive impulse** (i_p). The positive impulse itself basically depends on the peak overpressure and positive phase duration [93]. Many researchers, however, consider that the estimation of the overpressure only is generally sufficient to estimate the damage caused by the blast wave [16, 61]. The use of pressure-impulse diagram for assessing the damage is typically formidable because of the lack of data and the theoretical difficulties [129].

In what follows, the vulnerability models for assessing the damage of the explosion blast wave is particularly based on the level of the blast overpressure. Table 5.3 provides the typical scales of damage and related physical effects to people or structural building caused by different levels of blast peak overpressures.

5.2.2.1 The probit function and damage probability

For the purpose of assessing effects of blast waves on humans, consequences may also be expressed as conditional probability of death or injury. If property, such as structures and buildings, is the object of the study the consequences are partial or total destruction. In hazard assessment, the area of study dealing with the assessment of accidents affecting the vulnerable objects is also known as vulnerability analyses.

Basically, the damage aspects addressed by vulnerability models use a statistical method, which is called **dose-response** relationship. This relationship is commonly expressed in terms of probit (probability unit) equations. The probit method reflects a generalized relationship for any variable that has a probabilistic outcome that can be defined by a normal or log-normal distribution [11]. In fact, many probit functions have been developed for a wide range of vulnerability situations, including the blast overpressure, thermal radiation, or toxic exposure.

The relation between the response and hazard dose for a single exposure is typically represented with the probit function as a straight-line as given by the following equation [133]:

$$Y = k_1 + k_2 \cdot \ln V \tag{5.3}$$

where Y is the probit variable and V is the hazard dose representing the causative factor. Here, k_1 and k_2 are constants whose values are determined for any specific event. The hazard dose V is applied to any type of exposure, including the typical hazard from three major accidents, namely the blast overpressure, thermal radiation intensity and toxic dose.

The probit variable Y is related to a certain intensity of damage in terms of the damage probability, denoted by P_d, by means of a normal or log-normal distribution. In most cases, the damage probability by means of a normal distribution is commonly used. In this case, P_d is given

Table 5.3. *Typical scales of damage caused by different levels of blast peak overpressures, summarized from [59, 130, 131, 132]*

Damage levels & typical effects		
Minor damage: $\Delta p_o \leq 7.0$ kPa		
- Building performs function and is still reusable following an explosion.		
- Only minor repairs are needed. Very little risk to occupants because of building damage.		
Overpressure:	0.3 kPa	- Loud noise
	1.0 kPa	- Threshold for breakage of glass
	2.0 kPa	- "Safe distance" (probability 0.95 of no serious damage below this value
	3.0 kPa	- Limited minor structural damage
	4.0 kPa	- 90% window breakage. Damage to cladding. Minor structural damage
	7.0 kPa	- Glass fragment fly with enough force to injure
Moderate damage: 7.0 kPa $< \Delta p_o \leq$ 14.0 kPa		
- Possible deformation of structural members. Building may be reusable with repair		
- Possibly some debris formed. Personnel injury from debris is likely.		
Overpressure:	9.0 kPa	- Steel frame of clad building distorted
	10.0 kPa	- Limit of overpressures accepted by the KAS Germany for the people
		- 50% damage of atmospheric tank
	14.0 kPa	- Houses uninhabitable but not totally irreparable
		- Cement block buildings flattened
Major damage: 14.0 kPa $< \Delta p_o \leq$ 21.0 kPa		
- Possible failure of isolated structural members. Partial building is likely collapse		
- Building cannot be reused and must be replaced. Possible serious injury or fatality of some occupants.		
Overpressure:	16.0 kPa	- Lower limit of serious structural damage
	17.0 kPa	- 50% desctruction of brickwork of houses
	21.0 kPa	- Reinforced structures will distort.
		- 20% chance of fatality inside a building
Catastrophic damage: $\Delta p_o >$ 21.0 kPa		
- Complete collapse of structure.		
- Probable serious injury or fatality of all occupants.		
Overpressure:	27.0 kPa	- rupture of oil storage tanks
		- Cladding of light industrial buildings ruptures
	35.0 kPa	- On-set of severe structural damage. Nearly complete destruction of houses
		- 15% chance of fatality outdoors, 50% chance indoors
	70.0 kPa	- Almost complete demolition of all ordinary structures
		- Almost 100% chance of fatality indoors

by the following equation [33]:

$$P_d = \frac{1}{\sqrt{2\pi}} \int_{-\infty}^{Y-5} \exp\left(-\frac{x^2}{2}\right) \, dx \tag{5.4}$$

P_d is the impact probability of the hazard effect to the vulnerable object. Fundamentally, this

equation is the cumulative distribution function of the normal distribution.

The probit variable Y has a mean value of 5.0 and a standard deviation of 1.0. Once the probit variable is known, the probability of a certain effect can be estimated. Eq. (5.4) can be solved analytically or numerically. However, for the sake of simplicity, it is also possible to solve Eq. (5.4) using the following approach [123]:

$$P_d = 0.5 \left[1 + \mathbf{erf} \left(\frac{|Y - 5|}{\sqrt{2}} \right) \right] \tag{5.5}$$

Here, **erf** is the **error function** generally defined as follows:

$$\mathbf{erf}(x) = \frac{2}{\sqrt{x}} \int_0^x \exp\left(-t^2\right)\, dt \tag{5.6}$$

Applying either Eq. (5.4) or (5.5), it is understood that a probit value Y of 5 corresponds a damage probability of 50%, which means that 50% of the receptors will suffer the specified level of damage. Fig. 5.6 shows the conversion of probit variable (Y) to the damage probability percentage (P_d) graphically.

5.2.2.2 Models for the probit function for the effect of the blast overpressure to the people

In analyzing the consequences of blast wave from explosions on people the probit model is used. In terms of the potential impacts on people there are direct and indirect effects from the explosion blast wave [63]. These include:

- *Direct effects*: injury and death from pressure change that affects internal organs, such as the rupture of eardrums and lung damage
- *Indirect effects*, include impact of fragments and debris generated by the blast, bodily displacement causing impact of body parts or whole body on nearby structures, building or structural collapse, in the case of people inside structures

With respect to the blast wave overpressure, the direct effect of pressure change to the human lung is particularly important. This is because the lungs are known to be very susceptible to the blast overpressure resulting in lung haemorrhage. Haemorrhage may lead to death within minutes due to the obstruction of the airways by fluid.

A commonly used probit model for fatality as a result of lung damage and death due to direct effect of blast overpressure was the one developed by Eisenberg [11, 134]. According to his model, the probit variable Y is related to the blast wave overpressure in term of the peak side-on overpressure (Δp_o, Pa) by the following relation:

$$Y = -77.1 + 6.91 \cdot \ln \Delta p_o \tag{5.7}$$

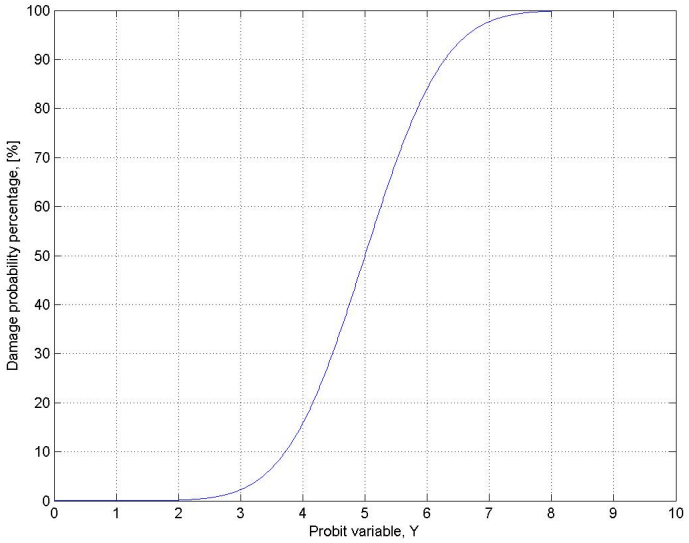

Figure 5.6. *Relationship between the damage probability P_d (%) and the probit variable Y*

Meanwhile, the probit variable for the injury related to the eardrum ruptures due to the blast wave overpressure (Δp_o, Pa) is given by [63]:

$$Y = -12.6 + 1.524 \cdot \ln \Delta p_o \tag{5.8}$$

Fig. 5.7 shows the probability of lung damage and death as well as the ear drum rupture due to several level of blast wave overpressure. According to this figure, a relatively high blast overpressure (greater than 1 bar) is required to produce fatality with respect to the lung damage (haemorrhage) or at least 50% injury with respect to the rupture of eardrums.

With respect to the calculation of the individual risk due to blast overpressure, the probit equation for the lung damage and death is further considered. Therefore, once the blast overpressure at a certain stand-off distance from the initial release point has been predicted and the probit variable Y has been determined using Eq. (5.7), the probability of death due to the blast can be estimated using Eq. (5.5). Thus, the individual risk to due the blast overpressure at a certain distance (x) from the initial release point is calculated in general by the following equation:

$$IR_{\mathsf{exp}}(x) = f_{\mathsf{VCE}} \times P_d(x) \tag{5.9}$$

where IR_{exp} is given in yr^{-1}. The probability of the vapor cloud explosion can be estimated, for example, by Eq. (5.1) assuming that the event tree for the release incident is relevant for the problem under consideration.

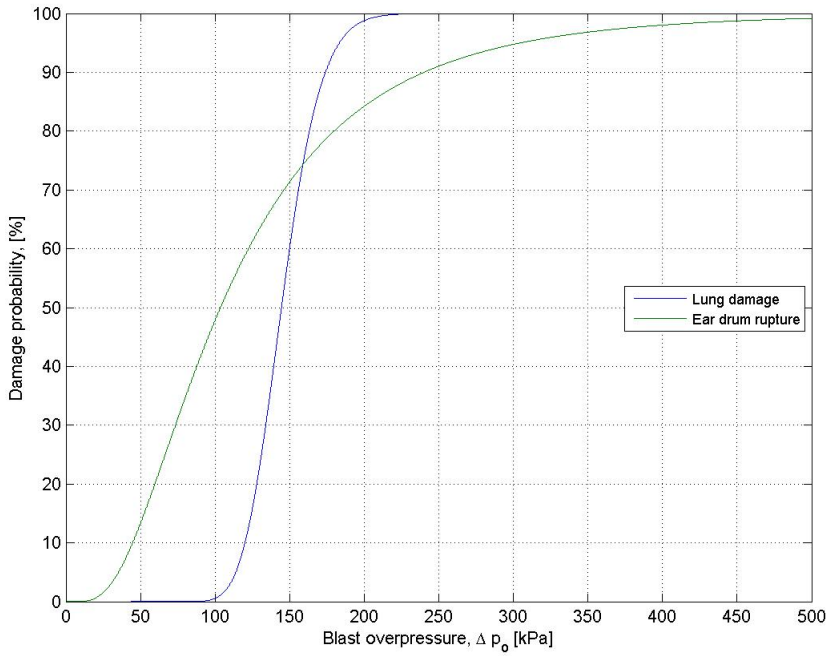

Figure 5.7. *The probability of the lung damage and the ear drum rupture due to the explosion blast wave overpressure.*

5.3 Methodology for accounting uncertainties for the calculation of the explosion risk

5.3.1 Important aspects to the determination of the blast overpressure

As explained in detail in Chapter 3, the determination of the blast overpressure is influenced by several factors, including the fuel reactivity, the initiation of the vapor cloud explosion, the confinement and congestion level in the area engulfed by the vapor cloud. However, the consideration for the use of these factors is particularly determined by the model to be used for the prediction of the blast overpressure. Furthermore, in the same chapter, the blast overpressure is estimated only using the empirical models. These are the most easiest, and perhaps, the most efficient method for solving such problem. For example, the TNT equivalent model does not take any of these factors into account, except probably for the fuel reactivity in order to estimate the explosion efficiency which can also not be determined exactly. The TNO Multi-Energy takes into account all these factors, even thought not all of them are treated quantitatively. The same situation may also be applicable for the Baker-Strehlow-Tang method.

With respect to the TNT equivalent model, the blast overpressure is predicted by taking into account only the mass of explosive material and estimating the explosion efficiency of the material involved. For the vapor cloud explosion, the mass of explosive material is the flammable mass of the vapor cloud which should be calculated from the dispersion analysis. This is the mass between

the lower and upper flammability limit. However, for the worst case scenario and conservative assumption, the maximum flammable mass in vapor cloud is the maximum mass which was released from the source. Meanwhile, the explosion efficiency is to be estimated according to the problem under consideration.

With respect to the TNO Multi-Energy and the Baker-Strehlow-Tang model, the most important steps are to determine the volume of flammable vapor cloud which is confined and congested (cloud size) and to estimate the initial blast strength, in the case of the TNO Multi-Energy model, or the initial flame speed, in the case of Baker-Strehlow-Tang model. In worst case scenario, it can be assumed that the maximum volume of the flammable vapor cloud is calculated from the maximum flammable mass of the vapor cloud considering that the flammable fuel is its stoichiometric concentration in the vapor cloud. Eq. (3.22) is then used to estimate the total volume of the flammable vapor cloud giving that no obstacles is present. The initial blast strength can be estimated quantitatively using Eq. (3.26) by considering four other parameters. Meanwhile, the flame speed in terms of the Eulerian Mach number is estimated from Eq. (3.31) after the determination of the maximum overpressure of the vapor cloud using Eq. (3.26)

5.3.2 Important aspects with regard to the probability distribution of the uncertain parameters

As mentioned before, for the uncertainty analysis, any parameter, which is uncertain, is not to be considered as a fixed quantity, but represented as a random variable following a certain probability distribution. Typical types of the distribution will depend on the availability of data which could be available in different conditions. There could be several values available, only two values or even only a single value with some other generic statement. For each situation, different probability distributions could be assigned for which the consideration for the selection of the appropriate distribution lies on several criteria as described before.

In the case that only two values is available without having any other information and both of them having similar probability, the uniform or rectangular probability distribution can be assumed for generating random variable of this parameter. The probability density function for the uniform distribution, as shown Fig. 5.8, is given by the following equation:

$$f(x) = \begin{cases} \dfrac{1}{b-a} & \text{for} \quad a \leq x \leq b \\ 0 & \text{otherwise} \end{cases} \tag{5.10}$$

for which the random quantity of the corresponding variable is given by:

$$X = a + (b-a) \times Z_p \tag{5.11}$$

where Z_p is the pseudo-random number to be generated from standard uniform distribution on the open interval $[0, 1]$. In this thesis, the pseudo-random number is generated using a MATLAB program.

Figure 5.8. *Probability density function of the uniform distribution*

If the random variable of the uncertain parameter is to be described using the normal distribution, the probability density function of this distribution, as shown in Fig. 5.9, is given by the following equation:

$$f(x) = \frac{1}{\sigma\sqrt{2\pi}} \exp\left[-\frac{(x-\mu)^2}{2\sigma^2}\right],\ -\infty < x < \infty,\ -\infty < \mu < \infty,\ \sigma > 0 \tag{5.12}$$

where μ and σ are the mean and standard deviation of the distribution. The random variable following this distribution is given by:

$$X = \mu + \left[\sqrt{-2\ln Z_{p,1}} \times \cos(2\pi \cdot Z_{p,2}) \times \sigma\right] \tag{5.13}$$

where $Z_{p,1}$ and $Z_{p,2}$ are two independent random number to be generated at the same time.

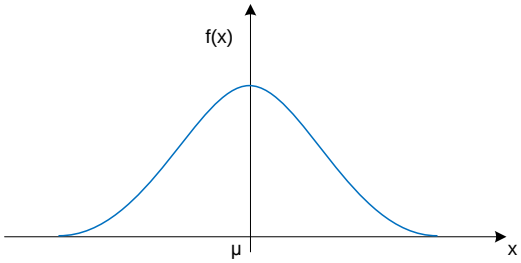

Figure 5.9. *Probability density function of the normal distribution*

For the log-normal distribution, its probability density function, as shown in Fig. 5.10, is given by:

$$f(x) = \frac{1}{x\sigma\sqrt{2\pi}} \exp\left[-\ln\left(\frac{x-\mu}{2\sigma}\right)^2\right],\ x > 0 \tag{5.14}$$

where μ is the mean value of the logarithms of the variable xm and s is the corresponding standard deviation. The random variable of the parameter following this distribution is given by:

$$X = \exp\left(\mu + \left[\sqrt{-2\ln Z_{p,1}} \times \cos(2\pi \cdot Z_{p,2}) \times \sigma\right]\right) \tag{5.15}$$

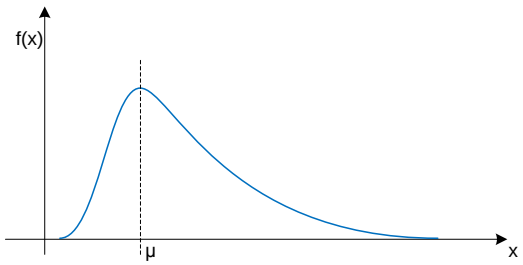

Figure 5.10. *Probability density function of the log-normal distribution*

5.4 Illustration example for the implementation of the procedure

5.4.1 The vulnerability study for the risk assessment

In what follows, the implementation of the aforementioned procedure for incorporating parameter uncertainties to determine the damage level of blast to the vulnerable objects are shown. There are two cases being considered. The first case is treated in this section, while the second case is explained in the next section.

In the first case, it is assumed that a liquefied propane incidentally released from the pressurized storage tank. Following the release, the flammable vapor cloud was formed due to the vaporization of the material into the atmosphere. The flammable mass was estimated to be about 42000 kg. The other properties of the material required for this calculation are listed in Table 5.4.

Table 5.4. *Material properties and other required data for testing the procedure*

Parameter	Symbol	Given value	Unit
Material		Liquefied propane	
- Lower explosion limit	LEL	2	% vol
- Upper explosion limit	UEL	9.5	% vol
- Stoichiometric concentration	c_{st}	4.1	% vol
- Vapor density	ρ	1.86	kg/m^3
- Flammable mass of the vapor cloud	$W_{e,\mathrm{f}}$	42000	kg
- Explosion energy	ΔH_c	46320	kJ/kg

With respect to the calculation of the blast overpressure, the TNT equivalent model was used. The blast overpressure at a certain distance from the blast origin was estimated by using the Kinney and Graham equations. The vapor cloud was exploded close to the ground with an efficiency of 3%. The reflection factor of 2.0 accounting for the hemipsherical blast was assumed. The probit model for the explosion effect due to blast overpressure used the Eisenberg model for the lung damage. The release frequency was 3.0×10^{-5} per year.

Although the explosion efficiency is also uncertain parameter, in the following analysis, this variable is not subject to uncertainty. This is only the location of ignition point to be treated as uncertain parameter. In order to do so, the calculation area was divided into two sub-regions, that

are between 0-100 m and 100-1000m relative to the initial release point according to the event tree in Fig. 5.5. This is because the probabilities of the vapor cloud being ignited in these two sub-regions are already specified. According to Fig. 5.5, the explosion probability is given by following equation:

$$p_{VCE}(x) = \begin{cases} f_{VCE,1} = 0.359, & \text{if} \quad 0 < x \leq 100 \\ f_{VCE,2} = 0.229, & \text{if} \quad 100 < x \leq 1000 \\ 0.0, & \text{if} \quad x > 1000 \end{cases} \tag{5.16}$$

Furthermore, the wind direction to which the vapor cloud would disperse was also taken into account. Since no exact information of wind distribution, it is assumed that the vapor cloud disperses uniformly to any direction as illustrated by Fig. 5.11. This means the wind distribution is not stochastic and also not subject to uncertainty. The calculation of risk should be made in all direction for which the result would shares the same probability.

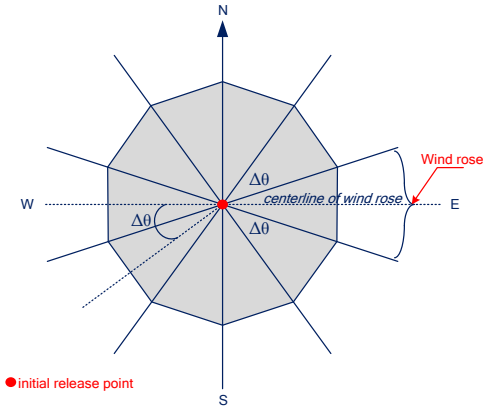

Figure 5.11. *Illustration of the wind distribution if no prior information is given. It is assumed that the wind is distributed uniformly to all directions.*

According to Fig. 5.11, the sector angle between the centerline of two neighboring wind roses are similar to the sector angle of the wind rose itself. In this figure, the angle of a wind rose is denoted by $\Delta\theta$. The center of wind contour is assumed to be the initial release point. If N is the total number of wind roses, the angle of a wind rose or the angle between centerline of two neighboring wind roses is given by the following equation:

$$\Delta\theta = \frac{360^0}{N} \tag{5.17}$$

In addition, the vapor cloud is assumed to be ignited only by a single ignition source which can be located anywhere within the calculation area. In order to analyze the uncertainty effect of the ignition location to the calculation result, the distance of the ignition source to the release point is assumed to be uniformly distributed in two sub-regions as defined before. Therefore, this ignition point is represented by two sharing sources, one located in the region between 0-100 m and the

other one in between 100-1000 m. As a consequence, a particular object (vulnerable object), e.g. people, seems to receive particular hazard (either from a fire or an explosion) from two possible sources. This situation can be illustrated in Fig. 5.12.

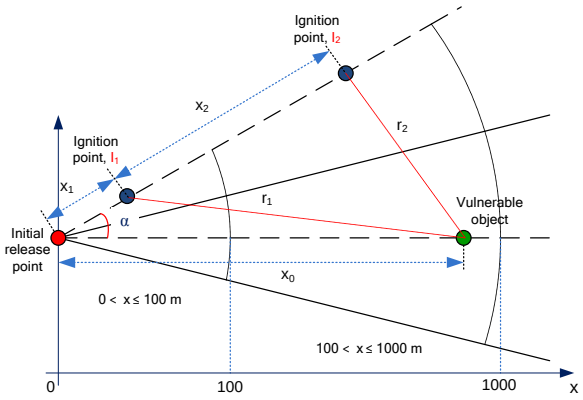

Figure 5.12. *The calculation area for the estimation of explosion risk using probabilistic approach for a single step of Monte Carlo simulation from M trials. In this figure the ignition point (featured by blue circles) are located at x_1 m and x_2 m from the release point. The vulnerable object is located at x_0 from the same point. This is only for a single wind direction from N times calculation after performing M times Monte Carlo trial.*

In this figure, the distance of the vulnerable object (e.g. people) to the initial release point is denoted by x_0. Meanwhile, the distance to the share ignition points are denoted by x_1 and x_2. The angle between the centerline of the wind rose in which the ignition points are located and the centerline in which the vulnerable object is located is denoted by α. In this case, $\alpha = 0$ means that the vulnerable object and both share ignition points are located at the same centerline.

Thus, the distance of a share ignition point to a vulnerable object of reference is described by the law of cosines as follows:

$$r_i = \sqrt{x_0^2 + x_i^2 - 2 \cdot x_0 \cdot x_i \cdot \cos\alpha}, \qquad \text{where} \qquad i = 1, 2 \tag{5.18}$$

By treating the location of the ignition source as uncertain parameter following a certain probability distribution, the stand-off distance of the vulnerable object relative to the blast origin will also distributed. This condition will affect the determination of the blast overpressure which is faced by the object. For the TNT equivalent model, it is important to mention also that the flammable mass of the material with respect to the location of the ignition point is always the same and treated to be a constant value until the end of simulation. Otherwise, the TNT equivalent should also be treated as uncertain parameter.

As mentioned before, the propagation of the ignition location uncertainty into the calculation of explosion risk based on the magnitude of the blast overpressure was performed by means of the Monte-Carlo simulation. In this case, the generation of the random variable representing the distance of the share ignition points was made using the MATLAB software. A set of 20000 random positions for each subregion of the calculation area was generated. In addition, 100 wind sectors

Table 5.5. *Distribution of the location of the ignition points*

Parameter	Symbol	Distribution type	Given interval	Unit
Position of the ignition point	x_1	Uniform distribution	$[0, 100]$	m
	x_2	Uniform distribution	$[100, 1000]$	m

were also taken into account. Table 5.5 summarizes the input for the uncertainty analysis.

Fig. 5.13 shows the calculation result if the share ignition points were assumed to be located at the center of each sub region as the representative location. No other consideration is taken into account. In general, it can be concluded that the individual risk are higher up to about 700 m from the initial release point and seems to be very conservative.

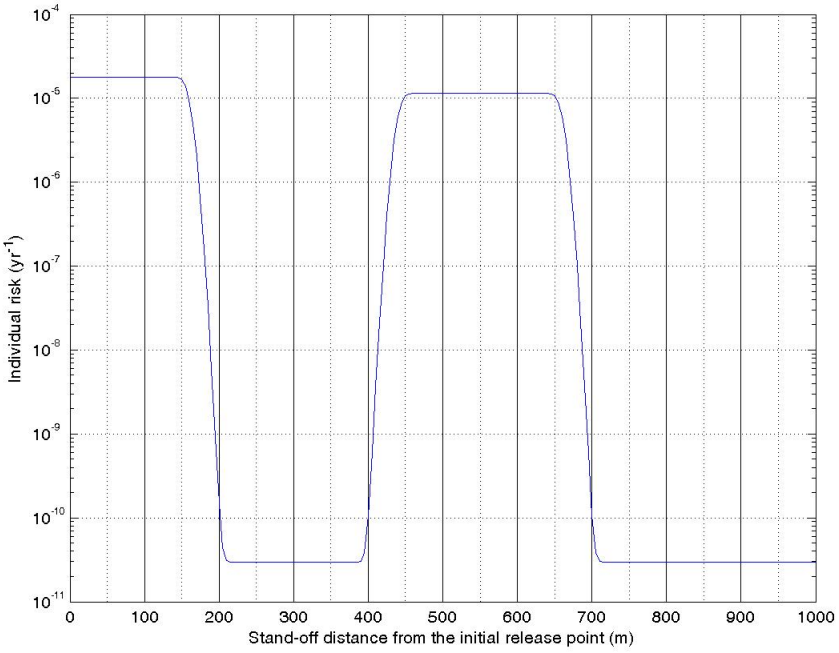

Figure 5.13. *The calculation of the individual risk based on the explosion blast overpressure versus stand-off distance relative to the initial release point using conservative method. The first peak: ignition location 1 about 55 m from the source, and the second peak: ignition location 2 about 550 m from the source*

Meanwhile, Fig. 5.14 shows the simulation result if the location of the ignition was subject to uncertainty and the vapor cloud was distributed uniformly to all direction. The profile of individual risk due to the blast overpressure is significantly improved. If assumed that the risk acceptance criteria of maximum 1×10^{-6} per year, the safe distance with respect to the effect of blast overpressure is about 180 m to the location of liquefied propane tank.

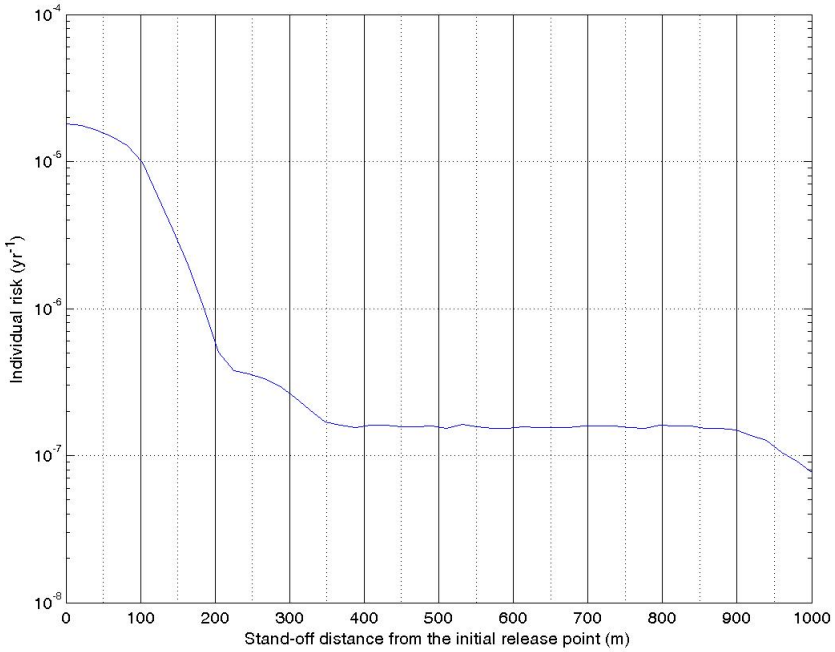

Figure 5.14. *The calculation of the individual risk based on the explosion blast overpressure versus stand-off distance relative to the initial release point using Monte-Carlo method for which the location of ignition is subject to uncertainty.*

5.4.2 The determination of the maximum explosion and blast wave overpressure

The second example has been intended to demonstrate the incorporation of parameter uncertainties to the determination of the maximum explosion overpressure of the vapor cloud and its influence to the simulation of blast wave propagation. For this particular example, a heat exchanger unit as shown in both Figs. 5.15 and 5.16 is taken into account. The initial configuration of this problem has been taken from [80].

There is no complete scheme to be presented in this example. In fact, the main layout as shown in both figures are sufficient to perform the calculation. According to this layout, the heat exchanger unit consists of obstacles (vessels, pipes and other supports) oriented in all three dimensions. A qualitative approach for this case has concluded that this unit is situated in open air, thus it can be further considered a 3D configuration for the determination of the explosion overpressure. A low ignition energy type is also assumed. The flammable material to be considered in this example is propane with a laminar burning velocity (S_L) of 0.45 m/s.

As explained in Chapter 3, the appropriate empirical correlation for the determination of the maximum explosion overpressure in the vapor cloud in 3D-flame expansion case is given by the following equation:

$$\Delta p_{o,\max} = 0.84 \times \left[\frac{\mathsf{VBR} \cdot L_p}{D}\right]^{2.75} \times S_L^{2.7} \times D^{0.7} \tag{5.19}$$

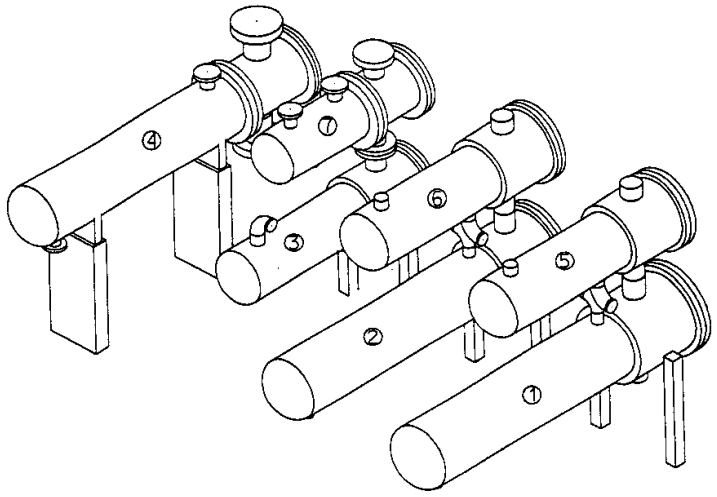

Figure 5.15. *Impression of large process vessel in the heat exchanger unit.*

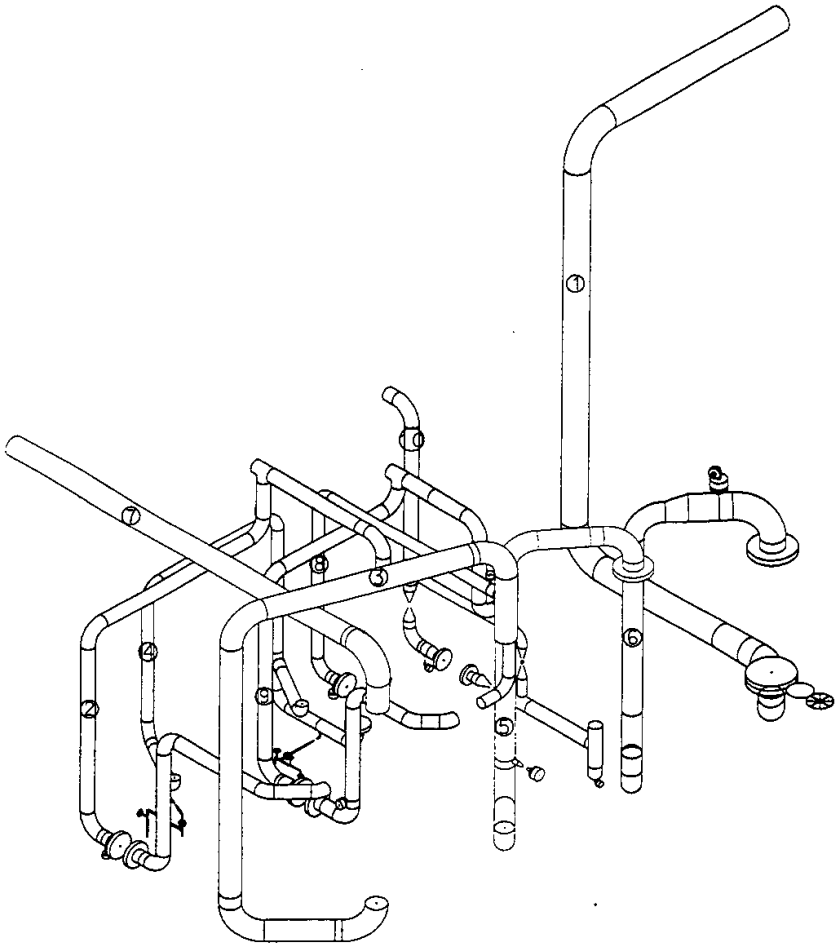

Figure 5.16. *Impression of connecting pipework in the heat exchanger unit.*

In order to determine $\Delta p_{o,\max}$, detailed dimensions for the vessels and pipework, such as diameter, length and volume are required. This information can be obtained from Tables 5.6 and 5.7. A few small obstacles and the supports, which can be ignored, are not included in these Tables.

Table 5.6. *Dimension of large process vessels and major supports in the heat exchanger unit*

Vessel no.	1	2	3	4	5	6	7	S1-3	S4
Diameter (m)	1.6	1.5	1.3	1.5	1.4	1.4	1.3	0.3 × 0.3	0.4 × 0.4
Length (m)	8.3	7.8	5.6	8.5	5.6	5.6	4.1	3.0	3.0
Volume (m^3)	16.7	13.8	7.4	14.8	8.6	8.6	5.4	0.27	1.68

Table 5.7. *Dimension of connecting pipes in the heat exchanger unit*

Pipe no.	1	2	3	4	5	6	7	8	9	10
Diameter (m)	0.61	0.32	0.51	0.27	0.46	0.46	0.51	0.27	0.32	0.32
Length (m)	25.6	26.1	20.2	27.2	13.2	7.2	12.6	14.6	22.6	14.9
Volume (m^3)	7.48	2.15	4.14	1.58	2.16	1.15	2.55	0.86	1.86	1.23

Thus, the average obstacle diameter (D) is determined by the following procedure:

- By using the standard averaging procedure for which the obstacle diameter is the average diameter of the all the cylinders which include vessels and pipes. Thus, according to data in Table 5.6 and 5.7, $D_1 = 0.60$ m
- By taking into account the average specific surface, which is the ratio of area to volume. Using this method, the obstacle diameter is obtained to be $D_2 = 0.43$ m

The obstructed region is assumed to be a box with a dimension of $12 \times 10 \times 7.5$ representing the length, width and height of the box. Therefore, the volume of the obstructed region is about 900 m^3. When the major process vessel only to be considered as the obstructed area, the minimum obstructed volume is estimated to be 510 m^3.

Meanwhile, with respect to the flame path length, the maximum extension of the obstructed area under consideration, which is the length of the box, is assumed to be the longest distance for the flame travel. While, the minimum distance covered by the flame is the width of the box. The volume blockage ratio (VBR) is estimated by two different values. The maximum VBR is the ratio between the maximum volume of the whole obstacles against the minimum volume of the obstructed region. This is about 0.20. While, the minimum value of VBR is the ratio between the maximum volume of the whole obstacle against the maximum volume of the obstructed region. This ratio is estimated 0.11.

Furthermore, it is assumed that all parameters involved in Eq. (5.19), except the laminar flame speed of the propane, are subject to uncertainty. The relevant probability distributions for these uncertain parameters are specified in Table 5.8.

Table 5.8. *Specification of uncertain parameters for the determination of the maximum explosion overpressure in the heat exchanger unit*

Uncertain parameter	Symbol	Distribution type	Given interval	Unit
Volume blockage ratio	VBR	Uniform distribution	$[0.11, 0.20]$	-
Flame path length	L_p	Uniform distribution	$[10, 12]$	m
Obstacle diameter	D	Uniform distribution	$[0.43, 0.60]$	m

Applying the Monte-Carlo procedure with 20000 independent trials, the probability distribution of the maximum explosion overpressure in the heat exchanger unit is depicted in Fig. 5.17. The log-normal distribution is found to fit this data well. The relevant statistical parameters for the distribution of the maximum explosion overpressure is given in Table 5.9.

According to the initial correlation in [80], a combination of several given conditions in the heat exchanger unit would give the maximum explosion overpressure between 0.6 up to 3.7 bar. The minimum value corresponds to $D = 0.60$ m, $VBR = 0.11$ and $L_p = 12$ m, while the maximum value corresponds to $D = 0.43$ m, $VBR = 0.20$ and $L_p = 10$ m. However, using this old methodology, it is difficult to determine its expected value. This old methodology is not able to present this value. This leads to the conclusion that the uncertainty analysis has capability of presenting more representative information.

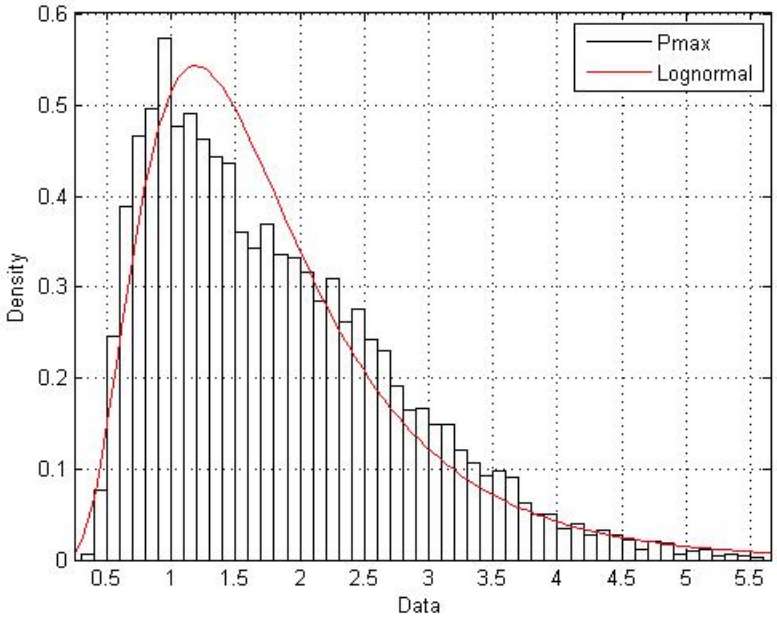

Figure 5.17. *The maximum explosion overpressure of the propane cloud in the heat exchanger unit if the parameter of volume blockage ratio, flame path length and obstacles density are subject to uncertainty.*

If the blast overpressure at a particular stand-off distance relative to the center of explosion is

Table 5.9. *Statistical parameters for the maximum explosion overpressure (bar)*

Distribution	Parameter	Value
Log-normal distribution	Mean	0.468
	Standard deviation	0.527
Summary	Expected value	1.835
	Variance	1.081
	Maximum value	5.547
	95% centile	3.601
	5% centile	0.659
	Minimum value	0.377

estimated using the TNO Multi-Energy model, some additional information is still required. This is provided in Table 5.10. According to the result in Table 5.9, the initial strength of the blast source would lie between the level number 6 (max. 50 kPa/0.5 bar) and number 9 (max. 500 kPa/5 bar). A stoichiometric propane vapor cloud filling the remaining free volume in the obstructed region is assumed. It is important to mention that the vapor cloud is assumed to be hemispherical. For anticipating the worst scenario, the maximum free volume of $0.89 \times 900 = 801$ m^3 was taken into account.

Table 5.10. *Data for the estimation of blast overpressure outside the propane vapor cloud*

Parameter	Symbol	Given value	Unit
Volume of the propane cloud	Vc	801	m^3
Volumetric heat of combustion	$\Delta H_{c,\text{vol}}$	3.46	MJ/m^3
Radius of the vapor cloud	R_0	7.25	m
Volumetric explosion energy	E_c	2.77×10^3	MJ

The estimated blast overpressure at various stand-off distances from the center of the vapor cloud according to the TNO Multi-Energy model is shown Table 5.11. In practice, according to this result, the safe distance with respect to the regulation in Germany defined by KAS (*Kommission für Anlagensicherheit*) is about 100 meters from the center of explosion.

Furthermore, apart from the TNO Multi-Energy model calculation above, the simulation of the blast wave propagation for a vapor cloud explosion in the heat exchanger unit using the procedure which has been developed in Chapter 4 is demonstrated. In this case, the expected value from Table 5.9 serves as the basis for determining the initial conditions for the simulation. It is still assumed that there is a hemispherical vapor cloud as the source of the blast wave. The center of this vapor cloud is also the center of the blast source. It is identified as a circular region centered at a local coordinate $[0, 0]$ (see Fig. 5.18 for time $t = 0$). The spatial boundaries of the obstructed region are considered transmissive boundaries, which means no physical boundaries are present in the vicinity. The computational domain of interest is $x - y$ plane where $0 < x < 50$ m and $0 < y < 50$ m. A

Table 5.11. *Estimated overpressure (bar) at various stand-off distances from the center of the vapor cloud*

	Stand-off distance (m)				
Reference maximum	10	25	50	75	100
overpressure of the vapor cloud	Scaled distance (-)				
($\Delta p_{o,\max}$, bar)	$\overline{R} = 0.33$	$\overline{R} = 0.83$	$\overline{R} = 1.66$	$\overline{R} = 2.49$	$\overline{R} = 3.32$
0.377 (Minimum value)	0.377	0.271	0.129	0.083	0.061
0.659 (5% centile)	0.659	0.434	0.185	0.112	0.080
1.835 (Expected value)	1.835	0.693	0.213	0.115	0.080
3.601 (95% centile)	3.601	0.716	0.213	0.115	0.080
5.547 (Maximum value)	5.131	0.716	0.213	0.115	0.080

uniform computational mesh of 50000 cells (250×250 at each direction) was generated. A CFL condition of 0.5 is assumed.

Results of this simulation for times $t = 20$, 40 and 80 ms are also shown in Fig. 5.18. It can be seen that the shock wave with a magnitude of 0.65 bar (overpressure) is estimated to reach the distance of about 15 m at time $t = 20$ ms. This front moves up to a distance of 25 m with an overpressure of around 0.60 bar after 40 ms. Unlike the TNO Multi-Energy calculation result, a simulation of the blast wave propagation gives not only the magnitude and the duration of blast overpressure, but also a possibility to evaluate and calculate the interaction of theblast wave with obstacles while it propagates away from its source.

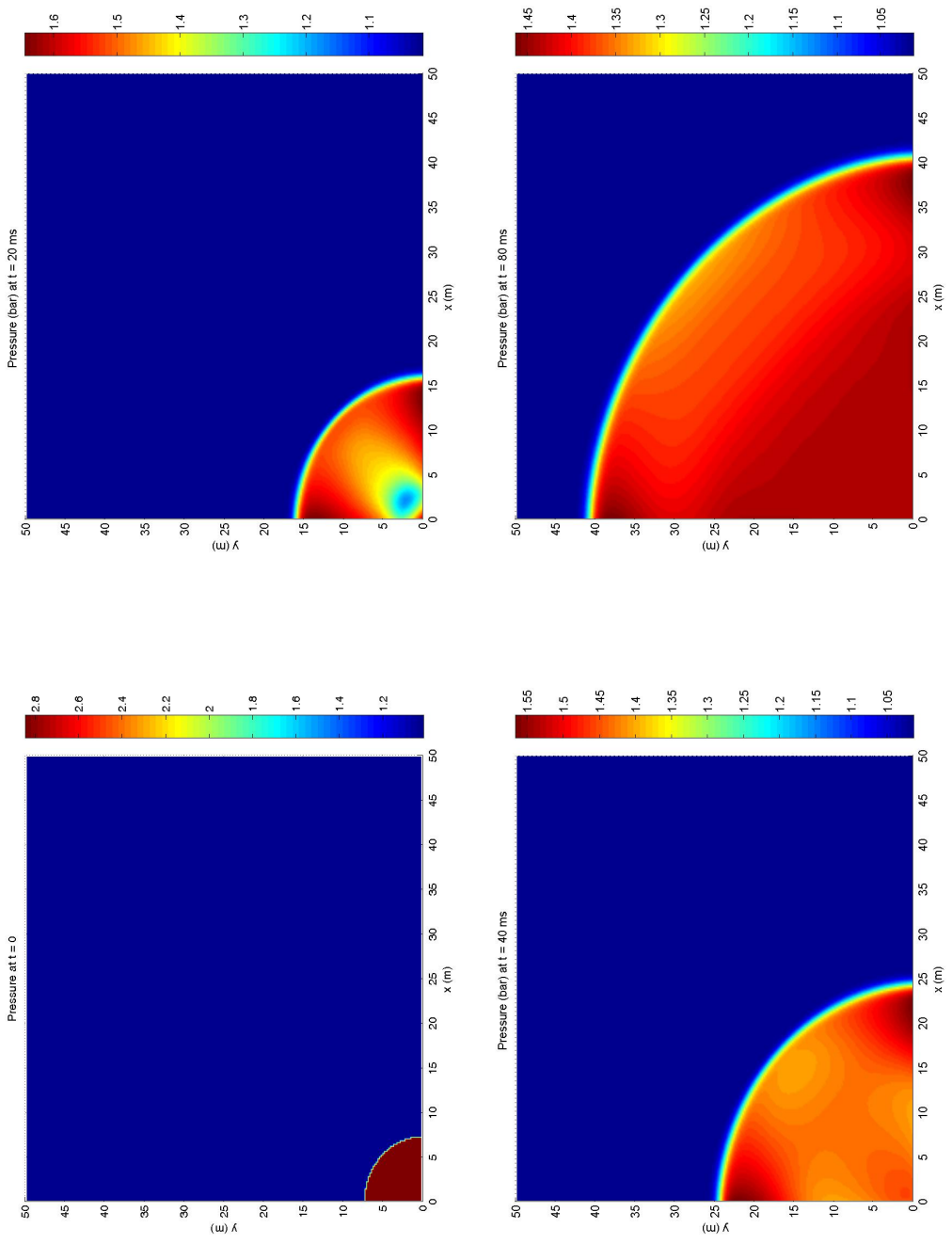

Figure 5.18. *Simulation results for the blast wave propagation due to an explosion in the heat exchanger unit. The expected value obtained from aforementioned probabilistic procedure is taken as the maximum overpressure which can be attained if the deflagration of the vapor cloud takes place. The top left frame shows the initial conditions of the simulated problem.*

Chapter 6

Conclusions and Outlook

6.1 Conclusions

An explosion is one of the most challenging problems in the chemical process industries. As a major hazard, an explosion is in fact a very complex phenomena. Many parameters have been identified to describe and quantify an explosion. The most important feature of an explosion is the generation of damaging blast overpressure. An ability to have a better prediction of this particular parameter and to develop a methodology for dealing with the interaction of the blast wave with the object in an efficient way has been the one of the goal of this work. In addition, the development of the procedure for incorporating the uncertainties into the prediction method of the blast overpressure and the vulnerability study of the risk assessment is another prime goal of this thesis.

In the industrial application, the prediction of the blast overpressure has been done mostly by employing available empirical techniques. Particular attention has been paid to the three classical models, namely the TNT equivalent model, the TNO Multi-Energy model and the Baker-Strehlow-Tang model. A systematic review to these models has been presented. The TNT equivalent model is based on the TNT detonation charge, thus it can be a good choice for predicting the properties of the detonation wave. Meanwhile, the other two models have been based on the explosive gas or vapor cloud, thus it is the best practical choice for analyzing the overpressure from vapor cloud explosions.

The numerical scheme for the Euler equations of gas dynamics which is intended to simulate the propagation of the blast wave has been developed using the Godunov method. The implementation of the procedure for the one- and two-dimensional problem demonstrated that the solver has a capability of estimating the properties and behavior of the blast wave at certain distances relative to the center of the blast source. This feature is particularly important, especially for anticipating the interaction between the blast wave and a particular object in the surroundings. The initial conditions for the Euler equations could have been obtained from the result of the combustion analysis of the vapor cloud. However, the primitive variables such as the density, velocity, pressure, specific energy and temperature are estimated. The maximum overpressure inside the vapor cloud is calculated from the correlation for the application of the TNO Multi-Energy model. This quantity

is assumed constant inside the cloud. By modifying the mechanism for the determination of the initial conditions, the modeling of the blast wave in this thesis can be considered as an intermediate solution between the simple empirical models and the much more complex computational fluid dynamics models.

The treatment of uncertainties has also been taken into consideration of this thesis. In fact, the parameter uncertainty could be problematic to be quantified. In this thesis, the methodology for choosing the probability distribution and the relevant statistical parameters for the uncertainty analysis were presented. The propagation of the uncertain parameter into the calculation model was performed by a standard Monte Carlo simulation. The sampling procedure aimed to generate a sufficient numbers of random variable representing the stochastic properties of the parameter under consideration. The procedure can be applied in different situations as illustrated by several case studies. The decision and degree of satisfaction of the uncertainty simulation will depend on how accurate the parameter quantification.

6.2 Outlook and recommendations

The procedure for incorporating the effect of uncertain parameters into the prediction of the blast overpressure and the vulnerability study of risk assessment has been proposed in this thesis. However, the analysis would be much better if the dispersion analysis is also performed. Thus, the best estimate of the dimension of the vapor cloud including the quantity of the flammable mass can be obtained. Several commercial software, such as DNV PHAST or ALOHA, has capability of providing such information in much detail. In the future, the simulation results from such a software can be integrated with the procedure for accounting the effect of uncertainty. With respect to the explosion modeling, some commercial softwares, such as PHAST, provide the blast overpressure as a fixed value based on a certain location of ignition. This location is often specified by the user, for example, at the cloud edge at which the lower flammability limit has been reached. There has been no model for integrating the stochastic position of the ignition location.

With respect to the uncertainty analysis itself, the sampling procedure was based on a standard Monte Carlo sampling. Recently, many advanced techniques have been made available with the main purpose to reduce the computational cost. These techniques could be integrated to the procedure mentioned above in order to improve the outcome.

With respect to the determination of the maximum overpressure in the vapor cloud while using the empirical models, since no correlations available for some categories which are not yet covered by current sets of correlation, some efforts are necessary to be made. These correlations can be obtained experimentally for different situations.

Bibliography

[1] J. S. Ramiro and P. B. Aisa, *Risk Analysis and Reduction in the Chemical Process Industry*, Blackie Academic & Professional, 1998.

[2] M. Rausand and A. Høyland, *System Reliability Theory: Models, Statistical Methods, and Applications*, John Wiley & Sons Inc. New Jersey, 2004.

[3] R. L. Brauer, *Safety and Health for Engineers*, John Wiley & Sons Inc. New Jersey, 2006.

[4] H. P. Cordi, Industrial Explosion, in *2010 NASA Occupational Health Conference, June 8th*, 2010.

[5] T. Abbasi, H. Pasman, and S. Abbasi, *Journal of Hazardous Materials* **174**, 270 (2010).

[6] C. E. Baukal and R. E. Schwartz, editors, *The John Zink Combustion Handbook*, CRC Press, 2001.

[7] *Major hazard control: A practical manual*, International Labour Organization, Geneva, 1993.

[8] J. A. Vlchez, V. Espejo, and J. Casal, *Journal of Loss Prevention in the Process Industries* **24**, 281 (2011).

[9] A. Di Benedetto, *Journal of Loss Prevention in the Process Industries* **22**, 257 (2009).

[10] S. Carol, J. A. Vilchez, and J. Casal, *Journal of Loss Prevention in the Process Industries* **15**, 517 (2002).

[11] F. P. Lees, *Loss Prevention in the Process Industries: hazard identification, assessment and control*, volume 2, Elsevier Butterworth-Heinemann, third edition, 2005.

[12] P. Davies, *Journal of Hazardous Materials* **33**, 1 (1993).

[13] J. Puttock, M. Yardley, and T. Cresswell, *Journal of Loss Prevention in the Process Industries* **13**, 419 (2000).

[14] *McGraw-Hill Encyclopedia of Science & Technology*, McGraw-Hill, 10th edition, 2007.

[15] *Guidelines for Consequence Analysis of Chemical Releases*, Center for Chemical Process Safety (CCPS) of the American Institute of Chemical Engineers, 1999.

[16] D. A. Crowl, *Understanding Explosions*, Center for Chemical Process Safety of the American Institute of Chemical Engineers, 2003.

[17] M. Liberman, Flame, detonation, explosion - When, where and how they occur, in *3rd International Disposal Conference, Karlskoga, Sweden*, 2003.

[18] J. Warnatz, U. Maas, and R. W. Dibble, *Combustion: Physical and Chemical Fundamentals, Modeling and Simulation, Experiments, Pollutant Formation*, Springer-Verlag Berlin Heidelberg, fourth edition, 2006.

[19] I. Zeldovich, G. Barenblatt, V. Librovich, and G. Makhviladze, *Mathematical theory of combustion and explosions*, Consultants Bureau,New York, NY, 1985.

[20] D. Bjerketvedt, J. R. Bakke, and K. van Wingerden, *Journal of Hazardous Materials* **52**, 1 (1997).

[21] W. Mercx and A. van den Berg, *Methods for the calculation of physical effects - CPR 14E ("Yellow Book")*, chapter Vapour cloud explosion, Committee for the Prevention of Disasters, The Netherlands, third edition, 1997.

[22] *Guidelines for Evaluating the Characteristics of Vapour Cloud Explosion, Flash Fires and BLEVEs*, Center for Chemical Process Safety (CCPS) of the American Institute of Chemical Engineers, 1994.

[23] N. Peters, *Turbulent combustion*, Cambridge University Press, Cambridge, 2000.

[24] D. P. Nolan, *Handbook of fire and explosion protection engineering principles for oil, gas, chemical, and related facilities*, Noyes Publications, 1996.

[25] R. Harris, *The investigation and control of gas explosions in buildings and heating plants*, British gas corporation, Midlands, England,, 1983.

[26] J. Zeeuwen, C. van Wingerden, and R. Dauwe, Experimental investigation into the blast effect produced by unconfined vapor cloud explosions, in *4th International Symposium on Loss Prevention and Safety Promotion in the Process Industries*, 80, pp. D20–D29, IChemE UK, 1983.

[27] O. Sæter, *Modelling and Simulation of gas explosions in complex geometries*, PhD thesis, Institute of Process Technology, Telemark College, Norway, 1998.

[28] B. J. Arntzen, *Modelling of turbulence and combustion for simulation of gas explosions in complex geometries*, PhD thesis, Norwegian University of Science and Technology, Trondheim, Norway, 1998.

[29] L. D. Landau and E. Lifshitz, *Fluid mechanics*, Pergamon Press Oxford, 1989.

[30] K.-L. Pan, *Physics of Fluids* **20**, 044106 (2008).

[31] R. C. Aldredge and B. Zuo, *Combustion and Flame* **127**, 2091 (2001).

[32] H. Philips, *Explosions in the Process Industries*, Institution of Chemical Engineers (IChemE), UK, second edition edition, 1994.

[33] *Guidelines for Chemical Process Quantitative Risk Analysis*, Center for Chemical Process Safety (CCPS) of the American Institute of Chemical Engineers, 2000.

[34] A. Masri, S. Ibrahim, and B. Cadwallader, *Experimental Thermal and Fluid Science* **30**, 687 (2006).

[35] V. Knudsen, *Hydrogen gas explosions in pipelines - modeling and experimental investigations*, PhD thesis, Telemark University College Norway & Norwegian University of Science and Technology, 2006.

[36] M. Neff, A Visual Model for Blast waves and Fracture, Master's thesis, Department of Computer Science, University of Toronto, Canada, 1998.

[37] W. E. Baker, *Explosions in air*, University of Texas Press, Austin, 1973.

[38] S. R. Avasarala, Blast Overpressure Relief Using Air Vacated Buffer Medium, Master's thesis, School of Engineering, Massachusetts Institute of Technology, 2009.

[39] C. Wilkinson and J. G. Anderson, An Introduction to Detonation and Blast for the Non Specialist, Technical report, Weapons Systems Division, DSTO Systems Sciences Laboratory, Australia, 2003.

[40] R. J. Spear and W. S. Wilson, *Journal of Energetic Materials* **2**, 61 149 (1984).

[41] G. Szuladzinski, *Formulas for Mechanical and Structural Shock and Impact*, CRC Press, Taylor and Francis Group, LLC, 2010.

[42] J. Akhavan, *The Chemistry of Explosives*, The Royal Society of Chemistry, UK, 1998.

[43] B. H. Hjertager, K. Fuhre, and M. Bjrkhaug, *Combustion Science and Technology* **62**, 239 (1988).

[44] D. Stull, Fundamentals of Fire and Explosion, AIChE Monograph Series No. 10, 1977.

[45] V. Marshall and S. Ruhemann, *Fundamentals of Process Safety*, Institution of Chemical Engineers (IChemE), 2001.

[46] E. M. Lenoir and J. A. Davenport, *Process Safety Progress* **12 Issue 1**, 12 (1993).

[47] S. Høiset, B. H. Hjertager, T. Solberg, and K. A. Malo, *Journal of Hazardous Materials* **77**, 1 (2000).

[48] K. van Wingerden, H.-C. Salvesen, and R. Perbal, *Proc. Safety Prog.* **14**, 173 (1995).

[49] A. M. Hull, D. A. Alexander, and S. Klein, *The British Journal of Psychiatry* **181**, 433 (2002).

[50] F. I. Khan and P. R. Amyotte, *Journal of Loss Prevention in the Process Industries* **20**, 387 (2007).

[51] BP Texas City Refinery Explosion and Fire - Investigation Report, Technical report, U.S. Chemical Safety and Hazard Investigation Board, 2007.

[52] The Buncefield Incident 11 December 2005: the final report of the Major Incident Investigation Board, Technical report, 2008.

[53] G. Chamberlain, The Buncefield Incident Formation of the flammable cloud and explosion mechanism., in *Magdeburger Brand-und Explosionschutztag I, 19th August*, 2008.

[54] Buncefield explosion mechanisms Phase 1: Volume 1 and 2, Technical report, Health and Safety Executive, UK, 2009.

[55] D. M. Johnson, *Journal of Loss Prevention in the Process Industries* **23**, 921 (2010).

[56] P. D. Smith and J. Hetherington., *Blast and Ballistic Loading of Structures*, Butterworth and Heinemann Ltd, 1994.

[57] J. Casal, *Evaluation of the effects and consequences of major accidents in industrial Plants*, Elsevier Amsterdam, 2008.

[58] D. J. Park, *Experimental Investigation Gas Explosions in Partially Confined Regions*, PhD thesis, School of Safety Science, The University of New South Wales, Sydney, 2007.

[59] R. A. Ogle, *Process Safety Progress* **18**, 170 (1999).

[60] P. F. Mlakar and D. Barker, *Handbook for Blast Resistant Design of Buildings*, chapter Blast Phenomena, pp. 159–181, John Wiley & Sons Inc. New Jersey, 2010.

[61] I. T. Cameron and R. E. Raman, Effect models for consequence analysis, in *Process Systems Risk Management*, edited by I. T. Cameron and R. Raman, volume 6, chapter 6, pp. 195–259, Academic Press, 2005.

[62] A. Przekwas, *Explosion and Blast-related Injuries*, chapter Multiscale Computational Modeling of Lung Blast Injuries, Elsevier Academic Press, 2008.

[63] *Methods for determining the potential damage to humans and the surrounding area resulting from the release of hazardous substances (Green Book)*, TNO, Dutch Ministry of Housing, Physical Planning and Environment. The Netherlands, 1992.

[64] T. A. Melton and J. D. Marx, *Journal of Loss Prevention in the Process Industries* (2009).

[65] P. R. Lee, *Explosive Effcets and Applications*, chapter Explosive Development and Fundamentals of Explosive Technology, pp. 23–45, Springer New York, 1998.

[66] H. Kleine, J. Dewey, K. Ohashi, T. Mizukaki, and K. Takayama, *Shock Waves* **13**, 123 (2003).

[67] W. E. Baker, P. A. Cox, P. S. Westine, J. J. Kulesz, and R. A. Strehlow, *Explosion hazards and evaluation*, Elsevier, Amsterdam, 1983.

[68] J. M. Dewey, *Shock Waves* (2007).

[69] M. Tang and Q. Baker, *Process Safety Progress* **18 issue 4**, 235 (1999).

[70] S. A. Formby and R. K. Wharton, *Journal of Hazardous Materials* **50**, 183 (1996).

[71] P. e. a. Philip J. DiNenno, editor, *SFPE Handbook of Fire Protection Engineering*, National Fire Protection Association, 3rd edition, 2002.

[72] A. van den Berg and A. Lannoy, *Journal of Hazardous Material* **34**, 151 (1993).

[73] H. L. Brode, *Journal of Applied Physics* **26**, 766 (1955).

[74] M. Held, *Propellants, Explosives, Pyrotechnics* **15**, 149 (1990).

[75] C. E. Needham, *Blast Waves*, Springer-Verlag Berlin Heidelberg, 2010.

[76] A. Birk, C. Davison, and M. Cunningham, *Journal of Loss Prevention in the Process Industries* **20**, 194 (2007).

[77] A. Pandey, R. Kumar, D. Paul, and D. Trikha, *Nuclear Engineering and Design* **236**, 993 (2006).

[78] D. A. Crowl and J. F. Louvar, *Chemical Process Safety: Fundamentals with Applications*, Prentice Hall , Inc., 2nd ed. edition, 2002.

[79] U. Hauptmanns, Brände und Explosionen im Rahmen Der Risikoermittlung, in *Magdeburger Brand- und Explosionsschutztag II*, 2010.

[80] J. Eggen, GAME: development of the application of the multi-energy method, Research report, TNO Prins Maurits Laboratory, 1998.

[81] A. F. Roberts and D. K. Pritchard, *Journal of Occupational Accidents* **3**, 231 (1982).

[82] A. Huser, T. Foyn, and M. Skottene, *Journal of Loss Prevention in the Process Industries* **22**, 324 (2009).

[83] *Methods for the calculation of the Physical Effects of the Escape of Dangerous Materials - CPR 14E*, Committee for the Prevention of Disasters, The Netherlands, 1979.

[84] B. J. Wiekema, *Journal of Hazardous Materials* **3**, 221 (1980).

[85] A. C. van den Berg, *Journal of Hazardous Materials* **12, Issue 1**, 1 (1985).

[86] W. Mercx, R. van Wees, and G. Opschoor, *Process Safety Progress* **12**, 222 (1993).

[87] W. Mercx, A. van den Berg, C. Hayhurst, N. Robertson, and K. Moran, *Journal of Hazardous Material* **71**, 301 (2000).

[88] A. J. Pierorazio, J. K. Thomas, Q. A. Baker, and D. E. Ketchum, *Process Safety Progress* **24**, 59 (2005).

[89] Det Norske Veritas (DNV) Software, *DNV PHAST Technical Documentation: Obstructed Region Explosion Model (OREM) Theory*, 2010.

[90] J. Zeeuwen and B. Wiekema, The measurement of relative reactivities of combustible gases, in *Conference on Mechanisms of Explosions in Dispersed Energetic Materials, Dover, NJ, USA*, 1978.

[91] Q. A. Baker, M. J. Tang, E. A. Scheirer, and G. J. Silva, *Process Safety Progress* **15**, 106 (1996).

[92] M. Roberts and W. Crowley, Evaluation of flammability hazards in non-nuclear safety analysis, in *14th EFCOG Safety Analysis Workshop. San Fransisco, CA*, 2004.

[93] F. D. Alonso, E. G. Ferradas, J. F. S. Perez, A. M. Aznar, J. R. Gimeno, and J. M. Alonso, *Journal of Loss Prevention in the Process Industries* **19**, 724 (2006).

[94] M. J. Assael and K. E. Kakosimos, *Fires, Explosions, and Toxic Gas Dispersions: Effect Calculation and Risk Analysis*, CRC Press Taylor & Francis Group, 2010.

[95] R. Strehlow, R. Luckritz, A. Adamczyk, and S. Shimpi, *Combustion and Flame* **35**, 297 (1979).

[96] Q. A. Baker, C. M. Doolittle, G. A. Fitzgerald, and M. J. Tang, *Process Safety Progress* **17**, 297 (1998).

[97] Det Norske Veritas, London, *DNV PHAST 6.7 Software*.

[98] H. K. Versteeg and W. Malalasekera, *An introduction to Computational Fluid Dynamics: The Finite Volume Method*, Longmann Scientific & Technical, England, 1995.

[99] H. I. Breckner, *Approximation and Optimal Control of the Stochastic Navier-Stokes Equation*, PhD thesis, Mathematisch-Naturwissenschaftlich-Technischen Fakultät der Martin-Luther-Universität Halle-Wittenberg, 1999.

[100] C. Helzel, *Numerical Approximation of Conservation Laws with Stiff Source Term for the Modelling of Detonation Waves*, PhD thesis, Otto-von-Guericke-University of Magdeburg, 2000.

[101] E. F. Toro, *Riemann Solvers and Numerical Methods for Fluid Dynamics : A Practical Introduction*, Springer-Verlag Berlin Heidelberg New York, third edition, 2009.

[102] W. C. Davis, *Explosive Effects and Application*, chapter Shock Waves, Rarefaction Waves, Equations of State, pp. 47–113, Springer New York, 1998.

[103] W. Griffith and W. Bleakney, *American Journal of Physics* **22**, 597 (1954).

[104] R. J. LeVeque, *Finite Volume Methods for Hyperbolic Problems*, Cambridge University Press, 2002.

[105] I. Danaila, P. Joly, S. M. Kaber, and M. Postel, *An Introduction to Scientific Computing: Twelve Computational Projects Solved with MATLAB*, Springer-Verlag New York, LLC, 2006.

[106] V. Guinot, *Godunov-type Schemes: An Introduction for Engineers*, Elsevier Science, 2003.

[107] G. Puigt and H. Deniau, CFD e-Learning: Euler equations and discretization of convection, Centre Européen de Recherche et de Formation Avancée en Calcul Scientifique (CERFACS), Tolouse, France, 2011.

[108] D. J. Higham and N. J. Higham, *MATLAB Guide*, Society for Industrial & Applied Mathematics, 2nd ed. edition, 2005.

[109] A. Gilat, *MATLAB: An Introduction with Applications*, Wiley, New York, 2008.

[110] B. R. Hunt, R. L. Lipsman, and J. M. Rosenberg, *A Guide to MATLAB for Beginners and Experienced Users*, Cambridge University Press, 2nd ed. edition, 2006.

[111] G. A. Sod, *Journal of Computational Physics* **27**, 1 (1978).

[112] C. B. Laney, *Computational gasdynamics*, Cambridge University Press, 1998.

[113] D. Stanescu, Comparison of several numerical methods for solving the Euler equations for compressible aerodynamic flows, Master's thesis, Department of Mechanical Engineering, McGill University, 1994.

[114] O. Zanotti and G. M. Manca, A very short introduction to Godunov methods, in *Lecture Notes for the COMPSTAR School on Computational Astrophysics, Caen, France, 8th-13th February*, Albert Einstein Institute, Max-Planck Institute for Gravitational Physics, Potsdam, Germany, 2010.

[115] A. Kurganov and E. Tadmor, *Numer. Methods Partial Differential Eq.* **18**, 584 (2002).

[116] *Risk Analysis and Uncertainty in Flood Reduction Studies*, National Research Council, US. National Academic Press, 2000.

[117] M. Abrahamsson, Uncertainty in Quantitative Risk Analysis - Characterisation and Method of Treatment, Master's thesis, Lund University, 2002.

[118] M. Dourin, G. Parry, J. Lehner, G. Martinez, J. LaChance, and T. Wheeler, Guidance on the Treatment of Uncertainties Associated with PRAs in Risk-Informed Decision Making, Technical report, US Nuclear Regulatory Commission, 2009.

[119] U. Hauptmanns, Determination of uncertainties in safety studies for nuclear and chemical plants and their interpretation, in *Proceedings of the European Conference on Safety and Reliability (ESREL), Trondheim, Norway.*, pp. 443–450, 1998.

[120] N. Johnson, S. Kotz, and N. Balakhrisnan, *Continuous Univariate Distributions*, volume I, John Wiley & Sons New York, 1994.

[121] N. Johnson, S. Kotz, and N. Balakhrisnan, *Continuous Univariate Distributions*, volume II, John Wiley & Sons, New York, 1995.

[122] U. Hauptmanns and W. Werner, *Engineering Risks - Evaluation and Valuation*, Springer, Berlin, 1991.

[123] Centre for External Safety, National Institute of Public Health and the Environment (RIVM), the Netherlands, *Reference Manual Bevi Risk Assessment version 3.1*, 2009.

[124] Illustrative model of a risk based land use planning system around petroleum storage sites., Technical report, Det Norske Veritas Ltd for Buncefield Major Incident Investigation Board, 2008.

[125] *Guidelines for quantitative risk assessment (Purple book)*, TNO, Dutch Ministry of Housing, Physical Planning and Environment. The Netherlands, 1999.

[126] B. J. Wiekema, *Journal of Hazardous Materials* **8**, 295 (1984).

[127] U. Hauptmanns and M. Marx, *Kriterien für die Beurteilung von Gefährdungen durch technische Anlagen*, Verlag VdTÜV, 2010.

[128] M. Gawlowski, M. Hailwood, I. Vela, and A. Schönbucher, *Chem. Eng. Technol.* **32**, 182 (2009).

[129] E. Salzano and V. Cozzani, *Reliability Engineering & System Safety* **90**, 271 (2005).

[130] Y.-D. Jo and J.-Y. Kim, *Korean Journal of Chemical Engineering* **18**, 292 (2001).

[131] V. Clancey, Diagnostic features of explosion damage, in *Sixth International Meeting of Forensic Sciences, Edinburgh*, 1972.

[132] Vulnerability models, in *Process Systems Risk Management*, edited by I. T. Cameron and R. Raman, volume 6, chapter 7, pp. 261–285, Academic Press, 2005.

[133] D. Finney, *Probit analysis*, Cambridge University Press, 1971.

[134] N. A. Eisenberg, C. J. Lynch, and R. J. Breeding, Vulnerability model: A simulation system for assessing damage resulting from marine spills, NTIS Report CG-D-136-75, U.S. Coast Guard Office of Research and Development, Washington DC, 1975.

This page intentionally left blank

Appendix A: Kingery-Bulmash Model

The Kingery-Bulmash equations can be used to predict the parameters of the blast wave parameters from a TNT charge detonation. Therefore, this equation can also be implemented for the TNT equivalent method giving that the TNT equivalent mass and explosion efficiency are given. IN general, for a given parameter ϕ representing the blast parameter of interest, the following relation is given by Kingery and Bulmash:

$$U = a + b \log z \tag{A.1}$$

where z is the Hopkinson's scaled distance. The function ϕ is expressed in the 8th and 11th order of polynomial equations which are written in general as follows:

$$\log \phi = \sum_{i=0}^{n} c_i \cdot U^i \tag{A.2}$$

The constant values of a, b and c for both the free air and surface explosion are listed the following Tables A.1 and A.2.

Table A.1. *Constants used in Kingery-Bulmash polynomial equations for a free air burst [11]*

Range		Parameter			
constant		Δp_o [kPa]	i_p [kPa.ms]	t_d [ms]	t_a [ms]
1		$0.0531 \leq z \leq 40$	$0.0531 \leq z \leq 0.792$	$0.147 \leq z \leq 0.888$	$0.0531 \leq z \leq 40$
2		-	$0.792 \leq z \leq 40$	$0.888 \leq z \leq 2.28$	-
3		-	-	$2.88 \leq z \leq 40$	-
1	a	-0.214 362 789 151	2.347 239 213 54	2.263 672 684 96	-0.253 273 111 999
2		-	-1.753 056 603 15	-1.333 612 067 14	-
3		-	-	-3.130 058 053 46	-
1	b	1.350 342 499 93	3.242 990 664 75	5.115 885 543 05	1.374 070 437 77
2		-	2.306 292 318 03	9.299 628 861 1	-
3		-	-	3.152 472 536 4	-
1	c_0	2.611 368 669	2.388 305 167 57	-0.686 608 550 419	0.072 070 778 763 7
2		-	1.551 972 271 15	0.230 318 410 78	-
3		-	-	0.621 036 276 475	-
1	c_1	-1.690 128 013 9	-0.443 749 377 691	-0.164 953 518 069	1.364 568 712 14
2		-	0.404 632 920 88	-0.029 794 426 896 9	-
3		-	-	0.096 703 199 555 2	-
1	c_2	0.008 049 735 919 51	0.168 825 414 684	0.127 788 499 497	-0.057 003 569 278 4
2		-	0.014 272 194 608 2	0.030 632 954 294 1	-
3		-	-	-0.008 013 020 596 67	-
1	c_3	0.336 743 114 941	0.034 813 803 030 8	0.002 91 430 135 946	-0.182 832 224 796
2		-	0.009 123 663 166 17	0.018 340 557 407 4	-
3		-	-	0.004 827 057 797 32	-
1	c_4	-0.005 162 263 513 34	-0.010 435 192 824	0.001 879 574 492 27	0.011 885 143 601 4
2		-	-0.000 675 068 140 4	-0.017 396 466 628 6	-
3		-	-	0.001 875 872 722 87	-
1	c_5	-0.080 922 861 988 8	-	0.017 341 396 254 3	0.043 264 868 762 7
2		-	-0.008 008 637 189 01	-0.001 063 219 635 76	-
3		-	-	0.002 467 385 093 21	-
1	c_6	-0.004 785 072 667 47	-	0.002 697 397 580 43	-0.000 799 736 783 4
2		-	0.003 148 195 159 31	0.005 620 600 312 8	-
3		-	-	-0.000 841 116 668	-
1	c_7	0.007 930 304 722 42	-	-0.003 619 765 027 98	-0.004 360 735 550 33
2		-	0.001 520 447 833 82	0.000 161 821 749 9	-
3		-	-	0.000 619 329 105 2	-
1	c_8	0.000 768 446 973 5	-	-0.001 009 265 779 34	-
2		-	0.000 747 026 589 9	-0.000 686 018 894 4	-
3		-	-	-	-

Table A.2. *Constants used in Kingery-Bulmash polynomial equations for a surface air burst [11]*

Range		Parameter			
constant		Δp_o [kPa]	i_p [kPa.ms]	t_d [ms]	t_a [ms]
1		$0.0674 \leq z \leq 40$	$0.0674 \leq z \leq 0.955$	$0.178 \leq z \leq 1.01$	$0.0674 \leq z \leq 40$
2		-	$0.955 \leq z \leq 40$	$1.01 \leq z \leq 2.78$	-
3		-	-	$2.78 \leq z \leq 40$	-
1	a	-0.214 362 789 151	2.067 619 087 21	1.929 461 540 68	0.202 425 716 178
2		-	-1.947 088 467 47	-2.124 925 252 16	-
3		-	-	-3.536 262 180 91	-
1	b	1.350 342 499 93	3.072 032 966 6	5.250 991 939 25	1.377 842 236 35
2		-	2.406 977 454 06	9.299 628 861 1	-
3		-	-	3.463 497 455 71	-
1	c_0	2.780 769 165 77	2.524 556 209 25	-0.614 227 603 559	0.059 163 428 804 6
2		-	1.672 816 458 63	0.315 409 245 784	-
3		-	-	0.686 906 642 409	-
1	c_1	-1.695 898 874 1	-0.502 992 763 686	0.130 143 717 675	1.357 064 962 58
2		-	0.384 519 026 965	-0.029 794 426 897 6	-
3		-	-	0.093 303 530 400 9	-
1	c_2	-0.154 159 376 846	0.171 335 645 235	0.134 872 511 954	0.052 492 798 645
2		-	-0.026 081 670 630 1	0.030 632 954 288	-
3		-	-	-0.000 584 942 088 3	-
1	c_3	0.514 060 730 593	0.045 017 696 305 1	0.039 157 427 690 6	-0.196 563 954 086
2		-	0.005 957 987 538 22	0.018 340 557 408 6	-
3		-	-	-0.002 268 849 950 13	-
1	c_4	0.098 853 436 527 4	-0.011 869 462 640 2	-0.004 759 336 647 02	-0.060 177 005 228 8
2		-	0.014 544 526 107	-0.017 369 466 621 1	-
3		-	-	-0.002 959 085 915 05	-
1	c_5	-0.293 912 623 038	-	-0.004 281 445 980 08	0.069 636 027 089 1
2		-	-0.006 632 893 347 34	0.001 063 219 636 33	-
3		-	-	0.001 480 298 689 29	-
1	c_6	-0.026 811 234 501 9	-	-	0.021 529 749 009 2
2		-	-0.002 841 893 272 04	0.005 620 600 309 77	-
3		-	-	-	-
1	c_7	0.109 097 469 421	-	-	-0.016 165 893 078 5
2		-	0.001 364 481 622 7	0.000 161 821 749 9	-
3		-	-	-	-
1	c_8	0.001 628 467 563 11	-	-	-0.002 325 319 702 94
2		-	0.000 747 026 589 9	-0.000 686 018 894 4	-
3		-	-	-	-
1	c_9	-0.021 463 103 024 2	-	-	0.001 477 520 675 24
2		-	0.000 747 026 589 9	-	-
3		-	-	-	-
1	c_{10}	0.000 145 672 338 2	-	-	-
2		-	0.000 747 026 589 9	-	-
3		-	-	-	-
1	c_{11}	0.001 678 477 522 66	-	-	-
2		-	0.000 747 026 589 9	-	-
3		-	-	-	-

Appendix B: Constants for the equations of the Blast curves

B.1 Constants for the fitted equations for the TNO Multi-Energy blast curve family

Table B.1. *Coefficients for Eq. (3.27)*

Blast strength	Range	a	b	c	d
Level 1	$0.23 \leq x < 0.53$	1.00E-2	-	-	-
	$x > 0.53$	6.23E-3	-0.95	-	-
Level 2	$0.23 \leq x < 0.60$	1.00E-2	-	-	-
	$x > 0.60$	1.22E-2	-0.98	-	-
Level 3	$0.23 \leq x < 0.60$	5.00E-2	-	-	-
	$x > 0.60$	3.05E-2	-0.97	-	-
Level 4	$0.23 \leq x < 0.55$	1.00E-1	-	-	-
	$x > 0.55$	6.20E-2	-0.97	-	-
Level 5	$0.23 \leq x < 0.55$	2.00E-1	-	-	-
	$x > 0.55$	1.10E-1	-0.99	-	-
Level 6	$0.23 \leq x < 0.56$	5.00E-1	-	-	-
	$0.56 \leq x \leq 3.50$	3.00E-1	-1.10	-	-
	$x > 3.50$	0	-	1.1188	0.5120
Level 7	$0.23 \leq x < 0.50$	1.00E+0	-	-	-
	$0.50 \leq x \leq 1.0$	4.60E-1	-1.20	-	-
	$1.00 \leq x \leq 2.50$	-	-	1.5236	0.3372
	$x > 2.50$	-	-	1.1188	0.5120
Level 8	$0.23 \leq x < 0.50$	2.00E+0	-	-	-
	$0.50 \leq x \leq 0.60$	4.67E-1	-2.08	-	-
	$0.60 \leq x \leq 1.0$	-	-	2.3721	0.3372
	$1.00 \leq x \leq 2.50$	-	-	1.5236	0.3372
	$x > 2.50$	-	-	1.1188	0.5120
Level 9	$0.23 \leq x < 0.35$	5.00E+0	-	-	-
	$0.35 \leq x \leq 1.00$	-	-	2.3721	0.3372
	$1.00 \leq x \leq 2.50$	-	-	1.5236	0.3372
	$x > 2.50$	-	-	1.1188	0.5120
Level 10	$0.23 \leq x < 1.00$	-	-	2.3721	0.3372
	$1.00 \leq x \leq 2.50$	-	-	1.5236	0.3372
	$x > 2.50$	-	-	1.1188	0.5120

B.2 Constants for the fitted equations for the Baker-Strehlow-Tang blast curve family

Table B.2. *Coefficients for Eq. (3.33)*

M_f	x range	a	b	c	d	e	f	g	h	p	q
0.07	$x \leq 0.15$	0.01	-	-	-	-	-	-	-	-	-
	$0.15 < x \leq 2.10$	-	-0.933128	-2.888832	-1.737895	0.920042	0.087748	-1.005685	-2.377646	-	-
	$x > 2.10$	-	-	-	-	-	-	-	-	-1.011736	-2.365616
0.12	$x \leq 0.15$	0.028	-	-	-	-	-	-	-	-	-
	$0.15 < x \leq 2.10$	-	-0.933128	-2.888832	-1.737895	0.920042	0.087748	-1.005685	-1.930488	-	-
	$x > 2.10$	-	-	-	-	-	-	-	-	-1.011736	-1.918458
0.20	$x \leq 0.15$	0.065739	-	-	-	-	-	-	-	-	-
	$0.15 < x \leq 2.10$	-	-0.933128	-2.888832	-1.737895	0.920042	0.087748	-1.005685	-1.559823	-	-
	$x > 2.10$	-	-	-	-	-	-	-	-	-1.011736	-1.547793
0.35	$x \leq 0.16$	0.218	-	-	-	-	-	-	-	-	-
	$0.16 < x \leq 1.70$	-	-0.058243	-1.513539	-1.509913	0.602095	0.106104	-1.005685	-0.962616	-	-
	$x > 1.70$	-	-	-	-	-	-	-	-	-0.996587	-1.037988
0.70	$x \leq 0.19$	0.68	-	-	-	-	-	-	-	-	-
	$0.19 < x \leq 2.37$	-	3.14094	4.025197	-0.520525	-1.615733	-0.553277	-0.724239	-0.523105	-	-
	$x > 2.37$	-	-	-	-	-	-	-	-	-1.160157	-0.494153
1.00	$x \leq 0.12$	1.24	-	-	-	-	-	-	-	-	-
	$0.12 < x \leq 2.26$	-	-2.650731	-5.975678	-2.655464	1.920581	0.417161	-1.408333	-0.488746	-	-
	$x > 2.26$	-	-	-	-	-	-	-	-	-1.113825	-0.535492
1.40	$x \leq 0.17$	2.00	-	-	-	-	-	-	-	-	-
	$0.17 < x \leq 2.21$	-	-2.318816	-8.107616	-6.830475	1.070003	1.567781	-1.353722	-0.492033	-	-
	$x > 2.21$	-	-	-	-	-	-	-	-	-1.138989	-0.475584
2.00	$x \leq 0.12$	5.00	-	-	-	-	-	-	-	-	-
	$0.12 < x \leq 2.27$	-	14.12624	22.55578	2.850864	-5.885056	-0.10116	-0.954886	-0.418265	-	-
	$x > 2.27$	-	-	-	-	-	-	-	-	-1.174514	-0.415406
3.00	$x \leq 0.18$	10.00	-	-	-	-	-	-	-	-	-
	$0.18 < x \leq 1.86$	-	-21.67565	-11.63587	7.95783	1.56914	-0.57778	-1.267661	-0.396133	-	-
	$x > 1.86$	-	-	-	-	-	-	-	-	-1.174514	-0.415406
4.00	$x \leq 0.16$	15.2	-	-	-	-	-	-	-	-	-
	$0.16 < x \leq 2.25$	-	-14.87262	-12.50994	2.727597	1.731734	0.159062	-1.319884	-0.405275	-	-
	$x > 2.25$	-	-	-	-	-	-	-	-	-1.174514	-0.415406
5.20	$x \leq 0.17$	20.0	-	-	-	-	-	-	-	-	-
	$0.17 < x \leq 2.27$	-	18.600175	19.416571	0.730754	-4.407614	-0.06318	-1.08988	-0.399327	-	-
	$x > 2.27$	-	-	-	-	-	-	-	-	-1.174514	-0.415406

Appendix C: Computational flow for solving the Euler equations of gas dynamics

C.1 The Exact Riemann Solver Module

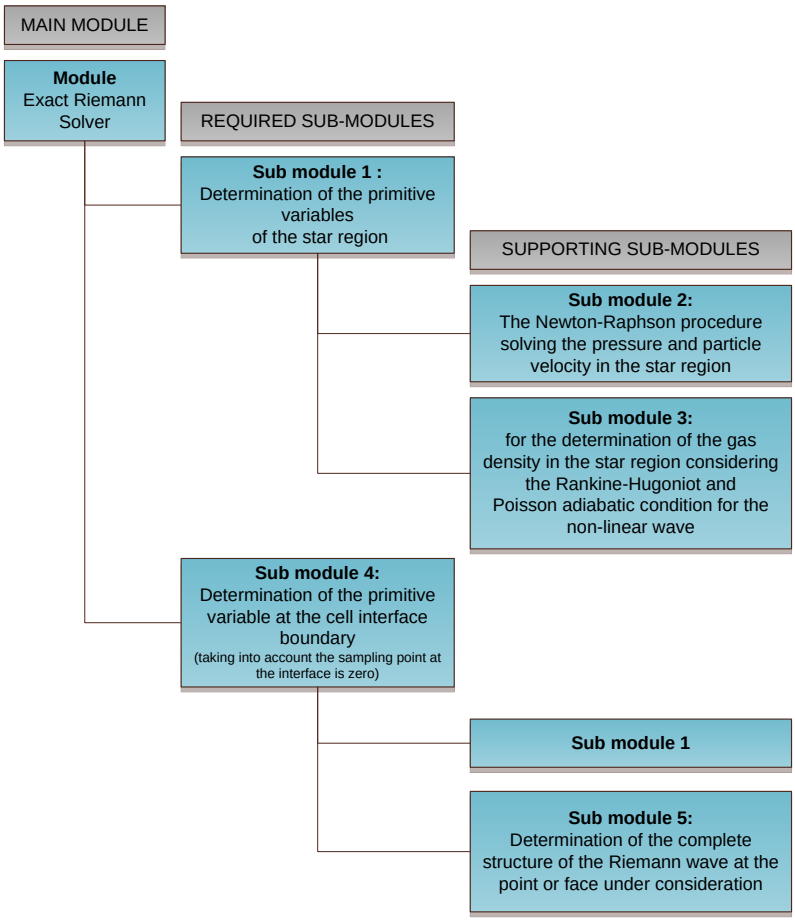

C.2 The Euler Equations Solver Module

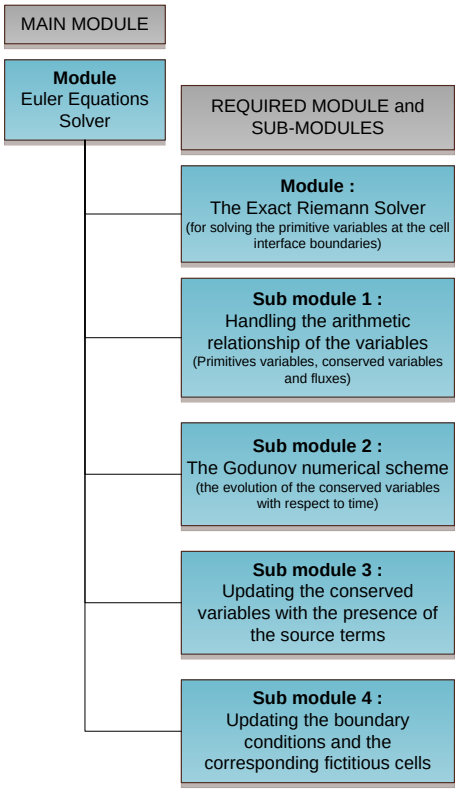

Lebenslauf

Name	:	Arizal
Adresse	:	Borbergstr. 16, 59065 Hamm
Geburtsdatum	:	22. September 1980
Geburtsort	:	Batusangkar, Indonesien
Staatsangehörigkeit	:	Indonesisch

Ausbildung:

Schulbildung

08.1986 - 06.1992	:	Grundschule in Batusangkar, Indonesien
08.1992 - 06.1995	:	Mittelschule in Batusangkar, Indonesien
08.1995 - 05.1998	:	Oberschule in Batusangkar, Indonesien

Studium

08.1998 - 01.2003	:	Studium der Kerntechnik an der Gadjah Mada Universität, Yogyakarta, Indonesien mit dem Abschluss als "Bachelor of Science (B.Sc)"
10.2005 - 11.2006	:	Studium der Masterstudiengang "Quality, Safety and Environment", an der Otto-von-Guericke Universität Magdeburg als Stipendiat des "Deutscher Akademischer Austauschdient (DAAD)" mit dem Abschluss als "Master of Science (M.Sc)"
ab 2007 - 08.2012	:	Doktorand am Lehrstuhl für Anlagentechnik und Anlagensicherheit der Fakultät für Verfahrens- und Systemtechnik, Otto-von-Guericke Universität Magdeburg

Berufserfahrung:

04.2002 - 05.2005	:	Wissenschaftlicher Mitarbeiter am Energie-Forschungszentrum der Gadjah Mada Universität Yogyakarta, Indonesien
ab 04.2012 -	:	Projektingenieur im Bereich Prozesssicherheit Inburex Consulting GmbH, Hamm